Spring 2014

Development of image processing tools and procedures for analyzing multi-site longitudinal diffusion-weighted imaging studies

Joy Tamiko Matsui
University of Iowa

DEVELOPMENT OF IMAGE PROCESSING TOOLS AND PROCEDURES FOR ANALYZING MULTI-SITE LONGITUDINAL DIFFUSION-WEIGHTED IMAGING STUDIES

by

Joy Tamiko Matsui

A thesis submitted in partial fulfillment of the
requirements for the Doctor of Philosophy
degree in Biomedical Engineering
in the Graduate College of
The University of Iowa

May 2014

Thesis Supervisor: Assistant Professor Hans J. Johnson

Graduate College
The University of Iowa
Iowa City, Iowa

CERTIFICATE OF APPROVAL

PH.D. THESIS

This is to certify that the Ph.D. thesis of

Joy Tamiko Matsui

has been approved by the Examining Committee for the thesis requirement for the Doctor of Philosophy degree in Biomedical Engineering at the May 2014 graduation.

Thesis Committee: _____
Hans J. Johnson, Thesis Supervisor

_____
Gary E. Christensen

_____
Dawei Liu

_____
Vincent A. Magnotta

_____
Peggy C. Nopoulos

_____
Joseph M. Reinhardt

_____
Daniel R. Thedens

To my late grandfather, Haines Susumu Matsui, the first research scientist of the family (his genes are making my career in medicine and engineering a reality).

To my grandmothers, Edna Takako Matsui and Hazel Tamiko Sonoda, two of the toughest women ever (their genes of pure iron keep me going).

ACKNOWLEDGEMENTS

Peg and Shannon (now Research Grandma): thank you for giving me a shot as a Doris Duke fellow and continuing to support me even after my fellowship. Hans and Vince: thank you for taking a chance by letting a medical student do image processing. My very multi-disciplinary thesis committee: thank you for all that you have taught me, especially Research Grandpa Gary. Regina: thank you for being my partner in crime and understanding how I felt 100% of the time. My lab: thank you for all the help and entertainment. I always felt I belonged with you folks. I feel very lucky to have worked with both talented and kind-hearted people. I will always have strange memories of Kent, Dave, Eric, and Daniel. I will have less strange memories of Kathy, Jacquie, Jessica, Ali, Mark, and Chen. Jatin: thank you for teaching me how to write papers so I can publish and not perish. Jeff and Jim: thank you for all the crash courses in stats. Liz: thank you for keeping the ball rolling and everyone laughing. Colleagues from the NA-MIC organization: thank you for my first open source experience.

Josh: thank you for still being with me. You deserve an honorary PhD for your patience, unconditional love, and remaining desire to get a PhD of your own. My Krew of PhD students: thank you for your kindness, friendship, and bluntness. Tara: thank you for always calming me down and making me see the big picture. Kenny: thank you for being my dog and "research assistant." My family: thank you for being supportive of my endeavors. If you're reading this, that means I made it.

ABSTRACT

The complexities of performing multi-site longitudinal diffusion-weighted imaging (DWI) studies requires careful construction of analysis tools and procedures. Proposed clinical trials for therapies in neurodegenerative disease are known to require several hundred subjects, thus mandating multiple site participation to obtain sufficient sample sizes. DWI is an important tool for monitoring diffusivity properties of white matter (WM) in disease progression. The multi-site nature of clinical trials requires new strategies in DWI processing and analysis to reliably measure longitudinal WM changes. This work describes the process of developing and validating robust analysis methodologies to process multi-site DWI data in a rare, neurodegenerative disease. Key processing components to accomplish a robust DWI processing system include: DICOM conversion, automated quality control, unbiased atlas construction, fiber tracking, and statistical analysis. Extensive validation studies were performed to characterize methodological results within and across the common confounds inherent in multi-site clinical trials.

The conversion and automated quality control tools optimized for this work both enhanced the ability to reliably obtain repeat diffusion tensor image (DTI) scalar measurements in a reliability analysis of healthy controls scanned at multiple sites using multiple scanner vendors. A DTI scalar analysis performed on focused WM regions showed it was possible to detect significant mean differences of DTI scalars among separate groups of a neurodegenerative disease population. The DTI scalar

analysis paved the way for an atlas-based cross-sectional fiber tracking analysis. In the cross-sectional fiber tracking analysis, multi-site data was brought into the same space, making major fiber tracts terminating in the focused WM regions of the scalar analysis from all participants comparable. Significant differences in diffusivity were found throughout each tract among separate groups of the neurodegenerative disease population. In addition, multiple neuropsychological cognitive variables that have a documented ability to track disease progression of the neurodegenerative disease, strongly correlated with many of the DTI scalars in each tract. The findings of the cross-sectional fiber tracking analysis were reinforced by similar findings produced by a longitudinal fiber tracking analysis. Collectively, these findings suggest that cognitive deficits seen in the neurodegenerative disease population could be explained by changes in diffusivity of the tracts explored in this work. In addition to the longitudinal fiber tracking analysis examining diffusivity, methods for a WM morphology analysis using parallel transport to apply longitudinal volume changes to a template was explored.

TABLE OF CONTENTS

LIST OF TABLES

Table

LIST OF FIGURES

Figure

CHAPTER 1
UNDERSTANDING DIFFUSION WEIGHTED IMAGING AND ITS ROLE IN INVESTIGATING WHITE MATTER DISEASE

1.1 Introduction

Huntington's disease (HD) is a fatal, autosomal-dominant disease that is characterized by its motor, cognitive, and psychiatric symptoms with no cure. Thus, efforts are being made to develop treatments that slow or stop disease progression before debilitating symptoms appear. The problem with developing treatments for an illness at its prodromal stage is that clinically observable indicators of disease progression that would determine treatment efficacy in clinical trials are often limited at best. Researchers have thus turned to imaging to identify a non-invasive continuous parameter that correlates with HD disease progression [2]. Volumetric imaging studies on prodromal HD patients have shown that white matter (WM) volume is abnormal as many as twenty years before symptom onset [3]. Therefore, quantifying WM changes with a method more sensitive than structural imaging has been targeted as a way to develop a biomarker of disease progression in prodromal HD patients. DWI could provide the level of sensitivity needed, given its ability to extract diffusivity information specific to different tissues.

Proposed clinical trials for therapies are anticipated to require several hundred subjects. Therefore, clinical studies investigating DWI variables to be used in clinical trials need to operate on grander scales by collecting DWI data at multiple sites to increase their volume of data. To meet their DWI data processing needs, researchers

often turn to the several easily accessible DWI processing tools. Many easily accessible DWI processing tools offer the basic discrete phases of DWI pre-processing deemed essential by the literature: file format conversion from DICOM files, $b = 0$ image averaging, removal of motion artifacts between gradient directions, diffusion tensor image (DTI) estimation, and scalar calculation. However, since these DWI pre-processing tools have primarily been developed for cross-sectional, single scanner analysis, compatibility issues arise because the tools have not been extensively tested on a wide range of data. In addition, it is difficult to ensure homogeneity of data quality collected at multiple sites. Operating on a grander scale also means expanding from cross-sectional to longitudinal studies with more elaborate DWI data analyses. A great body of work has been done in analyses that represent diffusion as a scalar value in regions of interest in the brain or physical representations of WM pathways. However, these existing studies are mostly cross-sectional and show only group differences in diffusivity. In order to meet the growing needs of large clinical trials, methods for conducting elaborate DWI analyses such as multi-site longitudinal fiber tracking studies that monitor changes in individual subjects must be investigated.

1.2 Huntington's disease

Huntington's disease (HD) is a progressive disorder characterized by motor, cognitive, and behavioral disturbances. HD is inherited in an autosomal dominant fashion where there is an expansion of polygutamine (cytosine-adenine-guanine, CAG) repeats in the huntingtin gene [4]. The manifestation of motor symptoms signals the

onset of the disease that on average occurs in the fourth decade of life with a duration of 15 to 20 years [5, 6]. Unfortunately, available pharmacologic options for treatment do not slow or stop disease progression and only target symptoms. Therefore, there are several groups, such as PREDICT-HD and TRACK-HD, whose primary interest is to identify biomarkers of disease progression to judge efficacy of new treatments [7, 8].

1.2.1 Imaging studies on prodromal HD and HD

1.2.1.1 Striatal volume studies

In the search for a realiable disease marker, MRI has uncovered several consistent features of disease progression in both symptomatic and prodromal (or pre-symptomatic) HD individuals. The first MRI studies revealed that symptomatic HD patients possessed marked atrophy of the caudate and putamen [9]. Decreased basal ganglia volumes have also been seen in the prodromal stage of HD and correlated with greater neurological impairment [10, 11], poorer performance on cognitive assessments [10], and years to motor sign/symptom onset [12, 11].

1.2.1.2 White matter volume studies

Tissue atrophy is not limted to the basal ganglia in HD indivdiuals. Decreased WM volume has been demonstrated in prodromal HD individuals more than 15 years from diagnosis [3, 13] and has a greater correlation with cognitive deficits in symptomatic HD individuals than decreased striatal volume and cognitive deficits [14]. As for specific regions of WM, features of frontal lobe WM have consistently tracked with

the clinical features of HD. Much like striatal volume, frontal lobe WM volume was first shown to be decreased in symptomatic HD individuals [15]. Frontal lobe WM atrophy has also been demonstrated in prodromal HD individuals over a two-year period, where the rate of atrophy was greater than those seen in both temporal and parietal lobe WM [16]. In fact, frontal lobe WM volume change may require the smallest sample size out of all volume outcome measures (i.e. basal ganglia or whole brain volumes) that are likely to be used in a prodromal HD clinical trial [16].

1.2.1.3 DTI studies

Although WM volume has been shown to correlate with features of disease progression, volume information alone does not reflect altered WM integrity. Researchers have thus turned to more sophisticated imaging methods to detect changes in brain structures that elucidate more specific informtion to the disease process. One such imaging method is diffusion-weighted imaging (DWI) that can detect varying levels of anisotropic diffusion that could represent altered WM integrity in diseased tissue [17, 18, 19]. Overall, DTI studies on prodromal and symptomatic HD participants demonstrate diffusivity changes in WM to explain increased motor signs with disease progression. Many DWI studies involving HD participants have focused on WM of the motor loop [20, 21, 22, 23], periventricular region [24], corpus callosum [20, 25, 21, 26, 27, 22, 23, 28, 29, 30], corona radiata [25, 21, 22, 23], and whole brain [24, 20]. Another region of interest in HD disease progression is the prefrontal cortex (PFC) due to its prominent striatal connections. The dorsolateral PFC projects

to the central to dorsal caudate (dorsal loop), while the orbital PFC and rostral anterior cingulate cortex projects to the ventromedial caudate and ventral striatum (ventral loop) [31, 32]. Based on the striatal dorsal-to-ventral progression of cell death [33], Lawrence and colleagues hypothesized that functions associated with the dorsal PFC-striatal loop may be impaired before motor sign/symptom onset, followed by impairment of functions associated with the ventral loop as neuronal loss increases [34]. Voxel-based scalar studies on PFC WM have reported clusters of voxels containing significant changes in diffusivity in both prodromal [35, 20, 36] and symptomatic HD [20, 37] participants in the form of both increased and/or decreased FA and increased MD in comparison to controls. ROI-based scalar analyses of PFC WM have also reported decreased FA and increased MD in WM passing through the superior frontal cortex in early HD [30].

Several groups have moved beyond ROI-based scalar analyses to examining the diffusivity of WM in the corticostriatal pathways in HD and prodromal HD participants with tract-based analyses. One type of tract-based analysis used by a few groups involved reconstructing the WM pathway between a start and end region with a fiber tracking algorithm [38, 39]. Once the fibers are reconstructed, either degree of connectivity between the start and end points was quantified or mean DTI scalars over the fibers were computed. In prodromal HD participants, the number of corticofugal fibers reaching the body of the caudate were reduced [40]. As for HD participants, various connections to the caudate were also reduced [41] and significant changes in diffusivity in connections to the striatum were seen in comparison to controls [42].

Another type of tract-based analysis that has been performed on HD participants is called tract-based spatial statistics (TBSS). The methodology of TBSS tries to isolate tract analysis to regions that have the highest likelihood of being WM by creating an FA skeleton along all WM in the brain based on FA images from all the participants in the study. FA values of voxels around the FA skeleton are projected to the skeleton to create weighted average FA values on the FA skeleton for each participant. The weighted averages of FA values on the FA skeleton are then used in a voxel-based analysis of voxels on the FA skeleton. These TBSS studies normally report decreased FA and increased MD, AD, and RD in various WM regions, such as the thalamic radiation, internal capsule, external capsule, and corticospinal tracts in prodromal HD and HD participants [21, 22, 23, 29].

1.2.1.4 Longitudinal studies

Early cross-sectional volumetric findings in the striatum [9] have been supported by several volumetric longitudinal studies that report greater rates of atrophy in the caudate and putamen of symptomatic HD patients over periods of time ranging from 10 to 27 months in comparison to controls [43, 44, 45, 46, 47, 48, 8, 49]. Similar findings of greater caudate and putamen atrophy rates in comparison to controls have also been reported by studies on prodromal HD individuals [50, 51, 47, 16, 52, 8, 49]. In addition, when prodromal HD participants were compared to symptomatic HD participants in the same study, similar atrophy patterns were seen in both groups but to a lesser degree in the prodromal group [47, 8, 49]. Aside from the striatum,

brain volume and the major tissue classes have been assessed longitudinally in HD. Whole brain atrophy can be detected across a time frame as short at six months in early symptomatic HD patients [53] and as early as prodromal participants close to symptom onset over a one-year period [54, 8]. Atrophy rates of major tissue classes as a whole (gray matter, WM, and CSF) [51] and in specific regions [47, 48, 8, 49] even in participants furthest from disease onset.

As for DWI, all existing longitudinal studies have been done on early to moderate HD participants and only one of them evaluated WM. Weaver et al. was among the first to perform a longitudinal analysis on HD participants, using two DWI scans collected one year apart and TBSS [25]. Weaver et al. showed widespread changes in AD, RD, and FA that were greater in HD participants in comparison to controls, and concluded that FA change in the corpus callosum was stable enough to possibly serve as a reliable biomarker of disease progression [25]. Another longitudinal study compared how well the diffusion trace of the striatum could track with disease progression in comparison to volume of the striatum in HD participants, and concluded that volume was more sensitive to disease progression than the diffusion trace [45]. The largest longitudinal study in HD found higher MD in the caudate and putamen bilaterally for 18 HD participants in comparison to 17 controls at two time points that were 1 year apart [27].

1.3 Diffusion-weighted imaging

1.3.1 The imaging sequence: Stejskal-Tanner sequence

Diffusion is normally measured with a Stejskal-Tanner sequence that is a spin-echo sequence with pulsed field gradients to spatially encode diffusion. The Stejskal-Tanner sequence begins with an initial magnetization vector aligned along the z-axis, which is the net magnetic moment of protons spinning at the same Larmor or resonance frequency of the main magnetic field. A slice-selecting 90^o radio frequency (RF) excitation pulse is applied to rotate the initial magnetization aligned along the z-axis into the transverse (xy) plane. While in the transverse plane, individual spins are allowed to precess at their individual Larmor frequencies or dephase from the resonance frequency of the main magnetic field. Dephasing occurs because different spins encounter different magnetic gradients depending on their location. As a result, the transverse magnetization vector decrease in magnitude. These individual Larmor frequencies are spatially encoded through the application of identical diffusion-sensitizing gradients in a given direction that surround an 180^o refocusing pulse. For example, if the diffusion-sensitizing gradient is applied in the x direction, the Larmor frequencies will vary with position in the x direction [55, 56].

If no diffusion occurs (excited spins do not change location in the x direction) during the first diffusion-sensitizing gradient, the 180^o refocusing pulse will realign a large percentage of those spins of the individual Larmor frequencies and restore the transverse magnetization vector. The transverse magnetization will be slightly less than its initial magnitude due to the spin-spin (T_2) relaxation. However, if spins

diffuse and change location during the first diffusion-sensitizing gradient, their Larmor frequencies will be different from the frequencies before the refocusing pulse. This change in Larmor frequencies is reflected in an inability to restore the transverse magnetization vector magnitude, where the decrease in magnitude is greater than that caused by spin-spin relaxation. The transverse magnetization is the net signal intensity (SI) and is detected during the echo. The faster that spins move in the direction of the diffusion-sensitizing gradient during the spin-echo period (TE, from 90^o pulse to the first echo), the greater the signal loss [55, 56].

A DWI image without a diffusion-sensitizing gradient looks similar to a standard morphometric T_2-weighted image because it is basically an echo-planar image (EPI) (CSF is bright, gray matter is bright gray, white matter is the dark gray). A DWI image with a diffusion-sensitizing gradient will instead have areas of signal loss (black) that represents diffusion occurring during the scan (Figure 1.1). Signal loss is also dependent on the strength and duration of the diffusion-sensitizing gradient field, also known as the diffusion-weighted factor or b factor (units = sec/mm^2), and D, the apparent diffusion coefficient or ADC (units = mm^2/sec). Net signal intensity decay in homogeneous, isotropic systems such as pure liquid can be modeled as monoexponential decay for b factors as high as 2000 s/mm^2:

$$SI = S_0 exp(-bD) \tag{1.1}$$

where S_0 is the signal intensity without diffusion-sensitizing gradients and includes the effects of proton density and T_2 relaxation [57, 58, 59, 60].

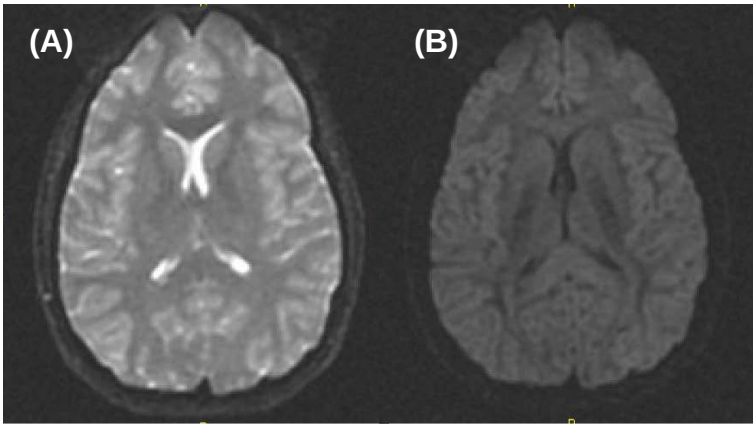

Figure 1.1: Images with and without a diffusion-sensitizing gradient. (A) DWI image without a diffusion-sensitizing gradient (CSF is white, gray matter is gray, WM is the darkest object). (B) DWI image with a diffusion-sensitizing gradient, where areas of signal loss or detected diffusion appear black.

1.3.2 Quantifying diffusion from imaging information

1.3.2.1 General mathematics used to quantify diffusion

It must be noted that Eq. 1.1 is a monoexponential model for net signal intensity decay with scalar quantities: the b factor is a predetermined parameter for the scanning protocol, SI and S_0 are empirically measured by the scanner during each image acquisition, and D is estimated after the scan. As mentioned earlier, the b factor is the strength and duration of the diffusion-sensitizing gradient field. It is obtained by integrating over k-space, over the trapezoidal diffusion-sensitizing gradient scheme at the echo time ($t = TE$) and simplifies to the following formula:

$$b = \gamma^2 G^2 [\delta^2(\Delta - \delta/3) + \varepsilon^2/30 - \delta\varepsilon^2/6] \tag{1.2}$$

where G is maximum gradient strength, ε is the rise and fall time of the gradient, δ is the gradient duration, and Δ is gradient separation time. The b factor of a gradient

(also known as the b value) is part of the **b** matrix that is used as input for the scanner to determine the direction of the diffusion weighting for each diffusion-sensitizing gradient. Therefore, each diffusion-sensitizing gradient has its own **b** matrix [61, 62, 63]. Section 1.3.2.2 covers the original derivation of the **b** matrix from diffusion weighting vector coordinates, along with a simplified method for **b** matrix design.

In practice, D is calculated by obtaining signal measurements (S_1 and S_2) at a low b factor, b_1, and a high b factor, b_2, while keeping all other parameters identical.

$$S_1 = S_0 exp(-b_1 D)$$

$$S_2 = S_0 exp(-b_2 D)$$

$$S_1/S_2 = exp[(b_2 - b_1)D]$$

$$D = ADC = ln(S_1/S_2)/(b_2 - b_1) \tag{1.3}$$

Signal measurements obtained at a low b factor are normally done using a spin-echo sequence in the absence of diffusion-sensitizing gradients. In the absence of diffusion-sensitizing gradients, b_1 is assumed to be assumed to be zero because imaging gradients usually provide a very low b factor. Since the same b factor will appear in b_1 and b_2, the b_1 factor will disappear in the term $b_2 - b_1$. Thus, Eq. 1.3 simplifies to:

$$D = ADC = ln(S_0/S_2)/b = (ln(S_0) - ln(S_2))/b \tag{1.4}$$

where b is equal to $b_2 - b_1$ and S_0 replaces S_1 to represent the signal intensity without a diffusion-sensitizing gradient [57, 58, 59, 60, 64].

The scalar, D, can also be expressed as a vector, **D**, that contains the six unique components of the estimated symmetric diffusion tensor. **D** can be calculated

at each voxel to produce a diffusion tensor image (DTI), which is one of the most popular models for estimating diffusion. In Section 1.3.3.1, two methods for calculating components of the diffusion tensor using information from multiple diffusion-sensitizing gradients and the overall concept of Eq. 1.4 are shown.

1.3.2.2 The b matrix

1.3.2.2.1 Calculation of the b matrix

In order to describe free diffusion in an anisotropic medium, Stejskal modified the Bloch-Torrey equation to read as follows [56]:

$$\frac{\partial \mathbf{M}}{\partial t} = \gamma \mathbf{M} \times \mathbf{B} - \frac{(M_x \hat{\imath} + M_y \hat{\jmath})}{T_2} + \frac{(M_0 - M_z)\hat{k}}{T_1} - \nabla \cdot \mathbf{vM} + \nabla \cdot \mathbf{D} \cdot \nabla \mathbf{M} \qquad (1.5)$$

The solution to Eq. 1.5 describes free diffusion in an anisotropic medium by relating echo intensity to the **b** matrix in terms of the applied magnetic-field-gradient vector ($\mathbf{G}(t)$) and its time integral ($\mathbf{F}(t)$). The gradient directions must be expressed in three orthogonal directions such as the x, y, and z-axes of the magnet's gradient system. Since it is good practice to measure diffusion in additional directions that are not parallel to the x, y, and z-axes, multiple gradients must be used simultaneously to create oblique diffusion-sensitizing gradients. When multiple gradients are turned on, a 3x3 symmetric **b** matrix is used to represent the oblique diffusion-weighting created for the 3D case (2x2 matrix for 2D) with six different terms: b_{xx}, b_{yy}, b_{zz}, $b_{xy} = b_{yx}$, $b_{xz} = b_{zx}$, and $b_{yz} = b_{zy}$ [56, 62, 64, 65].

The **b** matrix is calculated in three steps. First, the gradient column vector is

determined with the gradient intensities, $g(t'')$, in each direction at each time t'':

$$\mathbf{G}(t'') = [g_x(t''), g_y(t''), g_z(t'')]^T \tag{1.6}$$

Then, $\mathbf{G}(t'')$ is integrated over time t'' to determine the total field offset column vector, $\mathbf{F}(t')$, that is used to compute the k-space column vector. γ is the gyromagnetic ratio.

$$\mathbf{F}(t'') = [F_x(t'), F_y(t'), F_z(t')]^T \tag{1.7}$$

$$\mathbf{k}(t') = \gamma\mathbf{F}(t') = [k_x(t'), k_y(t'), k_z(t')]^T = [\gamma F_x(t'), \gamma F_y(t'), \gamma F_z(t')]^T \tag{1.8}$$

The overall equation for calculating the k-space column vector is as follows:

$$\mathbf{k}(t') = \gamma\mathbf{F}(t') = \gamma \int_0^{t'} \mathbf{G}(t'')\,\mathrm{d}t'' - 2H(t' - t_1)k(t_1^-) \tag{1.9}$$

The Heaviside unit-step function,

$$H(t) = \begin{cases} 0 & \text{if } t < 0 \\ \\ 1 & \text{if } t \geq 0 \end{cases} \tag{1.10}$$

accounts for the inversion of the accumulated k-space factor by the 180^o refocusing pulse at time t_1. Prior to the refocusing pulse, the formula for $\mathbf{k}(t')$ is:

$$\mathbf{k}(t' < t_1) = \gamma\mathbf{F}(t_1^-) = \gamma \int_0^{t'} \mathbf{G}(t'')\,\mathrm{d}t'' \tag{1.11}$$

The formula for $\mathbf{k}(t')$ after the 180_o refocusing pulse is:

$$\mathbf{k}(t' > t_1) = \gamma\mathbf{F}(t_1^-) = \gamma \int_0^{t'} \mathbf{G}(t'')\,\mathrm{d}t'' - 2H(t^- - t_1)\mathbf{k}(t_1^-) = \gamma \int_0^{t'} \mathbf{G}(t'')\,\mathrm{d}t'' - 2\mathbf{k}(t_1^-) \tag{1.12}$$

where $\mathbf{k}(t_1^-)$ is the k-space column vector at the time of the refocusing pulse and is equal to:

$$\mathbf{k}(t_1^-) = \gamma \mathbf{F}(t_1^-) = \gamma \int_0^{t_1} \mathbf{G}(t'')\, \mathrm{d}t'' \tag{1.13}$$

The final step is to integrate $k_i k_j$ over time t to calculate the b_{ij} matrix element. The overall $\mathbf{b}$ matrix elements are derived when $t = TE$. For example, the integral of k_x^2 is used to calculate b_{xx} (where $t = TE$):

$$\begin{aligned} b_{xx}(t) = \gamma^2 \int_0^t \left[\int_0^{t'} g_x(t'')\, \mathrm{d}t'' - 2H(t' - t_1) k_x(t_1^-) \right] \times \\ \left[\int_0^{t'} g_x(t'')\, \mathrm{d}t'' - 2H(t' - t_1) g_x(t_1^-) \right]^T \mathrm{d}t' \end{aligned} \tag{1.14}$$

The entire $\mathbf{b}$ matrix calculation can be expressed concisely as:

$$\mathbf{b}(t) = \int_0^t \mathbf{k}(t') \mathbf{k}^T(t')\, \mathrm{d}t' = \gamma^2 \int_0^t \mathbf{F}(t') \mathbf{F}^T(t')\, \mathrm{d}t' \tag{1.15}$$

$$\begin{aligned} \mathbf{b}(t) = \gamma^2 \int_0^t \left[\int_0^{t'} \mathbf{G}(t'')\, \mathrm{d}t'' - 2H(t' - t_1) \mathbf{k}(t_1^-) \right] \times \\ \left[\int_0^{t'} \mathbf{G}(t'')\, \mathrm{d}t'' - 2H(t' - t_1) \mathbf{k}(t_1^-) \right]^T \mathrm{d}t' \end{aligned} \tag{1.16}$$

where the first part of Eq. 1.16 is a column vector and the second is a row vector that will result in a symmetric 3x3 b matrix.

The $\mathbf{b}$ matrix is related to signal intensity by replacing the exponent in the monoexponential decay equation (Eq. 1.1) with the generalized dot product of the $\mathbf{b}$ matrix and the diffusion tensor $\mathbf{D}$:

$$SI = S_0 exp(-\mathbf{b} \cdot \mathbf{D})$$

$$\mathbf{b} \cdot \mathbf{D} = \int_0^{TE} \mathbf{k}^T(t') \mathbf{D} \mathbf{k}(t')\, \mathrm{d}t' = \gamma^2 \int_0^{TE} \mathbf{F}^T(t') \mathbf{D} \mathbf{F}(t')\, \mathrm{d}t' \tag{1.17}$$

$$\mathbf{b} \cdot \mathbf{D} = b_{xx} D_{xx} + b_{yy} D_{yy} + b_{zz} D_{zz} + b_{xy} D_{xy} + b_{xz} D_{xz} + b_{yz} D_{yz} \tag{1.18}$$

The **b** matrix of a gradient is useful in one type of tensor calculation covered in Section 1.3.3.1.3 [56, 62, 64, 65].

1.3.2.2.2 Simplified b matrix design

The process of designing the **b** matrix for each diffusion-sensitizing gradient can be simplified by following two rules. The first rule is to express each gradient's diffusion-weighting direction as a unit vector or normalized gradient vector, $\mathbf{G}_n$, so that its vector dot product of $\mathbf{G}_n \cdot \mathbf{G}_n$ equals 1.

$$\mathbf{G_n} = (g_x, g_y, g_z)^T \tag{1.19}$$

$$\mathbf{G_n} \cdot \mathbf{G_n} = g_x^2 + g_y^2 + g_z^2 = 1 \tag{1.20}$$

The second rule is to use the same high b factor for each diffusion-sensitizing gradient. The second rule also ensures that the total gradient amplitude will be the same for each diffusion-sensitizing gradient. Following the two rules above allows a simpler design of the **b** matrix via the product of the b factor, normalized gradient vector, and its transpose. The resulting **b** matrix can then be used as scanner input or in Eq. 1.18 as part of the process to estimate **D** [66].

$$\mathbf{g} = \mathbf{G_n G_n^T} = \begin{pmatrix} g_x \\ g_y \\ g_x \end{pmatrix} \begin{pmatrix} g_x & g_y & g_z \end{pmatrix} = \begin{pmatrix} g_x^2 & g_x g_y & g_x g_z \\ g_y g_x & g_y^2 & g_y g_z \\ g_z g_x & g_z g_y & g_z^2 \end{pmatrix} \tag{1.21}$$

$$\mathbf{b} = b\mathbf{g} \tag{1.22}$$

$$\mathbf{b} \cdot \mathbf{D} = b\mathbf{g} \cdot \mathbf{D} \tag{1.23}$$

1.3.3 Diffusion-weighted imaging data analysis

1.3.3.1 Diffusion tensor

One of the most commonly used models for estimating diffusion at the voxel level is the diffusion tensor. In order to estimate the diffusion tensor in each voxel of the tensor information such as signal intensity, **b** matrix from each diffusion-sensitizing gradient, and normalized gradient components are necessary. Therefore, the vectors for noisy observed data contain signal information from each gradient direction measurement, while the calculated vectors containing diffusion tensor components are the estimated diffusion for the corresponding voxel in the tensor image [63].

In general, a single high b factor is used per scan due to non-monoexponential signal decay. It is common practice to average all images in a scan whose b factor equals zero ($b = 0$ image) than to fit them individually. The $b = 0$ image is then used as the estimate for $ln(S_0)$ in Eq. 1.4.

There are two methods available for estimating the diffusion tensor and are both described below. Both methods offer an unweighted-linear least-squares fit of the logarithms of the signal intensities. The second method is used over the first when a weighted-linear least-squares fit of the logarithms of the signal intensities is necessary and offers more flexibility in the diffusion tensor estimation (described in Section 1.3.3.1.3). The fitted signal intensities that result from the weighted-linear least-squares fit should be closer to the true signal intensity values than the original noisy value and can be used in a repeat weighted-linear least-squares fit [63]. Any

linear least-squares fit can be used as a starting point for a nonlinear least-squares fit (not described in this thesis) in the face of high noise levels [67].

1.3.3.1.1 Tensor math

A tensor is a mathematical object with nth-rank in m-dimensional space where it has n indices and m^n components. Each tensor index ranges over the number of dimensions of space. Tensors have certain transformation properties, where objects that transform like zeroth-rank tensors, first- rank tensor, and second-rank tensors, are called scalars, vectors, and matrices, respectively [68]. The type of tensor that is applicable here is the symmetric tensor, which is of second-rank. Since the symmetric tensor is of second-rank, it can be expressed as a symmetric matrix, T [69]. The components of the symmetric matrix have the property of:

$$T^{mn} = T^{nm} \tag{1.24}$$

and has scalar invariants (one component quantities that do not vary with with rotations of the coordinate system) such as [69]:

$$s_1 = A_1 1 + A_2 2 + A_3 3 \tag{1.25}$$

$$s_2 = A_{22}A_{33} + A_{33}A_{11} + A_{11}A_{22} - A_{23}^2 - A_{31}^2 - A_{12}^2 \tag{1.26}$$

1.3.3.1.2 Tensor estimation method 1

In the first method for estimating the diffusion tensor, the **H** matrix is used to relate normalized gradient components to the observed data. The first method is used when a weighted-linear least-squares fit of the logarithms of the signal intensities

is not necessary. Multiple $b = 0$ acquisitions must be averaged to provide a single S_0 value estimate.

b is a six-element column vector use to express the six unique diffusion tensor elements:

$$\mathbf{d} = [D_{xx}, D_{yy}, D_{zz}, D_{xy}, D_{xz}, D_{yz}]^T \tag{1.27}$$

Each gradient encoding matrix is derived from the normalized gradient components, g_{xi}, g_{yi}, and g_{zi}, (for $i = 1$ to M number of gradients) and is represented as a six-element row matrix, $\mathbf{H}_i$ (Eq. 1.28. The $\mathbf{H}_i$ vectors are combined into a large Mx6 matrix, where M is the number of measurements whose $b > 0$.

$$\mathbf{H}_i = [g_{xi}^2, g_{yi}^2, g_{zi}^2, 2g_{xi}g_{yi}, 2g_{xi}g_{zi}, 2g_{yi}g_{zi}] \tag{1.28}$$

$$\mathbf{H} = \begin{pmatrix} g_{x1}^2 & g_{yi}^2 & g_{zi}^2 & 2g_{xi}g_{yi} & 2g_{xi}g_{zi} & 2g_{yi}g_{zi} \\ \vdots & \vdots & \vdots & \vdots & \vdots & \vdots \\ g_{xM}^2 & g_{yM}^2 & g_{zM}^2 & 2g_{xM}g_{yM} & 2g_{xM}g_{zM} & 2g_{yM}g_{zM} \end{pmatrix} \tag{1.29}$$

Observed data is expressed as the individual measured ADCs:

$$\mathbf{Y}_i = ln\left(\frac{S_0}{S_i}\right)/b \tag{1.30}$$

$$\mathbf{Y} = \left[\frac{ln\left(\frac{S_0}{S_1}\right)}{b}, \frac{ln\left(\frac{S_0}{S_2}\right)}{b}, \cdots, \frac{ln\left(\frac{S_0}{S_M}\right)}{b}\right]^T \tag{1.31}$$

where S_i is the observed signal for the $\hat{g}$ gradient. Note that Y_i is a volumetric image with noisy data and is expressed as:

$$\mathbf{Y} = \mathbf{Hd} + \boldsymbol{\eta} \tag{1.32}$$

for each acquisition. If $M = 6$, **d** can be determined by the following calculation (where $\boldsymbol{\eta} = 0$ since $\boldsymbol{\eta}$ is not able to be distinguished from **d**) [63, 66, 70]:

$$(\mathbf{H}^{-1}\mathbf{H})\mathbf{d} = \mathbf{d} = \mathbf{H}^{-1}\mathbf{Y} \tag{1.33}$$

However, if $M > 6$, an unweighted-linear least-squares fit of the logarithms of the signal intensities is necessary. The pseudoinverse of the **H** matrix must be used since **H** is not a square matrix and thus has no true inverse. The noisy data equation can be solved by first calculating the pseudoinverse of **H**, which is $\mathbf{H}^{\psi}$:

$$\mathbf{H}^{\psi}\mathbf{H} = \mathbf{I}_{6x6}$$

$$\mathbf{H}^{\psi} = (\mathbf{H}^{T}\mathbf{H})^{-1}\mathbf{H}^{T} \tag{1.34}$$

where $\mathbf{H}\mathbf{H}^{\psi}$ does not have to equal $\mathbf{I}_{MxM}$. The matrix product $\mathbf{H}^{T}\mathbf{H}$, which is a square 6x6 matrix, is formed from Eq. 1.32 before the application of the pseudoinverse (Eq. 1.34) to obtain **d**. It is again assumed that $\boldsymbol{\eta} = 0$ since $\boldsymbol{\eta}$ is not able to be distinguished from **d** [62, 63]:

$$\mathbf{H}^{T}\mathbf{Y} = \mathbf{H}^{T}\mathbf{H}\mathbf{d}$$

$$(\mathbf{H}^{T}\mathbf{H})^{-1}\mathbf{H}^{T}\mathbf{H}\mathbf{d} = \mathbf{d} = (\mathbf{H}^{T}\mathbf{H})^{-1}\mathbf{H}^{T}\mathbf{Y} \tag{1.35}$$

The pseudoinverse can also be obtained through singular value decomposition (SVD). The **H** matrix is decomposed into the product of three matrices (**U**, **V**, and **W**):

$$\mathbf{U} = \text{Mx6 column orthogonal}$$

$$\mathbf{V} = \text{6x6 row and column orthogonal}$$

$$\mathbf{W} = \text{6x6 diagonal}$$

$$\mathbf{V}\mathbf{V}^{T} = \mathbf{I}_{6x6}$$

$$\mathbf{U}^{T}\mathbf{U} = \mathbf{I}_{6x6}$$

$$(\mathbf{W}^{-1})_{ij} = \frac{1}{\mathbf{W}_{ij}}$$

$$\mathbf{H} = \mathbf{UWV}^T \tag{1.36}$$

and the pseudoinverse of $\mathbf{H}$ can be derived by [63]:

$$\mathbf{VW}^{-1}\mathbf{U}^T\mathbf{H} = \mathbf{VW}^{-1}\mathbf{U}^T\mathbf{UWV}^T = \mathbf{I}_{6x6} \tag{1.37}$$

$$\mathbf{H}^{\psi} = (\mathbf{H}^T\mathbf{H})^{-1}\mathbf{H}^T = \mathbf{VW}^{-1}\mathbf{U}^T \tag{1.38}$$

1.3.3.1.3 Tensor estimation method 2

In the second method for estimating the diffusion tensor, the $\mathbf{B}$ matrix is used to relate components of the $\mathbf{b}$ matrix to the observed data. The second method is used when a weighted-linear least-squares fit of the logarithms of the signal intensities is necessary. The second method also allows more flexibility than the first from several reasons: 1) it allows the use of two ore more different high b factors, 2) an estimate of $ln(S_0)$ is produced in the least-squares fit (while $ln(S_0)$ from the average $b = 0$ signal intensities is incorporated into the vector in the $\mathbf{H}$ matrix approach), 3) the individual $b = 0$ images can be fitted separately or as an average, 4) the option of using a weighted-linear least-squares fit exists, 5) a covariance matrix can be derived and used for propagation-of-error calculations and DTI parameter optimization [63].

$\boldsymbol{\alpha}$ is a seven-element column vector used to express the six diffusion tensor elements and log of the $b = 0$ signal intensity (S_0) [62]:

$$\boldsymbol{\alpha} = [D_{xx}, D_{yy}, D_{zz}, D_{xy}, D_{xz}, D_{yz}, ln(S_0)]^T \tag{1.39}$$

Each element of each gradient direction's $\mathbf{b}$ matrix is represented by a six-element row

vector, $\mathbf{b}_i$ (Eq. 1.40), which is included in a seven-element row vector, $\mathbf{B}_i$ (Eq. 1.41).

$$\mathbf{b}_i = (b_{xxi}, b_{yyi}, b_{zzi}, 2b_{xyi}, 2b_{xzi}, 2b_{bzi}) \tag{1.40}$$

$$\mathbf{B}_i = (-b_{xxi}, -b_{yyi}, -b_{zzi}, -2b_{xyi}, -2b_{xzi}, -2b_{bzi}, 1) \tag{1.41}$$

The $\mathbf{B}_i$ row vectors as presented in Eq. 1.41 are assembled into a large Nx7 $\mathbf{B}$ matrix, where N is the total number of measurements (gradients with $b = 0$ and $b > 0$):

$$\mathbf{B} = \begin{pmatrix} -b_{xx1} & -b_{yy1} & -b_{zz1} & -2b_{xy1} & -2b_{xz1} & -2b_{bz1} & 1 \\ \vdots & \vdots & \vdots & \vdots & \vdots & \vdots & 1 \\ -b_{xxN} & -b_{yyN} & -b_{zzN} & -2b_{xyN} & -2b_{xzN} & -2b_{bzN} & 1 \end{pmatrix} \tag{1.42}$$

In the absence of noise, the logarithms of the predicted signal intensities are given by an Nx1 column vector, $\boldsymbol{\xi}$:

$$\boldsymbol{\xi}_i = \mathbf{B}_i\boldsymbol{\alpha} = ln(S_i) = ln(S_0) - \mathbf{b}_i \cdot \mathbf{D} \tag{1.43}$$

$$\boldsymbol{\xi}_i = -b_{xxi}D_{xx} - b_{yyi}D_{yy} - b_{zzi}D_{zz} - 2b_{xyi}D_{xy} - 2b_{xzi}D_{xz} - 2b_{yzi}D_{yz} + ln(S_0)$$

$$\boldsymbol{\xi} = \mathbf{B}\boldsymbol{\alpha} = \begin{pmatrix} -b_{xx1}D_{xx} - b_{yy1}D_{yy} - b_{zz1}D_{zz} - 2b_{xy1}D_{xy} \\ \qquad - 2b_{xz1}D_{xz} - 2b_{yz1}D_{yz} + ln(S_0) \\ \vdots \\ -b_{xxN}D_{xx} - b_{yyN}D_{yy} - b_{zzN}D_{zz} - 2b_{xyN}D_{xy} \\ \qquad - 2b_{xzN}D_{xz} - 2b_{yzN}D_{yz} + ln(S_0) \end{pmatrix} \tag{1.44}$$

The noisy observed data for each acquisition is represented as an Nx1 column vector, $\mathbf{x}$, and is expressed with Eq. 1.44 and a noise vector, $\boldsymbol{\eta}$, as follows in Eq. 1.46:

$$\mathbf{x} = \begin{pmatrix} ln(S_1) \\ ln(S_2) \\ \vdots \\ ln(S_N) \end{pmatrix} \tag{1.45}$$

$$\mathbf{x} = \mathbf{B}\boldsymbol{\alpha} + \boldsymbol{\eta} = \boldsymbol{\xi} + \boldsymbol{\eta} \tag{1.46}$$

If $M = 6$ (where M is the number of measurements whose $b > 0$), the exact solution for the diffusion tensor values iw as followSe(where $\boldsymbol{\eta} = 0$ since it's not possible to distinguish $\boldsymbol{\eta}$ from $\boldsymbol{\alpha}$):

$$\mathbf{x} = \mathbf{B}\boldsymbol{\alpha} \tag{1.47}$$

$$(\mathbf{B}^{-1}\mathbf{B})\boldsymbol{\alpha} = \boldsymbol{\alpha} = \mathbf{B}^{-1}\mathbf{x} \tag{1.48}$$

When $M > 6$, the pseudoinverse of $\mathbf{B}$, $\mathbf{B}^{\psi}$, is calculated for an unweighted-linear least-squares fit with the $\mathbf{B}$ matrix.

$$(\mathbf{B}^T\mathbf{B})^{-1}\mathbf{B}^T\mathbf{B}\boldsymbol{\alpha} = (\mathbf{B}^T\mathbf{B})^{-1}\mathbf{B}^T\mathbf{x} \tag{1.49}$$

$$(\mathbf{B}^T\mathbf{B})^{-1}\mathbf{B}^T = \mathbf{B}^{\psi} \tag{1.50}$$

The pseudoinverse of $\mathbf{B}$ can also be found via singular value decomposition. In the unweighted-linear least-squares fit with the $\mathbf{B}$ (or $\mathbf{H}$) matrix, it is assumed that all data points are equally accurate. This assumption is true for the original signal intensities but does not hold for the logarithms of signal intensities. Therefore, a weighted-linear least-squares fit with the $\mathbf{B}$ matrix is needed to account for the expected variance in each measurement and correct the distortion introduced by the logarithm transformation of signal intensities. Thus, more weight will be given to the $ln(S_i)$ of higher S_i values. The equation for the weighted-linear least-squares fit of the $\mathbf{B}$ matrix is:

$$\boldsymbol{\alpha} = (\mathbf{B}^T\boldsymbol{\Sigma}^{-1}\mathbf{B})^{-1}(\mathbf{B}^T\boldsymbol{\Sigma}^{-1})\mathbf{x} \tag{1.51}$$

where $\boldsymbol{\Sigma}^{-1}$ is a diagonal NxN matrix whose elements are the squared signal value

divided by its variance and $(\mathbf{B}^T\mathbf{\Sigma}^{-1}\mathbf{B})$ is the covariance matrix:

$$\mathbf{\Sigma}^{-1} = diag\left(\frac{S_i^2}{\sigma_i^2}\right) = \begin{pmatrix} \frac{S_1^2}{\sigma_1^2} & \cdots & 0 \\ \vdots & \ddots & \vdots \\ 0 & \cdots & \frac{S_N^2}{\sigma_N^2} \end{pmatrix} \tag{1.52}$$

The variance for each gradient direction and $b = 0$ image can be modified to account for varying amounts of signal averaging. The S_i values are usually the observed noisy values. An unweighted-linear least-squares fit results when $\mathbf{\Sigma}^{-1}$ is replaced with an identify matrix [62, 63].

1.3.3.1.4 Eigenvectors and eigenvalues

The diffusion tensor is then used to calculate eigenvectors and eigenvalues that describe its diffusion properties. Eigenvectors and eigenvalues are related by the property that the product of the diffusion tensor and eigenvector is equal to the product of the eigenvalue and the same eigenvector.

$$\mathbf{D}\boldsymbol{\varepsilon}_i = \lambda_i\boldsymbol{\varepsilon}_i = \lambda_i\mathbf{I}\boldsymbol{\varepsilon}_i, \text{where i = 1, 2, 3} \tag{1.53}$$

Eq. 1.53 is used to calculate eigenvalues and eigenvectors by first subtracting $\lambda_i\mathbf{I}\boldsymbol{\varepsilon}_i$, from each side to form a set of homogeneous equation (shown in matrix notation in Eq. 1.55:

$$(\mathbf{D} - \lambda_i\mathbf{I})\boldsymbol{\varepsilon}_i = 0 \tag{1.54}$$

$$\begin{pmatrix} D_{xx} - \lambda_i & D_{xy} & D_{xz} \\ D_{xy} & D_{yy} - \lambda_i & D_{yz} \\ D_{xz} & D_{yz} & D_{zz} - \lambda_i \end{pmatrix} \begin{pmatrix} \varepsilon_{ix} \\ \varepsilon_{iy} \\ \varepsilon_{iz} \end{pmatrix} = \begin{pmatrix} 0 \\ 0 \\ 0 \end{pmatrix} \tag{1.55}$$

The determinant of Eq. 1.54 is set to zero (Eq. 1.56) to form a 3D cubic equation (Eq. 1.57, shown in terms of rotational invariants, I_i) then solving for the sorted

eigenvalues (Eqs. 1.58 through 1.60; $\lambda_1 > \lambda_2 > \lambda_3$) [66, 71]:

$$det(\mathbf{D} - \lambda_i \mathbf{I}) = 0 \tag{1.56}$$

$$\lambda^3 - I_1\lambda^2 + I_2\lambda - I_3 = 0 \tag{1.57}$$

$$I_1 = \lambda_1 + \lambda_2 + \lambda_3 = D_{xx} + D_{yy} + D_{zz}$$

$$I_2 = \lambda_1\lambda_2 + \lambda_2\lambda 3 + \lambda_3\lambda 1 = D_{xx}D_{yy} + D_{yy}D_{zz} + D_{zz}D_{xx} - (D_{xy}^2 + D_{xz}^2 + D_{yz}^2)$$

$$I_3 = \lambda_1\lambda_2\lambda 3 = D_{xx}D_{yy}D_{zz} + 2D_{xy}D_{xz}D_{yz} - (D_{zz}D_{xy}^2 + D_{yy}D_{xz}^2 + D_{xx}D_{yz}^2)$$

$$\lambda_1 = I_1/3 + 2v^{1/2}cos(\phi) \tag{1.58}$$

$$\lambda_2 = I_1/3 - 2v^{1/2}cos(\pi/3 + \phi) \tag{1.59}$$

$$\lambda_3 = I_1/3 - 2v^{1/2}cos(\pi/3 - \phi) = I_1 - \lambda_1 - \lambda_2 \tag{1.60}$$

where:

$$v = (I_1/3)^2 - I_2/3 = \mathbf{D}_{an} \cdot \mathbf{D}_{an}/6$$

$$\mathbf{D}_{an} \cdot \mathbf{D}_{an} = 6(I_1/3)^2 - 2I_2$$

$$s = (I_1/3)^3 - I_1I_2/6 + I_3/2$$

$$\phi = arccos[s/v^{3/2}]/3$$

The eigenvector/eigenvalue relationship property is then applied to each eigenvalue to determine any two of the three ratios: $\varepsilon_{iy}/\varepsilon_{ix}$, $\varepsilon_{iz}/\varepsilon_{iy}$, and $\varepsilon_{ix}/\varepsilon_{iz}$. The diagonal elements of the $\mathbf{D} - \lambda_i\mathbf{I}$ matrix in Eq. 1.55 are redefined as:

$$A_i = D_{xx} - \lambda_i$$

$$B_i = D_{yy} - \lambda_i$$

$$C_i = D_{zz} - \lambda_i$$

Eigenvector element ratios are used to solve for the eigenvector elements to form at least two individual eigenvectors, since the third can be calculated from the first two:

$$\hat{\boldsymbol{\varepsilon}}_i = \boldsymbol{\varepsilon}_i / \sqrt{\boldsymbol{\varepsilon}_i^T \boldsymbol{\varepsilon}_i} = \boldsymbol{\varepsilon}_i / \sqrt{\varepsilon_{ix}^2 + \varepsilon_{iy}^2 + \varepsilon_{iz}^2} \tag{1.61}$$

The eigenvector/eigenvalue relationship can be rewritten in matrix form as:

$$\mathbf{DE} = \mathbf{E\Lambda} \tag{1.62}$$

$$\begin{pmatrix} D_{xx} & D_{xy} & D_{xz} \\ D_{xy} & D_{yy} & D_{yz} \\ D_{xz} & D_{yz} & D_{zz} \end{pmatrix} \begin{pmatrix} \varepsilon_{1x} & \varepsilon_{2x} & \varepsilon_{3x} \\ \varepsilon_{1y} & \varepsilon_{2y} & \varepsilon_{3y} \\ \varepsilon_{1z} & \varepsilon_{2z} & \varepsilon_{3z} \end{pmatrix} = \begin{pmatrix} \varepsilon_{1x} & \varepsilon_{2x} & \varepsilon_{3x} \\ \varepsilon_{1y} & \varepsilon_{2y} & \varepsilon_{3y} \\ \varepsilon_{1z} & \varepsilon_{2z} & \varepsilon_{3z} \end{pmatrix} \begin{pmatrix} \lambda_1 & 0 & 0 \\ 0 & \lambda_2 & 0 \\ 0 & 0 & \lambda_3 \end{pmatrix} \tag{1.63}$$

where $\mathbf{E}$ is the eigenvector matrix that consists of the orthonormal eigenvectors as column vectors and $\mathbf{\Lambda}$ is the eigenvalue matrix. If the diffusion tensor is rotated, its eigenvalues will be the same but with differen eigenvectors (rotational invariance). Since the eigenvectors are orthonormal, its inverse is equal to its transporse, leading to the following formula to calculate $\mathbf{\Lambda}$ from $\mathbf{D}$:

$$\mathbf{E}^{-1} = \mathbf{E}^T \tag{1.64}$$

$$\mathbf{E}^T\mathbf{E\Lambda} = \mathbf{\Lambda} = \mathbf{E}^T\mathbf{DE} \tag{1.65}$$

$\mathbf{E}$ used in Eq. 1.65 to rotate the reference frame to the eigenvector position so the eigenvectors are aligned with the axes of the reference frame. The first eigenvector corresponds to λ_1 and so forth. If two or more eigenvalues are equal, they are degenerate and do not have unique eigenvector solutions [59, 61, 71, 72].

1.3.3.2 Rotationally invariant scalars

Rotationally invariant scalars (RISs) are generated from the resulting eigenvalue decomposition to describe the diffusion anisotropy and magnitude [17, 18]. Four scalars derived from the tensor model of diffusion often used (referred to as DTI scalars) include fractional anisotropy (FA), mean diffusivity (MD, units = mm^2/ sec), axial diffusivity (AD, units = mm^2/sec), and radial diffusivity (RD, units = mm^2/sec) (Table 1.1. FA reflects anisotropy of the diffusion tensor and is dimensionless, ranging from 0 (isotropic diffusion) to 1 (high anisotropy) [18]. MD is the average diffusion magnitude along three principal directions into which diffusion is decomposed [18]. AD is the magnitude of diffusion parallel to the principal direction of diffusion, where changes correlate with axonal injury [73]. Radial diffusivity (RD) is the magnitude of diffusion perpendicular to the principal direction of diffusion, where increases correlate with incomplete myelination [74] and myelin injury [73, 75]. Scalar measures have been used to examine normal-appearing WM that contains abnormalities (i.e. multiple sclerosis) (e.g. [76]) and developmental studies to characterize changes associated with aging (e.g. [77, 78].

1.3.3.3 Fiber tracking with the diffusion tensor model

Fiber tracking algorithms that use the diffusion tensor model can be split into two types: deterministic (Section 1.3.3.3.1) and probabilistic. The general idea behind deterministic fiber tracking is to use directional information provided by the diffusion tensor with a starting or "seed" point and termination criteria. Usually, the direc-

Table 1.1: Summary of commonly used DTI scalars.

RIS Name	Formula	Interpretation
Fractional anisotropy	$FA = \sqrt{\frac{3[(\lambda_1 - MD)^2 + (\lambda_2 - MD)^2 + (\lambda_3 - MD)^2]}{2(\lambda_1^2 + \lambda_2^2 + \lambda_3^2)}}$	Shape of diffusion
Mean diffusivity	$MD = \frac{\lambda_1 + \lambda_2 + \lambda_3}{3}$	Diffusion tensor trace average; size of diffusion
Radial diffusivity	$RD = \frac{\lambda_2 + \lambda_3}{2}$	Transverse diffusion
Axial diffusivity	$AD = \lambda_1$	Longitudinal diffusion

tional information used will be the principal eigenvector. The seed point is normally placed in WM and serves as the start of the deterministic tractogram that propagates along a trajectory determined by the directional information until termination. Termination criteria depends on the predicted connectivity pattern. Deterministic tractrography has shown that it is subject to variability due to the uncertainty in the estimations of fiber orientation. In order to accommodate the uncertainty, probabilistic tractrography replaces the discrete estimates of fiber orientation with probability density functions (PDFs) of orientation. Since this thesis will only incorporate deterministic tractography, this section (Section 1.3.3.3) will only summarize deterministic algorithms and their limitations.

1.3.3.3.1 Deterministic fiber tracking

1.3.3.3.1.1 Algorithms: streamline, tensor deflection

The simplest deterministic fiber tracking method is the streamline algorithm that was originally developed to visualize flow patterns in fluid mechanics. To demonstrate the capabilities of streamline tracking, an ideal example of the superior longitudinal fasciculus derived via streamline tractography is shown here [1]: Streamline

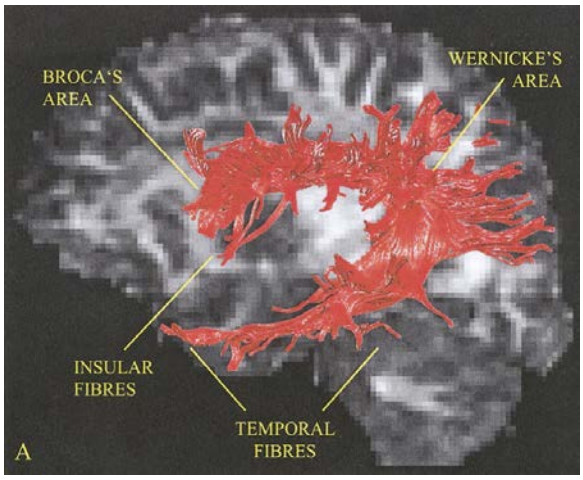

Figure 1.2: An ideal example of the superior longitudinal fasciculus derived via streamline tractography [1].

Source: M. Catani, R. J. Howard, S. Pajevic, and D. K. Jones, "Virtual in Vivo Interactive Dissection of White Matter Fasciculi in the Human Brain," *NeuroImage*, vol. 17, pp. 77-94, 2002.

tractography was first proposed by Basser [79] and is estimated by integrating the following partial differential equation (Eq. 1.66):

$$\frac{\partial \mathbf{r}(\tau)}{\partial \tau} = v_{traj}(\mathbf{r}(\tau)) \tag{1.66}$$

where $\mathbf{r}(\tau)$ is the path of the tractogram, $\partial\tau$ is the temporal step, and $\mathbf{v}_{traj}$ is the vector field that defines the tangent to the local path direction. $\mathbf{v}_{traj}$ is usually assigned to the principal eigenvector, $\mathbf{e_1}$, at each step [80, 81, 39]. There are several ways to integrate Eq. 1.66. The simplest integration methods approximate Eq. 1.66 using a Taylor series expansion [39]:

$$\mathbf{r}(\tau_1) \sim \mathbf{r}(\tau_0) + \alpha \mathbf{e_1}(\mathbf{r}(\tau_0)) \tag{1.67}$$

Two methods that use the Taylor series expansion include FACT (fiber assignment by continuous tracking) [81] (linear step-wise algorithm) or Euler integration [80]. α is usually small relative to the curvature of the local tract such that $\mathbf{r}(\tau_1)$ (estimated position) can be estimated at τ_1 from $\mathbf{r}(\tau_0)$ (initial position). For the Euler method, α is fixed and uses an interpolation of DTI data to estimate the local diffusion tensor and principal eigenvector. In the FACT method, α can vary and uses the same $\mathbf{e_1}$ over the entire voxel.

To increase accuracy in the estimation of curved tracts, different methods for interpolating the local $\mathbf{e_1}$ direction have been used. Interpolation methods include interpolation of the raw DWI data [80], interpolation of the local diffusion tensors (most common), and fitting a continuous description of the tensor field [82]. Higher order integration methods with continuous derivatives, such as second or fourth order Runge-Kutta, can also increase accuracy in the estimation of curved tracts [39].

To overcome directional ambiguity seen in less anisotropic tensors and areas with crossing fibers, some fiber tracking algorithms with utilize the entire tensor. One such algorithm is called tensor deflection or TEND that produces smoother results

than streamline algorithms. TEND defines the trajectory vector as the product of the diffusion tensor and the incoming vector direction [83]:

$$\mathbf{v}_{traj} = \mathbf{D} \cdot \mathbf{v}_{in} \tag{1.68}$$

TEND is designed to propagate through areas of low anisotropy and penalizes trajectories with high curvature. The direction of the output trajectory will be the same direction as the input trajectory when the tensor's anisotropy is parallel or perpendicular to the input trajectory. Therefore, for areas of isotropic diffusion, the estimated direction of the trajectory will not change for TEND because the principal eigenvector is not well-defined. TEND will also allow the fiber trajectory correctly when passing through the intersection of perpendicular crossing fibers. However, TEND may not follow the fiber trajectory correctly through the intersection of non-perpendicular crossing fibers [83]. A variation of TEND called tensorlines is weighted combination of the principal eigenvector, tensor deflection, and an undeviated component [84, 83]:

$$\mathbf{V}_{out} = f\mathbf{e}_1 + (1-f)((1-g)\mathbf{v}_{in} + g\mathbf{D} \cdot \mathbf{v}_{in} \tag{1.69}$$

1.3.3.3.1.2 Seeding and stopping criteria

White matter tractography is initiated in areas in the image called seed locations. Size of seeds range anywhere from a single voxel to a region of voxel to the entire brain. Multiple seeds can be place in a single voxel to sometimes generate multiple tract solutions through heterogenous white matter regions. However, these multiple solutions do not provide subvoxel resolution. Occasionally, regional seeds are used to select specific pathways. Care must be exercised during selection because this

process can lead to incomplete tract reconstructions. Whole-brain seeds are beneficial for generating nearly all possible pathways for the DTI data but with considerable redundancy [85].

Stopping criteria are used to terminate tracts once they have left the tract of interest or has become unreliable. One common stopping criterion is to terminate a tract once it has entered a region with low FA, whose threshold ranges from 0.1 to 0.2. The FA threshold has a similar purpose in RIS studies where it is used to limit the analysis to regions where the principal eigenvector is well-defined (WM). However, FA thresholding can cause tracking to terminate prematurely in regions of crossing fibers where the FA will be quite low. Another common stopping criterion is to terminate when the trajectory is bending more than a set angle threshold. Curvature criteria are based on the assumption that white matter trajectories are smooth and are used to prevent unrealistically large angular deviations in reconstructions. However, some pathways that are inherently highly curved, such as the Meyer's loop in the optic pathway and short subcortical U-fibers, suffer from inaccuracies due to curvature limits [85].

1.3.3.3.1.3 Combining good ideas

To overcome limitations of deterministic fiber tracking, sometimes it is useful to constrain the tract solutions. GTRACT allows the evaluation of multiple tract solutions, resulting in the selection of the solution with the lowest energy. The solution with the lowest energy is a function of the distance and the coherence of the local

tract directions and the principal eigenvector. In addition, in regions with crossing WM fibers, the tract solution will evaluate potential routes that are oblique to the principal eigenvector [86].

Some algorithms achieve tractography by estimating the global tractography solution that best fits the underlying DTI data instead of forward integration. One such example is the Gibbs tracking algorithm that uses an iterative optimization algorithm. The Gibbs tracking algorithm iterates through the following steps until an optimal solution is found: estimation of a global tracking pattern, generation of a corresponding synthetic DTI data set that is compared to the original DTI data, and perturbs the tract connection pattern to minimize the difference between the measured and synthetic data. The Gibbs tracking algorithm has shown to yield more diffuse and lateral connection patterns than its traditional streamline counterparts, at the cost of far more computational time [87].

1.3.3.4 Gradients for estimating anisotropic diffusion

In order to estimate diffusion in a single, symmetric 3x3 tensor, diffusion must be measured in a minimum of six directions plus a baseline image ($b = 0$ image). Therefore, in a diffusion-weighted imaging session, at least six gradient directions with the following properties must be used: no two gradient vectors are parallel or antiparallel (no positive or negative multiples of vectors), if three vectors are coplanar the remaining three vectors must not be coplanar, and no four vectors may be coplanar. Violation of the above three rules will result in using an undetermined **H**

(Eq. 1.29) or **B** (Eq. 1.42) matrix when computing the tensor [88].

There is a general consensus that the gradients should be as uniformly distributed as possible over a hemisphere of a sphere and then made negative (Figure 1.3). This will ensure uniform coverage of diffusion and minimize the effects of crossterms between the diffusion gradients and imaging gradients in D_{av} (average of three eigenvalues) and off-diagonal tensor elements [89]. Ideally, the measurements should have a high signal-to-noise ratio. A poor estimation of the diffusion tensor causes imprecise mean diffusivity values, over-estimation of anisotropic diffusion, and inadequate characterization of the principal direction of diffusion. Icosahedral schemes with 6, 101, 15, 16, 21, 25, or 31 directions provide well-spaced gradient vectors [66]. For schemes with greater numbers of directions, it is preferred to use the electrostatic repulsion model for selecting gradient vector coordinates. The electrostatic repulsion model falls into the category of numerically optimized schemes and is based on the minimum total interaction (Columbic) energy of 2 encoding directions (N_e) on the unit sphere. The charges experience vertex repulsion to prevent clustering and is defined by an expression analogous to total Coulombic energy (where $\hat{g}$ is a unit vector) [66, 38]:

$$E = \sum_{i=1}^{2N_e} \sum_{j>1}^{2N_e} \frac{1}{\|\hat{g}_i - \hat{g}_j\|} \tag{1.70}$$

The ideal number of unique gradient directions for estimating the diffusion tensor is still uncertain. There is an ongoing debate over the benefit of using a large number of different gradient orientations versus repeats of a smaller number of carefully chosen orientations. It seems that if gradient directions are uniformly spaced, more

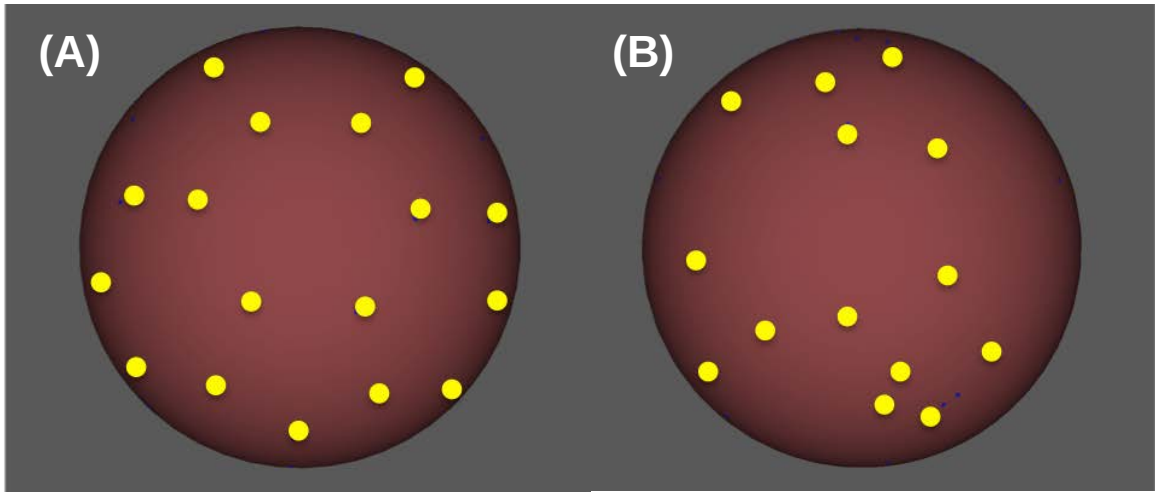

Figure 1.3: Examples of uniform and non-uniform gradient vector distributions, where the yellow dots represent terminal points of unit vectors on a unit sphere. (A) The uniformly distributed vectors exhibit a hexagonal pattern on the surface of the sphere, whereas the non-uniformly distributed vectors lack a consistent pattern on the sphere surface. (B) The non-uniformly sampled diffusion may be suitable for estimation of RISs but are often not suitable for fiber tracking or higher order tensor estimation due to directional biasing.

gradient directions (as opposed to multiple acquisitions of few directions) provides more constant variance in the calculated tensor parameters as the tensor is rotated, but does not improve the average variances over all possible rotations. An emerging rule of thumb is that at least 20 unique gradient directions should be acquired with a $b > 0$ for a robust estimation of FA, 30 for tensor-orientation and mean diffusivity. If fewer than 20 directions are collected, each acquisition should be repeated. Using 21 or more directions will yield a more uniform variance in calculated DTI parameters over all possible tensor orientations and minimizes the effect of signals that approach the noise level with very high anisotropy levels [90, 91, 92, 93, 94].

1.3.3.5 Pulsed gradient spin-echo sequence alterations

One variation of the pulsed gradient spin-echo sequence that has improved the acquisition of DWIs is the twice-refocused spin-echo (TRSE). Eddy current artifacts are likely to show up in DWI data due to the nature of the imaging sequence. The diffusion-weighting gradients provide unusually large eddy currents because they are at higher intensities and longer durations than the typical MRI scan. If the eddy current decays slow enough that a residual field remains in the image readout, the field behaves like an additional spatial encoding field and results in geometric distortion of the reconstructed images. The TRSE use two bipolar field gradients that produce equal and opposite eddy currents. Thus, the shorter the time between on and off transitions of the bipolar gradients, the greater the cancellation of the opposing eddy currents. Adding extra RF refocusing pulses to the sequence will further split the gradient pulses into shorter pulses. These shorter pulses produce specific exponentially decaying residual fields that can be entirely canceled. Timing of the second refocusing pulse is very flexible, thus leaving times between the excitation pulse and EPI readout available for diffusion-encoding pulsed gradients. The TRSE sequence also does not compromise efficiency or effectiveness of the underlying original Stejskal-Tanner spin-echo sequence [95].

Parallel imaging is often used because it reduces the echo time, preventing susceptibility artifacts caused by air-tissue interfaces. Parallel imaging also drastically reduces overall acquisition time by using multiple coils that detect only certain parts of the field of view. The multiple coil arrangement allows several areas of the field of

view to be imaged simultaneously without aliasing because each coil has no sensitivity in the region where aliasing would occur. Imaging time is even further reduced because each coil acquires only a fraction of the phase-encoding steps over its field of view [96, 97].

1.3.3.6 Human subject considerations

The optimal imaging sequence will need to strike a balance between the desired number of diffusion-weighted gradients and human subject comfort. More directions translate into more time in the scanner. Practical limitations on scan time may be shortened even further when the demographics of the human subjects are taken into account. For example, it would be impractical to scan neonates or subjects with a movement disorder such as Huntington's disease for long periods of time.

1.3.3.7 Multiple imaging sites

In order to collect larger volumes of data from more subjects, it would be practical to utilize multiple sites. PREDICT-HD is one example of a multi-center collaboration, with 32 sites throughout the world collecting symptom, neuropsychological, imaging, and genetic data on HD subjects. Out of the 32 PREDICT-HD sites, imaging data is being collected at 30 locations. Using multiple sites is a particularly useful strategy for recruiting large numbers of subjects with a rare genetic disease like HD. Given the advantages of using multiple sites to collect imaging data, information on reliability of results across sites and within subjects would be useful to investigators. Sources of variability arise when different sites use different scanner

vendors or even scanner software versions.

In regards to DWI data, degree of variability in DTI measures are usually reported via coefficient of variation (CV) or intra-class correlation (ICC) values. When comparing two 1.5T scanners from the same vendor, Pfefferbaum et al. showed that scanner effect was statistically significant [98]. It must be noted that the two scanners had different gradient systems but the same pulse sequence and gradient directions were used. However, the significant scanner effect only resulted in a 2% difference in FA values and a 1% difference in trace values [98]. When comparing two scanner vendors (both 1.5T), Cercignani et al. reported CVs between 5.4 - 7.5% for FA and 1.7 - 5.6% for MD [99]. As for 3T scanner assessments, Vollmar et al. compared two 3T scanners from the same vendor and showed CVs of 1.1% for whole brain and 1.2% for corpus callosum FA measures [100]. Vollmar et al. also produced reproducibility maps to demonstrate low variation ($> 5\%$) in main WM structures and higher variation (10 - 15%) in gray matter structures [100]. One of the most comprehensive studies to date on multi-site DWI data was done by Pagani et al. [101] who used both 1.5 and 3T field strengths on both Siemens and Philips scanners. Pagani et al. found an intra-site CV of 5.1 - 5.7% in FA and 6.2 - 7.9% in MD in the corpus callosum [101]. Through the comparison of different field strengths, Pagani et al. demonstrated that magnetic field strengths and scanner vendor significantly affected MD and AD measures [101].

As for reliability studies involving fiber tracking, investigators have yet to go beyond intra-site. To assess reproducibility of FA values on the same scanner within a

short time frame, Cheng et al. obtained two sets of fiber tracts between the cerebellum and thalamus from scans collected 24 hours apart. A correlation value of 0.82 was found between the tracts from the two time points [86]. Danielian et al. showed ICC values of 0.8 for MD, FA, and RD up to one year apart in the corticospinal tract, uncinate fasciculus, and corpus callosum derived via deterministic fiber tracking [102]. An example of a comprehensive intra-site fiber tracking reliability study was done by Wang et al., where fiber tracking was used to define regions of interest in multiple scans taken on the same subjects. 60 tractography measurements were made across subjects, of which 43 had intersession CV values $\leq 10\%$ and/or ICC values ≥ 0.70 for scans of 30 gradient directions repeated twice [103].

1.4 What is needed to study WM disease using DWI?

In order for clinical trials to use a tool such as DWI for monitoring disease progression in WM disease, data collection must occur at multiple sites to obtain sufficient sample sizes. Proper preparation for the scale of clinical trials for a WM disease will require DWI data processing and analysis to adapt to accommodate multi-site data. Therefore, a robust DWI data processing pipeline must be able to process a wide range of data collected with different scanner software versions and models from all major MRI scanner vendors. Since DWI data tends to be noisy due to the violent nature of the scanning process, a robust DWI data processing pipeline needs to incorporate an automated quality control step in addition to visual inspections. When investigating new possible imaging biomarkers of disease progression, established non-

imaging biomarkers must be used to select regions of interest for analysis and to support new imaging findings. As established earlier, there are several types of DWI analyses, each with a different level of complexity. When investigating a new region of WM, the first analysis should always compare mean DTI scalars across that region of WM from the WM disease population to healthy controls. If differences in diffusivity in the new region of WM can be detected between the WM disease population and healthy controls, a cross-sectional fiber tracking analysis of WM tracts connecting to the region of interest (or perhaps the region of interest is a WM tract) is the next step. Finally, the fiber tracking analysis needs to be done longitudinally to determine if the diffusivity changes in the WM region of interest can be monitored over time.

The purpose of this thesis was to address the above requirements in preparing for a large scale clinical trial using measurements derived from DWIs as biomarkers for disease progression in a WM disease. Each requirement is addressed separately in the following chapters. Chapter 2 describes several tools that solve mulit-site data issues, such as DWI DICOM data compatibility and quality control, and their application to DWI data from healthy controls collected at multiple sites in a DTI scalar reliability analysis. Chapter 3 describes a mean DTI scalar analysis in focused regions of PFC WM. Given that disease progression of the current WM disease model, prodromal HD, is well-characterized by measures of cognitive performance, the WM of the PFC was chosen for analysis based on its presumed role in cognitive functions. Chapter 4 addresses the requirements of a cross-sectional fiber tracking study: selection of relevant WM tracts and finding a way to compare data from all participants along

a tract. The forceps minor, anterior thalamic radiations, inferior fronto-occipital fasciculi, and uncinate fasciculi were chosen because they all have extensions to the PFC. These four tracts are also well-established in humans and the intention of using them in this thesis was to avoid the uncertainty involved in analyzing a tract whose existence is questionable. An atlas-based approach was used to create a space for analysis. The TBSS algorithm was used on tracts to skeletonize them into an average representation of the tract. However, unlike the traditional TBSS method, tracts were first derived and then skeletonized individually to preserve individual morphologies. Chapter 5 is the longitudinal extension of the cross-sectional fiber tracking analysis, along with an exploration of parallel transport methods to investigate longitudinal WM morphology changes.

CHAPTER 2
TRAVELING HUMAN PHANTOM STUDY

2.1 Introduction

The overall goal of this study was to show that it is possible to reliably collect DWI data from multiple participants at multiple sites and incorporate that data into a single analysis. Reliability of DWI data across site and longitudinally across time is extremely important to a rare disease study like PREDICT-HD that depends upon the combination of results from multiple imaging sites. In order to investigate issues that arise with the use of multiple imaging sites, DWI data from eight geographically distributed sites, including 2 distinct vendors (Siemens and Philips) and 4 different scanner software configurations were analyzed. The homogeneity properties of DWI analysis were investigated only on 3T data on five healthy subjects (the Traveling Human Phantoms or THPs). Two imaging protocols with different numbers of diffusion-sensitizing gradients that were vendor standards were applied to assess intra-subject and inter-site variability. Diffusivity of white matter by lobe was quantified with commonly-used RISs (FA, MD, RD, and AD).

2.2 Methods

2.2.1 Imaging

Five healthy volunteers were recruited and informed consent was obtained in accordance with the Institutional Review Board at each imaging site. Each subject was imaged at all of the eight sites within a 30-day period. All eight sites used 3T

scanners, where five sites used a Siemens TIM Trio (gradient strength = 45mT/m, slew rate = 200 T/m/s) and three sites used a Philips Achieva scanner (gradient strength = 80 mT/m, slew rate = 200 T/m/s) with varying scanner software versions (Table 2.1). All imaging data was transferred to the University of Iowa for processing and analysis.

Table 2.1: Sites and scanners used in the Traveling Human Phantom study.

Site	Vendor	Model	Software Version	Gradient Specifications	Head Coil
University of Iowa	Siemens	TIM Trio	B13	$\frac{45mT/m}{200T/m/s}$	12 Channel
University of Minnesota	Siemens	TIM Trio	B15	$\frac{45mT/m}{200T/m/s}$	12 Channel
University of California, Irvine	Siemens	TIM Trio	B15	$\frac{45mT/m}{200T/m/s}$	12 Channel
Massachusetts General Hospital	Siemens	TIM Trio	B15	$\frac{45mT/m}{200T/m/s}$	12 Channel
Cleveland Clinic	Siemens	TIM Trio	B15	$\frac{45mT/m}{200T/m/s}$	12 Channel
Johns Hopkins	Philips	Achieva	2.6.1	$\frac{80mT/m}{200T/m/s}$	8 Channel
Darthmouth	Philips	Achieva	2.5.3	$\frac{80mT/m}{200T/m/s}$	8 Channel
University of Washington	Philips	Achieva	2.5.3	$\frac{80mT/m}{200T/m/s}$	8 channel

Source: V. A. Magnotta, J. T. Matsui, D. Liu, H. J. Johnson, J. D. Long, B. D. Bolster, B. A. Mueller, K. O. Lim, S. Mori, K. Helmer, J. A. Turner, M. Lowe, E. Ayl- ward, L. A. Flashman, G. Bonett, and J. S. Paulsen, Multi-Center Reliability of Diffusion Tensor Imaging., *Brain connectivity*, 2012.

All DWI scans were vendor standard sequences without cardiac gating. Siemens scanners used a double refocused spin-echo sequence, while Philips scanners used a

Stejskal-Tanner sequence. Two types of scanning protocols were used: a vendor-provided DWI gradient directions table (30 unique gradient directions and 1 baseline image for Siemens scanners, 32 unique gradient directions and 1 baseline image for Philips scanners) and a custom gradient encoding scheme designed using electrostatic repulsion (71 unique gradient directions and 8 baseline images for both Siemens and Philips scanners). A b-value of 1000 sec/mm^2 was used for each gradient with diffusion weighting. Four repetitions of the 30 or 32 direction sequence were acquired with 70 slices per volume, while two repetitions of the 71 direction sequence were acquired at 50 slices per volume. All DWI sequences had the same field of view (256 $\times$ 256 mm), matrix size (128 $\times$ 128), echo-time (TE = 92 ms), bandwidth (1565 Hz/pixel), and slice thickness/gap (2.0/0.0 mm). 70 slices per volume were collected for the 30 or 32 direction sequences, while 50 slices per volume were collected for the 71 direction sequence. Siemens scanners used TR times of 10000 and 12000 ms for the 71 and 30 direction sequences, respectively. Philips scanners used TR times of 9750 and 7000 ms for the 71 and 32 direction sequences, respectively. Durations of scans were approximately 6.5 and 15 minutes for the 30/32 and 71 direction sequences, respectively.

Structural images were also acquired at each site using three-dimensional (3D) T1- (MP-RAGE) and T2-weighted sequences. For this analysis, only anatomical images acquired at the University of Iowa site were used. Therefore, only Siemens scanner parameters for anatomical images will be reported. T1-weighted images were collected in the coronal plane with the following parameters: TI = 900 ms, TE =

2.85 ms, TR = 2300 ms, flip angle = 10^o, NEX = 1, Bandwidth = 240 Hz/pixel, FOV = 260 × 260 × 264 mm, Matrix = 256 × 256 × 240. T2-weighted images were collected in the coronal plane with the following parameters: TE = 452 ms, TR = 4800 ms, Bandwidth = 590 Hz/pixel, Matrix = 256 × 186 × 120, FOV = 256 × 186 × 160 mm.

2.2.2 Structural image pre-processing

Structural image pre-processing was performed using a derivative of the fully-automated BRAINS (Brain Research: Analysis of Image, Networks, and Systems) AutoWorkup software package [104, 105, 106, 107]. T1- and T2-weighted images collected at the University of Iowa were first anterior commissure (AC)-posterior commissure (PC) aligned. Talairach parameters were defined in order to warp the Talairach grid onto the subject data. Tissue classification [11] and skull stripping using an artificial neural network [108] were performed. The following regions of interest were defined based on the Talairach atlas (cerebrum, frontal lobe, temporal lobe, parietal lobe, occipital lobe, and subcortical area) [109].

2.2.3 Conversion of DWI data from DICOM

The NRRD (nearly raw raster data) file format is becoming an increasingly popular method of DWI data storage. The NRRD file is useful for DWI data because of its ability to consistently store all the necessary metadata from DICOM files for DWI analysis. DicomToNrrdConverter was the first program designed to convert DWI DICOM data into the NRRD file format in a consistent manner [110]. DicomToNr-

rdConverter was originally developed by Xiaodong Tao, PhD at the General Electric Global Research Center to convert GE signal DWI DICOM data. When work began on DWI data from the PREDICT-HD study that had many more DWI DICOM data types aside from GE, it it was discovered that many DWI DICOM data sets were indecipherable or incorrectly converted with the DicomToNrrdConverter. As a result, in 2010, through the combined efforts of developers at the University of Iowa and the University of North Carolina and Dr. Tao, DicomToNrrdConverter compatibility was expanded to convert 15 varieties of DWI DICOM data, with GE, Siemens and Philips vendor coverage (all are included in Table 2.2.) Eventually, those at the University of Iowa convinced the NAMIC community that DWI DICOM compatibility will continue to be a recurring problem because scanners will always be upgraded. Thus, in 2012, with the assistance of Norman K. Williams and the NAMIC community, DicomToNrrdConverter was refactored into an extensible and easily modifiable program called DWIConvert [111]. DWIConvert has been expanded to support the conversion of 18 known varieties of DWI DICOM data to NRRD and NIFTI file format (Table 2.2). This number of compatible DICOM varieties is based on work performed on DWI data from the PREDICT-HD study.

The most significant issue encountered when making DicomToNrrdConverter compatible with DWI data from multiple vendors was simply extracting and interpreting correct metadata from DWI DICOM files created by different scanner vendors. Types of metadata that are most important for calculating DTI data include: image space, image size, slice thickness, space directions, space origin, measurement frame,

Table 2.2: DWI DICOM data types that are able to be converted with DWIConvert based on work performed on DWI data from the PREDICT-HD study.

Vendor	Scanner Model	Scanner Software Version
GE	Signa HDxt	14 LX MR Software release:14.0 M5 0737.f
GE	Signa HDxt	14 LX MR Software release:14.0 M5A 0828.b
GE	Signa HDxt	15 LX MR Software release:15.0 M4 0910.a
GE	Signa HDxt	15 LX MR Software release:15.0 M4A 0947.a
Philips	Achieva	2.1.3.6
Philips	Achieva	2.5.3.0
Philips	Achieva	2.5.3.3
Philips	Achieva	2.6.3.2
Philips	Achieva	2.6.3.4
Philips	Achieva	2.6.3.5
Philips	Achieva	3.2.1.0
Philips	Intera	10.6.2.6
Siemens	Allegra	syngo MR A30 4VA30A
Siemens	TrioTim	syngo MR B13 4VB13A
Siemens	TrioTim	syngo MR B15
Siemens	TrioTim	syngo MR B17
Siemens	Verio	syngo MR B15V
Siemens	Verio	syngo MR B17

b factor, diffusion-weighted gradient direction coordinates, and all the gradients in a single 4D file. A DWI scan often has 2,000 to 53,000 file components to represent a single 4D data set, depending on the scanner vendor used. Each type of metadata is housed in DICOM files in its own element tag. The element tag contains a tag group and element numbers in hexidecimal as given in the DICOM standard guidelines [112].

In general, the use of public element tags to store metadata is encouraged because public element tags should contain the same type of metadata across scanner vendors and software versions. However, metadata in the public element tags become

a problem when their contents are not accurate. A common difficulty in DICOM file conversion is obtaining the correct diffusion-weighted gradient direction coordinates. Accurate diffusion-weighted gradient direction coordinates are vital to reliable fiber tracking and being able to compare DTI results collected from different scanners. The coordinates are sometimes incorrect due to miscalculations from the **b** matrix or input error at scan time. A quick solution for incorrect coordinates is to directly calculate the diffusion gradient direction coordinates and b value from the **b** matrix of the gradient. The **b** matrix values are often in a private element tag, an element tag whose contents are not regulated by the DICOM standard guidelines, and thus can vary from vendor to vendor. The following table (Table 2.3) contains a subset of private element tags that identify important DWI scan information necessary for DTI calculations, separated by scanner vendor. To add to the complexity of the situation, the contents of private element tags are not published material (this was obtained from the scanner vendors directory) and can even vary within a vendor's scanner software versions.

To overcome inaccuracies in public element tag gradient direction coordinates, joint development from the University of Iowa and the University of North Carolina has enhanced DicomToNrrdConverter to support the derivation of diffusion gradient vector coordinates from each gradient's **b** matrix private element tag. Currently, the feature is only available for Siemens data. The six values in the **b** matrix tag represent the six unique elements of the **b** matrix. Once the **b** matrix is reassembled from the DICOM header, the trace of the **b** matrix is the b factor for the gradient. A singular

Table 2.3: Private element tags (except for measurement frame) for DICOM data produced by a subset of GE, Siemens, and Philips MRI scanners.

Element tag	GE (Signa)	Siemens (Trio Tim)	Siemens (Verio)	Philips (Achieva)
B value	0043,1039	0029,1010	0029,1010	2001,1003
Gradient vector coordinates	0019,10BB (x) 0019,10BC (y) 0019,10BD (z)	0029,100E	0029,100E	2001,1004
Mosaic size parameters		0051,100B 0029,100A	0051,100B 0051,100B	
Measurement frame		0020,0032	0020,0032	0020,0032
B matrix		0019,100E		

Note: Scanner vendor brand is listed at the head of each column with its scanner version in parentheses.

value decomposition of the **b** is then performed to extract the diffusion gradient direction coordinates, which is the first column of the 3x3 column orthogonal matrix. The diffusion gradient direction vector will be a unit vector, which is an assumption that allows the ability to calculate the b factor and gradient coordinates from the **b** matrix [66].

2.2.4 Quality control of diffusion data: DTIPrep

This part of the study involved the testing and deployment of quality control steps for DWI data that are possibly the most comprehensive available in the literature. These comprehensive quality control features were packaged in an automated quality control tool called DTIPrep and has been jointly developed at the University of Iowa and University of North Carolina. Adding DTIPrep as a pre-processing step had two main purposes: 1) remove gradients containing artifacts common to DWI in

an automated fashion to further ensure homogeneity of data, and 2) check scan protocol parameters to verify that data from different sites are comparable in an automated fashion. The DTIPrep pipeline also terminated at any step if less than six diffusion gradients remained or all of the baseline image were removed due to failing quality standards [113]. This termination step prevented unusable scans from being included in further analyses. Ultimately, the removal of artifacts could potentially improve DWI analyses, particularly fiber tracking. The following sections (Sections 2.2.4.1 through 2.2.4.8) outline each step of DTIPrep's pipeline.

2.2.4.1 Image information check

DTIPrep initiated its pipeline by verifying that the protocol used to collect the diffusion-weighted data is consistent with its assigned template protocol (data acquisition protocol). Image information was checked for mismatches in image size, origin, and voxel spacing. The pipeline terminated if mismatches voxel spacing were found while mismatches in image origin were reported [113].

2.2.4.2 Diffusion information check

Diffusion information was checked to detect scans with incorrect numbers of diffusion gradients, diffusion gradient directions, and applied b factor. In the event of a mismatch in diffusion gradient vector coordinates between the data acquisition protocol and the scan of interest, a series of tolerance tests are executed to determine whether these vectors were colinear. The criterion for colinearity is an angle difference of less than one degree between the vectors in the data acquisition protocol and scan

of interest. To maintain consistency in this check, all vectors from scan and protocol were checked for colinearity in anatomical space. The need for this transformation was realized when processing Philips data. Philips data is based on two separate sets of axes: scanner and anatomical (patient) space (Figure 2.1). The diffusion gradient vector and diffusion information is measured in anatomical space, while the diffusion gradient vector is recorded in the DICOM header in scanner space. Fortunately, the direction cosines matrix for transforming from anatomical to scanner space is provided in the DICOM header as the measurement frame (non-identity matrix for Philips). Therefore, to bring the vectors from scanner to anatomical space, the vectors are multiplied by the inverses of their respective normalized measurement frames. The same check is done for Siemens data but is much simpler since Siemens defines scanner and anatomical space share the same axes (Figure 2.1) [113].

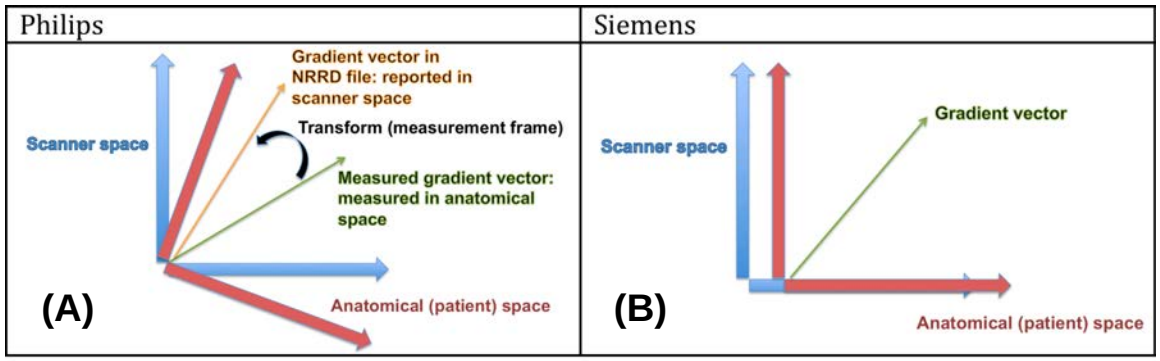

Figure 2.1: Illustration of the different axes and gradient vector representation in different scanners. Axes for two scanner vendors are shown: Philips (A) and Siemens (B).

Figure 2.2 serves to illustrate the importance of ensuring that accurate gradient vector coordinates are in each NRRD file with RGB-scaled color glyphs that represent maximum eigenvector orientation. The left panel of Figure 2.2 contains RGB-scaled color glyphs that correspond to the maximum eigenvector glyphs oriented perpendicular to their expected orientations as the result of having incorrect gradient coordinates in the NRRD file (emphasized by the yellow circle). Data containing incorrect gradient coordinates could therefore adversely affect fiber tracking by creating incorrect reconstructions of white matter. The right panel of Figure 2.2 contains RGB-scaled color glyphs that represent the maximum eigenvectors that are properly oriented as the result of having gradient coordinates in the NRRD file that are consistent with anatomical a-priori information.

2.2.4.3 Slice-wise intensity-related artifact checking

After the imaging protocol parameter checks, DTIPrep determined the presence of intensity-related artifacts (Figure 2.3 across all diffusion-sensitized gradients using a slice-wise checking algorithm. The normalized correlation (NC) value was computed on a pixel-by-pixel basis between two successive slices (A and B) and normalized by the square root of the autocorrelation of the slices, where N was the number of pixels considered:

$$NC(A,B) = \frac{\sum_{i=1}^{N}(A_i * B_i)}{\sqrt{\sum_{i=1}^{N} A_i * \sum_{i=1}^{N} B_i}} \tag{2.1}$$

It is assumed these correlation values will form a normal distribution across the diffusion gradient directions. The user can define the number of standard deviations

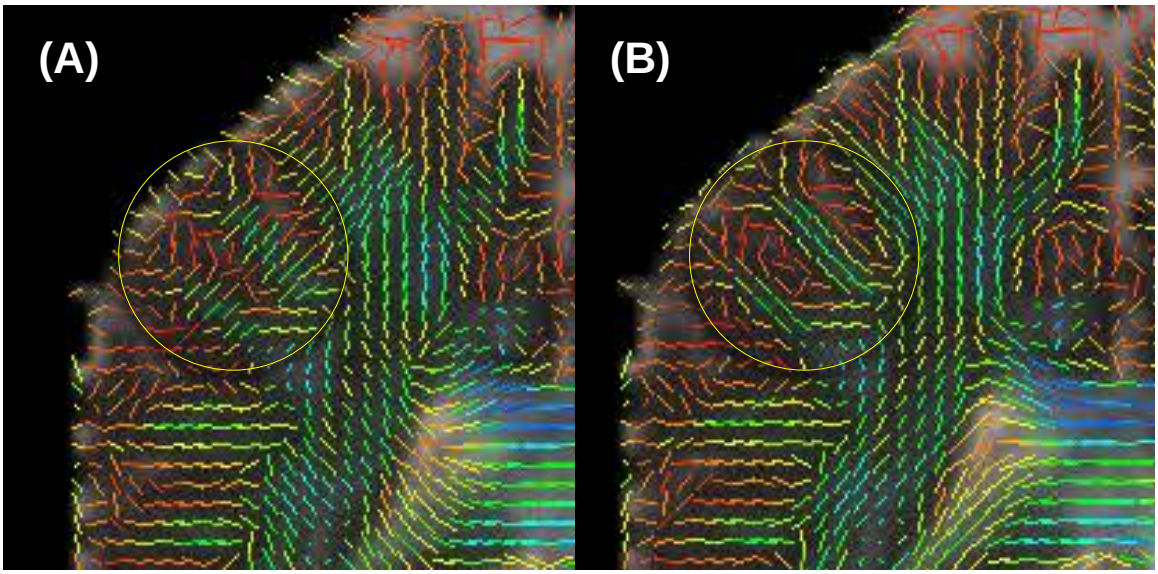

Figure 2.2: Proper and improper orientation of maximum eigenvector glyphs in DTI data. (A) Green maximum eigenvector glyphs representing white matter traveling to the cortex that are oriented perpendicular to their expected orientations. (B) Green maximum eigenvector glyphs representing white matter traveling to the cortex that are properly oriented.

used to define an outlier for the correlation values. In this study, 3.1 and 3.6 standard deviations were used for the $b = 0$ and DWIs, respectively. NC values outside of the user-defined number of standard deviations from the mean NC for a given gradient represent slices containing intensity artifacts and their corresponding gradients are removed. This slice-wise intensity check is used to remove gradient directions that exhibit large changes in signal intensity that are not related to the diffusion encoding gradients such as table vibrations and spike noise [113].

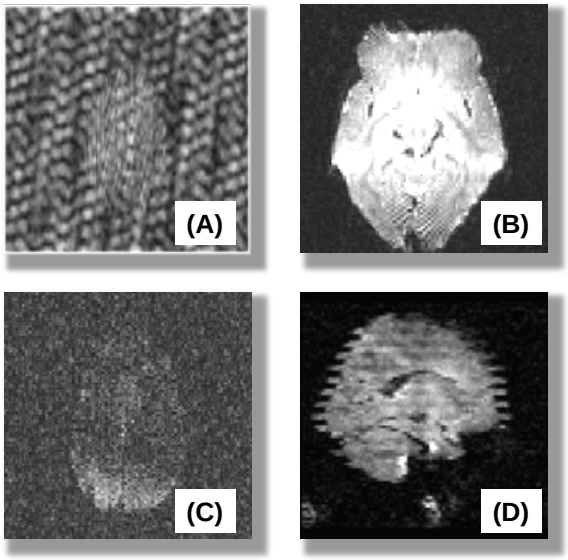

Figure 2.3: Examples of intensity-related artifacts detected and removed by DTIPrep. (A) Radio frequency interference. (B) Signal dropout in the checkerboard area. (C) Badly recorded slice. (D) Venetian blind artifact.

Source: Z. Liu, Y. Wang, G. Gerig, S. Gouttard, R. Tao, T. Fletcher, and M. Styner, Quality control of diffusion weighted images, *Proceedings of SPIE*, vol. 7628, pp. 76280J1, 2010.

2.2.4.4 Interlace-wise venetian blind artifact checking

Venetian blind artifacts result from subject motion between the interleaves of a multi-pass acquisition. There are two steps in detecting venetian blind artifacts: calculation of NC values between interleaving parts of each gradient and motion parameters. The NC here is used similarly to the NC used in the slice-wise check, where a gradient whose NC is outside of the user-defined number of standard deviations from the mean NC for the scan removed. In this study, 2.5 and 3.0 standard deviations were used for $b = 0$ and DWIs, respectively. Motion parameters are obtained by performing a rigid registration between the even and odd slices of the dataset for each

diffusion-sensitizing gradient. The resulting estimates for translation and rotation are compared to user-defined thresholds (2.0 mm translation and 0.5 degrees rotation in this study), and gradients that exceed these thresholds are removed from the analysis [113].

2.2.4.5 Baseline averaging

Motion between baseline scans is then estimated by DTIPrep and used to align all the $b = 0$ images together. The resulting average baseline image is then used as a reference for subsequent motion and eddy current correction for the DWIs. Motion and eddy current artifacts are corrected by estimating an affine transform between each of the DWIs and the average baseline image. There is an option of using a mutual information metric to account for differences in signal intensity between the images. In this study, a mutual information metric with a stop condition of less than 0.02 was used to align the $b = 0$ images. The gradient directions are also updated based on the rotation component of the affine transformation [113, 114].

2.2.4.6 Eddy current, head motion artifacts checking

As mentioned in Section 1.3.3.5, eddy current artifacts are likely to show up in DWI data due to the nature of the imaging sequence. Eddy current-induced distortions can lead to misregistration between different DWIs and eventually to error in the tensor image in all voxels. Thus, it is good practice to remove the eddy current artifacts by coregistering all diffusion-weighted gradients to the first gradient (usually a $b = 0$ image) before deriving the tensor image. In DTIPrep, a mutual

information metric cost function is used, where the differences in signal intensity drives the registration. A full affine registration is used to accommodate for eddy current artifacts and take care of motion artifacts as well [113]. In this study, the affine registration used a relaxation factor of 0.5 and a maximum step size of 0.1.

2.2.4.7 Gradient-wise checking

The final step of DTIPrep is meant to remove residual motion artifacts after the eddy current and head motion corrections. This step allows the user to remove gradients when the estimated translation or rotation exceeds a user-defined threshold (2.0 mm translation and 0.5 degrees rotation in this study) relative to the (averaged) baseline gradient [113].

2.2.4.8 Final output of DTIPrep

DTIPrep also performs a post-registration step that retrospectively computes a rigid rotation to bring all gradients into anatomical space. The transformation into anatomical space will account for the scan's individual measurement frame and transformations that occurred during the DTIPrep pipeline. A new NRRD file that reflects the overall transformation and excludes all bad gradients (Figure 2.4) is the final output of DTIPrep, in addition to a report file describing all exclusions [113].

2.2.5 Diffusion tensor image data processing

The two sets of DWI scans described in Section 2.2.7 were then analyzed with the Guided Tensor Resored Anatomical Connectivity (GTRACT) software [86]. Dif-

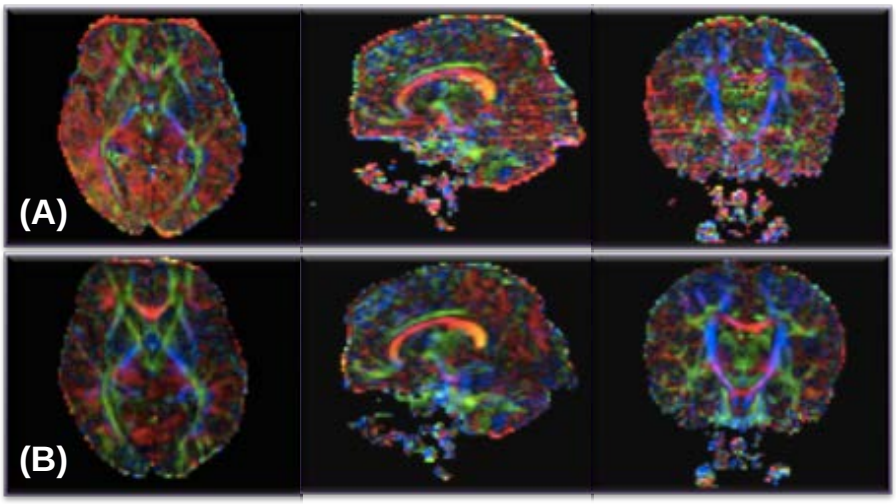

Figure 2.4: Illustration of how DTIPrep can improve DTI quality by removing gradients containing artifacts. Color maps reflecting the degree and orientation of anisotropy without quality control processing by DTIPrep (A) and with DTIPrep (B).

Source: Z. Liu, Y. Wang, G. Gerig, S. Gouttard, R. Tao, T. Fletcher, and M. Styner, Quality control of diffusion weighted images, *Proceedings of SPIE*, vol. 7628, pp. 76280J-1, 2010.

fusion tensor images were estimated from each DWI with and without the application of a 3 x 3 x 3 voxel median filter to the $b = 0$ and diffusion-weighted volumes. The following RIS images were computed from the tensor images: FA, MD, RD, and AD. A B-Spline transform was derived via a two-step registration procedure between the averaged baseline of each DWI scan and the corresponding subject's T1-weighted image to remove susceptibility artifacts from the EPI images [115]. The first step of the registration was a six parameter rigid registration (3 translations and 3 rotations) that aligned the averaged baseline to the T1-weighted image. The second step of the registration was a non-linear B-Spline registration initialized with the rigid transform.

The B-Spline transform was then used to resample the RIS images into the space of each subject's T1-weighted and tissue-classified image. White matter was defined in an automated fashion in the RIS images through the intersection with the tissue classified image's definition of white matter and the threshold of the FA image at 0.1. Refining the white matter definition allowed the removal of regions that were lost due to susceptibility artifacts. Regional RIS measures were obtained by left and right hemisphere and both hemispheres for the entire cerebrum, frontal lobe, occipital lobe, parietal lobe, temporal lobe, and subcortical area.

2.2.6 Manual review of imaging data

All imaging data was manually reviewed for artifacts, missing volumes, and quality of registration with the anatomical image. Data with image artifacts or missing volumes were excluded from this study. Less than optimal registrations were fixed with either a new manually generated rigid body transformation or using the T2-weighted image as the fixed image instead. Gradients removed by DTIPrep were also documented and evaluated for trends.

2.2.7 Experimental set-up

Once converted into NRRD file format, repeat acquisitions of DWI scans were combined or concatenated together at different levels. Since the 30 or 32 direction protocol was acquired four times per subject at each site, three different levels of concatenated 30 or 32 direction scans were created: two (60 or 64 directions), three (90 or 96 directions), and four (120 or 128 directions) scan repeats. The same con-

catenation procedure was done for the 71 direction protocol, creating an additional level of concatenated scans (142 directions). At this point, all individual and concatenated scans were subjected to two types of processing, with and without quality control, creating two sets of DWI scans that were then propagated through the same DTI processing. The first set of DWI scans was created by subjecting all individual and concatenated scans to an extensive quality control procedure performed by a program called DTIPrep (as described in Section 2.2.4), where artifacts commonly seen in DWIs were removed. The second set of DWI scans was created by skipping the use of DTIPrep and undergoing traditional basic DWI processing steps: baseline averaging via a mutual information metric and correction for motion and eddy current artifacts. DTIPrep included baseline averaging and motion and eddy current artifact correction in the same manner, in addition to non-traditional DWI processing steps. The two sets of resulting DWI scans (with and without quality control) were used to estimate two separate sets of tensor and RIS images (Table 2.4). Analyzing RISs from tensor images estimated from DWI scans in both individual and concatenated forms allowed the assessment of the effects of signal-to-noise ratio (SNR) on the reliability of results. Analyzing RISs from tensor images estimated from DWI scans with and without quality control allowed the assessment of the effects of common DWI artifacts on the reliability of results.

Table 2.4: Types of DWI scans that were created per subject and site, and proceeded to tensor estimation and DTI scalar analysis.

Directions per initial scan	Scan repeats	Directions in concatenated scan	DTIPrep used?	Baseline averaging outside DTIPrep?	Eddy current and motion correction outside DTIPrep?
30/32	1	30/32	No	Yes	Yes
30/32	1	30/32	Yes	No	No
30/32	2	60/64	No	Yes	Yes
30/32	2	60/64	Yes	No	No
30/32	3	90/96	No	Yes	Yes
30/32	3	90/96	Yes	No	No
30/32	4	120/128	No	Yes	Yes
30/32	4	120/128	Yes	No	No
71	1	71	No	Yes	Yes
71	1	71	Yes	No	No
71	2	142	No	Yes	Yes
71	2	142	Yes	No	No

2.2.8 Statistical analysis

Both within-subject reliability (whether RIS values can be reliably reproduced in repeated scans) and between-site reliability (whether RIS values can be reliably measured across site) of RIS values were evaluated. Since average scalar measures in large regions of interest were used in this study, reliability was quantified using the coefficient of variation (CV). Thus, decreased CV values indicated better reliability. Covariates that were accounted for included scanner vendor (Siemens, Philips), site (eight imaging sites), use of DTIPrep (yes, no), scanning protocol (high, low number of gradient directions per scan), median spatial filtering (yes, no), and number of concatenations (1, 2, 3, 4). Within-subject CV was calculated between repeated

scans from each subject on the same scanner and scanning protocol within the same site. Within-subject CVs were compared across RIS type, regions of interest, scanner vendor, scanning protocol, and sites. Between-site CV was calculated between scans from each subject across all eight sites. Between-site CVs were compared across RIS type and regions of interest. To quantify central tendency and variability of the study sample, mean and standard deviation (SD) of CVs were computed. Linear mixed-effects models were utilized to evaluate the covariate effects. CVs were plotted with R (http://cran.r-project.org/) and statistical analyses were carried out with SAS (Cary, NC).

2.3 Results

2.3.1 Data exclusion

Five 30 or 32 direction scans from a single vendor (two from Dartmouth and three from Johns Hopkins) were identified by DTIPrep as having too many corrupted gradients for subsequent processing. These five scans were removed from all further processing and analyses as they also contained significant subject motion artifacts. As for the remaining DWI scans, DTIPrep eliminated 9.57% to 20.47% of 3D gradient volumes per site, where a 3D volume was considered a baseline image or one with diffusion-weighting (Table 2.5). On average, DTIPrep removed 12.76% of 3D gradient volumes per site. Nearly all gradient removal occurred during the slice-wise checking step. Only a small percentage of gradients were removed by the gradient-wise checking step. Based on these results, it can be inferred that DTIPrep removes the majority

of artifacts before baseline averaging. An analysis of the excluded gradients with diffusion weighting showed that the most frequently removed gradients were those with dominant axes in the z-direction (Figure 2.5).

Table 2.5: Number of gradients removed by DTIPrep during each artifact detection step for each site.

Site	Slice-wise Check	Venetian Blind Check	Gradient-wise Check	Total
University of Iowa	136 (10.15%)	1 (0.075%)	0 (0%)	137 (10.22%)
University of Minnesota	167 (11.84%)	3 (0.21%)	0 (0%)	170 (12.06%)
University of California, Irvine	133 (9.43%)	2 (0.14%)	0 (0%)	170 (12.06%)
Massachusetts General Hospital	136 (9.65%)	1 (0.071%)	0 (0%)	137 (9.72%)
Cleveland Clinic	171 (12.13%)	1 (0.071%)	0 (0%)	172 (12.20%)
Johns Hopkins	143 (11.16%)	2 (0.16%)	3 (0.23%)	148 (11.55%)
Dartmouth	269 (20.47%)	0 (0%)	0 (0%)	269 (20.47%)
University of Washington	222 (16.08%)	3 (0.22%)	0 (0%)	225 (16.30%)

Source: V. A. Magnotta, J. T. Matsui, D. Liu, H. J. Johnson, J. D. Long, B. D. Bolster, B. A. Mueller, K. O. Lim, S. Mori, K. Helmer, J. A. Turner, M. Lowe, E. Ayl- ward, L. A. Flashman, G. Bonett, and J. S. Paulsen, Multi-Center Reliability of Diffusion Tensor Imaging., *Brain connectivity*, 2012.

2.3.2 Mean FA and MD values

Since mean RIS values for combined hemispheres were similar to those in the left and right, only combined hemisphere results are presented. Mean FA values ranged from 0.218 to 0.372 across regions with the use of median filtering, where the ordering of FA from smallest to largest by region was follows: occipital lobe, temporal

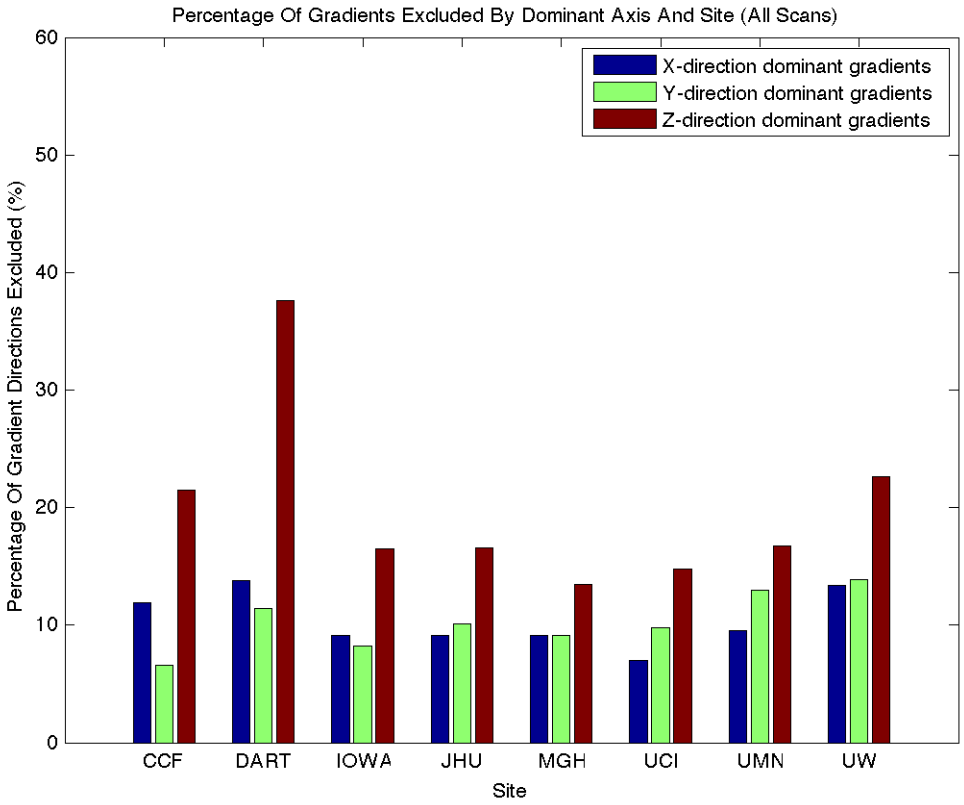

Figure 2.5: Percentages of gradients excluded by diffusion measured along the dominant axis.

Source: V. A. Magnotta, J. T. Matsui, D. Liu, H. J. Johnson, J. D. Long, B. D. Bolster, B. A. Mueller, K. O. Lim, S. Mori, K. Helmer, J. A. Turner, M. Lowe, E. Ayl- ward, L. A. Flashman, G. Bonett, and J. S. Paulsen, Multi-Center Reliability of Diffusion Tensor Imaging., *Brain connectivity*, 2012.

lobe, cerebrum, parietal lobe, frontal lobe, and subcortical region. When median filtering was not used, FA values increased and ranged from 0.280 to 0.437 (Table 2.6). However, the ordering of FA values across regions remained the same as when median filtering was used. Mean FA values ranged from 0.294 to 0.309 across site with median filtering and 0.346 to 0.374 without median filtering. The standard deviations for FA

across site were approximately 0.04 for all sites (Table 2.7). Mean FA values for Siemens scanners were slightly less than those from Philips scanners (Table 2.8). Mean FA values computed from scans with 71 gradient directions were lower than those computed from scans with 30 or 32 gradient directions. All differences in FA were evaluated by a mixed-effects model analysis and deemed statistically significant. Differences in FA appeared small to small standard errors. MD values were not affected by the median filter, whereas the median filter increased RD and decreased AD. Siemens scanners had slightly greater MD values than Philips. Standard errors were small as well in MD, AD, and RD values. Therefore, all differences in MD, AD, and RD were also statistically significant. MD values and their standard deviations were similar between scanning protocols.

2.3.3 Within-subject reliability analysis

The within-subject reliability analysis (Figure 2.6, left panel) showed that CVs were less than 1.5% across all RIS measures for all brain regions when median filtering was used (Figure 2.6, right panel). Mean CVs were all less than 1% across all sites and RIS measures, except for Johns Hopkins that had CVs for FA and AD greater than 1% (Table 2.9). When median filtering was not applied, all RIS measures from Johns Hopkins and FA values from the University of Iowa and University of California, Irvine were above 1%. The mean CV for the 71 gradient direction protocol (0.46% with median filtering, 0.60% without) was slightly less than the mean CV for the 30/32 gradient direction protocol (0.56% with median filtering, 0.71% without). A

Table 2.6: Mean and standard deviation of DTI scalars by region across all sites.

RIS	Region	Mean with median filter	Standard deviation with median filter	Mean without median median	Standard deviation without median filter
MD	Cerebrum	0.767×10^{-3}	1.874×10^{-5}	0.773×10^{-3}	1.86×10^{-5}
	Frontal lobe	0.766×10^{-3}	1.876×10^{-5}	0.772×10^{-3}	1.82×10^{-5}
	Occipital lobe	0.767×10^{-3}	2.984×10^{-5}	0.767×10^{-3}	2.58×10^{-5}
	Parietal lobe	0.774×10^{-3}	2.630×10^{-5}	0.776×10^{-3}	2.77×10^{-5}
	Subcortical	0.773×10^{-3}	2.113×10^{-5}	0.773×10^{-3}	2.19×10^{-5}
	Temporal lobe	0.771×10^{-3}	2.059×10^{-5}	0.785×10^{-3}	1.59×10^{-5}
RD	Cerebrum	0.653×10^{-3}	1.81×10^{-5}	0.608×10^{-3}	2.22×10^{-5}
	Frontal lobe	0.642×10^{-3}	1.74×10^{-5}	0.603×10^{-3}	1.99×10^{-5}
	Occipital lobe	0.694×10^{-3}	2.75×10^{-5}	0.636×10^{-3}	3.13×10^{-5}
	Parietal lobe	0.653×10^{-3}	2.60×10^{-5}	0.608×10^{-3}	3.25×10^{-5}
	Subcortical	0.612×10^{-3}	2.05×10^{-5}	0.566×10^{-3}	2.53×10^{-5}
	Temporal lobe	0.665×10^{-3}	1.48×10^{-5}	0.624×10^{-3}	1.65×10^{-5}
AD	Cerebrum	1.00×10^{-3}	2.27×10^{-5}	1.07×10^{-3}	2.27×10^{-5}
	Frontal lobe	1.02×10^{-3}	2.43×10^{-5}	1.08×10^{-3}	2.56×10^{-5}
	Occipital lobe	0.925×10^{-3}	2.66×10^{-5}	0.984×10^{-3}	2.50×10^{-5}
	Parietal lobe	1.02×10^{-3}	3.01×10^{-5}	1.08×10^{-3}	3.16×10^{-5}
	Subcortical	1.10×10^{-3}	2.97×10^{-5}	1.16×10^{-3}	2.99×10^{-5}
	Temporal region	1.01×10^{-3}	2.42×10^{-5}	1.08×10^{-3}	2.56×10^{-5}
FA	Cerebrum	0.295	0.0078	0.349	0.015
	Frontal lobe	0.309	0.0081	0.364	0.014
	Occipital lobe	0.218	0.0116	0.279	0.020
	Parietal lobe	0.305	0.0116	0.355	0.020
	Subcortical	0.372	0.015	0.437	0.23
	Temporal lobe	0.289	0.0086	0.345	0.016

Source: V. A. Magnotta, J. T. Matsui, D. Liu, H. J. Johnson, J. D. Long, B. D. Bolster, B. A. Mueller, K. O. Lim, S. Mori, K. Helmer, J. A. Turner, M. Lowe, E. Ayl- ward, L. A. Flashman, G. Bonett, and J. S. Paulsen, Multi-Center Reliability of Diffusion Tensor Imaging., *Brain connectivity*, 2012.

mixed-effects model analysis showed that the number of gradient directions, use of median filtering, and scanner vendor had a significant effect on within-subject CV. However, the mixed-effects model also showed that DTIPrep did not have a significant

effect on the within-subject CV.

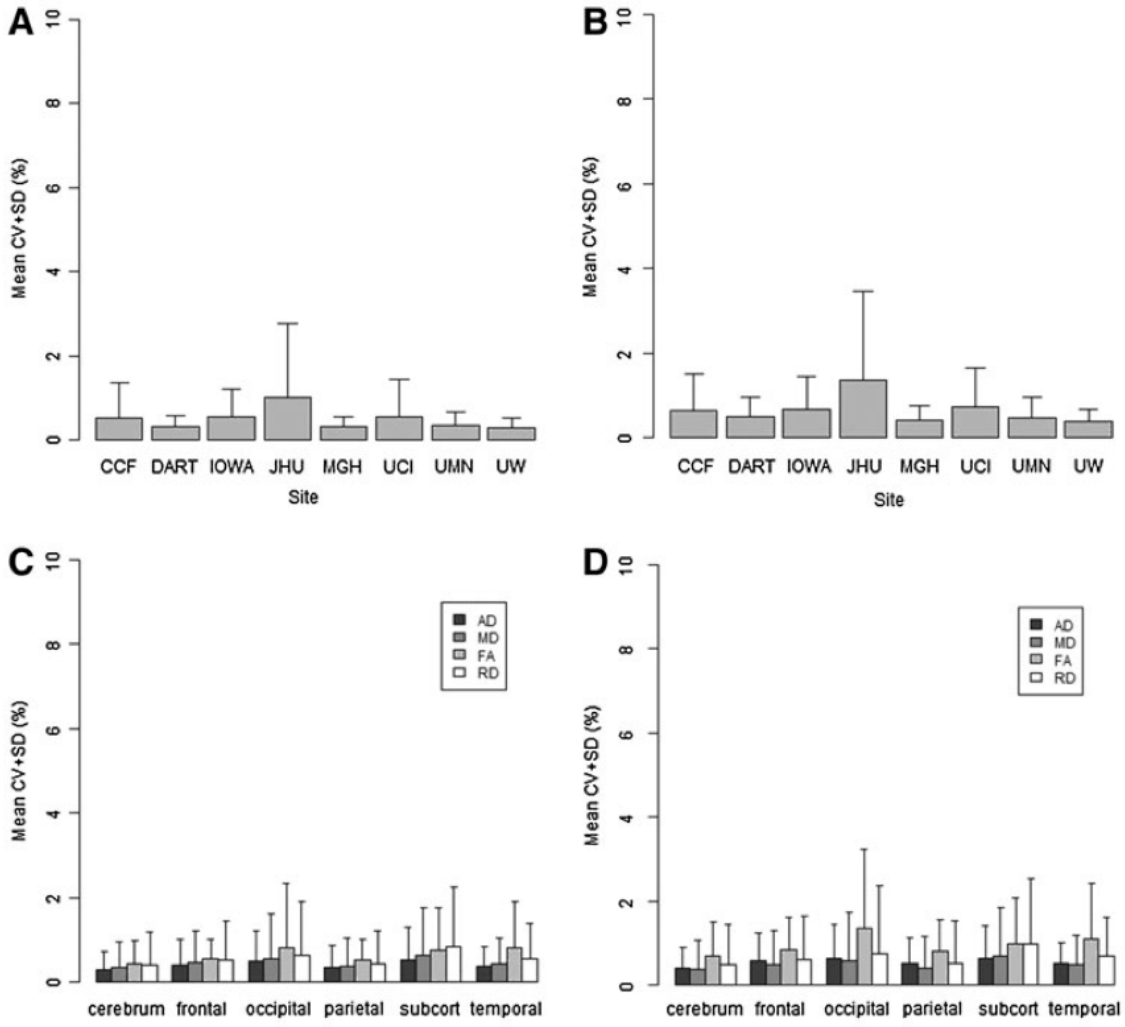

Figure 2.6: Intra-site reliability analysis showing the mean CV. The top row show CV by site for FA, with (A) and without (B) median filtering. The bottom row shows the CV by region and scalar measure, with (C) and without (D) median filtering.

Source: V. A. Magnotta, J. T. Matsui, D. Liu, H. J. Johnson, J. D. Long, B. D. Bolster, B. A. Mueller, K. O. Lim, S. Mori, K. Helmer, J. A. Turner, M. Lowe, E. Ayl- ward, L. A. Flashman, G. Bonett, and J. S. Paulsen, Multi-Center Reliability of Diffusion Tensor Imaging., *Brain connectivity*, 2012.

2.3.4 Between-site reliability analysis

In comparison to the within-subject analysis, the between-site reliability analysis showed increased CVs (Figure 2.7). Mean CVs were less than 3% in all regions except for FA in the occipital lobe where the CV was 3.2% (Figure 2.7, left panel). Mean CVs were approximately 2% across all scalar measures (Figure 2.7, right panel). The mean CV in the occipital lobe was higher than all other regions across all RIS measures. Mean CV for the 71 gradient direction protocol (2.15%) was higher than the mean CV for the 30/32 gradient direction protocol (1.78%). A mixed-effect model analysis showed that protocol type, scanner vendor, use of median filtering, and concatenation had significant effects on between-site CVs, but DTIPrep did not. There was an interaction effect between scanner and protocol type: for 71 gradient direction protocols, Siemens had a lower CV than Philips. For the 30/32 gradient direction protocol, the interaction effect between scanner and protocol type was reversed: Siemens had a higher CV than Philips.

2.4 Discussion

On average, DTIPrep removed 13.4% of the gradient directions available in this study. As a result, tensor images were estimated using approximately 26 gradient directions for 30 or 32 direction scans and 62 gradient directions for 71 direction scans. Therefore, reliable tensor, tensor orientation, and mean diffusivity were possible since each scan had a number of gradient directions close to the recommended 30 directions [94]. Although the reliability of tensor estimation was not evaluated in this study,

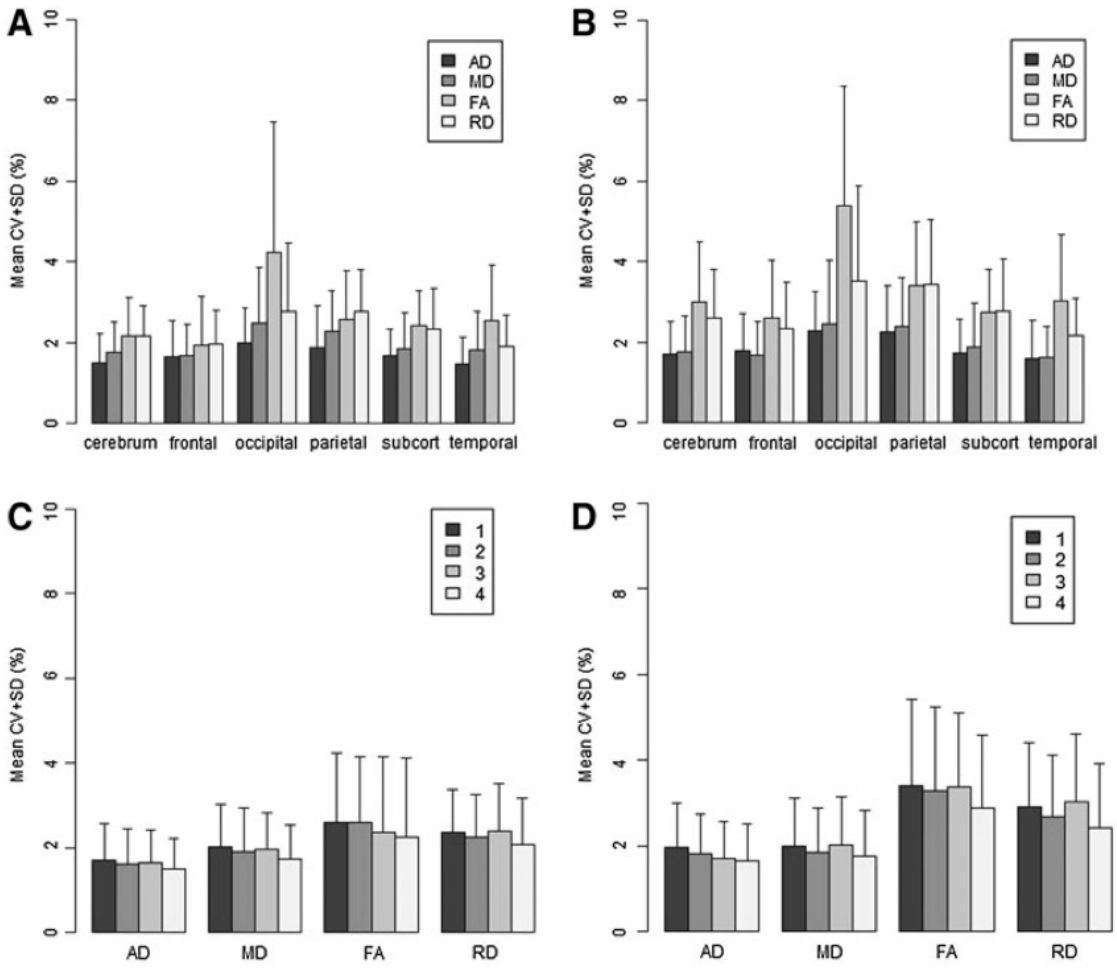

Figure 2.7: Inter-site reliability analysis showing the mean CV. The top row shows the CV by brain region and scalar type with (A) and without (B) median filtering. The bottom row shows the CV based on the number of concatenations and scalar measure for the low-diffusion gradient protocol with (C) and without (D) median filtering.

Source: V. A. Magnotta, J. T. Matsui, D. Liu, H. J. Johnson, J. D. Long, B. D. Bolster, B. A. Mueller, K. O. Lim, S. Mori, K. Helmer, J. A. Turner, M. Lowe, E. Ayl- ward, L. A. Flashman, G. Bonett, and J. S. Paulsen, Multi-Center Reliability of Diffusion Tensor Imaging., *Brain connectivity*, 2012.

FA and MD measures had similar CV values of less than 1%, suggesting that MD can be reliably estimated with 26 gradient directions. Although DTIPrep did not

significantly improve results, it was able to identify gradient directions that were deemed noisy during visual inspection because they contained artifacts. The image processing steps leading up to RIS measurements in regions of interest (quantifying RIS values in voxels classified as white matter by the tissue classified image and with FA values above 0.1) may have also made the RIS measurements immune to certain artifacts. Based on visual inspections, artifacts that would be present without the use of DTIPrep tended to be located in gray matter regions (Figure 2.8). Since these artifacts were in gray matter regions, they would be excluded from the analysis due to the requirement that analyzable voxels had to classified as white matter. In addition, five scans of DWI data were excluded from both with and without DTIPrep analyses because they did not contain a sufficient number of gradient directions. Therefore, FA values in this study could have been elevated due to the data inclusion rules.

DTIPrep removed gradient directions when diffusion was measured predominantly in the z-direction (direction of scanner bore) twice as many times as compared to the other two axes. This z-direction gradient removal trend was quite consistent across site and vendor. One site had an especially large percentage of gradients removed that were applied along the z-axis (Figure 2.5). An unbalanced removal of gradients along the three main axes (x, y, and z) may suggest a problem with the gradient amplifier or significant table vibrations. In either case, DTIPrep could be useful in identifying scanner hardware problems that may require service.

In this study, the use of a median filter significantly improved the reliability of RIS measures. CV and FA values were approximately 20% and 15% smaller,

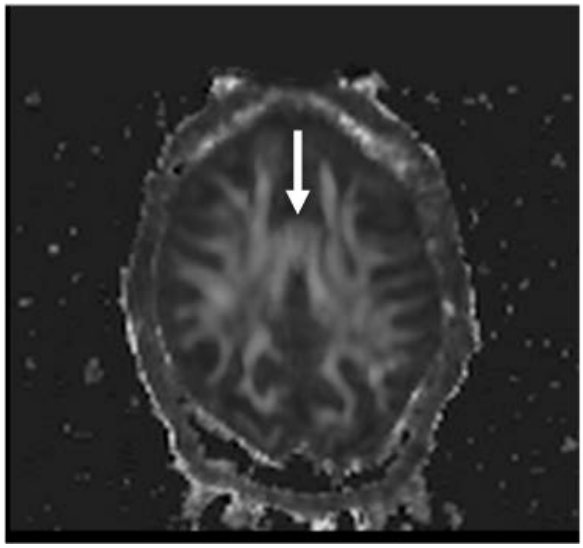

Figure 2.8: FA artifact resulting from table vibrations. The increased FA appears in gray matter regions above the corpus callosum.

Source: V. A. Magnotta, J. T. Matsui, D. Liu, H. J. Johnson, J. D. Long, B. D. Bolster, B. A. Mueller, K. O. Lim, S. Mori, K. Helmer, J. A. Turner, M. Lowe, E. Ayl- ward, L. A. Flashman, G. Bonett, and J. S. Paulsen, Multi-Center Reliability of Diffusion Tensor Imaging., *Brain connectivity*, 2012.

respectively, with median filtering as compared to without median filtering. In addition, median filtering increased AD by approximately 3% and decreased RD by approximately 6%, while MD remained constant.

When compared to a previous DTI reliability study by Pagani et al. [101], the data in this study showed a similar level of reliability. Pagani et al. reported an average CV across imaging sites of approximately 5% for all RIS across regions studied [101]. This study found mean CVs for within subject of approximately 0.5% and between sites of approximately 2%. The main difference between this study and that done by Pagani et al. was that this study was restricted to 3T scanners while

Pagani et al. examined reliability across different field strengths (1.5T and 3T) [101].

Given the difference between mean FA and MD measures across scanners, it is likely that Siemens and Philips use slightly different formulas for determining the gradient magnitude applied based on the b-value specified at the scanner console. The different imaging sequences (dual-echo for Siemens, Stejskal-Tanner for Philips) may also account for some of the variability in FA and MD measures. Participants also informally reported more vibration from Siemens scanners in comparison to Philips scanners. Other differences between scanners reported by participants included comfort of the head pad and how their heads were restrained inside the head coil. Thus, varying levels of comfort provided by each scanner could also account for variability in FA and MD measures due to subject motion.

The within subject variability found in this study was quite small with CVs of approximately 0.5% across all scanners and regions evaluated. The amount of variability found in this study was relatively small in comparison to the variation seen in a previous study involving prodromal HD subjects. In the previous study, there was a FA value change of approximately 0.1 across the five year probability of onset [36]. However, this study still contained several aspects that may have contributed to the variability in the diffusion tensor estimates, such as diffusion encoding, susceptibility artifacts, and image registration. Efforts were made to minimize the effects of noise by using a median filter before tensor estimation on all DWI images with the hope of increasing the SNR in the images while maintaining the white matter tracks. However, an analysis that accounted for all sources of variability showed that the use of a median

filter reduced FA (by 20%) and AD and increased RD values. In order to ensure that intra-subject variability could be measured, subjects were not repositioned in the scanner between scans. If subjects had been repositioned between scans, an intra-subject variability greater than 0.5% would have been expected with an upper limit of the inter-site CV. An extension of this study would be to estimate reliability in white matter regions more specific than those used here or in specific fiber tracts. To facilitate such investigations, the data from this study has been made public (https://predict-hd.net/xnat/). Studies looking at RIS values in gray matter regions could be another additional analysis to obtain valuable information on underlying architecture.

2.5 Conclusion

In summary, this study shows that diffusion tensor RIS can be robustly estimated within a site with very little variation (CV of approximately 0.5%) using standard diffusion encoding sequences (30 or 32 directions) provided by vendors. This suggests that changes in white matter architecture could be evaluated longitudinally in subjects scanned on the same scanner. It was found that four averages of a 30 or 32 direction gradient encoding scheme were needed to significantly improve reliability, which would be approximately 15 additional minutes of scan time. When multiple sites and vendors were included in the analysis, a four-fold increase in variability was seen. A 3% difference in RIS measures between vendors was observed, which is most likely due to varying methods of converting the entered b-value into gradient

amplitude and diffusion encoding schemes (Stejskal-Tanner for Philips versus double refocused spin-echo for Siemens) used by different vendors. Thus, the same scanner should be used throughout a longitudinal study in order to minimize the number of subjects required. Lastly, scanner software upgrades evaluated in this study are not the only types of upgrades to expect during studies of extended duration. Hardware upgrades, such as those in gradient coils, were not evaluated in this analysis. Therefore, the reliability resulting from software upgrades will be smaller than the measured inter-site variability measured within vendor but larger than the intra-site reliability estimated in this study. Further work is needed to assess how hardware changes impact reliability measures. However, the inter-site reliability estimated in this study is expected to serve as an upper bound for the coefficient of variation.

Table 2.7: Mean and standard deviation of DTI scalars across all anatomical regions by site: Massachusetts General Hospital (MGH), University of California, Irvine (UCI), Univeristy of Minnesota (UMN), University of Washington (UW).

RIS	Region	Mean with median filter	Standard deviation with median filter	Mean without median median	Standard deviation without median filter
MD	Cleveland Clinic	0.791×10^{-3}	2.15×10^{-5}	0.795×10^{-3}	2.19×10^{-5}
	Dartmouth	0.753×10^{-3}	1.68×10^{-5}	0.755×10^{-3}	1.97×10^{-5}
	University of Iowa	0.779×10^{-3}	1.76×10^{-5}	0.782×10^{-3}	1.71×10^{-5}
	Johns Hopkins	0.754×10^{-3}	1.45×10^{-5}	0.764×10^{-3}	1.87×10^{-5}
	MGH	0.780×10^{-3}	2.56×10^{-5}	0.783×10^{-3}	2.10×10^{-5}
	UCI	0.780×10^{-3}	1.70×10^{-5}	0.784×10^{-3}	1.55×10^{-5}
	UMN	0.770×10^{-3}	1.54×10^{-5}	0.774×10^{-3}	1.24×10^{-5}
	UW	0.759×10^{-3}	1.68×10^{-5}	0.762×10^{-3}	1.92×10^{-5}
RD	Cleveland Clinic	0.672×10^{-3}	2.76×10^{-5}	0.630×10^{-3}	2.56×10^{-5}
	Dartmouth	0.634×10^{-3}	2.72×10^{-5}	0.580×10^{-3}	2.81×10^{-5}
	University of Iowa	0.659×10^{-3}	2.95×10^{-5}	0.617×10^{-3}	2.71×10^{-5}
	Johns Hopkins	0.635×10^{-3}	2.54×10^{-5}	0.586×10^{-3}	2.78×10^{-5}
	MGH	0.661×10^{-3}	2.72×10^{-5}	0.619×10^{-3}	2.36×10^{-5}
	UCI	0.660×10^{-3}	3.01×10^{-5}	0.619×10^{-3}	2.81×10^{-5}
	UMN	0.655×10^{-3}	2.47×10^{-5}	0.614×10^{-3}	2.24×10^{-5}
	UW	0.641×10^{-3}	2.60×10^{-5}	0.587×10^{-5}	2.58×10^{-5}
AD	Cleveland Clinic	1.03×10^{-3}	5.52×10^{-5}	1.10×10^{-3}	5.57×10^{-5}
	Dartmouth	0.993×10^{-3}	4.57×10^{-5}	1.07×10^{-3}	5.29×10^{-5}
	University of Iowa	1.02×10^{-3}	5.03×10^{-5}	1.11×10^{-3}	5.06×10^{-5}
	Johns Hopkins	1.00×10^{-3}	4.48×10^{-5}	1.10×10^{-3}	4.98×10^{-5}
	Massachusetts	1.03×10^{-3}	5.17×10^{-5}	1.08×10^{-3}	5.20×10^{-5}
	UCI	1.03×10^{-3}	4.78×10^{-5}	1.09×10^{-3}	4.66×10^{-5}
	UMN	1.01×10^{-3}	5.01×10^{-5}	1.07×10^{-3}	4.94×10^{-5}
	UW	1.01×10^{-3}	4.70×10^{-5}	1.07×10^{-3}	5.08×10^{-5}
FA	Cleveland Clinic	0.295	0.0403	0.348	0.0421
	Dartmouth	0.304	0.0381	0.374	0.0439
	University of Iowa	0.300	0.0437	0.353	0.0452
	Johns Hopkins	0.309	0.0368	0.377	0.0403
	MGH	0.297	0.0400	0.352	0.0403
	UCI	0.301	0.0439	0.359	0.0449
	UMN	0.294	0.0423	0.347	0.0435
	UW	0.302	0.0373	0.370	0.0426

Source: V. A. Magnotta, J. T. Matsui, D. Liu, H. J. Johnson, J. D. Long, B. D. Bolster, B. A. Mueller, K. O. Lim, S. Mori, K. Helmer, J. A. Turner, M. Lowe, E. Ayl- ward, L. A. Flashman, G. Bonett, and J. S. Paulsen, Multi-Center Reliability of Diffusion Tensor Imaging., *Brain connectivity*, 2012.

Table 2.8: Mean and standard deviation of DTI scalars across all anatomical regions by scanner vendor.

Type	Manufacturer	Mean with median filter	Standard deviation with median filter	Mean without median median	Standard deviation without median filter
MD	Philips	0.755×10^{-3}	1.63×10^{-5}	0.760×10^{-3}	1.96×10^{-5}
	Siemens	0.780×10^{-3}	2.09×10^{-5}	0.783×10^{-3}	1.90×10^{-5}
RD	Philips	0.638×10^{-3}	2.59×10^{-5}	0.586×10^{-3}	2.67×10^{-5}
	Siemens	0.697×10^{-3}	2.99×10^{-5}	0.613×10^{-3}	3.00×10^{-5}
AD	Philips	1.00×10^{-3}	4.59×10^{-5}	1.08×10^{-3}	5.09×10^{-5}
	Siemens	1.02×10^{-3}	5.19×10^{-5}	1.08×10^{-3}	5.24×10^{-5}
FA	Philips	0.305	0.0375	0.374	0.0424
	Siemens	0.297	0.0421	0.351	0.0433

Source: V. A. Magnotta, J. T. Matsui, D. Liu, H. J. Johnson, J. D. Long, B. D. Bolster, B. A. Mueller, K. O. Lim, S. Mori, K. Helmer, J. A. Turner, M. Lowe, E. Ayl- ward, L. A. Flashman, G. Bonett, and J. S. Paulsen, Multi-Center Reliability of Diffusion Tensor Imaging., *Brain connectivity*, 2012.

Table 2.9: Mean and standard deviation of within-subject coefficient of variation by site: Massachusetts General Hospital (MGH), University of California, Irvine (UCI), Univeristy of Minnesota (UMN), University of Washington (UW).

Site	Coefficient of variation with median filtering	Standard deviation with median filtering	Coefficient of variation without median filtering	Standard deviation without median filtering
Cleveland Clinic	0.528	0.826	0.632	0.869
Dartmouth	0.328	0.249	0.494	0.446
University of Iowa	0.554	0.681	0.673	0.779
Johns Hopkins	1.000	1.760	1.359	2.104
MGH	0.305	0.237	0.411	0.333
UCI	0.556	0.873	0.708	0.945
UMN	0.348	0.301	0.473	0.472
UW	0.297	0.210	0.372	0.281

Source: V. A. Magnotta, J. T. Matsui, D. Liu, H. J. Johnson, J. D. Long, B. D. Bolster, B. A. Mueller, K. O. Lim, S. Mori, K. Helmer, J. A. Turner, M. Lowe, E. Ayl- ward, L. A. Flashman, G. Bonett, and J. S. Paulsen, Multi-Center Reliability of Diffusion Tensor Imaging., *Brain connectivity*, 2012.

CHAPTER 3
CROSS-SECTIONAL SCALAR STUDY

3.1 Introduction

This study strives to build upon past prodromal HD studies on frontal lobe white matter (WM) by examining WM diffusivity in sub-regions of the prefrontal cortex (PFC) defined by FreeSurfer in 53 prodromal HD participants and 34 controls. Prodromal HD individuals were separated into three CAG-Age Product (CAP) groups (16 low, 22 medium, 15 high) that indexed baseline progression. It was hypothesized that diffusivity differences would be seen in PFC WM regions among CAP groups relative to controls. It was also hypothesized that the difference relative to controls would be a function of CAP group with the high group showing the greatest difference.

3.2 Methods

3.2.1 Participants

This analysis used structural images, diffusion-weighted images, and clinical data from the first time point of a larger longitudinal functional MRI study, Cognitive and Functional Brain Changes in Preclinical Huntingtons Disease (HD-fMRI; NS054893: P.I. J.S. Paulsen). This was a two-site collaboration whose goal is to utilize neurobiological and clinical markers to understand the progression of HD before diagnosis and to provide candidate disease markers to assist future preventive HD clinical trials. Consent was obtained in accordance with the Institutional Review Board at each site. Controls were participants from HD families but who were free

of the CAG-expansion (i.e., CAG $\leq$ 35). Thirty-four healthy controls (11 male/23 female, mean age 49.1, SD = 10.4) and 53 prodromal CAG-expanded individuals were recruited from the HD Registries at the University of Iowa and the Cleveland Clinic. Prodromal CAG-expanded individuals were stratified into low (n = 16; CAP $<$ 287.16), medium (n = 22; 287.16 $<$ CAP $<$ 367.12), and high (n = 15; CAP $>$ 367.12) groups based on their CAG-Age Product or CAP designation, as previously described [116]. CAP groups are used to reflect the individuals progression through the disease process, from presymptomatic through manifest HD, based on CAG and age. It is meant to encompass terms such as disease burden and genetic burden that have been used in previous literature. The formula for CAP is as follows:

$$CAP = Age_0 x(CAG - 33.6600) \tag{3.1}$$

where Age_0 represents age of the participant at the time of scan for this study (i.e., baseline) [116].

3.2.2 Measures

Participants were evaluated by clinicians experienced in the administration of the Unified Huntingtons Disease Rating Scale (UHDRS) and certified by the Huntington Study Group (HSG). Formal diagnosis of HD was based on the Diagnostic Confidence Level rating of four indicating the examining clinician felt the participant showed unequivocal presence of an otherwise unexplained extrapyramidal movement disorder with $>$ 99% confidence [117]. Participants with a rating of DCL = 4 were excluded to restrict this particular analysis to prodromal HD subjects. The sum of

all the individual motor ratings from the UHDRS (total motor impairment score) is reported as well [117]. Several cognitive measures were assessed alongside the imaging measures and included the Symbol Digit Modalities Test (SDMT), the Stroop Color Word Test, and the Trail Making Test (TMT). The SDMT measures psychomotor speed and working memory by counting the number of correct matches between numbers to their designated symbol based on a key [118]. The Stroop Color Word Test measures processing speed and executive functions by counting the number of correct responses in three conditions: color-naming (name colors), word-reading (read color names), and interference (inhibition of dominant reading response while naming color) [119]. The TMT measures psychomotor speed and executive function by recording the time it takes participants to connect numbers alone (TMT Part A, TMTA) and connect alternating numbers and letters (TMT Part B, TMTB) both in ascending order [120]. A greater time required to complete the TMT results in a higher score, which indicates worse performance or poorer function. A summary of participant characteristics is provided in Table 3.1.

3.2.3 Imaging

Imaging data was collected at two large medical research universities (University of Iowa and Cleveland Clinic). Both sites used a Siemens 3T TIM Trio scanner. Structural imaging consisted of T1- and T2-weighted images both collected in the coronal plane. T1-weighted images had the following parameters: TI = 900 ms, TE = 3.09 ms, TR = 2530 ms, flip angle = 10^o, NEX = 1, bandwidth = 220

Hz/pixel, FOV = 256 x 256 x 220 mm, matrix = 256 x 256 x 220. T2-weighted images had the following range of parameters: $TE \approx 440$ ms, $TR = 4800$ ms, bandwidth = 590 Hz/pixel, FOV = 220 x 256 x 224 mm, matrix = 214 x 256 x 160 mm. A diffusion-weighted sequence (71 non-collinear diffusion-weighting gradients with diffusion-weighting of $b = 1000$ sec/mm^2 and eight $b = 0$ sec/mm^2 acquisitions, 256 x 256 mm FOV, 128 x 128 matrix, 50 2 mm-thick axial slices with zero gap, TE = 92 ms, $TR = 7700$ ms (CCF) or 8000 ms (Iowa), and bandwidth = 1562 Hz/pixel (CCF) or 1565 Hz/pixel (Iowa)) was acquired three times. All scans were transferred to The University of Iowa for processing and analysis.

3.2.4 Structural image pre-processing

Structural image pre-processing was performed using a derivative of the fully-automated BRAINS (Brain Research: Analysis of Image, Networks, and Systems) AutoWorkup software package [107]. T1- and T2-weighted images for each subject were anterior commissure (AC)-posterior commissure (PC) aligned. The AC-PC-aligned images were then bias-field corrected using an atlas-based classification algorithm. The pre-processed T1-weighted images were used in FreeSurfer (version 5.1.0) image analysis suite (documented and freely available for download online at http://surfer.nmr.mgh.harvard.edu/) for volumetric segmentation of the cortical WM regions. An illustration of the WM labels used in this study is provided in Figure 3.1.

3.2.5 Diffusion-weighted image pre-processing

Each DWI scan was visually inspected individually to identify artifacts. Repeat DWI scans from the same subject from a single scan session were concatenated (resulting in 3x redundancy of each gradient directions) before quality control checking with DTIPrep [113]. DTIPrep performs several quality assurance steps and removes volumes within a scan that do not meet its minimal quality criteria. Individual steps of the DTIPrep pipeline were described in Section 2.2.4. The final dataset contained an averaged baseline image and only those diffusion-weighted images that passed all quality assurance tests [113].

3.2.6 Imaging variables in regions of interest

The output files from DTIPrep were used to estimate the tensor images, and subsequently the fractional anisotropy (FA), mean diffusivity (MD), axial diffusivity (AD), and radial diffusivity (RD) images were computed from the tensor images using components of the GTRACT software [86]. A visual inspection of all FreeSurfer labels revealed that voxels posterior to the caudate were often included in the segmentation of both left and right medial orbitofrontal WM regions. To create a consistent regional definition, the medial orbitofrontal WM segmentation for each subject was edited by removing all voxels posterior to the centroid of the ipsilateral caudate. The FreeSurfer WM labels and brain masks were both resampled into DWI space using a B-Spline transformation from the T2-weighted image to the averaged b0 baseline image from the output DTIPrep file and visual inspections of registration quality were performed.

The resampled FreeSurfer WM labels were used to obtain measurements of volume and mean rotationally invariant scalar measures or DTI scalars. The ratio of label volume to intracranial volume will be referred to as the WM volume throughout the remainder of this manuscript. Mean FA, MD, AD, and RD values were computed in FreeSurfer WM labels intersected with the thresholded FA binary mask (subjects FA image containing FA values above 0.1) using components of SimpleITK ($http : //www.itk.org/Wiki/ITK/Release_4/SimpleITK$).

3.2.7 Statistical analysis

Statistical analyses were performed using general linear models (GLM) with PROC GLM in SAS 9.2. For each FreeSurfer defined PFC region, differences in WM volume and mean FA, mean MD, mean AD, and mean RD among groups determined by CAP designation were investigated using analysis of covariance models with age, years of education, gender, and site of data collection as covariates. Partial Pearson correlations were computed between regional WM volume, mean FA, mean MD, mean AD, and mean RD and SDMT, Stroop Word, Stroop Color, Stroop Interference, TMTA, and TMTB scores for prodromal HD subjects only with age, years of education, gender, and site of data collection as covariates. In the GLM and correlation analyses, a false-discovery rate (FDR) correction was performed to adjust for multiple comparisons across ROIs using the procedures of Benjamini and Hochberg [121] as implemented in PROC MULTTEST. FDR correction was used for the GLM omnibus test of any group difference. A criterion of $q < 0.05$ was used to elevate

omnibus statistical significance, with q being the FDR-adjusted p-value. For each significant result based on the q-value, unadjusted p-values were used to evaluate pair-wise group differences. A criterion of $p < 0.05$ was used to evaluate pair-wise statistical significance.

3.3 Results

3.3.1 GLM groups analysis

The results for the GLM group analysis are listed in Tables 2 through 6. In each table, the omnibus results are presented in three columns for mean FA (Table 3.2), MD (Table 3.3), RD (Table 3.3), AD (Table 3.5), and WM volume (Table 3.6). As the tables show, differences among groups that remained significant after FDR correction included those measuring diffusivity (Tables 3.3 and 3.4) as opposed to volume (Table 3.6). Model-based group means (adjusted for covariates) for regions whose differences among groups that remained significant after FDR correction are plotted in Figure 3.1. Figure 3.1 illustrates that differences among groups that remained significant after FDR correction were mainly in regions of the inferior and lateral frontal lobe.

As seen in Table 3.3, there were statistically significant differences in MD among groups in the left rostral middle frontal ($q = 0.033$) and right lateral orbitofrontal ($q = 0.033$) regions. Figure CAP group, as shown by significantly higher MD values in the left rostral middle frontal region for both medium ($p < 0.01$) and high CAP ($p < 0.005$) groups and in the right lateral orbitofrontal region for the high CAP ($p < 0.005$) group in comparison to controls. As seen in Table 3.3, the left

rostral middle frontal ($q = 0.022$) and right lateral orbitofrontal ($q = 0.022$) regions also had statistically significant differences in RD among groups, along with the left lateral orbitofrontal ($q = 0.022$) and all inferior frontal lobe regions (left pars opercularis, $q = 0.025$; left pars triangularis, $q = 0.022$; right pars opercularis, $q = 0.012$; right pars orbitalis, $q = 0.039$; right pars triangularis, $q = 0.035$) bilaterally except for the left pars orbitalis. RD also increased with progression. Most regions had significantly higher RD values for both medium ($p < 0.01$ to 0.05) and high CAP ($p < 0.0005$ to 0.01) groups in comparison to controls, except for the left pars opercularis ($p < 0.005$), right lateral orbitofrontal ($p < 0.001$), and right pars orbitalis ($p < 0.01$) regions that had higher RD values for the high CAP group only (Figure 3.1).

3.3.2 Cognitive variable partial correlations

After the application of FDR correction to all correlations between cognitive and imaging variables, TMTB was the only cognitive variable that showed significant partial correlation with two imaging variables in several regions. Amongst the regions that demonstrated significant differences in imaging variables among groups, the mean FA in two regions (right pars opercularis and right pars triangularis) in addition to the right medial orbitofrontal region negatively correlated with TMTB score (all $q = 0.037$). TMTB score also positively correlated with mean RD in the right pars triangularis region ($q = 0.044$) (Tables A.5 and A.5). Complete summaries on the correlations between imaging variables and the SDMT (Tables A.1 and A.2), TMTA (Tables A.3 and A.4), TMTB (Tables A.5 and A.5), Stroop Word (Tables A.7 and

A.8), Stroop Color (Tables A.9 and A.9), and Stroop Interference (Tables A.11 and A.12) can be found in Appendix A.5.1 in Tables A.1 through A.12.

3.4 Discussion

The main goal of this study was to build upon past prodromal HD studies on the frontal lobe by examining focused regions of PFC WM in prodromal HD individuals using four commonly used measures of diffusivity (FA, MD, RD, and AD) and WM volume. Mean measures of diffusivity and WM volume for each region were compared across four groups (controls and three prodromal HD groups) and correlated with several measures of cognitive performance. In this study, much like the differences in cognitive performance seen in prodromal HD subjects at varying stages before diagnosis [122], statistically significant increases in MD and RD in CAP groups relative to controls were seen in inferior and lateral PFC regions. In comparison to controls, a gradient of effects was seen in MD and RD, where the smallest effect was seen in the low group and the largest effect in the high group. Significant correlations between TMTB score and mean fractional anisotropy (FA) and/or RD paralleled the group differences in mean MD and/or RD in several right hemisphere regions. The gradient effect of lower anisotropy with CAP group could be explained by larger axon diameter or lower packing density of axons that both discourage anisotropic diffusion [123]. Specifically, significant differences in RD in the presence of no findings in AD has been seen in an animal study that attributed this effect to demyelination [74]. In addition, changes in diffusivity that reflect a loss of directionality in diffusion seen in

two other animal studies (lower FA, higher RD) [73, 75] were demonstrated in the same regions of the right lateral PFC that showed group differences in MD and RD and correlated with a poorer performance on one of the cognitive tests used in this study (TMTB). In summary, this study detected changes in diffusivity for the first time in a region that has not been closely examined in the context of prodromal HD. The meanings of these changes in diffusivity were further supported by correlating with scores on a cognitive test (TMTB) that has a documented ability to detect cognitive deficits in prodromal HD subjects. The gradient of effects suggests DWI can provide reliable markers of disease progression in the form of increasing diffusivity changes in the lateral PFC of prodromal HD individuals. Therefore, the results of this study suggest that mean RD in regions of the right lateral PFC could serve as a reliable biomarker to monitor disease progression in the prodromal HD stage.

The lack of findings for FA and MD in this study emphasizes the importance of investigating directional measures of diffusivity in addition to rotationally invariant diffusivity measures. FA and MD are commonly used measures of diffusivity because they summarize general shape and magnitude of diffusion, respectively, by accounting for diffusion magnitudes along three orthogonal directions at once [18]. The three orthogonal directions are numbered as eigenvectors based on the descending order of their corresponding diffusion magnitudes (first, second, and third eigenvalues) [17, 18]. In comparison to other summary measures of diffusivity (e.g. volume ratio and relative anisotropy), FA is less susceptible to noise and provides the highest signal-to-noise ratio (SNR) [91]. However, when changes in diffusion are subtle and in one

or two of the orthogonal directions, these changes may not be reflected in summary measures that normalize or average across all diffusion magnitudes. It may be more helpful to examine these subtle changes using directional measures of diffusivity to see diffusion magnitudes perpendicular and parallel to the first eigenvector. For example, Acosta-Cabronero and colleagues demonstrated increases in AD, RD, and MD that were more highly significant and sensitive to white matter changes in early Alzheimers patients than reductions in FA [124]. In addition, the increases in AD, RD, and MD were located in areas where tract degeneration was expected to occur based on prior gray matter lesion studies, further challenging the notion that reduced FA alone is able to fully capture changes in axonal integrity in Alzheimers disease [124].

When using measures of directional diffusivity, it is common to see changes in both RD and AD in a given region because the processes that cause changes in these measures (axonal death and demyelination) often occur in close proximity [73]. As mentioned earlier, AD describes diffusion along the largest eigenvector [18]. Animal studies have demonstrated that a decrease in AD is associated with axonal injury and degeneration because normal parallel diffusion along axons is being hindered by dysfunctional tissue [73]. RD describes diffusion perpendicular to the first eigenvector. In contrast to AD, an increase in RD is associated with demyelination since diffusion perpendicular to the axon is increased when there is less myelination [73, 75].

In this study, only increases in RD were seen in the prodromal HD individuals. It is important to remember that since RD is the mean of two eigenvalues it will be less noisy than AD, a measure that consists of a single eigenvalue. Therefore, in this

study RD may have been more sensitive to tissue changes and AD has yet to reach significance. An increase in RD with no change in AD has been documented in a very specific type of myelin pathology called dysmyelination [74]. Dysmyelination is the incomplete myelination of functional axons, as opposed to demyelination that is the complete loss of myelination [74]. Song et al. examined diffusivity changes in the setting of dysmyelination by using Shiverer mice. Shiverer mice are homozygous for a recessive autosomal mutation for myelin basic protein, causing incomplete myelination in the central nervous system [125, 126, 127, 128]. Song et al. showed that major WM tracts in Shiverer mice have increased RD but identical AD in comparison to the same tracts in control mice [74]. At this point in time, it is not possible to unambiguously interpret increased RD in the lateral PFC without AD changes in this study as a dysmyelintation process in prodromal HD individuals without longitudinal or histological data to pinpoint the exact process affecting diffusivity [19]. However, it must be emphasized that this study demonstrated a consistent gradient effect of increased RD without AD changes throughout the lateral PFC bilaterally.

The lack of WM volume findings in this study was initially surprising, given that previous studies have shown decreases in WM volume in prodromal HD [16] and correlations between morphological abnormalities and cognitive deficits in early HD subjects (Beglinger et al., 2005). It must be noted that if abnormal WM volume findings in the literature are specific to the frontal lobe (either prodromal or symptomatic HD), they tend to be in the entire frontal lobe [15, 129, 16]. An aspect of this study that could have prevented frontal lobe WM volume findings was that a precen-

tral gyrus region was not included in any part of the analysis. Perhaps WM volume abnormalities in prodromal HD individuals are specific to the precentral gyrus. It was not possible to include the precentral gyrus because the DWI data used here did not consistently include the most superior portions of the frontal and parietal lobes. Although the FreeSurfer WM definition has been shown to produce similar mean FA values in the same WM regions defined by other methods [130, 131] and variability within regions are replicated across groups [132], it still may not be the true volume of WM associated with the cortical region.

In this study, significant group differences relative to controls in MD and RD were mostly located in the lateral PFC, specifically in the ventrolateral or lateral left and right inferior regions. Traditionally, the left inferior frontal area is known to be involved in language, where lesions to the posterior portion cause Brocas aphasia [133]. However, the lateral inferior regions are broadly implicated in a number of higher-order executive processes [134]. Therefore, the significant correlations between FA, RD, and TMTB in most of the same right inferior regions containing group differences may further suggest a link between the lateral inferior regions and higher-order executive processes. Overall, the TMT is a cognitive measure that has a documented ability to differentiate among prodromal HD individuals in the CAP groups considered in this analysis [135]. Specifically, TMTB involves subjects connecting alternating letters and numbers to test cognitive flexibility and working memory, where the score is the time necessary to complete the task. Poor performance on the TMTB is reflected in a longer completion time [135]. TMTB scores negatively correlating with FA and

positively correlating with RD in this study can possibly be interpreted together as prodromal HD individuals experiencing greater impairment in executive functioning, processing speed, and working memory with disease progression due to a white matter disease process that can be detected by measures of diffusivity [19].

As for the significant findings in the dorsolateral and orbitofrontal PFC regions, these results may be explained by the dorsal-to-ventral progression cell death in the striatum observed in HD [33] affecting components of corticostriatal loops [34]. Specifically, Lawrence and colleagues hypothesized that functions associated with the dorsal PFC-striatal loop may be impaired before motor symptom onset, followed by impairment of functions associated with the ventral loop as neuronal loss increases with disease progression [33, 34]. Based on anatomical studies done by Alexander et al. and Arikuni et al., the dorsal PFC striatal loop includes dorsolateral PFC projections to the central to dorsal caudate, while the ventral loop includes orbitofrontal PFC projections to the ventromedial caudate [31, 32]. Therefore, the significant findings in the dorsolateral (increased MD and RD in the left rostral middle frontal region) and the orbitofrontal (increased MD and RD in the right lateral orbitofrontal and increased RD in the left lateral orbitofrontal regions) PFC in this study may be explained by the pattern of cell death in the striatum affecting components of the corticostriatal loops as implied by changes in diffusivity [19].

The main limitation of this study was that WM regions of the PFC were only explored with WM volume and a limited set of scalar diffusivity measures derived from the tensor model. Another metric for detecting differences in diffusivity among

tissue types in future studies of white matter integrity in Huntingtons Disease is diffusional kurtosis imaging (DKI). Diffusional kurotosis values quantify diffusional non-Gaussianity as a consequence of tissue structure creating barriers and compartments [136]. Diffusional kurtosis values may provide greater sensitivity to differences between largely isotropic tissues and have been used in ischemic stroke [137, 138], aging [139], schizophrenia [140], and attention deficit disorder [141]. Analyzing WM regions derived from WM fiber tracts that connected cortical gray matter to the striatum instead of WM regions based on proximity to cortical gray matter would have provided a means for specifically examining corticostriatal tracts. Additionally, using methods more sophisticated than the tensor model, such as high angular resolution diffusion imaging (HARDI) to resolve multiple fiber orientations in white matter containing crossing fibers, would be important to examine in the future with the number diffusion-weighted gradients per scan used in this study [142]. The additional information on multiple fiber orientations per voxel could possibly make scalar diffusivity measures more sensitive to changes in white matter and assist with more reliable fiber tract reconstructions in future studies [142]. Another limitation of this study was the incomplete coverage of superior frontal and parietal lobes in DWI scans mentioned earlier that led to clipping in the superior frontal, caudal middle frontal, and rostral middle frontal regions. The rostral middle frontal areas were the least affected and perhaps that is why findings were strongest there. However, it is uncertain whether the superior frontal and caudal middle frontal regions contain findings in this study as these regions were visibly substantially clipped.

Future directions include expanding upon these findings in the PFC in the form of more complex analyses. The next step is to perform cross-sectional fiber tracking to obtain representations of the PFC WM that can be analyzed for changes along each WM region. In addition to WM in the PFC, it may also be useful to examine WM extending to the PFC from the striatum and beyond to characterize how HD affects corticostriatal loops in their entirety. Ultimately, the above analyses will be expanded to characterize changes in individual subjects longitudinally.

3.5 Conclusion

The main goal of this study was to build upon past prodromal HD studies on the frontal lobe by examining focused regions of PFC WM in three groups of prodromal HD individuals stratified by baseline progression (low, medium, and high groups) using four commonly used measures of diffusivity (FA, MD, RD, and AD) and WM volume. In summary, this study was able to detect differences in diffusivity based on baseline disease progression for the first time in the lateral PFC, a region that has not been closely examined in the context of prodromal HD. The meaning of these changes in diffusivity were further supported by correlating WM measures with scores on a cognitive test that has a documented ability to detect cognitive deficits in prodromal HD. Therefore, the results of this study suggest that mean RD in regions of the right lateral PFC could serve as a reliable biomarker to monitor disease progression in the prodromal HD stage in future longitudinal studies.

Table 3.1: Summary of demographic and clinical data for study participants.

	Controls (Mean; SD (N))	Low (Mean; SD (N))	Medium (Mean; SD (N))	High (Mean; D (N))
Age (years)	49.1; 10.4 (34)	32.1; 8.8 (16)	39.4; 10.8 (22)	47.8; 12.2 (15)
Education (years)	15.6; 2.0 (34)	14.8; 2.5 (16)	15.0; 2.2 (22)	13.7; 2.7 (15)
Gender	11M/23F (34)	3M/13F (16)	6M/16F (22)	2M/13F (15)
UHDRS Total Motor	4.7; 3.3 (32)	3.7; 2.7 (16)	7.1; 9.3 (22)	15.2; 10.5 (14)
Symbol Digit Modalities Test	54.0; 11.0 (31)	55.1; 9.8 (15)	54.7; 12.5 (21)	46.2; 9.7 (15)
Stroop Color	84.4; 11.7 (31)	84.1; 11.1 (15)	83.4; 3.8 (20)	64.8; 15.6 (14)
Stroop Word	106.1; 18.1 (31)	106.9; 13.5 (15)	99.3; 18.3 (20)	77.6; 19.2 (14)
Stroop Interference	49.2; 9.4 (31)	52.4; 13.4 (15)	50.5; 12.8 (20)	36.5; 10.9 (14)
Trail Making Test A	22.1; 5.6 (30)	20.9; 6.5 (15)	21.5; 7.5 (21)	27.6; 9.1 (15)
Trail Making Test B	55.2; 24.4 (30)	46.9; 16.6 (15)	52.4; 24.7 (21)	78.6; 38.3 (14)

Source: J. T. Matsui, J. G. Vaidya, H. J. Johnson, V. A. Magnotta, J. D. Long, J. A. Mills, M. J. Lowe, K. E. Sakaie, S. M. Rao, M. M. Smith, and J. S. Paulsen, Diffusion weighted imaging of prefrontal cortex in prodromal huntingtons disease., Human Brain Mapping, 2013.

Note: UHDRS Total Motor = sum of all items of the Motor Assessment scale.

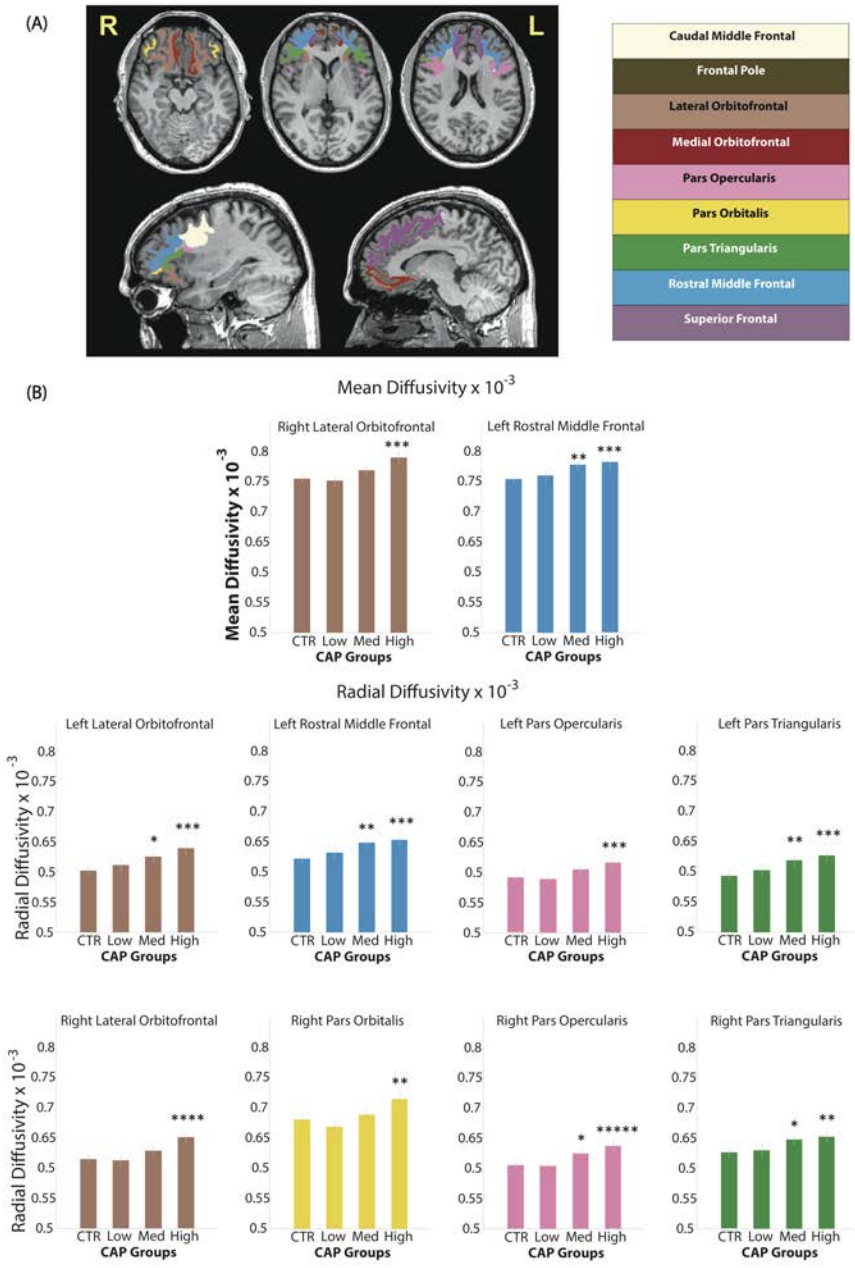

Figure 3.1: PFC WM ROIs for DTI scalar analysis. (A) WM labels generated by FreeSurfer on T1-weighted images shown in sagittal and axial views. Radiologic convention is used for the axial view. (B) Significant CAP group differences in MD (top) and RD (bottom) in comparison to controls. $^{*}p < 0.05$, $^{**}p < 0.01$, $^{***}p < 0.005$, $^{****}p < 0.001$, $^{*****}p < 0.0005$.

Source: J. T. Matsui, J. G. Vaidya, H. J. Johnson, V. A. Magnotta, J. D. Long, J. A. Mills, M. J. Lowe, K. E. Sakaie, S. M. Rao, M. M. Smith, and J. S. Paulsen, Diffusion weighted imaging of prefrontal cortex in prodromal huntingtons disease., *Human Brain Mapping*, 2013.

Table 3.2: Summary of general linear model results for regional FA findings for DTI scalar analysis of PFC white matter.

Region	F value*	Raw p-value	FDR q-value
Left caudal middle frontal	1.106	0.352	0.463
Left frontal pole	1.350	0.264	0.416
Left lateral orbitofrontal	2.520	0.064	0.230
Left medial orbitofrontal	2.372	0.077	0.230
Left pars opercularis	1.309	0.277	0.416
Left pars orbitalis	1.451	0.234	0.416
Left pars triangularis	3.244	0.026	0.158
Left rostral middle frontal	1.840	0.147	0.369
Left superior frontal	1.490	0.224	0.416
Right caudal middle frontal	0.509	0.677	0.677
Right frontal pole	0.901	0.445	0.500
Right lateral orbitofrontal	1.748	0.164	0.369
Right medial orbitofrontal	1.085	0.360	0.463
Right pars opercularis	3.333	0.024	0.158
Right pars orbitalis	2.991	0.036	0.161
Right pars triangularis	4.447	0.006	0.110
Right rostral middle frontal	1.001	0.397	0.476
Right superior frontal	0.704	0.553	0.585

Source: J. T. Matsui, J. G. Vaidya, H. J. Johnson, V. A. Magnotta, J. D. Long, J. A. Mills, M. J. Lowe, K. E. Sakaie, S. M. Rao, M. M. Smith, and J. S. Paulsen, Diffusion weighted imaging of prefrontal cortex in prodromal huntingtons disease., *Human Brain Mapping*, 2013.

Note: *The F-test reported in the table represents the main effect of CAP group from an analysis of covariance model that includes four groups (controls, low, medium, and high CAP groups) and age, years of education, gender, and site as covariates. $df_1 = 3$ and $df_2 = 79$ for all F-tests.

Table 3.3: Summary of general linear model results for regional MD findings for DTI scalar analysis of PFC white matter.

Region	F value*	Raw p-value	FDR q-value
Left caudal middle frontal	2.370	0.077	0.126
Left frontal pole	0.598	0.618	0.655
Left lateral orbitofrontal	4.181	0.008	0.051
Left medial orbitofrontal	2.553	0.061	0.118
Left pars opercularis	2.911	0.040	0.089
Left pars orbitalis	1.560	0.206	0.265
Left pars triangularis	3.647	0.016	0.055
Left rostral middle frontal	4.883	0.004	0.033
Left superior frontal	1.312	0.276	0.332
Right caudal middle frontal	2.971	0.037	0.089
Right frontal pole	0.102	0.959	0.959
Right lateral orbitofrontal	4.949	0.003	0.033
Right medial orbitofrontal	1.255	0.296	0.333
Right pars opercularis	3.933	0.011	0.051
Right pars orbitalis	2.498	0.066	0.118
Right pars triangularis	1.926	0.132	0.198
Right rostral middle frontal	3.537	0.018	0.055
Right superior frontal	1.847	0.145	0.201

Source: J. T. Matsui, J. G. Vaidya, H. J. Johnson, V. A. Magnotta, J. D. Long, J. A. Mills, M. J. Lowe, K. E. Sakaie, S. M. Rao, M. M. Smith, and J. S. Paulsen, Diffusion weighted imaging of prefrontal cortex in prodromal huntingtons disease., *Human Brain Mapping*, 2013.

Note: *The F-test reported in the table represents the main effect of CAP group from an analysis of covariance model that includes four groups (controls, low, medium, and high CAP groups) and age, years of education, gender, and site as covariates. $df_1 = 3$ and $df_2 = 79$ for all F-tests.

Table 3.4: Summary of general linear model results for regional RD findings for DTI scalar analysis of PFC white matter.

Region	F value*	Raw p-value	FDR q-value
Left caudal middle frontal	2.889	0.041	0.067
Left frontal pole	0.436	0.728	0.771
Left lateral orbitofrontal	4.430	0.006	0.022
Left medial orbitofrontal	3.142	0.030	0.054
Left pars opercularis	4.186	0.008	0.025
Left pars orbitalis	2.024	0.117	0.176
Left pars triangularis	4.550	0.005	0.022
Left rostral middle frontal	4.657	0.005	0.022
Left superior frontal	1.793	0.155	0.186
Right caudal middle frontal	1.901	0.136	0.182
Right frontal pole	0.207	0.891	0.891
Right lateral orbitofrontal	5.091	0.003	0.022
Right medial orbitofrontal	1.162	0.330	0.371
Right pars opercularis	6.345	0.001	0.012
Right pars orbitalis	3.594	0.017	0.039
Right pars triangularis	3.788	0.014	0.035
Right rostral middle frontal	3.200	0.028	0.054
Right superior frontal	1.868	0.142	0.182

Source: J. T. Matsui, J. G. Vaidya, H. J. Johnson, V. A. Magnotta, J. D. Long, J. A. Mills, M. J. Lowe, K. E. Sakaie, S. M. Rao, M. M. Smith, and J. S. Paulsen, Diffusion weighted imaging of prefrontal cortex in prodromal huntingtons disease., *Human Brain Mapping*, 2013.

Note: *The F-test reported in the table represents the main effect of CAP group from an analysis of covariance model that includes four groups (controls, low, medium, and high CAP groups) and age, years of education, gender, and site as covariates. $df_1 = 3$ and $df_2 = 79$ for all F-tests.

Table 3.5: Summary of general linear model results for regional AD findings for DTI scalar analysis of PFC white matter.

Region	F value*	Raw p-value	FDR q-value
Left caudal middle frontal	1.323	0.273	0.639
Left frontal pole	0.650	0.585	0.676
Left lateral orbitofrontal	3.007	0.035	0.131
Left medial orbitofrontal	1.082	0.362	0.656
Left pars opercularis	0.862	0.465	0.676
Left pars orbitalis	0.657	0.581	0.676
Left pars triangularis	1.289	0.284	0.639
Left rostral middle frontal	3.368	0.023	0.131
Left superior frontal	0.625	0.601	0.676
Right caudal middle frontal	3.581	0.017	0.131
Right frontal pole	0.024	0.995	0.995
Right lateral orbitofrontal	2.982	0.036	0.131
Right medial orbitofrontal	1.076	0.364	0.656
Right pars opercularis	0.793	0.502	0.676
Right pars orbitalis	0.858	0.466	0.676
Right pars triangularis	0.386	0.763	0.808
Right rostral middle frontal	3.161	0.029	0.131
Right superior frontal	1.534	0.212	0.637

Source: J. T. Matsui, J. G. Vaidya, H. J. Johnson, V. A. Magnotta, J. D. Long, J. A. Mills, M. J. Lowe, K. E. Sakaie, S. M. Rao, M. M. Smith, and J. S. Paulsen, Diffusion weighted imaging of prefrontal cortex in prodromal huntingtons disease., *Human Brain Mapping*, 2013.

Note: *The F-test reported in the table represents the main effect of CAP group from an analysis of covariance model that includes four groups (controls, low, medium, and high CAP groups) and age, years of education, gender, and site as covariates. $df_1 = 3$ and $df_2 = 79$ for all F-tests.

Table 3.6: Summary of general linear model results for regional volume findings of PFC white matter.

Region	F value*	Raw p-value	FDR q-value
Left caudal middle frontal	0.247	0.863	0.971
Left frontal pole	0.321	0.810	0.971
Left lateral orbitofrontal	0.892	0.449	0.850
Left medial orbitofrontal	0.847	0.472	0.850
Left pars opercularis	2.654	0.054	0.488
Left pars orbitalis	0.996	0.399	0.850
Left pars triangularis	1.713	0.171	0.770
Left rostral middle frontal	0.470	0.704	0.917
Left superior frontal	0.490	0.690	0.917
Right caudal middle frontal	1.876	0.140	0.770
Right frontal pole	0.014	0.998	0.998
Right lateral orbitofrontal	0.491	0.690	0.917
Right medial orbitofrontal	0.457	0.713	0.917
Right pars opercularis	4.034	0.010	0.181
Right pars orbitalis	0.953	0.419	0.850
Right pars triangularis	1.002	0.397	0.850
Right rostral middle frontal	0.155	0.926	0.980
Right superior frontal	1.115	0.348	0.850

Source: J. T. Matsui, J. G. Vaidya, H. J. Johnson, V. A. Magnotta, J. D. Long, J. A. Mills, M. J. Lowe, K. E. Sakaie, S. M. Rao, M. M. Smith, and J. S. Paulsen, Diffusion weighted imaging of prefrontal cortex in prodromal huntingtons disease., *Human Brain Mapping*, 2013.

Note: *The F-test reported in the table represents the main effect of CAP group from an analysis of covariance model that includes four groups (controls, low, medium, and high CAP groups) and age, years of education, gender, and site as covariates. $df_1 = 3$ and $df_2 = 79$ for all F-tests.

CHAPTER 4
CROSS-SECTIONAL FIBER TRACKING STUDY

4.1 Introduction

This study strives to build upon prodromal HD diffusion tensor scalar studies that have identified subregions of the prefrontal cortex (PFC) whose white matter (WM) diffusivity are affected by HD disease progression by performing a tract-based analysis on four well-established fiber tracts that terminate in the PFC. The four fiber tracts include the forceps minor (FM), (left and right) anterior thalamic radiations (ATRs), (left and right) inferior fronto-occipital fasciculi (IFOs), and (left and right) uncinate fasciculi (UNCs). The FM is a large inter-hemispheric tract of fibers that project from the genu of the corpus callosum [143] and has been shown to play a role in language development [144]. The ATR runs through the anterior limb of the internal capsule and connects the PFC to the mediodorsal thalamic nucleus [143], which is believed to be involved with declarative memory [145, 146]. Specifically, the mediodorsal nuclei are responsible for retrival of materials in memory [145, 146]. The IFO connects to the orbitofrontal areas to the ventral occpital lobe, while coursing through the external capsule [143, 147]. The IFO is believed to only exist in humans [148] and may have a role in reading [149], attention [150], and visual processing [151]. The UNC connects the orbitofrontal cortex to the anterior lobe [143, 147] and is may be involved in episodic memory, language, and social emotional processing [152]. It was hypothesized that diffusivity differences along each tract will be seen

among groups of prodromal HD participants separated by degree of disease burden relative to controls. It was also hypothesized that the differences in diffusivity relative to controls would be a function of disease burden (determined by age and CAG repeat length), where the group with the highest disease burden showing the greatest difference. In addition, perhaps cognitive performance (measured by SDMT, Stroop Word, Stroop Color, Stroop Interference, TMTA, and TMTB) will correlate with changes in diffusivity.

4.2 Methods

4.2.1 Imaging and clinical data

Three separate diffusion tensor atlases were built for this cross-sectional study from three sets of 3T imaging data collected at PREDICT-HD study sites. Two of the three imaging data sets were associated with clinical data collected within six months of scan acquisition. Imaging data consisted of the first 3T imaging session for each PREDICT-HD study participant eligible for inclusion in this cross-sectional analysis. Each data set will be described separately in Sections 4.2.1.1 through 4.2.1.4.

4.2.1.1 Single-participant, multi-site data

The single-participant, multi-site (SPMS) data set consisted of imaging data for a single healthy participant from the Traveling Human Phantom (THP) study. Therefore, the SPMS data set consisted of two DWI scans, one T1-weighted scan, and one T2-weighted scans acquired at eight different sites (five Siemens and three Philips 3T MRI scanners) all on the same single subject (Section 2.2.1). Each DWI scan was

acquired using the standard, vendor-provided DWI scanning protocol that was either 30 unique gradient directions and one baseline image (Siemens) or 32 unique gradient directions and one baseline image (Philips). Structural images were acquired using three-dimensional (3D) T1- (MP-RAGE) and T2-weighted sequences in the coronal plane (Tables 4.1 and 4.2).

Table 4.1: Scanner parameters for T1-weighted images collected at the Traveling Human Phantom (THP) study sites.

Site	TI (ms)	TE (ms)	TR (ms)	Flip Angle	NEX	Bandwidth (Hz/pixel)	FOV (mm)	Matrix (mm)
CCF	900	2.87	2300	10^o	1	240	256x256	256x256
DART	0	3.50	7.69	8^o	1	241	224x224	220x218
IOWA	900	2.85	2300	10^o	1	240	256x256	256x256
JHU	0	3.50	7.70	8^o	1	241	224x224	220x218
MGH	900	2.87	2300	10^o	1	240	256x256	256x256
UCI	900	2.85	2300	10^o	1	240	256x256	256x256
UMN	900	2.87	2300	10^o	1	240	256x256	256x256
UW	0	3.50	7.69	8^o	1	241	224x224	220x218

Note: TI = Inversion time. TE = Echo time. TR = Repetition time. NEX = Number of excitations. FOV = Field of view. CCF = Cleveland Clinic. DART = Dartmouth. IOWA = University of Iowa. JHU = Johns Hopkins. MGH = Massachusetts General Hospital. UCI = University of California, Irvine. UMN = University of Minnesota. UW = University of Washington.

4.2.1.2 Multi-participant, single-site data

The multi-participant, single-site (MPSS) data set consisted of both clinical and imaging data collected at the University of Iowa for 8 controls and 22 prodromal CAG-expanded individuals. Prodromal CAG-expanded individuals were stratified

Table 4.2: Scanner parameters for T2-weighted images collected at the Traveling Human Phantom (THP) study sites.

Site	TE (ms)	TR (ms)	Flip Angle	NEX	Bandwidth (Hz/pixel)	FOV (mm)	Matrix (mm)
CCF	458	4800	120^o	1	590	256x220	256x214
DART	183	2500	90^o	1	523	224x224	220x218
IOWA	452	4800	150^o	1	590	256x220	256x214
JHU	250	2500	90^o	1	497	224x224	220x218
MGH	458	4800	120^o	1	590	256x220	256x214
UCI	458	4800	120^o	1	590	256x220	256x214
UMN	458	4800	120^o	1	590	256x220	256x214
UW	250	2500	90^o	1	497	224x224	220x218

Note: TE = Echo time. TR = Repetition time. NEX = Number of excitations. FOV = Field of view. CCF = Cleveland Clinic. DART = Dartmouth. IOWA = University of Iowa. JHU = Johns Hopkins. MGH = Massachusetts General Hospital. UCI = University of California, Irvine. UMN = University of Minnesota. UW = University of Washington.

into low ($n = 5$; CAP < 287.16), medium ($n = 9$; $287.16 <$ CAP < 367.12), and high ($n = 8$; CAP > 367.12) groups based on their CAG-Age Product or CAP designation [116]. Clinical data types used with the MPSS imaging data included age at imaging session, years of education, gender, CAG-Age Product or CAP designation, UHDRS Total Motor Score (sum of all items of the Motor Assessment scale), Symbol Digit Modalities Test (SDMT), Stroop Color, Stoop Word, Stroop Interference, Trail Making Test A (TMTA), and Trail Making Test B (TMTB). A summary of participant characteristics in the MPSS data set are listed in Table 4.3, while descriptions of the clinical data types can be found in Sections 3.2.1 and 3.2.2.

DWI data consisted of one to two repetitions of a scanning protocol with 30 gradient directions using a b-value of 1,000 sec/mm^2 for gradients with diffu-

sion weighting. Structural images were also acquired using three-dimensional (3D) T1- (MP-RAGE) and T2-weighted sequences in the coronal plane. Parameters for both DWI and structural image scanning protocols are listed in the extended multi-participant, multi-site (EMPMS) data set section (Section 4.2.1.4) in Tables 4.6, 4.7, and 4.8 because University of Iowa data was included in the EMPMS data set.

Table 4.3: Summary of demographic and clinical data for multi-participant, single-site (MPSS) participants.

	Cont (Mean; (SD (N))	Low (Mean; SD (N))	Med (Mean; SD (N))	High (Mean; SD (N))
Age (years)	46.7; 10.2 (8)	30.8; 10.9 (5)	40.3; 8.8 (9)	46.5; 11.0 (8)
Educ (years)	15.4; 2.2 (8)	14.2; 1.6 (5)	14.4; 2.0 (9)	15.8; 2.4 (8)
Gender	2M/6F (8)	2M/3F (5)	5M/4F (9)	3M/5F (8)
Motor	4.8; 3.1 (8)	7.4; 6.5 (5)	7.1; 2.7 (9)	11.8; 8.1 (8)
SDMT	54.1; 5.9 (8)	53.8; 10.2 (5)	54.7; 3.3 (9)	46.9; 12.7 (8)
S Color	86.4; 8.4 (8)	84.0; 4.7 (5)	82.2; 6.8 (9)	73.0; 17.7 (8)
S Word	109.9; 13.7 (8)	106.2; 9.1 (5)	100.9; 10.5 (9)	89.4; 21.5 (8)
S Interference	47.3; 7.2 (8)	48.6; 12.8 (5)	54.8; 8.8 (9)	41.8; 7.1 (8)
TMTA	21.0; 2.0 (8)	19.0; 6.2 (5)	21.6; 9.1 (9)	28.4; 9.2 (8)
TMTB	59.9; 38.6 (8)	45.4; 16.1 (5)	46.9; 8.7 (9)	62.0; 22.4 (8)

Note: Cont = Controls. Med = Medium. Educ = Education. Motor = Sum of all items of the UHDRS Motor Assessment scale. SDMT = Symbol Digit Modalities Test. S = Stroop. TMTA = Trail Making Test A. TMTB = Trail Making Test B.

4.2.1.3 Multi-participant, multi-site data

The multi-participant, multi-site (MPMS) data set was much like the MPSS data set except that data was collected from six PREDICT-HD study sites and included 20 controls and 60 prodromal CAG-expanded individuals. Prodromal CAG-

expanded individuals were again stratified into low ($n = 20$; CAP < 287.16), medium ($n = 20$; $287.16 <$ CAP < 367.12), and high ($n = 20$; CAP > 367.12) groups based on their CAG-Age Product or CAP designation [116]. A summary of participant characteristics in the MPMS data set are listed in Table 4.4, while imaging parameters are shown in the EMPMS data section (Section 4.2.1.4) in Tables 4.6 for DWIs and Tables 4.7 and 4.8 for structural images.

Table 4.4: Summary of demographic and clinical data for multi-participant, multi-site (MPMS) participants, including number of participants from each site in each group.

	Cont (Mean; SD (N))	Low (Mean; SD (N))	Med (Mean; SD (N))	High (Mean; SD (N))
Age (years)	42.0; 11.9 (20)	35.2; 8.3 (20)	42.8; 9.6 (20)	46.3; 13.5 (20)
Educ (years)	16.3; 1.8 (20)	14.8; 2.5 (20)	15.2; 2.5 (20)	15.7; 2.5 (20)
Gender	7M/13F (20)	5M/15F (20)	7M/13F (20)	6M/14F (20)
Motor	3.0; 2.6 (20)	2.4; 3.0 (20)	6.7; 4.6 (20)	8.2; 8.6 (20)
SDMT	55.0; 10.4 (20)	59.3; 9.8 (20)	50.1; 7.9 (20)	47.6; 9.6 (20)
S Color	87.9; 11.3 (20)	85.0; 8.3 (20)	79.4; 9.4 (20)	77.8; 12.9 (20)
S Word	107.6; 16.5 (20)	107.6; 11.4 (20)	99.5; 11.1 (20)	95.6; 18.2 (20)
S Interference	52.2; 8.4 (20)	50.9; 8.3 (20)	46.5; 8.5 (20)	41.9; 9.8 (20)
TMTA	21.1; 7.3 (20)	20.2; 6.5 (20)	24.2; 7.4 (20)	23.4; 6.1 (20)
TMTB	47.7; 24.9 (20)	51.3; 14.8 (20)	49.0; 14.4 (20)	61.9; 26.2 (20)
Site 024	(6)	(7)	(8)	(7)
Site 027	(4)	(2)	(2)	(3)
Site 048	(0)	(2)	(1)	(0)
Site 054	(2)	(3)	(2)	(3)
Site 073	(3)	(3)	(3)	(3)
Site 120	(5)	(3)	(4)	(4)

Note: Sites 024, 027, 073, and 120 have Siemens vendor scanners. Site 048 has a Philips vendor scanner. Site 054 has a GE vendor scanner. Cont = Controls. Med = Medium. Educ = Education. Motor = Sum of all items of the UHDRS Motor Assessment scale. SDMT = Symbol Digit Modalities Test. S = Stroop. TMTA = Trail Making Test A. TMTB = Trail Making Test B.

4.2.1.4 Expanded multi-participant, multi-site data

The expanded multi-participant, multi-site (EMPMS) data set was an expanded version of the MPMS data set. Data was collected from 15 PREDICT-HD sites to include 65 controls and 146 prodromal CAG-expanded individuals. Prodromal CAG-expanded individuals were again stratified into low ($n = 46$; CAP < 287.16), medium ($n = 54$; $287.16 <$ CAP < 367.12), and high ($n = 49$; CAP > 367.12) groups based on their CAG-Age Product or CAP designation [116]. A summary of participant characteristics in the EMPMS data set are listed in Table 4.5, while imaging parameters are shown in Tables 4.6 for DWIs and Tables 4.7 and 4.8 for structural images.

4.2.2 Structural image pre-processing

All visual inspections and pre-processing of images were completed at the University of Iowa Scalable Informatics, Neuroimaging, Analaysis, Processing, and Software Engineering (SINAPSE) Laboratory while blinded to participant group status. Corresponding T1- and T2-weighted images collected in the same scan session were processed together with the BRAINSTools package [153], which is a derivative of the fully-automated BRAINS (Brain Research: Analysis of Images, Networks, and Systems) AutoWorkup suite [107] with symmetric image normalization (SyN) registration from ANTs (the Advanced Normalization Toolkit) [154, 155]. SyN registration will be described in Section 4.2.3. Images from multiple modalities were processed together to improve robustness of the procedure by using complimentary informa-

Table 4.5: Summary of demographic and clinical data for expanded multi-participant, multi-site (EMPMS) participants, including number of participants from each site in each group.

	Cont (Mean; (SD (N))	Low (Mean; SD (N))	Med (Mean; (SD (N))	High (Mean; SD (N))
Age (years)	46.4; 11.4 (65)	34.4; 8.6 (43)	40.8; 9.9 (54)	45.3; 12.0 (49)
Educ (years)	15.4; 2.2 (65)	14.7; 2.5 (43)	15.0; 2.3 (54)	14.9; 2.9 (49)
Gender	22M/43F (65)	9M/34F (43)	16M/38F (54)	13M/36F (49)
Motor	3.8; 3.6 (65)	2.5; 3.5 (43)	6.1; 4.7 (54)	7.7; 7.1 (49)
SDMT	54.8; 10.4 (65)	60.0; 10.3 (43)	52.0; 9.6 (54)	48.1; 10.1 (49)
S Color	84.7; 12.4 (65)	87.1; 13.6 (43)	78.8; 11.6 (54)	74.9; 14.3 (49)
S Word	104.6; 15.1 (65)	106.9; 17.6 (43)	99.4; 16.6 (54)	98.1; 19.9 (49)
S Interference	49.6; 9.5 (65)	52.5; 11.7 (43)	48.0; 10.4 (54)	44.9; 11.9 (49)
TMTA	21.5; 6.3 (65)	20.6; 6.0 (43)	23.2; 7.7 (54)	25.1; 7.5 (49)
TMTB	51.4; 22.7 (65)	49.9; 16.9 (43)	56.3; 24.8 (54)	60.9; 23.6 (49)
Site 001	(0)	(0)	(2)	(0)
Site 002	(1)	(0)	(0)	(0)
Site 007	(0)	(1)	(0)	(1)
Site 024	(28)	(11)	(18)	(19)
Site 027	(6)	(2)	(3)	(3)
Site 032	(0)	(2)	(3)	(0)
Site 045	(5)	(1)	(4)	(1)
Site 048	(0)	(2)	(1)	(0)
Site 050	(2)	(3)	(4)	(3)
Site 054	(2)	(4)	(5)	(5)
Site 061	(1)	(4)	(3)	(0)
Site 073	(4)	(4)	(4)	(7)
Site 120	(11)	(4)	(6)	(5)
Site 144	(5)	(2)	(0)	(1)
Site 177	(0)	(3)	(1)	(4)

Note: Sites 007, 024, 027, 032, 045, 050, 061, 073, 120, 144, and 177 have Siemens vendor scanners. Sites 002 and 048 have Philips vendor scanners. Sites 001 and 054 have GE vendor scanners. Cont = Controls. Med = Medium. Educ = Education. Motor = Sum of all items of the UHDRS Motor Assessment scale. SDMT = Symbol Digit Modalities Test. S = Stroop. TMTA = Trail Making Test A. TMTB = Trail Making Test B.

tion, but it is possible to run BRAINSTools on a single T1-weighted image. Before entering the BRAINSTools pipeline, all T1- and T2-weighted images were visually inspected and given a quality rating ranging from zero (unusable) to ten (best quality). Images that received a quality rating lower than six were excluded from further processing and analysis. The best-rated T1-weighted image within a scan session was spatially normalized to the BRAINS T1-weighted template with a constellation-based landmark detection algorithm (where the anterior and posterior commissures and the mid-sagittal plane are a few of the most prominent landmarks) [156]. The remaining T1- and T2-weighted images that passed visual inspection were then rigidly aligned to the spatially normalized T1-weighted image. AC-PC-aligned images were bias-field corrected using an atlas-based classification algorithm, resulting in 17 tissue probability maps and average images of each modality resampled to a 1 mm x 1 mm x 1 mm voxel lattice. Tissue probability maps were collectively treated as a rough brain mask. Aberrant islands surrounding the brain and tissue classified as blood were removed to ensure the brain mask only covered cerebral and cerebellar tissues. The edited brain mask was then used to skull-strip the participant's corresponding averaged bias-field corrected T1- and T2-weighted images.

4.2.3 Diffusion-weighted image pre-processing

DTIPrep performed several quality assurance steps and removed volumes within a scan that did not meet its minimal quality criteria. In addition, multiple baseline images within a concatenation were averaged and all volumes with diffusion weighting

were coregistered to the averaged baseline. If a participant received multiple DWI scans in a single session, the repetitions were concatenated end to end and processed by DTIPrep [113]. Details on the individual steps of the DTIPrep pipeline were provided in Section 2.2.4. The final dataset contained an averaged baseline image and only those diffusion-weighted images that passed all quality assurance tests [113]. The output of DTIPrep was again visually inspected to ensure that the DWI scan was indeed free of interlace artifact, dropout, and major susceptibility artifacts. DWI scans that contained lobar cropping were excluded from further analysis.

The transformation from the averaged baseline image from a participant's DWI to the corresponding bias field corrected T2-weighted image was derived using the symmetric image normalization (SyN) registration method [154] from the Advanced Normalization Tools package [155]. The remainder of this section will consist of a description the SyN algorithm developed by Avants et al. as it was an integral part of deriving high quality transformations between the different imaging modalities in subject space and from subject to atlas space in this study. The SyN algorithm is a symmetric diffeomorphic optimizer that maximizes the cross-correlation between two images in the space of the diffeomorphisms [154]. Given that the moving and fixed images are elements in the diffeomorphic space, the output deformation field from the SyN algorithm is a geodesic path (ϕ) or the shortest diffeomorphism from the moving to fixed image (from I to J) in the discrete domain Ω [154]. A diffeomorphism (ϕ) is a forward mapping ($\phi(\mathbf{x}, 1)$) of an image (I) into a new coordinate system within a

period of time ($t \in [0, 1]$) and is expressed as a composition of the two [157]:

$$\phi I = I \circ \phi(\mathbf{x}, t = 1) = I(\phi(\mathbf{x}, t = 1)) \tag{4.1}$$

ϕ is parameterized by time (t), a spatial coordinate ($\mathbf{x}$), and a velocity field ($\mathbf{v}$) all on domain Ω [157]. If $t \in [0, 1]$, ϕ can be obtained by integrating the velocity fields from $t = 0$ to $t = 1$, while the shortest distance or geodesic between images I and I warped by $\phi(\mathbf{x}, 1)$ can be expressed as the infimum over all possible paths between $\phi(\mathbf{x}, 0)$ and $\phi(\mathbf{x}, 1)$ [157]:

$$D(\phi(\mathbf{x}, 0), \phi(\mathbf{x}, 1)) = \inf_{\phi} \int_0^1 ||\mathbf{v}(\phi(\mathbf{x}, t))||_L \, dt \tag{4.2}$$

In Eq. 4.2, L is the linear operator regularizing velocity (ensuring that the velocity field is smooth) and $|| \cdot ||_L$ is the Sobolev norm with respect to linear operator L that induces regularity on the velocity field [157]. One of the useful properties of a diffeomorphism is its ability to be decomposed into parts that are also diffeomorphisms [157]. In SyN registration, ϕ is derived from two halves of ϕ where each half is half of two separate geodesics (ϕ_1 and ϕ_2) both indexed by the image registration optimization time ($t \in [0, 1]$) in opposite directions [154]. The ends of the geodesic are a moving image (I) and a fixed image (J) that contribute equally to the path, where ϕ maps homologous anatomy in both images [154]. Given that $\mathbf{x}$ is the identity position of a point in moving image I and $\mathbf{z}$ is the identity position of a point in fixed image J, the constraint that both images contribute equally to the deformation can be expressed as equal distances from each image to the center of the geodesic [154]:

$$D(\mathbf{Id}, \phi_1(\mathbf{x}, 0.5)) = D(\mathbf{Id}, \phi_2(\mathbf{x}, 0.5)) \tag{4.3}$$

Therefore, the solution to the optimization problem is to find the variational energy that splits ϕ_1 and ϕ_2 such that I and J contribute equally to the total ϕ [154]. The forward and backward optimization problem is shown in Eq. 4.4 where integrating to time $t = 0.5$ produces a symmetric normalization solution by minimizing with respect to ϕ_1 and ϕ_2 [154].

$$E_{sym}(I, J) = \inf_{\phi_1} \inf_{\phi_2} \int_{t=0}^{0.5} \left\{ ||\mathbf{v}_1(\mathbf{x}, t)||_L^2 + ||\mathbf{v}_2(\mathbf{x}, t)||_L^2 \right\} dt + \int_\Omega |I(\phi_1(0.5)) - J(\phi_2(0.5))|^2 d\Omega \tag{4.4}$$

The distance constraint (Eq. 4.3) is expressed in the optimization problem as a similarity measure between I and J halfway across the geodesic, which begins as $I(\phi_1(\mathbf{x}, 1)) = J$ or $|I(\phi_1(\mathbf{x}, 1)) - J|$ [154, 157]. The similarity measure can be written in terms of both ϕ_1 and ϕ_2 as $|I(\phi_1(\mathbf{x}, t)) - J(\phi_2(\mathbf{z}, 1-t))|^2$ or $|\phi_1(0.5)I - \phi_2(0.5)J|^2$ when $t = 0.5$ [154, 157]. In SyN registration, cross-correlation is used as the similarity metric as it is more suitable for multi-modality registrations [154]. Thus, the variation optimization problem using cross-correlation as the similarity metric is as follows, where $\overline{I}$ and $\overline{J}$ are I and J with its local mean subtracted, respectively [154]:

$$E_{sym}(\overline{I}, \overline{J}) = \inf_{\phi_1} \inf_{\phi_2} \int_{t=0}^{0.5} \left\{ ||\mathbf{v}_1(\mathbf{x}, t)||_L^2 + ||\mathbf{v}_2(\mathbf{x}, t)||_L^2 \right\} dt + \int_\Omega CC(\overline{I}, \overline{J}, \mathbf{x},) d\Omega \tag{4.5}$$

Taking the variation of Eq. 4.5 with respect to ϕ_1 and ϕ_2 both at time 0.5 will provide the parts of the geodesic that parameterize the forward and inverse mapping from image I to J (in this case, from the averaged baseline of the participant's DWI image to corresponding bias field corrected T2-weighted image) assuming that ϕ_1 and ϕ_2 are true diffeomorphisms (one-to-one and on-to) [154]. The outputs of the SyN

registration method are an affine transform and an invertible deformation field that collectively make up the total transformation from DWI to structural image space.

4.2.4 Diffusion tensor image pre-processing

The inverse of the transformation from the averaged baseline image of a participant's DWI to the corresponding bias field corrected T2-weighted image derived from SyN registration was then used to resample the edited brain mask from structural image space to DWI space. A diffusion tensor image (DTI) was estimated in the original DWI space, using the resampled brain mask to limit the tensor estimation area to non-zero voxels and a weighted least squares tensor estimation method [63].

The transformation from the averaged baseline image of a participant's DWI to the corresponding bias field T2-weighted image was then used to resample the resulting DTI to structural image space. Maintaining directionality of DTI eigenvectors during DTI resampling is crucial for the validity of analysis and is a challenging task. Thus, a resampling tool called ResampleDTILogEuclidean that preserved the directionality information corresponding to both moving and fixed images when resampling DTIs to structural image space. ResampleDTILogEuclidean used both the affine transform and deformation field outputs from the SyN registration in preservation of principal direction (PPD) mode with linear interpolation [158, 159, 160]. ResampleDTILogEuclidean initially transformed the first and second eigenvectors ($\underline{e}_1$ and $\underline{e}_2$) of the moving DTI with a given transformation file to produce two new eigenvectors [158]. Then, the rotation matrix (R) that rotates the original first and second

eigenvectors into normalized versions of the new eigenvectors ($\underline{n}_1$ and $\underline{n}_2$) was derived [158]. R has to be recomputed for each tensor and thus preserves the principal direction up to the second eigenvector for varying shapes of diffusion tensors [158, 159, 160]. The PPD method of diffusion tensor reorientation is applicable to affine transforms and can be extended to deformation or displacement fields. R can be computed for a displacement field by modeling the transformation by the displacement field as a local affine model where the transformation for each tensor is the sum of an identity matrix and Jacobian of the displacement field [158]. An additional feature of the ResampleDTILogEuclidean tool is that the tensors in the output resampled DTI are positive symmetric semi-definite matrices to avoid negative eigenvalues (or negative magnitudes of diffusion direction) because the resampling operation is computed in the Log-Euclidean domain [161, 159].

4.2.5 Unbiased cross-sectional DTI template building

An unbiased template space based on T1-weighted images was determined for each set of data in this study using the unbiased template building algorithm originally proposed by Avants et al. [162, 163]. The unbiased template building algorithm by Avants et al. will be summarized in this section. First, T1-weighted images from all participants in a data set were averaged ($T1_0$). Transformations between $T1_0$ and the T1-weighted image from each participant were then estimated using the SyN registration algorithm as described in Section 4.2.3. Affine transformations and deformation fields from the SyN registration step were used to resample the original

T1-weighted images into the $T1_0$ space, whose resampled outputs were averaged to create a new T1-weighted average ($T1_1$). All affine transformations and deformation fields were averaged to create an average affine transformation ($\bar{\mathbb{T}}$) and average deformation field ($\bar{\mathbb{D}}$). $\bar{\mathbb{T}}$ and $\bar{\mathbb{D}}$ were then used to resample $T1_1$ into the final T1-weighted template ($T1_{final}$). Assuming that the moving images (T1-weighted images from all participants in a data set) and fixed image (average of T1-weighted images from all participants in a data set) are elements in a diffeomorphic space and the paths between them are geodesics, the transformations represent average forces that move all input images to the mean shape configuration [162]. New affine transforms ($\mathbb{T}'$) and deformation fields ($\mathbb{D}'$) were derived via SyN registration between each original T1-weighted input and $T1_{final}$. $\mathbb{T}'_i$ and $\mathbb{D}'_i$ derived from T1-weighted images were then used to resample each participant's DTI with the ResampleDTILogEuclidean tool [159] that were already in the T1-weighted image space, as suggested by Tustison et al. to minimize circularity bias of this study's experimental design [164]. Resampled DTIs were then averaged with a tool called dtiaverage [160] to form the final DTI template (DTI_{final}) that served as the unbiased DTI template for fiber tracking. Each unbiased DTI template was visually inspected to ensure valid alignment with its corresponding T1-weighted template and correct orientation of large fiber tracts (i.e. inferior tracts were oriented anterior to posterior, while corticospinal tracts were oriented superior to inferior).

4.2.6 Fiber tracking on the unbiased DTI template

Full brain tractography was performed on each data set's unbiased diffusion tensor template using the streamline tractography module available in 3DSlicer called TractographyLabelMapSeeding [165]. All unbiased diffusion tensor templates had voxels sized at 1 x 1 x 1 mm^3. The basic streamline tractography algorithm was described in Section 1.3.3.3.1. A seed was placed in each 0.75 x 0.75 x 0.75 mm^3 sub-voxel whose linear measure was greater than or equal to 0.3. Criteria for terminating a tract included exceeding a length of 800 mm, developing a radius of curvature less than 0.7 degrees per millimeter, or encountering a voxel whose fractional anisotropy was less than 0.1. An integration step length of 0.5 mm^3 was used and tracts below 10 mm in length were excluded.

4.2.7 Fiber tract selection

Fiber tracts were selected manually with a graphical user interface tool called TractographyDisplay, which is a module in the Slicer toolkit, that allowed positive and negative inclusion of individual tracts with an adjustable selection box [166]. Several WM tractography atlases and teaching resources were used for anatomical reference [143, 167, 147, 168], as well as frequent consultations with a tractography expert. The following major fiber tracts terminating in the PFC were selected for analysis: uncinate fasciculus (UNC), forceps minor (FM), inferior fronto-occipital fasciculus (IFO), and anterior thalamic radiations (ATR). Full descriptions and illustrations of the selection of each fiber tract can be found in Appendix B, Section A.1.

4.2.8 Processing of fiber tracts

A tract probability map (TPM) (whose values ranged from 0 to 1) was computed for each fiber tract using the method described by Wasserman et al [169, 170] to create a continuous function that could be sampled at any resolution. Each fiber tract consisted of a tract of individual fiber trajectories that could each be modeled as a blurred indicator function (where a three dimensional point on the trajectory is equal to 1 and decays to 0 as the point moved further from the trajectory) or Gaussian process. Individual fiber trajectories could be combined into a fiber tract represented by another blurred indicator function. Since each point on the trajectories had a univariate Gaussian distribution, the mean and covariance of the Gaussian distribution for the fiber tract indicator function could be computed, which was used to compute the probability at each voxel in the TPM [169, 170].

Each TPM was then skeletonized in the space of its DTI atlas using the TBSS skeletonization tool [171], which is available in the FMRIB's (Analysis Group at the Oxford Centre for Functional MRI of the Brain) Software Library (FSL, v5.0.4) [172]. The skeleton of each tract was approximately a curved sheet to represent the curved surface along the center of the tract. The skeletonization process begins by searching for the local tract surface orientation at each voxel in the TPM. At each voxel, the center of gravity based on probability values is computed in a 3x3x3 voxel neighborhood. The vector from the current voxel to the local center of gravity pointed to the tract center, which was perpendicular to the local tract structure. Each direction estimate was then replaced with the mode of the direction estimate

in the 3x3x3 region. The probability value in each voxel was then compared to its two neighboring voxels along the direction estimate and the voxel with a greater probability was marked as lying on the skeleton [171].

DTI scalar values (FA, MD, AD, and RD) from each participant were then projected to each tract's skeletonized TPM. For each voxel on the TPM skeleton, the DTI scalar map is searched along the direction perpendicular to the tract within an area restricted by a distance map of the TPM skeleton to find the maximum DTI scalar value. The maximum DTI scalar value is then assigned to the voxel on the TPM skeleton [171, 170].

4.2.9 Statistical analysis

4.2.9.1 SPMS data: DTI scalar variability analysis

Two sets of percentages of coefficients of variation (CVs; ratio of the standard deviation to the mean, multiplied by 100) were computed for each type of DTI scalar (FA, MD, AD, and RD) and will be referred to as CVs. The first set of CVs was computed for the average scalar value over the region masked by each fiber tract across images collected from each site. The second set of CVs was computed for the average scalar value over the region masked by the skeletonized TPM for each tract across images collected from each site.

4.2.9.2 Mean DTI scalars: controls versus CAP groups

In order to detect differences in mean FA, mean MD, mean AD, and mean RD along tract skeletons between controls and CAP group, a permutation tests program

called randomise was used for the MPSS, MPMS, and EMPMS data sets. randomise is part of FSL and allows for modelling and inference using a general linear model (GLM). Permutation tests are a type of nonparametric test that provides a mechanism for inference on statistic maps when the null distribution of the data is unknown. Permutation tests are often performed at the voxel level in neuroimaging studies to establish the actual distribution of the data and can be applied to common GLMs [173]. Permutation tests require the observations to be exchangeable in order establish the null hypothesis that the distributions of the populations in question have the same shape or mean. Data labels are permuted where each permutation consists of a unique relabeling of the data and is called a block. Each block produces a statistic (i.e. difference in means between pairs of items in a block) that is part of a distribution of values formed by the permutations. Under the null hypothesis, each block statistic produced is equally likely. p-value is the proportion of statistic values that are greater than or equal to the statistic produced by the properly labeled block. Therefore, the null hypothesis is rejected when the p-value is less than a pre-determined α (i.e. 0.05) [173]. When nuisance variables are included in the GLM, randomise will provide an approximate inference because exchangeability of the observations is no longer present. Therefore, randomise will estimate the nuisance signal first by fitting the data to the nuisance effects alone and permuting the nuisance-only residuals. The nuisance signal is then added to the data to create an approximate realization of the data under the null hypothesis, followed by the computation of the test statistic requested [174].

randomise was used to detect differences in mean FA, mean MD, mean AD, and mean RD along tract skeletons between controls and CAP groups using analysis of covariance GLM models with age, years of education, gender, and site of data collection as covariates via unpaired two-sample t-tests for MPSS, MPMS, and EMPMS data sets. Twenty-thousand permutations were used for MPSS and MPMS data sets, while 50,000 was used for the EMPMS data set. An additional experiment comparing mean RD in the right IFO between the lower third of the controls in the EMPMS data set ranked by age to the upper third was performed using years of education, gender, and site of data collection as covariates. The additional age experiment was performed to see if randomise was able to detect mean RD differences in groups of different ages, as RD is known to increase with age (i.e. [175]). Instructions for implementation of the GLM in randomise can be found in Section A.2.

The following approaches were used to perform the t-tests, each using the same GLM: voxel-based thresholding, cluster-based thresholding, and threshold-free cluster enhancement (TFCE). All approaches were used on the MPSS and MPMS data sets to compute t-tests in order to select the method that extracted the most meaningful results from the EMPMS data set. TFCE was the only method used to perform t-tests on the EMPMS data set.

Voxel-based thresholding was used to determine voxelwise differences in mean DTI scalars between controls and CAP groups by computing the t-statistic at each voxel for the MPSS and MPMS data sets. To control for multiple comparisons (family-wise Type I error) across voxels within a tract skeleton, the single threshold test was

used to find a critical threshold over the entire tract skeleton. The critical threshold is found by first obtaining the distribution of the maximum statistic over the entire tract skeleton by permuting the labels for a given contrast. The critical threshold is member number $c + 1$ of the permutation distribution when arranged in ascending order. c is equal to αN rounded down to the nearest whole number, where α is the p-value threshold (0.05 in this case) and N is the number of permutations. If the maximal statistic of the actual labeling of the experiment is greater than or equal to the critical threshold, the omnibus hypothesis can be rejected at 0.05. Also, any voxel with a statistic greater than the critical threshold can then have its null hypothesis rejected (i.e. where the null hypothesis is the mean DTI scalar values are equal for controls and CAP group). A corrected p-value map of the tract skeleton results, where each voxel's p-value is the proportion of the maximal statistic distribution that was greater than or equal to the voxel statistic [176, 173].

Cluster-based thresholding was performed at three different primary statistic image thresholds (t = 2.0, 3.0, and 4.0) for the MPSS and MPMS data sets to help find diffuse to focal areas (with increasing statistic image threshold) containing differences in DTI scalar values between controls and CAP groups. Once the primary threshold was applied to the statistic image, cluster patterns were assessed in the remaining non-zero voxels. To control for multiple comparisons (family-wise Type I error) across clusters within a single tract skeleton, a suprathreshold cluster test was employed, which is identical to the single threshold test but uses cluster size instead [176, 173].

TFCE tests were performed on the MPSS, MPMS, and EMPMS data sets to

avoid setting a primary statistic threshold on the tract skeleton of interest before looking for differences in DTI scalar values between controls and CAP groups. The main advantage of using the TFCE approach is that it is designed to find both focal and diffuse areas containing significant differences in signal [177]. The TFCE approach computes a TFCE score for each voxel that is determined by the voxel itself and immediately adjacent voxels that are contributing signal. Using a score for each voxel for statistical inference instead of the raw signal is supposed to enhance areas of signal that may be part of a cluster without a primary statistic image threshold (such as that in cluster-based thresholding) so it is easier to discriminate between background noise and signal. The TFCE score is calculated at every voxel (p) by summing the product of the extent of connecting voxels (e) raised to a set power ($E = 0.5$) and height (h) raised to a set power ($H = 2$) over increments of the total voxel height (h_p) or voxel signal intensity. The TFCE score calculation can be summarized as an integral, where height begins at zero (h_0) and is incremented at a finite dh to h_p (Eq. 4.6) [177].

$$TFCE(p) = \int_{h=h_0}^{h_p} e(h)^E h^H dh \tag{4.6}$$

TFCE score was used for statistical inference in the same manner as voxel-based thresholding to form uncorrected and corrected p-value maps (that have been corrected for multiple comparisons or family-wise Type I error across voxels within tract skeleton with the single threshold test) [177].

Two approaches with different levels of stringency to account for multiple comparisons across different contrasts were explored on the MPMS data set: false

discovery rate (FDR) procedure and Bonferroni correction (Table 4.9). Different levels of multiple comparison correction stringency were tested on the MPMS data set to determine which method would extract the most meaningful results from the EMPMS data set. (FDR was eventually selected). Multiple comparison correction was not explored on the MPSS data set due to its unstable t-test findings that was most likely due to the small numbers of participants in each groups. FDR controls for false positives by controlling the expected proportion of error among null hypotheses that have been rejected, which is less stringent than Bonferroni that removes the risk for all false positives [121]. For the voxelwise analyses (voxel-based thresholding and TFCE), the FDR procedure was applied to the uncorrected p-value maps. For the cluster-based thresholding tests, the FDR procedure was applied to the p-values of the clusters that remained after controlling for family-wise Type I error within tract skeleton and thresholding at $p < 0.05$. A criterion of $q < 0.05$ was used for all FDR applications. Bonferroni correction was applied by thresholding all p-value maps corrected for family-wise Type I error within tract skeleton at 0.000595, (0.05 was divided by the number of contrasts performed; 7 tracts x 4 DTI scalars x 3 contrasts per DTI scalar).

4.2.9.3 DTI scalars and cognitive variable correlations

randomise was also used to determine how DTI scalars (FA, MD, AD, and RD) correlated with cognitive performance on the following cognitive variables: SDMT, Stroop Word, Stroop Color, Stroop Inference, TMTA, and TMTB for the EMPMS

data set only using the TFCE method. Only prodromal HD participants were included in the correlation analysis with age, years of education, gender, and site of data collection as covariates. A correlation analysis was not pursued with the MPSS data because results from previous statistical tests seemed unstable due to small numbers of participants in some of the groups. Correlation analyses were also not performed on the MPMS data set as statistical test exploration with the unpaired t-tests seemed adequate to select the TFCE method for subsequent statistical analyses. Statistical inference was made on the correlation coefficients for the EMPMS data via t-tests in the same manner as the differences in DTI scalars between controls and CAP groups with slight changes to the GLM (Section A.3). Correction for multiple comparisons within tract skeleton and across contrasts were done on the p-value maps with FDR at a criterion of $q < 0.05$.

4.3 Results

4.3.1 T1-weighted and DTI atlases

Figure 4.1 shows the T1-weighted template (left) whose space was used to construct the corresponding DTI template (right) for the EMPMS data set. T1-weighted and DTI atlases for the other data sets can be found in Section A.4 in Figures A.13 (SPMS), A.14 (MPSS), and A.15 (MPMS).

4.3.2 Fiber tracts

Figure 4.2 shows several views of the fiber tracts (UNC, FM, IFO, and ATR) derived from whole brain tractograms of the DTI templates overlaid on the T1-

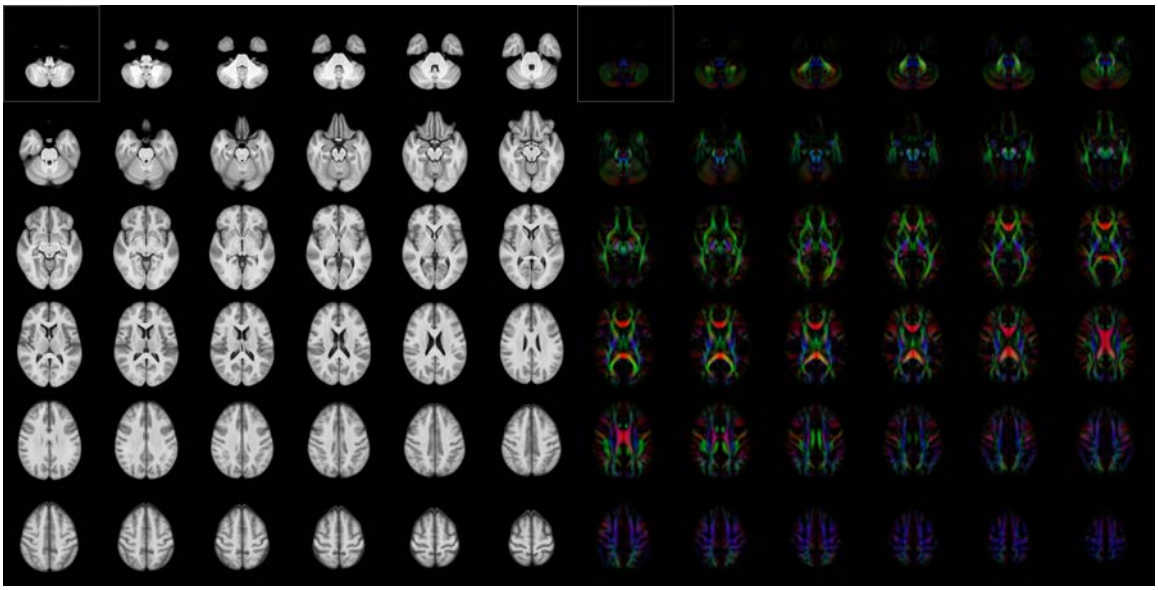

Figure 4.1: T1-weighted and DTI templates for EMPMS data.

weighted template for each of the data sets: SPMS, MPSS, MPSS, and EMPMS. Different tracts are highlighted with different colors: left UNC (light blue), right UNC (dark blue), FM (yellow), left IFO (light red), right IFO (dark red), left ATR (light green), and right ATR (dark green). In Figure 4.2, a noticeable increase in tract uniformity can be observed as more participants are used to construct the DTI atlas.

4.3.3 SPMS data: DTI scalar variability analysis

4.3.3.1 Variability of mean DTI scalars of fiber tracts

CVs of mean DTI scalars in all tracts ranged from 1.02 to 9.88% and are displayed in Table 4.10. Mean MD seemed to have the least variability with an average CV of 2.51% across all tracts, followed by mean AD, mean RD, and then mean

FA. Mean FA had the most variability with an average CV of 6.12%. The inferior fronto-occipital fasciculi had the least variability across DTI scalar measurements with CVs of 2.59% and 2.07% in left and right hemispheres, respectively. Amount of variability in fiber tracts across DTI scalar measurements increased in the following order: FM, ATRs, and uncinate fasciculi. The uncinate fasciculi possessed the most variability across DTI scalar measures with CVs of 6.23% and 5.06% for left and right hemispheres, respectively. Plots of mean DTI scalar values across each tract for all scans are provided in Figure 4.3.

4.3.3.2 Variability of mean DTI scalars in skeleton

CVs of mean DTI scalars in all DTI scalars projected to skeletonized TPMs ranged from 1.49 to 13.71% and are displayed in Table 4.11. Mean AD seemed to have the least variability with an average of 4.58% across all skeletonized TPMs, followed by mean MD, mean FA, and mean RD. Mean RD had the most variability with an average CV of 5.13%. The right IFO had the least variability across DTI scalar measurements with a CV of 2.29%. Amount of variability in skeletonized TPMs across DTI scalar measurements increased in the following order: FM, right and left ATRs, left IFO, and right and left uncinate fasciculi. The uncinate fasciculi possessed the most variability across DTI scalar measures with CVs of 7.29% and 10.08% for right and left hemispheres, respectively. Plots of mean DTI scalar values across each tract skeleton for all scans are provided in Figure 4.4. It should be noted that mean DTI scalar values across each tract skeleton are generally greater than their corresponding

means across entire tracts.

4.3.4 Multi-participant, single-site data

As stated earlier, t-tests were performed on the MPSS data set to find significant differences in mean DTI scalars between controls and CAP groups using voxel-based thresholding, cluster-based thresholding (at various primary statistic thresholds), and TFCE tests using single threshold or suprathreshold cluster test to correct for multiple comparison within tracts. However, exploration of FDR and Bonferroni methods for multiple comparison correction and correlations between DTI scalars and cognitive variables were not pursued with the MPSS data set due to unstable t-test results. Results from the left ATR and right IFO t-tests will be used to illustrate the problems of the MPSS data set. Plots of mean DTI scalars across the left ATR tract and tract skeleton in Figure 4.5 show that even after the removal of outliers, there were probably too few samples to properly represent the true means of each group. In addition, Table 4.12 shows that significant differences in MD and RD were present in clusters in the left ATR between the control and low CAP group, but not between controls and those with higher disease burden. Aside from the left ATR findings, the right IFO from the MPSS data set counterintuitively had a greater number of voxels where AD was significantly greater in the medium CAP group than controls than the contrast comparing controls and the high CAP group. In general, a greater effect is expected in participants with greater disease burden (high CAP group) and not the opposite.

4.3.5 Multi-participant, multi-site data

The purpose of the MPMS data set was to illustrate how examining the different aspects of each permutation test and methods for multiple comparison correction dictated the decision to use the TFCE test and FDR for the EMPMS data set. The right IFO was selected to be featured in this section since it contains multiple regions of the lateral PFC that may be involved in prodromal HD progression [178]. In addition, two particular sets of results that were found in a previous study were acquired again in the MPMS data set through the right IFO: (1) increased mean RD in the right lateral orbitofrontal and right pars triangularis WM regions defined by FreeSurfer in the high CAP group in comparison to controls; (2) and a negative correlation between TMTB score and FA in the right pars triangularis and right medial orbitofrontal WM regions defined by FreeSurfer in prodromal HD participants [178]. The following abbreviations that have been influenced by the FreeSurfer labeling convention will be used to refer to regions of the IFO (Figure 4.12): IFO1 (medial orbitofrontal gyrus), IFO2 (lateral orbitofrontal WM), IFO3 (pars orbitalis WM), IFO4 (pars triangularis WM), IFO5 (WM lateral to the putamen, medial to the insular gyrus), IFO6 (WM posterior to the putamen but does not terminate in the occipital or parietal lobe), IFO7 (WM that projects to the occipital lobe), and IFO8 (WM that projects to the parietal lobe). It is important to note that the FreeSurfer labeling convention includes the medial orbitofrontal gyrus in its lateral orbitofrontal region [179]. The IFO generated in this study does not enter the area FreeSurfer has designated as its medial orbitofrontal region (gyrus rectus) [179] but does enter the

medial orbitofrontal gyrus, which has been made into a separate region (IFO1).

4.3.5.1 Mean RD: controls versus CAP groups

The TFCE method proved to be the most reliable permutation test among voxel-based thresholding, cluster-based thresholding, and TFCE methods. As for methods of multiple comparison correction, FDR seemed to be the most appropriate for the MPMS data set. Between the voxelwise and cluster-based approaches, cluster-based thresholding did not report any clusters in the lateral PFC with significant differences in mean RD between controls and CAP groups (Figure 4.6). Between the two voxelwise approaches, voxel-based thresholding and TFCE, voxel-based thresholding produced many individual significant voxels that were detached from any clusters that appeared, while the TFCE method provided large clusters with few detached voxels. In addition, the TFCE method helped to enhance findings in the lateral PFC that voxel-based thresholding suggested with a few significant voxels, as shown in the right lateral orbitofrontal gyrus in Figure 4.7 and right pars triangularis in Figure 4.8, which were found in a previous study [178]. As for correction for multiple comparisons, the FWE alone and with the Bonferroni methods proved too stringent for this experiment as both eliminated all findings in the lateral PFC. All clusters that remained after controlling for FWE with the maximal statistic distribution remained after correction with FDR at a criterion of $q < 0.05$ and are therefore not shown.

The part of the right IFO that contained the most significant differences in RD between controls and CAP groups tended to be region IFO6 (WM posterior to

the putamen but did not terminate in the occipital or parietal lobe). Upon visual inspection of region IFO6, a large portion presented a statistically significant group difference (p-value < 0.001) along the entire region. The most significant region of group differences (p-value < 0.001) also seemed to be concentrated in the area immediately posterior to the putamen, as this region often remained significant after Bonferroni correction (one of most conservative correction) and in contrasts where the effect of RD would be less (controls versus medium CAP group).

4.3.5.2 Negative correlation between FA and TMTB

The suitability of the TFCE method and FDR correction for detecting differences in RD between controls and CAP groups seemed to extend to the correlation analysis. The results of the correlation analyses using voxel-based and cluster-based thresholding seemed to match the t-test contrasts using the same tests as they also did not report significant correlations in the lateral PFC when looking for a negative correlation between FA and TMTB. The TFCE method again helped to enhance a significant negative correlation between FA and TMTB in the right pars triangularis WM (Figure 4.9) that was also seen in a previous study [178]. Again, FWE alone and with the Bonferroni methods proved too stringent for this experiment as both eliminated nearly all findings in the lateral PFC. All clusters that remained after controlling for FWE with the maximal statistic distribution remained after correction with FDR at a criterion of $q < 0.05$ and are therefore not shown.

The part of the right IFO that contained the most significant negative corre-

lations between FA and TMTB time was again region IFO6 (WM posterior to the putamen but did not terminate in the occipital or parietal lobe) (Table 4.14). Again, the most significant group differences (p-value < 0.05) seemed to be concentrated immediately posterior to the putamen and remained significant even after Bonferroni correction (although not visible in the axial plane displayed in Figure 4.9).

4.3.6 Expanded multi-participant, multi-site data

Descriptions of the EMPMS data results will be referring to the regions identified in Figures 4.10, 4.11, 4.12, and 4.13 for the FM, ATR, IFO, and UNC fiber tracts, respectively. Again, these labels have been influenced by the convention FreeSurfer uses to label WM regions. The medial orbitofrontal gyrus has been given a separate label in the IFO and UNC since it is included in the lateral orbitofrontal region defined by FreeSurfer [179].

4.3.6.1 Age effect on RD using controls

When the mean RD of the right IFO from the lower and upper thirds of controls ranked by age were compared (Table 4.15), mean RD for the upper third was significantly higher in various regions of the right IFO. Specifically, the upper third of control participants ranked by age had a higher RD in 41.44% of the voxels in the right IFO after controlling for years of education, gender, and site of data collection and correcting with FDR with a criterion of $q < 0.05$. Regions of the right IFO that contained significant voxels included right IFO2 (lateral orbitofrontal WM), IFO4 (pars triangularis), IFO5 (lateral to the putamen, medial to the insular gyrus),

IFO6 (WM posterior to the putamen but not extending to occipital or parietal lobes), IFO7 (WM extending to the occipital lobe), and IFO8 (WM extending to the parietal lobe) (Figure 4.14).

4.3.6.2 Mean DTI scalars: controls versus CAP groups

Regions referred to in Table 4.16 were defined in Figures 4.10 through 4.13. In general, mean MD, AD, and RD for the high CAP group were all significantly higher than the means of controls in at least 10% of the voxels in all tracts except for the left UNC (MD and RD only) (Figure 4.15 and Table 4.16). When comparing the control and high CAP group, the largest percentages of significant voxels were usually seen when assessing MD and RD (except for the right UNC). When a significant difference in mean DTI scalar was present between the control and medium CAP group, it was usually seen in MD and/or RD. For the control versus medium CAP groups contrasts, mean MD and RD were again higher than controls and the number of voxels containing findings was less than the control versus high CAP groups contrast. The only tract that had significant differences in AD between the control and medium CAP groups was the ATR, where mean AD was higher lateral to the caudate for the medium CAP group bilaterally. Mean DTI scalar differences between the control and low CAP groups and for FA (except for limited areas in the left and right IFOs) were not detectable in this experiment. Plots to illustrate the mean DTI scalar values across the significant voxels for controls versus medium and/or high CAP group(s) are provided in Figures 4.16 and 4.17.

4.3.6.3 Cognitive variable correlations with DTI scalars

Regions referred to in Tables 4.17 and 4.18were defined in Figures 4.10 through 4.13. For reference, increased MD, AD, and RD and decreased FA values in WM are generally associated with increased disease burden, while decreased SDMT, Stroop Color, Stroop Word, and Stroop Interference and increased TMTA and TMTB times indicate decline in cognitive performance. Results discussed here pertain to more widespread findings where significant correlations were present in more than 20% of voxels within a tract. Increased MD and RD and decreased FA, but not increased AD, often correlated with declines in cognitive performance in many of the tracts examined in this experiment. Stroop Color and Stroop Word scores positively correlated most often with FA in the FM, while negatively correlating most often with MD and RD in both the FM and ATR tracts. SDMT score correlations were much like Stroop Color and Stroop Word, with additional negative correlations with MD and RD in the IFO tracts. TMTA and TMTB times differentiated themselves from the other cognitive variables by positively correlating with MD and RD in the UNC tracts. TMTA and TMTB times also produced results like those seen with SDMT, Stroop Color, and Stroop Word scores. There was an absence of findings involving Stroop Interference score in this experiment.

4.4 Discussion

The main goal of this study was to build upon past volume and DTI scalar studies on the frontal lobe in prodromal HD by examining the diffusivity properties of

major WM tracts terminating in the PFC. Unbiased DTI atlases of increasing population complexity (healthy controls, single to multi-site sampling of both healthy controls and prodromal HD participants) were built using non-linear transformations derived from T1-weighted images and were used to create four major WM tracts terminating in the PFC: FM, left and right ATR, left and right IFO, and left and right UNC. Tract skeletons were derived for each tract and FA, MD, AD, and RD were projected to each tract skeleton. Fiber tracts derived from the DTI atlas built from healthy controls (SPMS data set) showed that mean CVs for DTI scalar values remained under 10% for both tracts and tract skeletons, where FA had the highest CV. Mean CVs of DTI scalar values across all tracts and tract skeletons also remained under 10% except for the left UNC. Fiber tracts derived from DTI atlases built from populations of increasing complexity (MPSS and MPMS data sets) demonstrated that randomise is a suitable tool for investigating WM changes in prodromal HD participants in comparison to controls with permutation methods using data from multiple sites. randomise provided widespread findings once the appropriate method for detecting significant voxels (TFCE), method for correcting for multiple comparisons (FDR), and number of participants (greater than seven to eight per group) were used. Increased MD, AD, and RD are usually associated with increased disease burden. For the EMPMS data set, mean MD, AD, and RD for the high CAP group were all significantly greater than the means of controls in at least 10% of the voxels in all tracts except for the left UNC (MD and RD only). If a significant finding was present between the medium CAP and controls, it was usually for MD

and RD in the IFO tracts. As for correlations, increased MD and RD and decreased FA (with a slightly lower frequency) decreased FA correlated with poorer cognitive performance with many of the tracts in this study. TMTA and TMTB times had the most widespread significant correlations because they correlated with FA, MD, and RD in nearly every tract. SDMT had the second most widespread significant correlations but did not have as many findings in the UNC tracts as the TMT times. Stroop Word and Color scores seemed limited to significant correlations in the FM and ATR tracts. Together, the gradient of effects seen in the differences in DTI scalar values and their correlations with cognitive variables that have a documented ability in detecting cognitive deficits in prodromal HD participants suggest that DWI can provide reliable markers of disease progression. Specifically, the results of this study suggest that monitoring MD and RD in the IFO while measuring TMT time could serve as a reliable biomarker to monitor disease progression in the prodromal HD stage.

Left and right UNCs consistently had the highest CVs in comparison to all other tracts. Greater variation in UNC CV could be due to imaging artifacts caused by proximity to an air-tissue interface that could vary the number and quality of fibers estimated. CVs derived in this study (less than 10%) are consistent with another study that used CVs of mean DTI scalars across fiber tracts in repeat scans to evaluate reliability of measurements derived from fiber tracts [103].

The MPSS data set was problematic mainly due to its small samples sizes for each group. randomise performs its statistical tests based on the distribution of

statistic values derived from permutations of unique relabelings of the data. The number of unique permutations randomise can achieve for a given statistical test is limited by the number of samples it is provided. The formula for computing the number of unique permutations possible for a two-sample t-test, where n_1 and n_2 are the sizes of the two samples, is as follows [180, 181]:

$$Permutations = (n_1 + n_2)!/(n_1! \times n_2!) \tag{4.7}$$

Therefore, when performing a contrast between the control ($n_1 = 8$) and low CAP group ($n_2 = 5$) for the MPSS data set using 10,000 permutations, the result could not be considered reliable because there were only 1,287 possible unique permutations. randomise recommends using at least unique 5,000 permutations to build a somewhat representative distribution that would only serve as a quick test to determine if significant findings are present [180, 181]. The expected instability of the controls versus low CAP group contrast could explain why it would be significant in the absence significant findings in the control versus medium or high CAP group contrast. As for the other contrasts tested using the MPSS data set, the sample sizes for controls versus medium CAP group would allow for 24,310 unique permutations while the controls versus high CAP group would have 12,870. Although the controls versus medium and controls versus high CAP groups technically would provide a suitable number of unique permutations, the number of significant voxels were often very small. Some significant voxel counts amounted to less than 10, which could be explained by the lack of power with these minimal sample sizes or skewed means of groups due to non-uniform sampling of the population.

The fact that the TFCE method proved to be a more reliable permutation method than voxel-based and cluster-based thresholding is not too surprising since the TFCE method was developed to overcome the limitations of the other methods [177]. Many of the limitations of simple voxel-based and cluster-based thresholding methods are based on the fact that the expected signal extent is rarely known [177]. As stated by Smith et al., simple voxel-based thresholding is not very sensitive to finding true signals because voxels are analyzed separately. When using simple voxel-based thresholding, variance smoothing to increase signal is an option. However, the smoothing size is an arbitrary number set during implementation and usually without knowing the true signal in the data [177]. Cluster-based thresholding is supposed to be more sensitive than simple voxel-based [182]. However, the primary statistic threshold required for cluster-based thresholding is set arbitrarily without knowledge of the actual signal extent and will have a large impact on the final output [177]. In addition, the logic behind setting the primary threshold is no more sophisticated than selecting a lower statistic value to find broader clusters and a higher for smaller clusters [183]. Therefore, TFCE bypasses the need for user-defined thresholds since its algorithm will detect unknown signal in a given voxel and how that signal corresponds to signal in neighboring voxels using signal height and signal extent parameters that have been optimized for a wide range of data [177].

Much like the TFCE method, FDR-controlling procedures for multiple comparison correction was developed with the goal of finding a method that is more appropriate for solving neuroimaging problems [184]. Therefore, it was not too sur-

prising that FDR seemed more appropriate than Bonferroni correction, single threshold test, and suprathreshold cluster test. Bonferroni correction traditionally been used because it has a strong control of Type I error. However, if applied to voxelwise study in neuroimaging where every voxel contains a test, Bonferroni correction is very wasteful because α is being reduced to unreasonably low values. Another way to use Bonferroni correction is to consider the number of contrast is the number of tests that will divide α. In addition, to limit the strength of Bonferroni correction, one may limit the number of contrasts done in an experiment. Even when considering the number of contrasts as the number of tests, Bonferroni correction still ends up being wasteful because it is not always possible to perform a small number of tests and has a tendency to wipe out both false and true positives when applied to an entire data set regardless [184]. For permutation tests, single threshold and suprathreshold cluster tests were specifically designed to control for Type I error by using the distribution of the maximum statistic values from permuting the labels of the given data. However, single threshold and suprathreshold cluster tests are also considered very strong controllers of Type I error rate and seemed to remove too many findings even in this experiment. FDR-controlling procedures instead control the expected proportion of the rejected hypotheses that are falsely rejected and is adaptable to different datasets, and thus do not eliminate signal unnecessarily [184].

As for the large EMPMS data set, MD and RD seemed to be the most robust of the DTI scalars as both produced the most findings in the mean differences between groups and correlation analyses. Out of the cognitive measures evaluated, TMT times

seemed to be the most robust by correlating with diffusivity changes in almost every tract. These findings with MD, RD, and TMT times are consistent with a previous study looking at mean scalar values WM regions of the PFC (Chapter 3). In the scalar study, increased MD and RD were seen in both left and right lateral and inferior PFC WM in both medium and high CAP groups versus controls, while TMTB negatively correlated with FA in the right inferior frontal and medial orbitofrontal WM and positively correlated with RD in the right inferior frontal WM [178]. This study produced findings similar to the scalar study in Chapter 3 that examined WM of the PFC, in addition to many other findings. The widespread positive correlations between increased TMT times and increased MD and RD and decreased FA seen in this study could be explained by the many cognitive functions the TMTs assess [135]. Increased TMTA times demonstrated in the prodromal HD participants here could be explained by deficits in attention and visual processing caused by diffusivity changes in the WM of the IFOs that reflect increased disease burden [150, 151], while increased TMTB time could be due to deficits in memory caused by diffusivity changes in the WM of the ATRs and UNCs that reflect increased disease burden [145, 146, 152, 135]. Since SDMT score is a measure of working memory, perhaps decreased SDMT scores can be explained by memory deficits caused by diffusivity changes the ATRs and left UNC [118, 152].

The main limitation of this study was that the fiber tracking and scalar measurements used were single tensor-based like the analysis performed in Chapter 3, where the use of other models for diffusion have been addressed. Specifically for this

study, although use of a single tensor model for diffusion did not completely limit the types of fiber tracking algorithms to streamline tracking, DTI atlases will continue to prevent the use of multi-tensor fiber tracking algorithms that require a DWI as input. Therefore, atlas-based fiber tracking analyses will be limited to using DTI atlases until DWI atlases becomes commonplace. Future directions include expanding upon these findings in the PFC by perhaps using the same methods in other tracts of interest to prodromal HD. In addition to WM in the PFC, it may also be useful to examine WM extending to the PFC from the striatum and beyond to characterize how HD affects corticostriatal loops in their entirety. Ultimately, the above analyses will be expanded to characterize changes in individual subjects longitudinally.

4.5 Conclusion

The main goal of this study was to build upon past volume and DTI scalar studies on the frontal lobe in prodromal HD by examining the diffusivity properties of major WM tracts terminating in the PFC. In this study, the gradient of effects seen in the differences in DTI scalar values and their correlations with cognitive variables that have a documented ability in detecting cognitive deficits in prodromal HD participants suggest that DWI can provide reliable markers of disease progression. Specifically, the results of this study suggest that monitoring MD and RD in the IFO while measuring TMT time could serve as a reliable biomarker to monitor disease progression in the prodromal HD stage.

Table 4.6: Scanner parameters for diffusion-weighted images with 30 to 35 unique gradient directions per scan with a b-value of 1,000 sec/mm^2 collected at various PREDICT-HD study sites with zero gap between axial slices.

Site	Vendor	Scans	b0s	Grads	Voxel (mm)	Slices	TE (ms)	TR (ms)	BW (Hz/ pixel)	FOV (mm)	Matrix (mm)
001	GE	1	2	35	1.0x1.0x2.4	61	85.5	17000	1953	256x256	128x128
002	Philips	2	1	32	2.0x2.0x2.0	70	92.0	11761	1276	128x128	128x126
007	Siemens	2	1	30	2.0x2.0x2.0	70	92.0	12000	1565	1152x1152	128x128
024	Siemens	2	1	30	2.0x2.0x2.0	70	92.0	12000	1395	1152x1152	128x128
027	Siemens	2	1	30	2.0x2.0x2.0	70	92.0	12000	1563	1152x1152	128x128
032	Siemens	1-2	1	30	2.0x2.0x2.0	70	104.0	12000	1565	1152x1152	128x128
045	Siemens	2	1	30	2.0x2.0x2.0	70	92.0	12000	1563	1152x1152	128x128
048	Philips	2	1	32	2.0x2.0x2.0	70	92.0	9679		128x128	
050	Siemens	1	1	30	2.0x2.0x2.0	70	92.0	12000	1563-1565	1152x1152	128x128
054	GE	2	1-2	35	1.0x1.0x2.4	61	85.5-96.5	17000	1953	256x256	128x128
061	Philips	1	1	30	2.0x2.0x2.0	70	92.0	12000	1565	1152x1152	128x128
073	Siemens	2	1	30	2.0x2.0x2.0	70	92.0	12000	1565	1152x1152	128x128
120	Siemens	2	1	30	2.0x2.0x2.0	70	92.0	12000	1563-1565	1152x1152	128x128
144	Siemens	1	1	30	2.0x2.0x2.0	70	111.0	14500	1563-1565	1152x1152	128x128
177	Siemens	2	1	30	2.0x2.0x2.0	70	92.0	12000	1395	1152x1152	128x128

Note: Scans = Number of scans collected per participant. Grads = Number of non-collinear gradient directions per scan. Voxel = Voxel dimensions. Slices = Number of slices per 3D volume in the 4D diffusion-weighted image. TE = Echo time. TR = Repetition time. BW = Pixel bandwidth. FOV = Field of view.

Table 4.7: Scanner parameters for T1-weighted images from PREDICT-HD sites.

Site	Vendor	TI (ms)	TE (ms)	TR (ms)	Flip Angle	NEX	Bandwidth (Hz/pixel)	FOV (mm)	Matrix (mm)
001	GE	450	2.98	7.79	12^o	1	244	256x256	256x256
002	Philips		3.50	7.69				224x224	
007	Siemens	900	2.87	2300	10^o	1	240	256x256	256x256
024	Siemens	900	2.87	2300	10^o	1	238	256x256	256x256
027	Siemens	900	2.87	2300	10^o	1	238	256x256	256x256
032	Siemens	900	1.91	2300	10^o	1	240	256x256	256x256
045	Siemens	900	2.87	2300	10^o	1	238	256x256	256x256
048	Philips		3.50	7.70	8^o			224x224	
050	Siemens	900	2.85	2300	10^o	1	240	256x256	256x256
054	GE	450	2.79	6.50	12^o	1	244	256x256	256x256
061	Siemens	900	2.87	2300	10^o	1	240	256x256	256x256
073	Siemens	900	2.92	2300	10^o	1	240	256x256	256x256
120	Siemens	900	2.87	2300	10^o	1	238	256x256	256x256
144	Siemens	900	1.93	2300	10^o	1	240	512x512	256x256
177	Siemens	900	2.87	2300	10^o	1	240	256x256	256x256

Note: TI = Inversion time. TE = Echo time. TR = Repetition time. NEX = Number of excitations. FOV = Field of view.

Table 4.8: Scanner parameters for T2-weighted images from PREDICT-HD sites.

Site	Vendor	TE (ms)	TR (ms)	Flip Angle	NEX	Bandwidth (Hz/pixel)	FOV (mm)	Matrix (mm)
001	GE	99.0	4900	90^o	2	163	512x512	288x288
002	Philips	184	2500				224x224	
007	Siemens	433	4800	120^o	1	590	256x256	256x250
024	Siemens	430	4800	120^o	1	592	256x256	256x250
027	Siemens	430	4800	120^o	1	592	256x256	256x250
032	Siemens	459	4800	120^o	1	590	256x256	256x250
045	Siemens	430	4800	120^o	1	592	256x256	256x250
048	Philips	183	2500	90^o			224x224	
050	Siemens	435	4800	120^o	1	590	256x256	256x254
054	GE	69.2	3000	90^o	1	244	512x512	288x288
061	Siemens	433	4800	120^o	1	590	256x256	256x250
073	Siemens	433	4800	120^o	1	590	256x256	256x250
120	Siemens	430	4800	120^o	1	592	256x256	256x250
144	Siemens	433	4800	120^o	1	750	256x256	256x250
177	Siemens	433	4800	120^o	1	590	256x256	256x250

Note: TE = Echo time. TR = Repetition time. NEX = Number of excitations. FOV = Field of view.

Table 4.9: Correction for multiple comparisons within tract skeleton and across contrasts performed on the MPMS data set with different levels of stringency, where FDR was less strict.

t-test procedure	Correction within tract skeleton	Correction across contrasts
Voxel-wise thresholding	FDR on uncorrected p-value map	FDR on uncorrected p-value map
Voxel-wise thresholding	Single threshold test	Bonferroni on corrected p-value map
Cluster-based thresholding	Suprathreshold cluster test	FDR on p-values of significant clusters
Cluster-based thresholding	Suprathreshold cluster test	Bonferroni on corrected p-value map
TFCE	FDR on uncorrected p-value map	FDR on uncorrected p-value map
TFCE	Single threshold p-value map	Bonferroni on corrected p-value map

Note: FDR = False discovery rate. TFCE = Threshold free cluster enhancement.

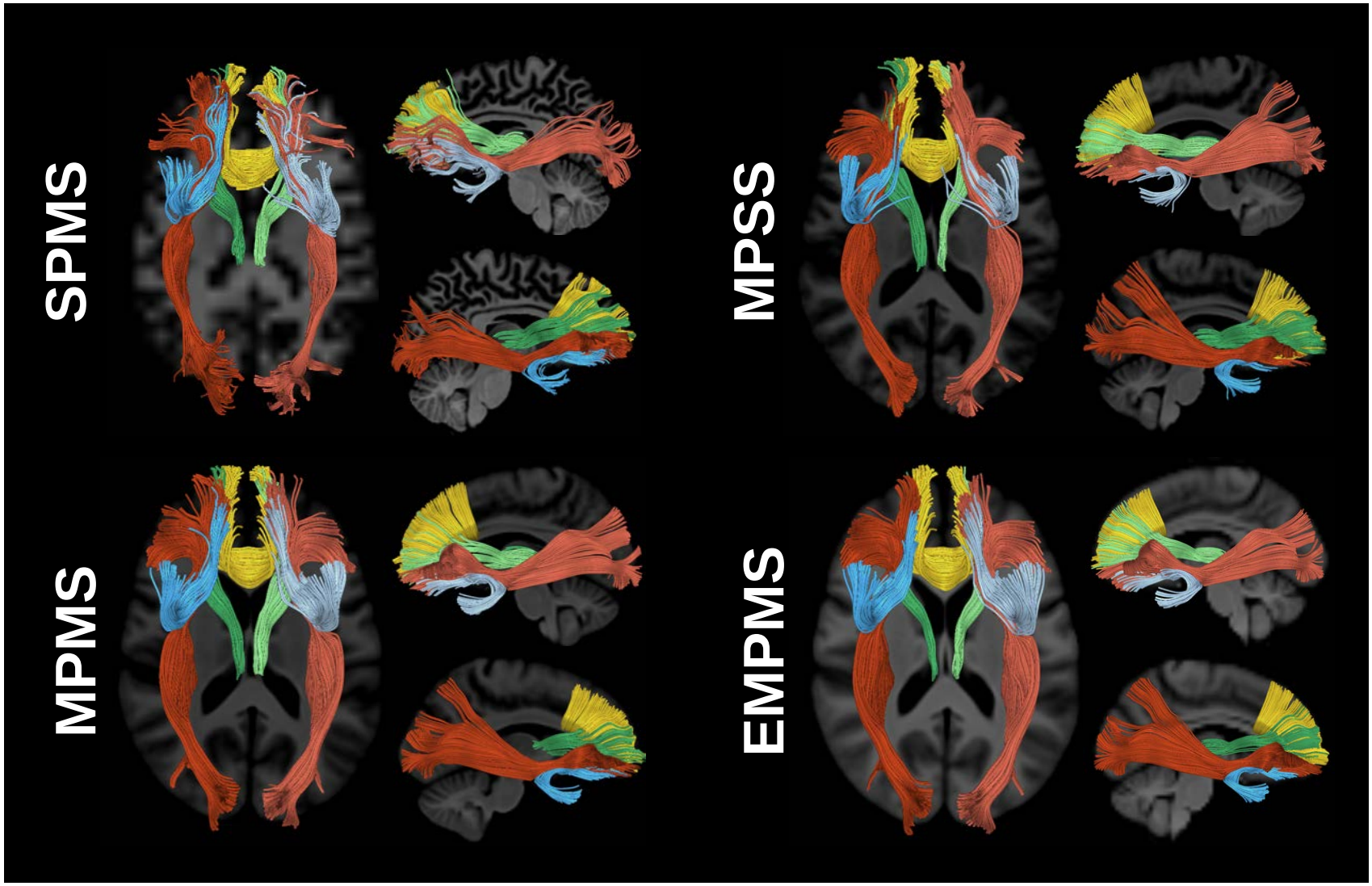

Figure 4.2: Fiber tracts for SPMS, MPMSS, MPSS, and EMPMS data. Different tracts are highlighted with different colors: left UNC (light blue), right UNC (dark blue), FM (yellow), left IFO (light red), right IFO (dark red), left ATR (light green), and right ATR (dark green).

Table 4.10: Coefficients of variation (CVs) for mean DTI scalar values across each fiber tract from scans of a single, healthy subject collected at eight different sites (SPMS data).

Fiber Tract	FA (%)	MD (%)	AD (%)	RD (%)	Average CV (%)
FM	4.35	1.99	2.74	2.89	2.99
Left ATR	7.08	2.42	2.64	3.81	3.99
Left IFO	4.03	1.71	2.30	2.34	2.59
Left UNC	9.85	4.58	3.25	7.24	6.23
Right ATR	5.65	1.88	3.25	2.18	3.24
Right IFO	3.91	1.02	1.36	1.99	2.07
Right UNC	7.94	3.95	2.84	5.50	5.06
Average CV (%)	6.12	2.51	2.62	3.71	

Note: Average CVs for each DTI scalar and fiber tract are also shown. FA = Fractional anisotropy. MD = Mean diffusivity. AD = Axial diffusivity. RD = Radial diffusivity. FM = Forceps minor. ATR = Anterior thalamic radiations. IFO = Inferior fronto-occipital fasciculus. UNC = Uncinate fasciculus.

Table 4.11: Coefficients of variation (CVs) for mean DTI scalar values across each fiber tract skeleton from scans of a single, healthy subject collected at eight different sites (SPMS data).

Fiber Tract	FA (%)	MD (%)	AD (%)	RD (%)	Average CV (%)
FM	3.40	1.88	1.88	2.62	2.44
Left ATR	4.16	2.89	3.08	3.10	3.31
Left IFO	4.89	4.50	3.48	5.23	4.53
Left UNC	7.78	11.44	7.39	13.71	10.08
Right ATR	4.44	1.55	2.43	1.49	2.48
Right IFO	3.50	1.92	1.63	2.13	2.29
Right UNC	6.26	7.91	7.33	7.65	7.29
Average CV (%)	4.92	4.58	3.89	5.13	

Note: Average CVs for each DTI scalar and fiber tract are also shown. FA = Fractional anisotropy. MD = Mean diffusivity. AD = Axial diffusivity. RD = Radial diffusivity. FM = Forceps minor. ATR = Anterior thalamic radiations. IFO = Inferior fronto-occipital fasciculus. UNC = Uncinate fasciculus.

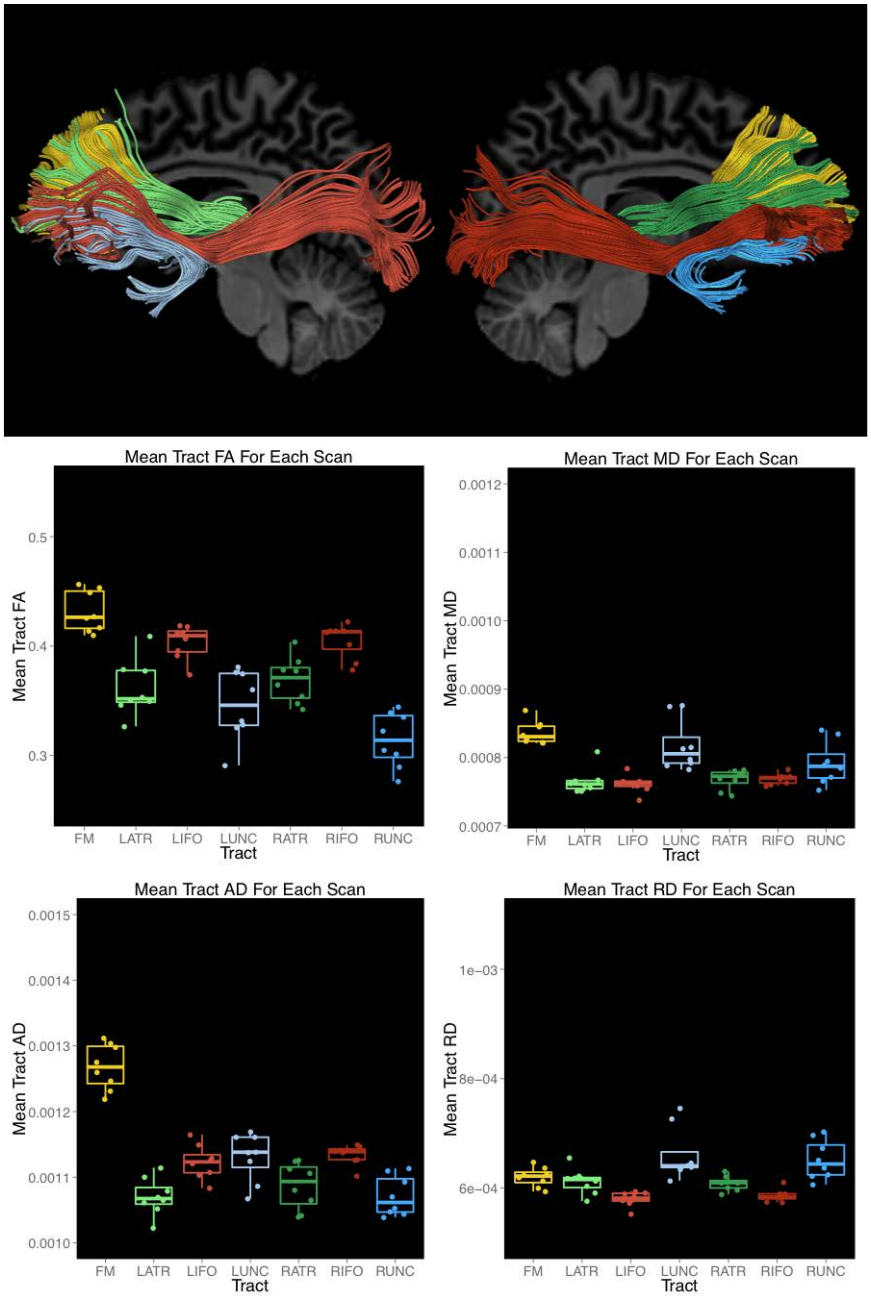

Figure 4.3: Plots of mean DTI scalars across tracts for SPMS data. Tract colors correspond to plots colors. FA = Fractional anisotropy. MD = Mean diffusivity. AD = Axial diffusivity. RD = Radial diffusivity. FM = Forceps minor (yellow). LATR = Left anterior thalamic radiations (light green). LIFO = Left inferior fronto-occipital fasciculus (light red). LUNC = Left uncinate fasciculus (light blue). RATR = Right anterior thalamic radiations (dark green). RIFO = Right inferior fronto-occipital fasciculus (dark red). RUNC = Right uncinate fasciculus (dark blue).

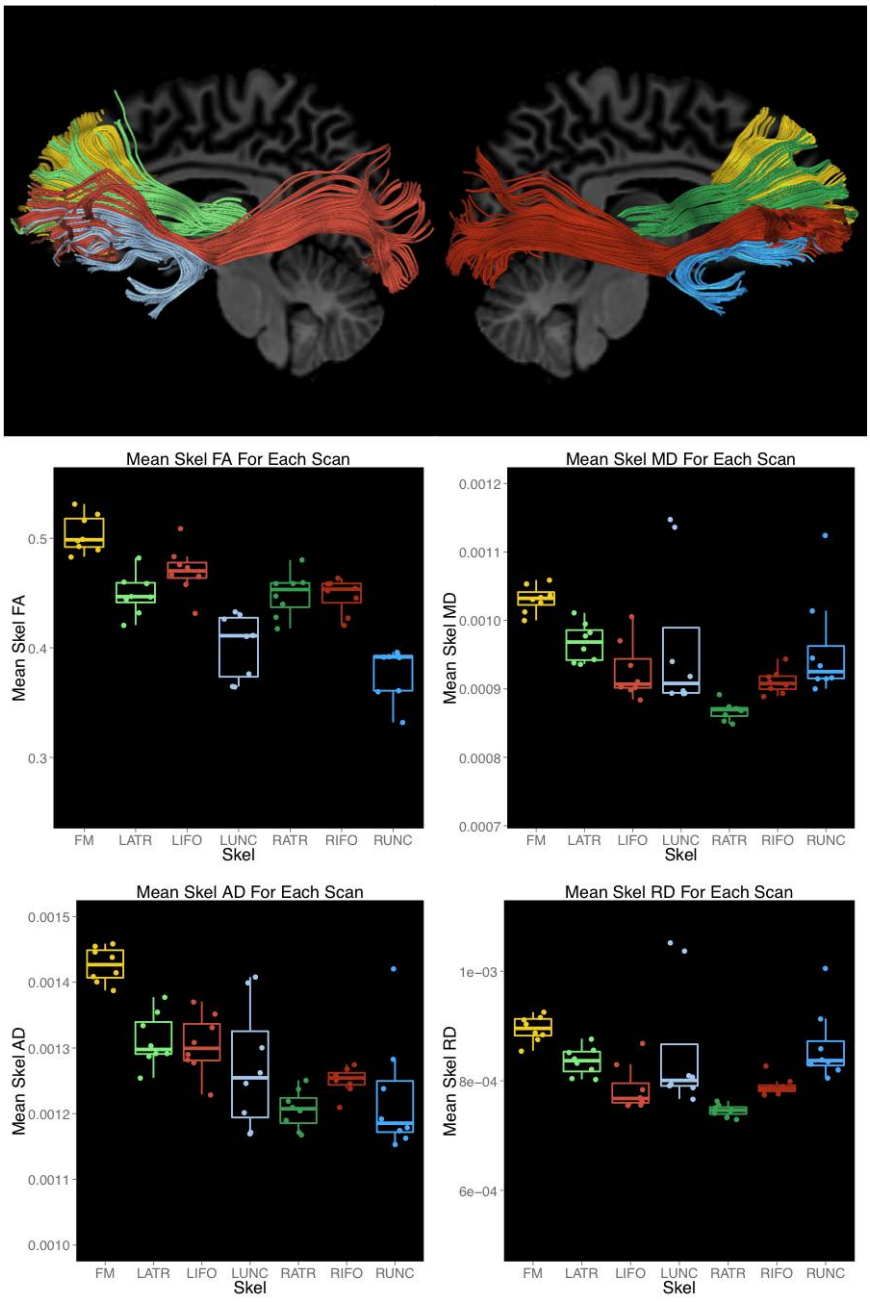

Figure 4.4: Plots of mean DTI scalars across tract skeletons for SPMS data. Tract colors correspond to plots colors. FA = Fractional anisotropy. MD = Mean diffusivity. AD = Axial diffusivity. RD = Radial diffusivity. FM = Forceps minor (yellow). LATR = Left anterior thalamic radiations (light green). LIFO = Left inferior fronto-occipital fasciculus (light red). LUNC = Left uncinate fasciculus (light blue). RATR = Right anterior thalamic radiations (dark green). RIFO = Right inferior fronto-occipital fasciculus (dark red). RUNC = Right uncinate fasciculus (dark blue).

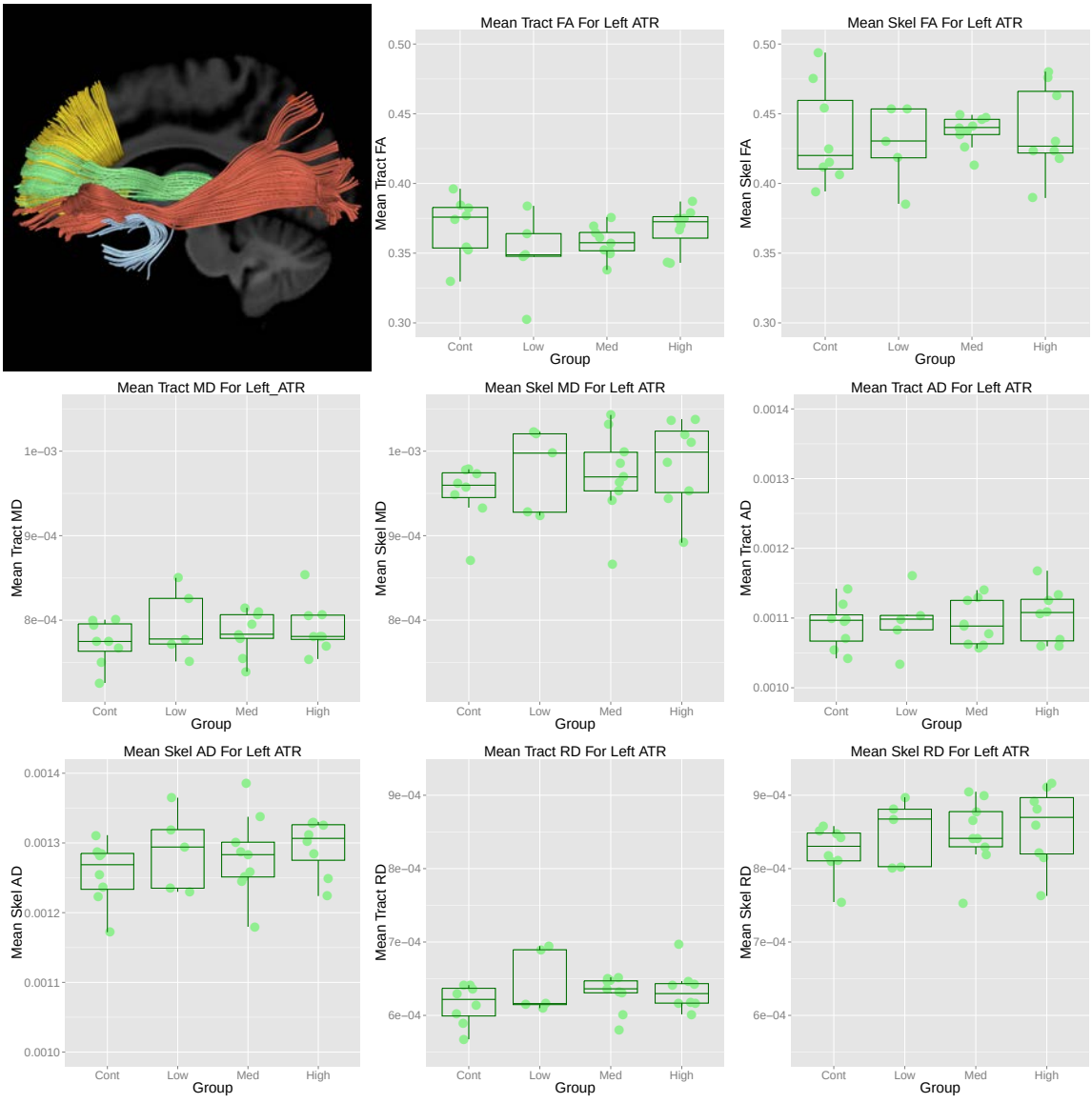

Figure 4.5: Mean DTI scalars (FA, MD, AD, and RD) across the entire left ATR tract and the left ATR tract skeleton for MPSS data.

Table 4.12: Areas with threshold free cluster enhancement-based differences between control (C) and CAP groups (L, M, H) in DTI scalars for MPSS data where statistic maps have been corrected for family-wise error with a single threshold test and thresholded at $p < 0.05$, but were not corrected for number of total contrasts done in this experiment (no Bonferroni).

Tract	Scalar	Contrast	Cluster Number	Size	p	Location
FM	RD	C < H	1/2	16	0.048	Right Zone 1
			2/2	24	0.044	Right Zone 1
Left ATR	MD	C < L	1/1	34	0.032	Left Zone 1
Left ATR	RD	C < L	1/1	5	0.044	Left Zone 1
Left IFO	MD	C < M	1/1	420	0.023	Left Zone 2, 4
		C < H	1/2	25	0.048	Left Zone 3
			2/2	831	0.006	Left Zone 2, 3, 4
Left IFO	RD	C < L	1/2	12	0.046	Left Zone 4
			2/2	99	0.042	Left Zone 2, 4
		C < M	1/1	98	0.021	Left Zone 2, 4
		C < H	1/1	749	0.003	Left Zone 2, 3, 4
Left UNC	FA	C > H	1/1	10	0.021	MO gyrus
Right IFO	FA	C > H	1/2	2	0.049	Right Zone 4
			2/2	69	0.040	Right Zone 4
Right IFO	MD	C < M	1/2	6	0.049	Right Zone 3
			2/2	11	0.048	Right Zone 3
		C < H	1/1	1514	0.006	Right Zone 2, 3, 4
Right IFO	AD	C < M	1/1	116	0.011	Right Zone 3, 4
		C < H	1/4	1	0.050	Right Zone 2
			2/4	10	0.040	Right Zone 2
			3/4	15	0.045	Right Zone 2
			4/4	39	0.040	Right Zone 2
Right IFO	RD	C < H	1/2	136	0.036	Right Zone 3
			2/2	733	0.019	Right Zone 2, 4
Right UNC	RD	C < H	1/1	3	0.041	Right Zone 5

Note: Cluster number = Number out of total clusters for statistic map. Size = Cluster size (voxels). MO = Medial orbitofrontal. Zone 1 = Lateral to superior frontal gyrus, medial to rostral middle frontal gyrus. Zone 2 = Posterior to putamen, lateral to precuneus. Zone 3 = Lateral to lingual gyrus or cuneus, medial to lateral occipital gyrus. Zone 4 = Lateral to precuneus, medial to the inferior parietal lobule. Zone 5 = Connection between temporal and frontal lobes, medial to insular gyrus.

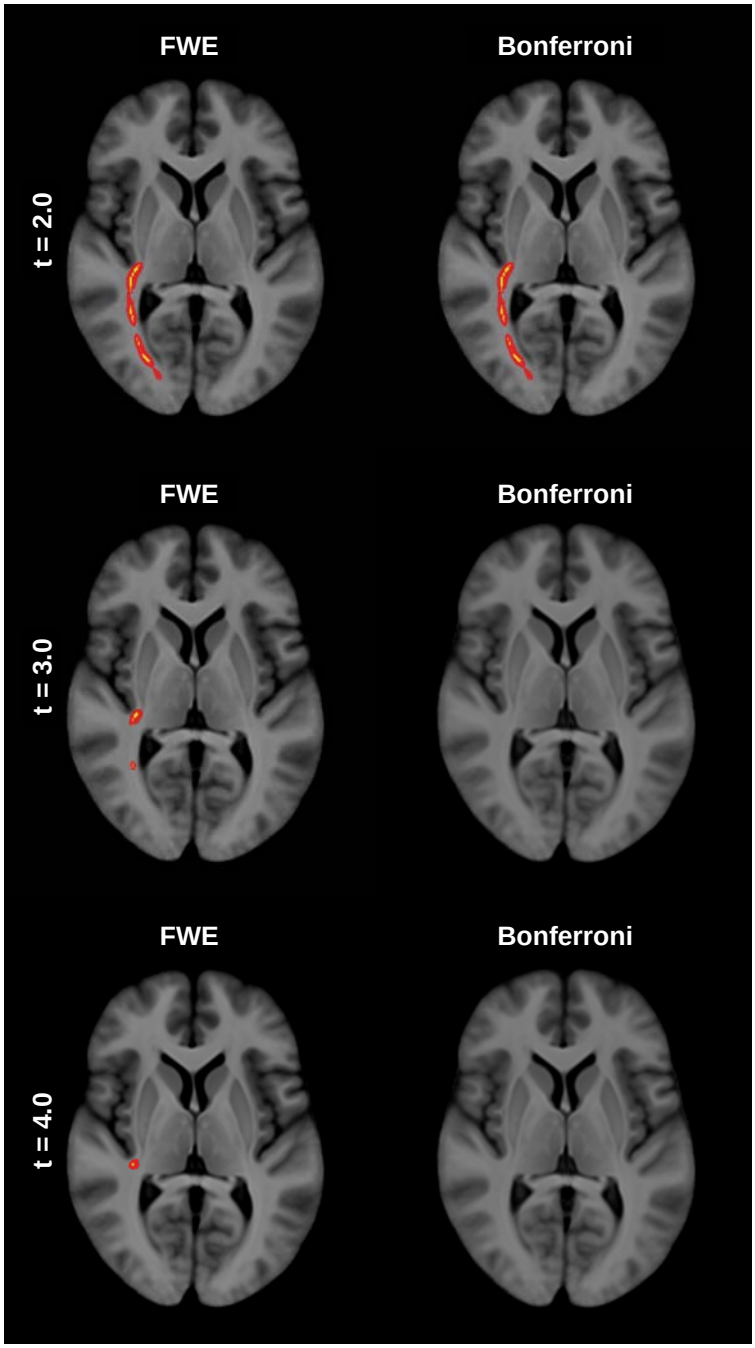

Figure 4.6: Clusters with significant differences in RD found with t-tests between controls and the high CAP group in the right IFO using the cluster-based thresholding at three different primary thresholds (t = 2.0, 3.0, 4.0). Significant clusters were in regions IFO5, IFO6, and IFO7 with FWE correction (and FDR) and Bonferroni correction, but not in the lateral PFC.

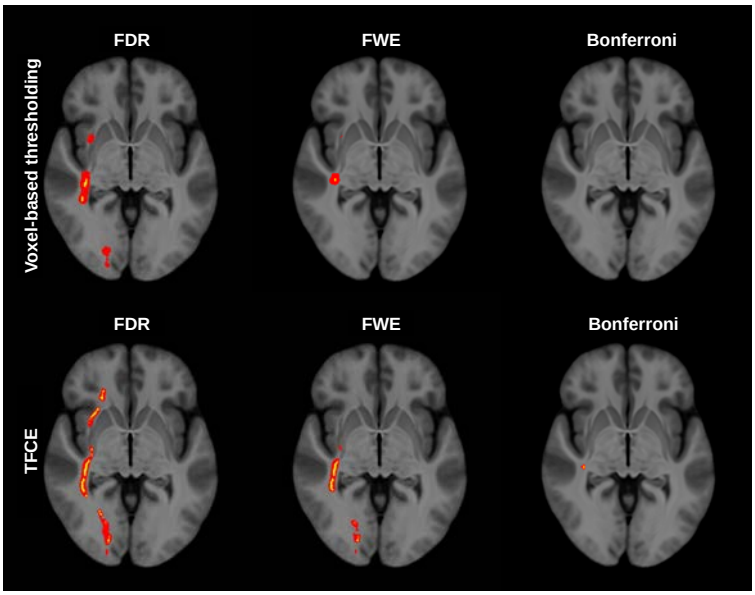

Figure 4.7: Clusters with significant differences in RD found with t-tests between controls and the high CAP group in the right IFO (right lateral orbitofrontal WM) using voxel-based thresholding and TFCE with different types of correction for multiple comparisons. The TFCE test with FDR correction does not eliminate significant findings in the right lateral orbitofrontal WM.

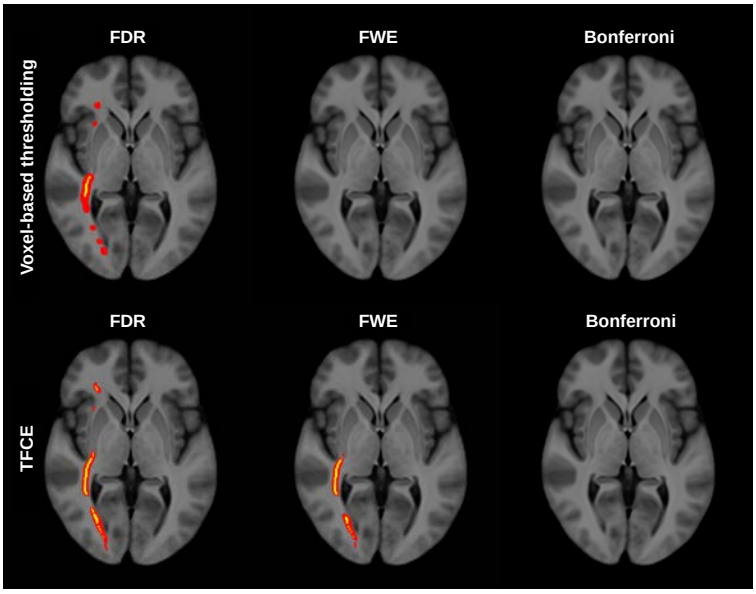

Figure 4.8: Clusters with significant differences in RD found with t-tests between controls and the high CAP group in the right IFO (right pars triangularis WM) using voxel-based thresholding and TFCE with different types of correction for multiple comparisons. The TFCE test with FDR correction does not eliminate significant findings in the right pars triangularis WM.

Table 4.13: Percentages of the right IFO tract skeleton voxels that contained significant differences in mean RD between control (C) and the medium and/or high CAP groups (M, H) and the general location of these voxels.

Test	Contrast	Within tract	Across tests	Significant voxels (%)	Regions with significant differences (IFO#)
Voxel-based thresholding	C < M	FDR	FDR	0.21	6
		FWE	None	0.02	6
		FWE	Bonferroni	0.00	None
	C < H	FDR	FDR	10.09	2, 4, 5, 6, 7, 8
		FWE	None	0.28	5, 6
		FWE	Bonferroni	0.00	None
CBT, t = 2.0	C < H	FWE	None	14.37	6, 7
		FWE	Bonferroni	14.37	6, 7
CBT, t = 3.0	C < H	FWE	None	3.58	5, 6
		FWE	Bonferroni	0.00	None
CBT, t = 4.0	C < H	FWE	None	0.37	6
		FWE	Bonferroni	0.00	None
TFCE	C < H	FDR	FDR	58.67	1, 2, 3, 4, 5, 6, 7, 8
		FWE	None	33.20	5, 6, 7
		FWE	Bonferroni	1.54	6

Note: Type of permutation test and correction method within tract and across contrasts are noted. All clusters that remained after controlling for FWE with the maximal statistic distribution remained after correction with FDR at a criterion of $q < 0.05$. CBT = Cluster-based thresholding.

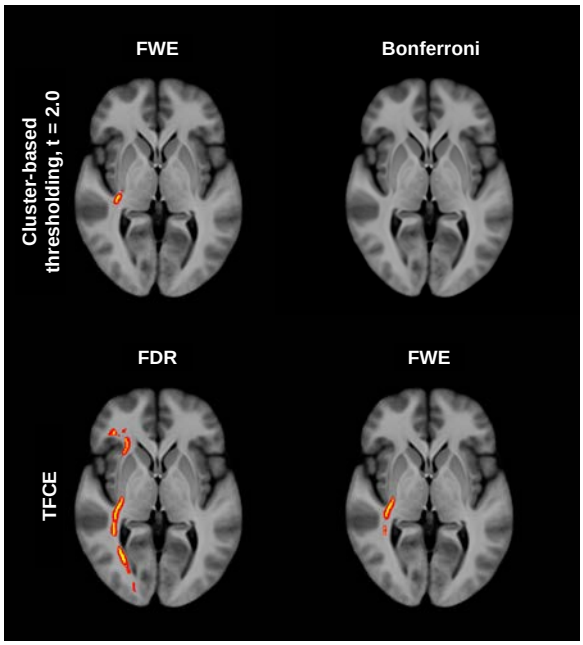

Figure 4.9: Clusters with significant negative correlations between FA and TMTB score in prodromal HD participants in the right IFO using cluster-based thresholding (t = 2.0) and TFCE methods with different types of correction for multiple comparisons. The TFCE test with FDR correction eliminated the least significant findings in the right pars triangularis WM.

Table 4.14: Percentages of the right IFO tract skeleton voxels that contained significant negative correlations between FA and TMTB score for prodromal HD participants.

Test	Within tract	Across tests	Significant voxels (%)	Regions with significant differences (IFO#)
Voxel-based	FDR	FDR	0.00	None
thresholding	FWE	None	0.00	None
	FWE	Bonferroni	0.00	None
CBT,	FWE	None	6.53	6
t = 2.0	FWE	Bonferroni	0.00	None
CBT,	FWE	None	0.00	None
t = 3.0	FWE	Bonferroni	0.00	None
CBT,	FWE	None	0.00	None
t = 4.0	FWE	Bonferroni	0.00	None
TFCE	FDR	FDR	55.62	1, 2, 3, 4, 5, 6, 7, 8
	FWE	None	13.16	6
	FWE	Bonferroni	0.00	None

Note: Type of permutation test and correction method within tract and across contrasts are noted. All clusters that remained after controlling for FWE with the maximal statistic distribution remained after correction with FDR at a criterion of $q < 0.05$. CBT = Cluster-based thresholding.

Table 4.15: Summary of demographic and clinical data for 40 controls from EMPMS data set whose data was used to test age effect on RD in the right IFO.

	Lower third of controls (Mean; SD (N))	Upper third of controls (Mean; SD (N))
Age (years)	32.5; 5.3 (20)	58.9; 4.2 (20)
Education (years)	15.8; 1.7 (20)	15.3; 2.8 (20)
Gender	7M/13F (20)	5M/15F (20)
Site 024	(8)	(7)
Site 027	(3)	(1)
Site 045	(1)	(1)
Site 050	(2)	(0)
Site 054	(1)	(0)
Site 061	(0)	(1)
Site 073	(3)	(1)
Site 120	(1)	(5)
Site 144	(1)	(4)

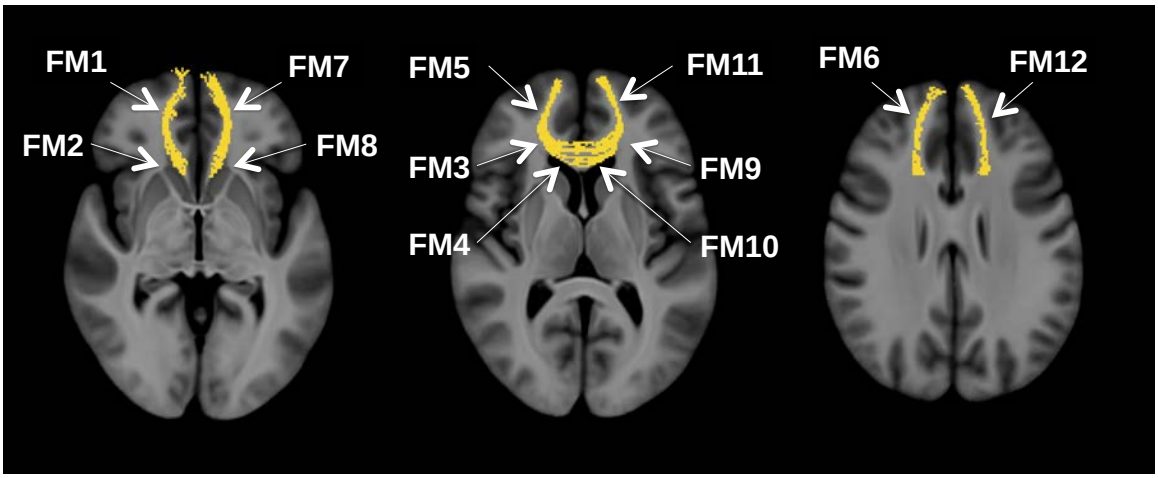

Figure 4.10: FM with labeled regions. FM1 = Right medial orbitofrontal WM. FM2 = Posterior to right anterior cingulate WM. FM3 = Lateral to right rostral anterior cingulate WM. FM4 = Inferior to right caudal anterior cingulate. FM5 = Lateral to right superior frontal WM, medial to right rostral middle frontal WM. FM6 = Right superior frontal WM. FM7 = Left medial orbitofrontal WM. FM8 = Posterior to left anterior cingulate WM. FM9 = Lateral to left rostral anterior cingulate WM. FM10 = Inferior to left caudal anterior cingulate. FM11 = Lateral to left superior frontal WM, medial to left rostral middle frontal WM.

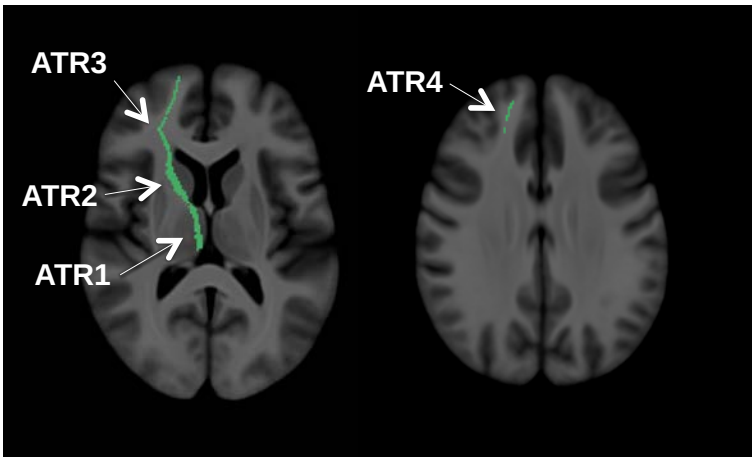

Figure 4.11: ATR with labeled regions. ATR1 = Thalamus. ATR2 = Lateral to caudate. ATR3 = Lateral to rostral anterior cingulate WM. ATR4 = Lateral to superior frontal WM, medial to rostral middle frontal WM. ATR5 = Superior frontal WM.

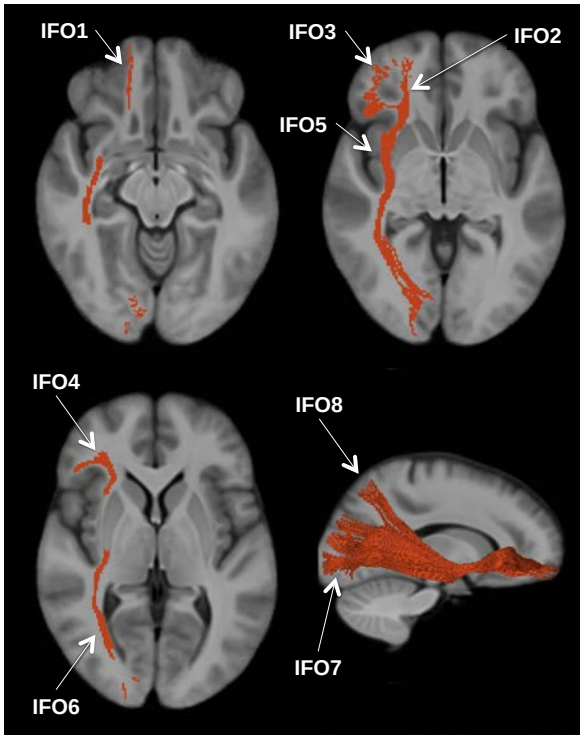

Figure 4.12: IFO with labeled regions. IFO1 = Medial orbitofrontal gyrus. IFO2 = Lateral orbitofrontal WM. IFO3 = Pars orbitalis WM. IFO4 = Pars triangularis WM. IFO5 = WM lateral to the putamen, medial to the insular gyrus. IFO6 = WM posterior to the putamen but does not terminate in the occipital or parietal lobe. IFO7 = WM that projects to the occipital lobe. IFO8 = WM that projects to the parietal lobe.

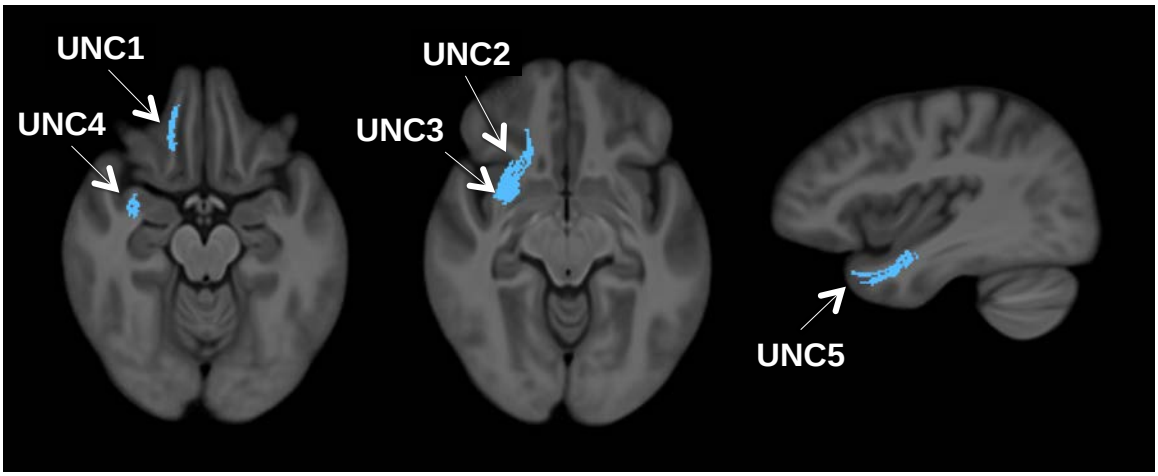

Figure 4.13: UNC with labeled regions. UNC1 = Medial orbitofrontal gyrus. UNC2 = Posterior portion of lateral orbitofrontal WM. UNC3 = Connecting point between temporal and frontal lobe, lateral to insular gyrus. UNC4 = Lateral to amygdala, medial to superior temporal gyrus. UNC5 = Superior temporal WM.

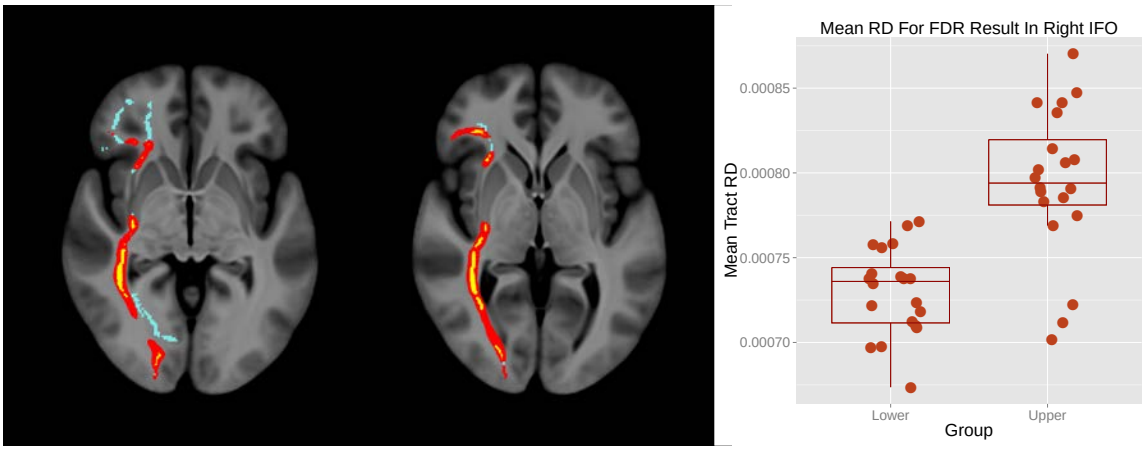

Figure 4.14: Areas containing voxels where RD was significantly greater in the upper third of controls ranked by age than the lower third (yellow and red) in the right IFO tract skeleton (light blue), along with the mean RD across significant voxels for each control grouped by lower and upper third age ranking. Mean RD values for plot did not account for the covariates used in the unpaired two sample t-test (site of data collection, gender, and years of education).

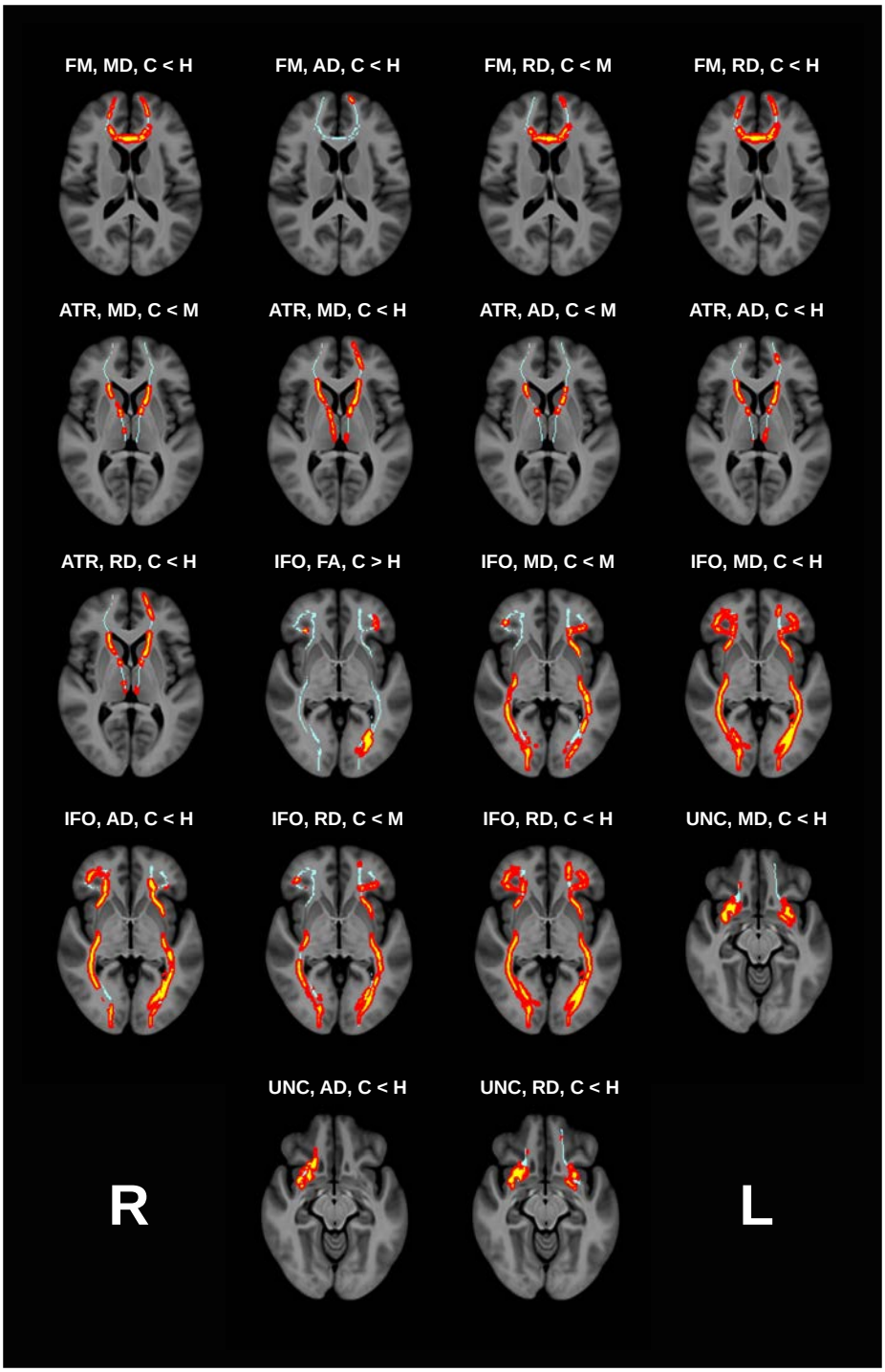

Figure 4.15: Differences in DTI scalars between controls and med/high CAP groups. Highlighted regions (yellow and red) of each tract skeleton overlaid the tract skeleton (light blue) containing voxels with significant differences in DTI scalars between controls (C) and medium (M) and high (H) CAP groups for EMPMS data. These results were acquired with the TFCE method at 50,000 permutations and corrected with FDR at a criterion of $q < 0.05$ and are displayed in radiologic convention.

Table 4.16: Percentages of all tract skeleton voxels that contained significant mean differences in DTI scalars between control (C) and CAP groups (L, M, H) and general locations of these voxels for the EMPMS data.

Tract	DTI Scalar	Contrast	Significant voxels (%)	Regions with significant differences
FM	MD	C < H	73.43	1, 2, 3, 4, 5, 6, 7, 8, 9, 10, 11, 12
	AD	C < H	11.26	6, 8, 12
	RD	C < M	27.73	1, 2, 3, 4, 7, 8, 9, 10, 12
		C < H	70.10	1, 2, 3, 4, 5, 6, 7, 8, 9, 10, 11, 12
LeftATR	MD	C < M	16.83	1, 2, 5
		C < H	67.40	1, 2, 3, 4, 5
	AD	C < M	11.98	1, 2
		C < H	37.45	1, 2, 3, 4, 5
	RD	C < H	49.50	1, 2, 3, 4, 5
LeftIFO	FA	C > H	9.49	2, 3, 6, 7
	MD	C < M	53.60	2, 3, 4, 5, 6, 7, 8
		C < H	76.23	1, 2, 3, 4, 5, 6, 7, 8
	AD	C < H	55.47	1, 2, 3, 4, 5, 6, 7, 8
	RD	C < M	61.88	1, 2, 3, 4, 5, 6, 7, 8
		C < H	79.36	1, 2, 3, 4, 5, 6, 7, 8
LeftUNC	MD	C < H	42.17	1, 2, 3, 4, 5
	RD	C < H	38.10	1, 2, 3, 4, 5
RightATR	MD	C < M	12.97	1, 2, 5
		C < H	39.97	1, 2, 3, 4, 5
	AD	C < M	6.77	1, 2
		C < H	25.30	1, 2, 3, 5
	RD	C < H	27.24	1, 2, 4, 5
RightIFO	FA	C > H	0.05	2
	MD	C < M	35.02	3, 5, 6, 7, 8
		C < H	85.30	1, 2, 3, 4, 5, 6, 7, 8
	AD	C < H	63.20	1, 2, 3, 4, 5, 6, 7, 8
	RD	C < M	29.32	2, 3, 5, 6, 7, 8
		C < H	79.77	1, 2, 3, 4, 5, 6, 7, 8
RightUNC	MD	C < H	63.74	1, 2, 3, 4, 5
	AD	C < H	61.37	1, 2, 3, 4, 5
	RD	C < H	49.48	1, 2, 3, 4, 5

Note: These results were acquired with the TFCE method at 50,000 permutations and corrected with FDR at a criterion of $q < 0.05$.

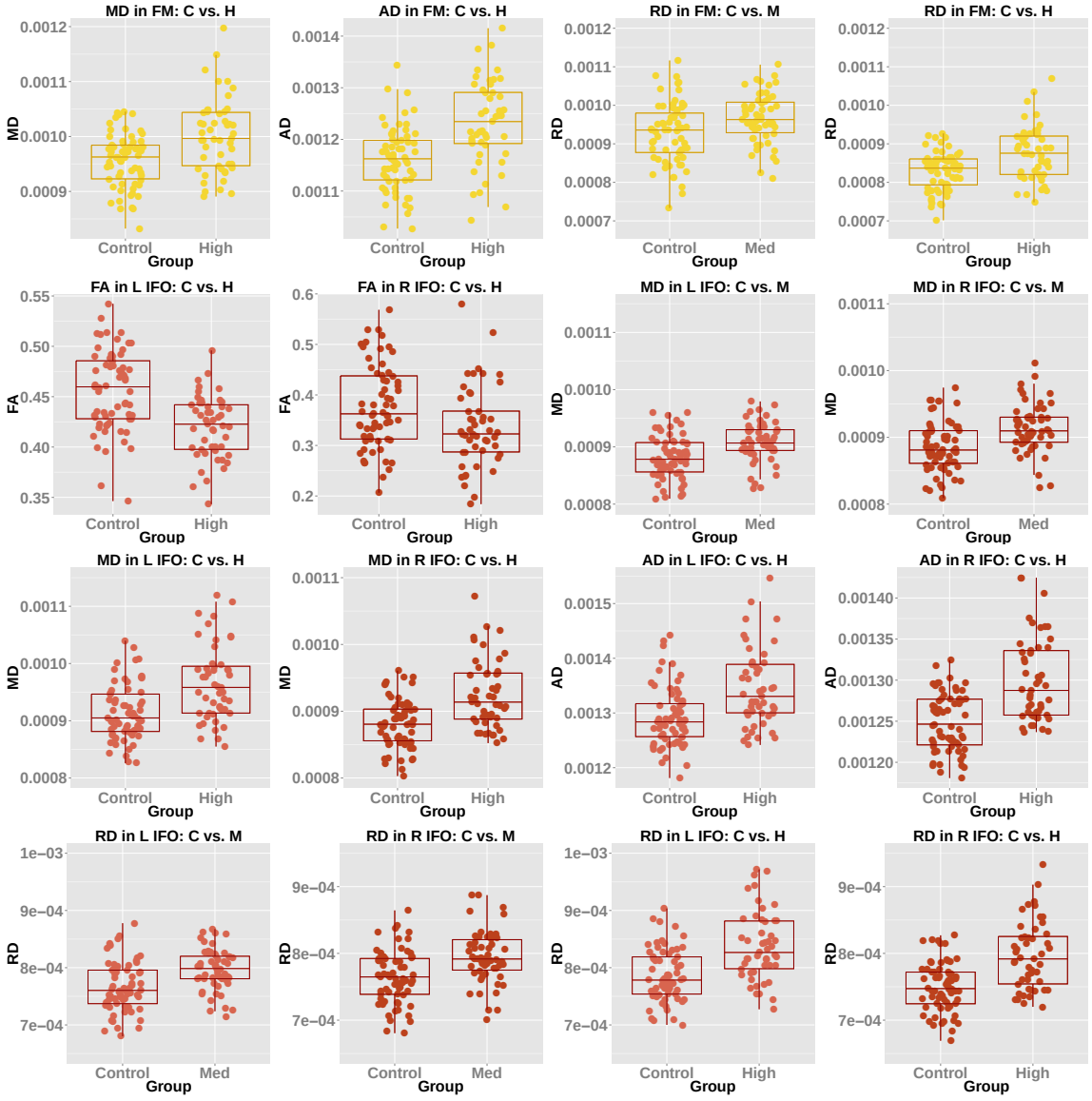

Figure 4.16: Plots of mean DTI scalars across significant voxels for controls versus medium and high CAP group(s) in the FM and left and right IFO for EMPMS data. These results were acquired with the TFCE method at 50,000 permutations and corrected with FDR at a criterion of $q < 0.05$.

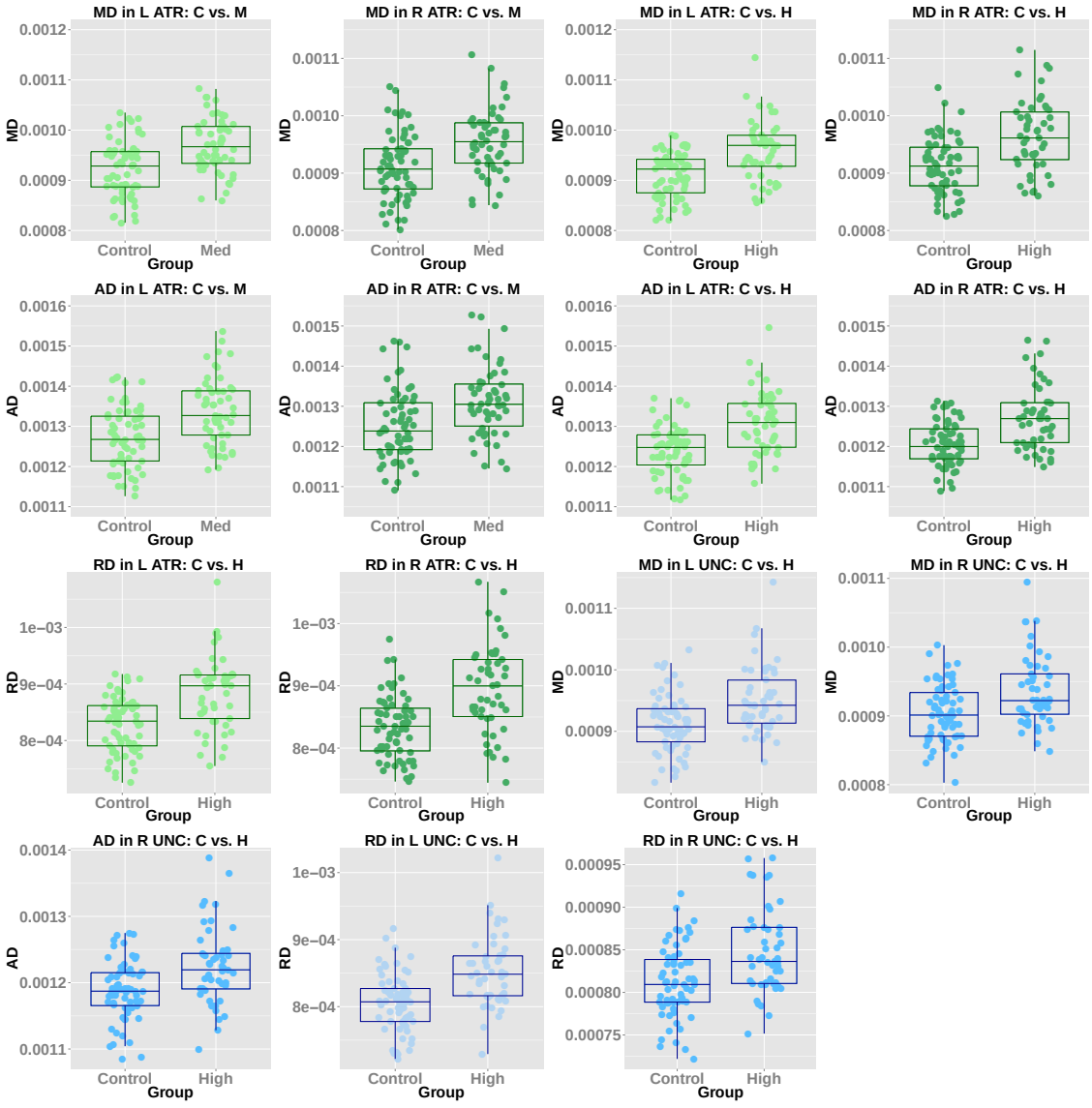

Figure 4.17: Plots of mean DTI scalars across significant voxels for controls versus medium and high CAP group(s) in the left and right ATR and UNC for EMPMS data. These results were acquired with the TFCE method at 50,000 permutations and corrected with FDR at a criterion of $q < 0.05$.

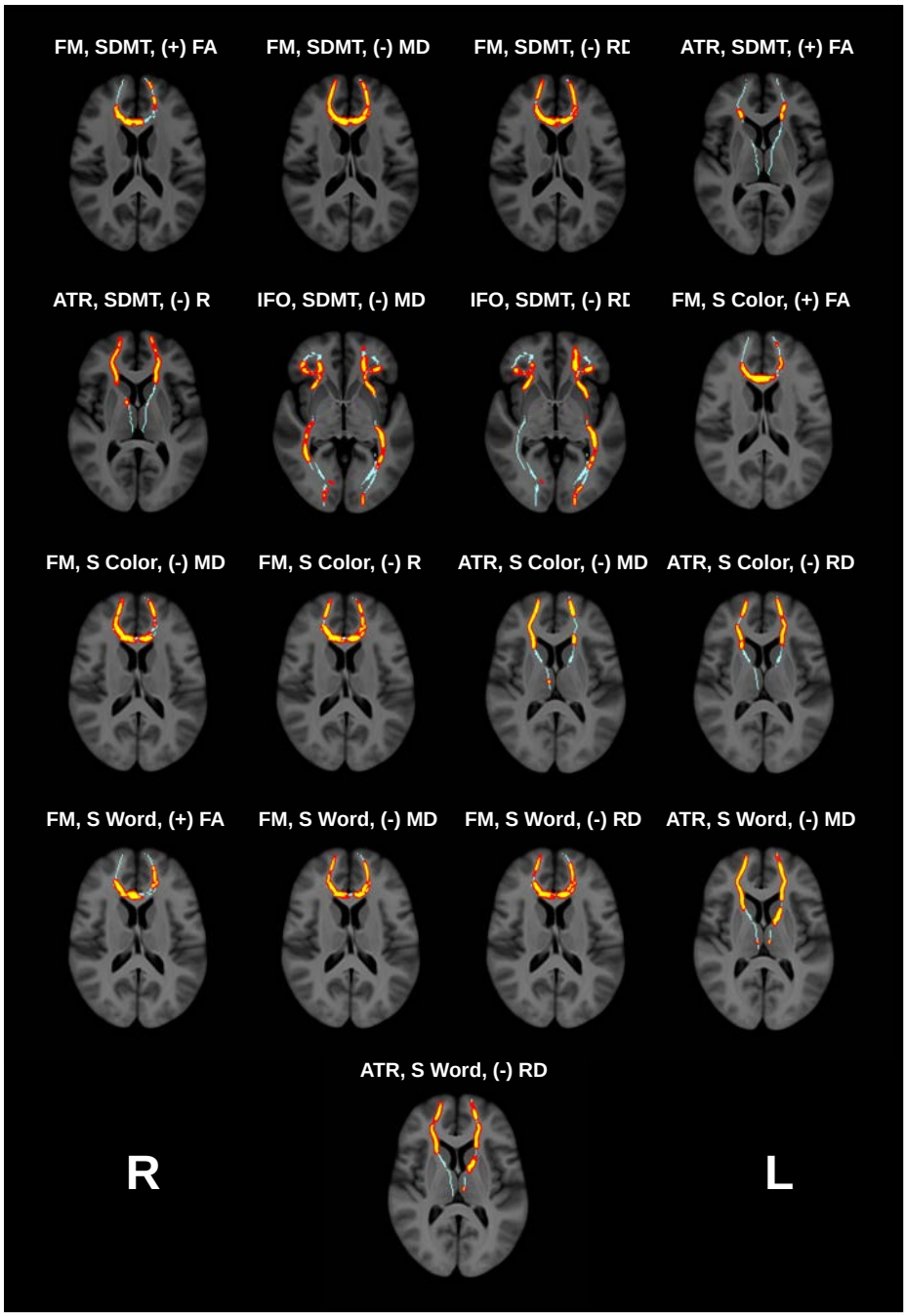

Figure 4.18: Images showing locations of correlations between DTI scalars and cognitive variables, part 1. Highlighted regions (yellow and red) of each tract skeleton overlaid the tract skeleton (light blue) containing voxels with significant positive (+) and negative (-) correlations between DTI scalars and SDMT, Stroop Color (S Color), and Stroop Word (S Word) variables for EMPMS data. These results were acquired with the TFCE method at 50,000 permutations, corrected with FDR at a criterion of $q < 0.05$, and are displayed in radiologic convention.

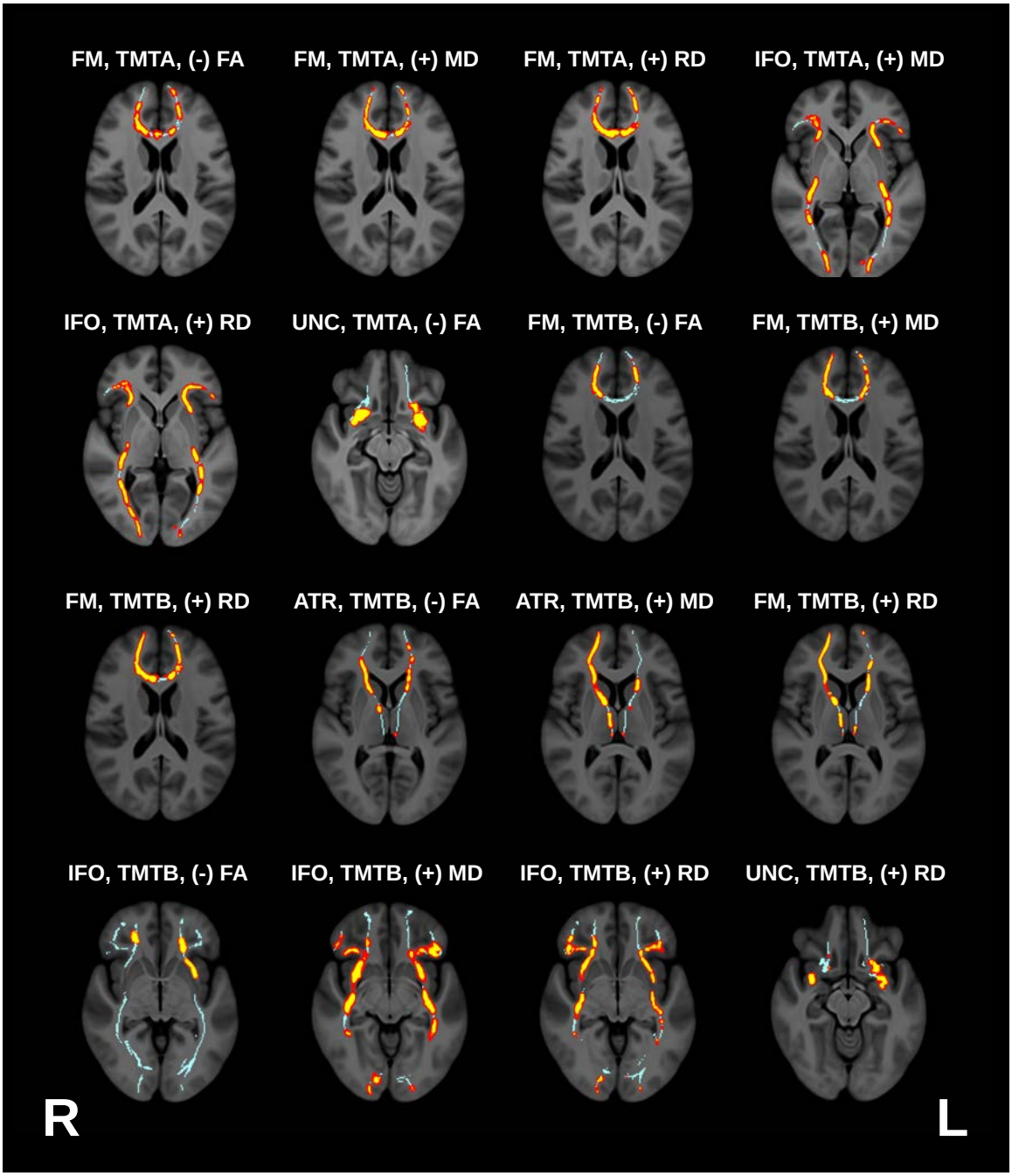

Figure 4.19: Images showing locations of correlations between DTI scalars and cognitive variables, part 2. Highlighted regions (yellow and red) of each tract skeleton overlaid the tract skeleton (light blue) containing voxels with significant positive (+) and negative (-) correlations between DTI scalars and TMTA and TMTB variables for EMPMS data. These results were acquired with the TFCE method at 50,000 permutations, corrected with FDR at a criterion of $q < 0.05$, and are displayed in radiologic convention.

Table 4.17: Percentages of all tract skeleton voxels that contained significant correlations between DTI scalars and SDMT, Stroop Color, Stroop Word, and Stroop Intermediate cognitive variables for prodromal HD participants.

Cognitive variable	DTI scalar	Contrast	Tract	Significant voxels (%)	Regions with significant correlations
SDMT	FA	Positive	FM	44.60	1,2,3,4,7,8,11,12
			LeftATR	17.91	3,4,5
			RightATR	3.95	3
			RightIFO	3.53	8
	MD	Negative	FM	69.06	1,2,3,4,5,6,7,8,9,10,11,12
			LeftIFO	55.20	1,2,3,4,5,6,7,8
			LeftUNC	17.29	1,2,3,4
			RightATR	68.09	1,2,3,4,5
			RightIFO	36.11	2,3,4,5,6,7,8
	RD	Negative	FM	59.94	1,2,3,4,5,6,7,8,9,10,11,12
			LeftATR	51.26	2,3,4,5
			LeftIFO	66.01	1,2,3,4,5,6,7,8
			LeftUNC	16.74	1,2,3,4
			RightATR	54.31	2,3,4,5
			RightIFO	11.96	2,3,4,7,8
S Color	FA	Positive	FM	45.68	1,2,3,4,6,7,8,11,12
			LeftATR	33.73	1,2,4,5
			RightIFO	8.20	2,3,4,8
			RightUNC	4.90	2,3
	MD	Negative	FM	46.32	1,2,3,4,5,6,7,9,10,11,12
			LeftATR	14.06	3,4,5
			RightATR	55.04	1,2,3,4,5
	RD	Negative	FM	55.72	1,2,3,4,5,6,7,8,9,10,11,12
			LeftATR	41.17	3,4,5
			LeftIFO	16.88	2,3,4,5,6,7
			RightATR	38.44	2,3,4
S Word	FA	Positive	FM	39.16	1,2,3,4,6,7,8,11,12
	AD	Negative	RightATR	7.66	4
	MD	Negative	FM	55.67	1,2,3,4,5,6,7,8,9,10,11,12
			LeftATR	51.32	1,2,3,4,5
			LeftIFO	5.90	4,5
			RightATR	59.07	1,2,3,4,5
	RD	Negative	FM	51.53	1,2,3,4,5,6,7,8,9,10,11,12
			LeftATR	50.00	1,2,3,4,5
			RightATR	43.59	2,3,4

Note: These results were acquired with the TFCE method with 50,000 permutations and corrected with FDR at a criterion of $q < 0.05$.

Table 4.18: Percentages of all tract skeleton voxels that contained significant correlations between DTI scalars and TMTA and TMTB cognitive variables for prodromal HD participants.

Cognitive variable	DTI scalar	Contrast	Tract	Significant voxels (%)	Regions with significant correlations
TMTA	FA	Negative	FM	39.93	1,2,3,4,5,7,8,10,11,12
			LeftUNC	17.74	1,2,3
			RightUNC	13.97	2,3
	MD	Positive	FM	50.41	3,4,5,6,7,9,10,11,12
			LeftIFO	51.22	1,2,3,4,5,6,7,8
			LeftUNC	25.61	1,2,3,4
			RightATR	51.73	1,2,3,4
			RightIFO	42.90	2,3,4,5,6,7,8
	RD	Positive	FM	46.85	1,2,3,4,5,7,9,10,11,12
			LeftIFO	50.18	1,2,3,4,5,6,7,8
			LeftUNC	28.42	1,2,3,4,5
			RightATR	41.58	1,2,3,4
			RightIFO	43.65	2,3,4,5,6,7,8
TMTB	FA	Negative	FM	23.21	1,3,5,6,7,11,12
			LeftATR	33.67	1,2,3,4,5
			LeftIFO	6.44	1,2,5
			LeftUNC	18.73	1,2,3,4
			RightATR	33.68	1,2,3,4,5
			RightIFO	6.93	2,4,8
	MD	Positive	FM	41.79	3,5,6,9,10,11,12
			LeftATR	23.77	1,2,4,5
			LeftIFO	44.95	1,2,3,4,5,6,7,8
			LeftUNC	47.60	1,2,3,4,5
			RightATR	75.26	1,2,3,4,5
			RightIFO	52.81	2,3,4,5,6,7,8
	RD	Positive	FM	61.84	1,2,3,4,5,6,7,9,10,11,12
			LeftATR	51.64	1,2,3,4,5
			LeftIFO	40.11	1,2,3,4,5,6,7,8
			LeftUNC	46.97	1,2,3,4,5
			RightATR	79.37	1,2,3,4,5
			RightIFO	45.14	2,3,4,5,6,7,8
			RightUNC	33.28	1,2,3,4,5

Note: These results were acquired with the TFCE method with 50,000 permutations and corrected with FDR at a criterion of $q < 0.05$.

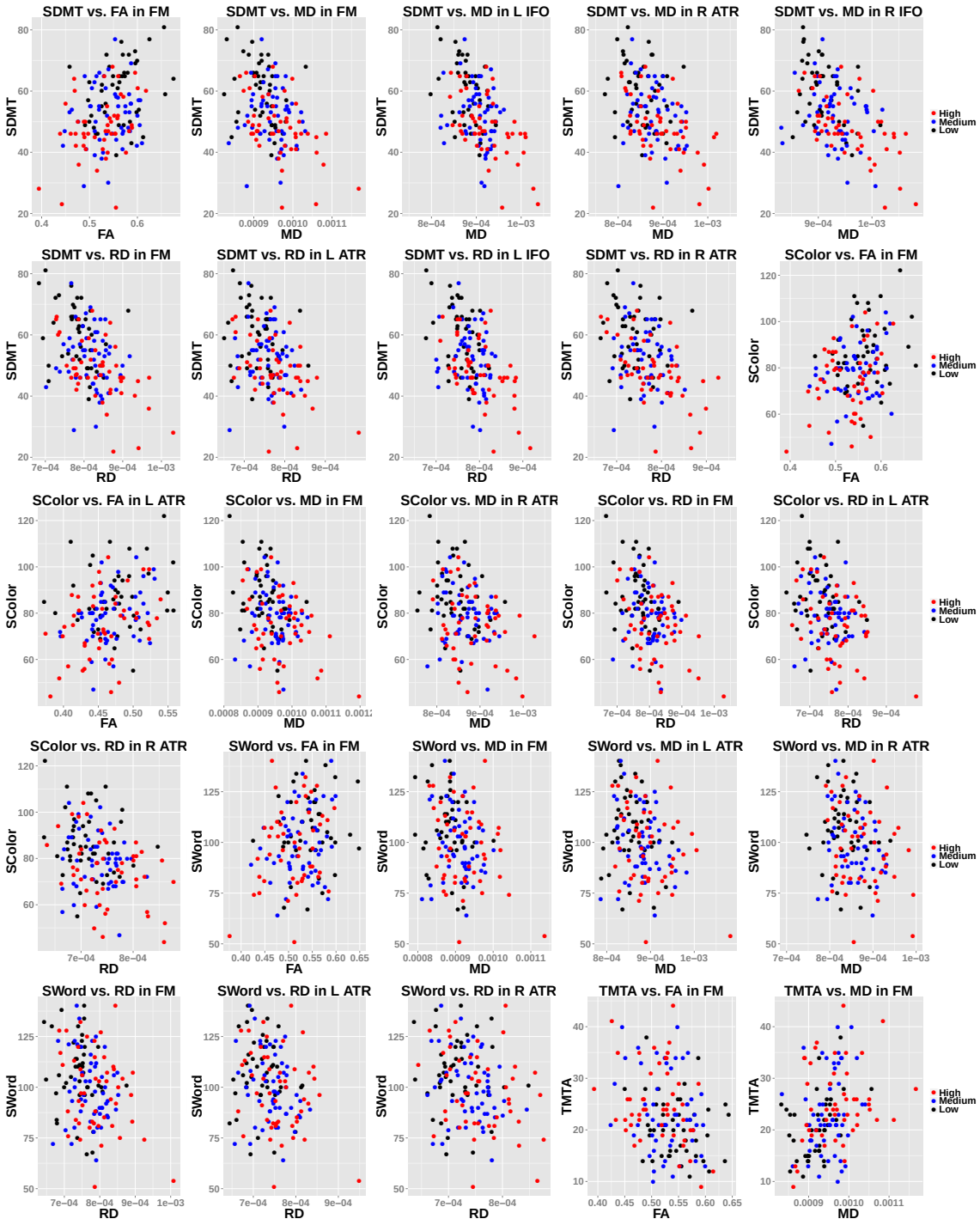

Figure 4.20: Plots of correlations between DTI scalars and cognitive variables, plots part 1. Plots of SDMT, Stroop Color (S Color), Stroop Word (S Word), and Trail Making Test A (TMTA) variables versus mean DTI scalars across clusters that covered more than 20% of a given tract skeleton for EMPMS data. These results were acquired with the TFCE method at 50,000 permutations and corrected with FDR at a criterion of $q < 0.05$.

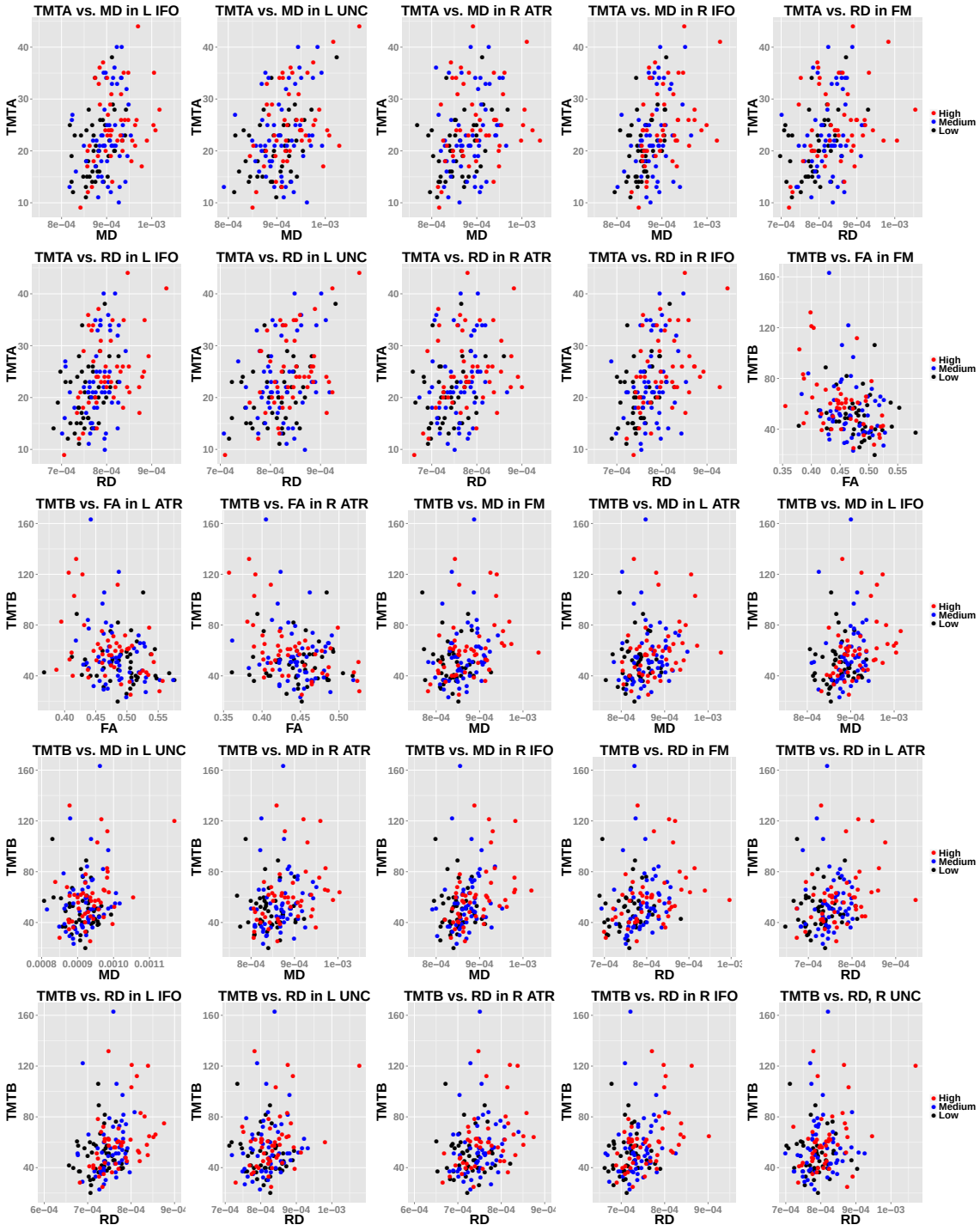

Figure 4.21: Plots of correlations between DTI scalars and cognitive variables, plots part 2. Plots of Trail Making Tests A (TMTA) and B (TMTB) variables versus mean DTI scalars across clusters that covered more than 20% of a given tract skeleton for EMPMS data. These results were acquired with the TFCE method at 50,000 permutations and corrected with FDR at a criterion of $q < 0.05$.

CHAPTER 5
LONGITUDINAL FIBER TRACKING STUDY

5.1 Introduction

The main goal of this study was to build upon past volume, DTI scalar, and cross-sectional fiber tracking studies related to the frontal lobe in prodromal HD by detecting longitudinal changes in major WM (WM) tracts terminating in the PFC over a two year period. One of the longitudinal changes investigated in this study was diffusivity along the WM tracts in the form of DTI scalars. Another type of longitudinal change that was investigated was WM morphology, where WM volume changes were encoded in a stationary velocity field and transported to a template via Schild's ladder. Once in template space, individual subject changes along WM tracts in the form of log Jacobian values were investigated. To demonstrate how changes in a subject across time is parallel transported to a template, two synthetic image experiments were performed before deploying the parallel transport method on real patient data. The purpose of this particular test was to show that changes in synthetic subject data could be transported to a template. The objective behind obtaining diffusivity and morphology changes simultaneously in the same tracts was to better characterize WM pathology in prodromal HD.

5.2 Methods

This section describes two experiments: synthetic images and synthetic warping experiments.

5.2.1 Synthetic images experiment

5.2.1.1 Synthetic images

The two dimensional (2D) image test case described here using circles and ellipses of varying size was modeled after an experiment performed by Lorenzi et al. that compared multiple implementations of parallel transport of stationary velocity fields (SVFs) [185]. All 2D images were 256 x 256 mm in size with 1 x 1 mm pixels. Brain images from an individual subject were represented with circles, where the initial time point, I_0, was a combination of black and white semi-circles whose radii were both 21 mm, evenly surrounded by a gray circle that was 84 mm in diameter. These circle dimensions were selected to create an object that was a third of the total image size and could be centered. To simulate tissue atrophy around a fixed object in the subject's brain across time, three more circle images were created where the volume of the gray circle decreased by 5% and the semi-circle volume increased by 5% (time points I_1 through I_3) relative to the initial time point with each subsequent time increment (Figure 5.1). A template image (which is usually an atlas image that represents the population in question), R_0, was represented with the same black and white semi-circles but with a surrounding gray ellipse. R_0 was similar to I_0, but its gray top and bottom edges were stretched 10% of the total diameter of I_0 to create a gray ellipse and rotated 45 degrees to the right. The template shape was changed to demonstrate that parallel transport can project volume changes in the subject data to a different shape. Given that i is the time index, R_i, where $i > 0$, will refer to R_0 that has been transformed with the parallel transported SVF transformation from I_0

to I_i. Warped template images, R_1 through R_3, were created manually from R_0 by decreasing its gray volume by 5% and increasing its semi-circle volume by 5% with each subsequent time point to serve as verification images while testing the parallel transport algorithm (Figure 5.1). Three-dimensional (3D) versions of the 2D test images were also created in a similar manner.

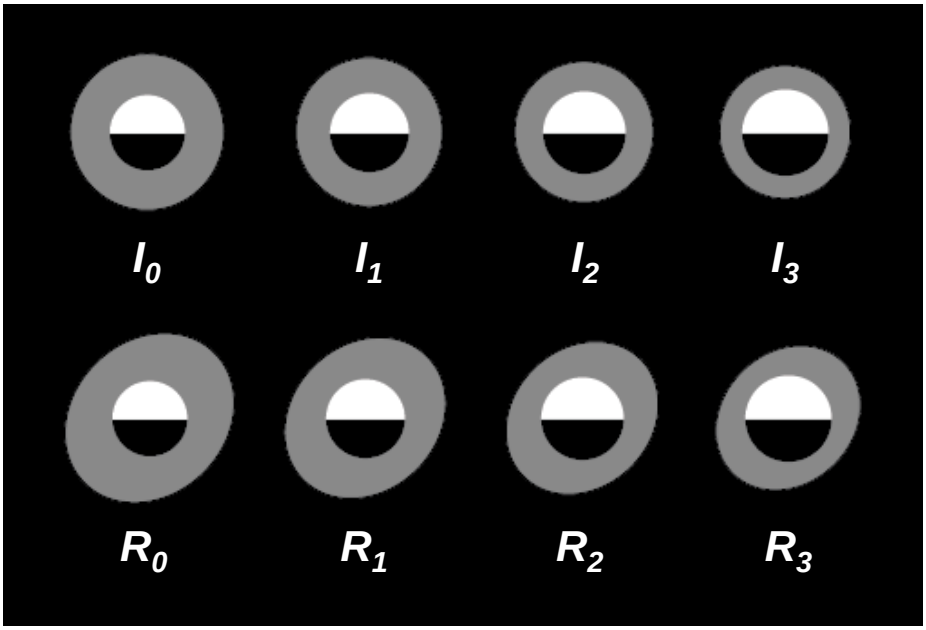

Figure 5.1: 2D synthetic images for Schild's ladder demonstration. 2D circle (synthetic simulated subject data) and ellipse (synthetic simulated template and warped template images) images with decreasing gray portions and increasing black and white semi-circle portions to simulate tissue atrophy around a fixed object.

5.2.1.2 Symmetric demons and parallel transport

Stationary velocity fields (SVFs) from I_0 to I_i (u) and from I_i to R_0 (v) were required for the parallel transport of changes in subject data to template (justification

of the use of SVFs will be explained later in this section). These SVFs were derived with the symmetric log-domain diffeomorphic demons image registration algorithm or symmetric demons [186, 187]. Symmetric demons is a symmetric variant of Thirion's demons algorithm that works in the log-domain to provide an invertible mapping of moving and fixed images in the form of a stationary velocity field [186, 187]. Cachier et al. showed that the demons algorithm can be seen as an optimization of global energy [188]. Vercauteren et al. symmetrized the optimization of global energy by creating a symmetrized cost function for s, the starting spatial transformation or vector field between fixed (F) and moving (M) images [186, 187]:

$$s_{opt} = \underset{x}{\operatorname{argmin}}(E(I_0, I_1, s) + E(I_0, I_1, s^{-1})) \tag{5.1}$$

Since transformations are computed in diffeomorphic space with a Lie group structure, the diffeomorphism s can be computed by taking the exponential of a, the updated velocity field, with the Lie group exponential operator at each iteration.

$$s = exp(a) \tag{5.2}$$

a is in the vector space of the velocity fields and can be updated directly in the Lie algebra by b in the log domain using a second order truncation of the Baker-Campbell-Hausdorff (BCH) formula:

$$BCH(a,b) = log(exp(a) \circ exp(b)) \approx a + b + \frac{1}{2}[a,b] + \frac{1}{12}[a,[a,b]] - \frac{1}{12}[b,[a,b]] \tag{5.3}$$

Thus, to solve the symmetrized cost function, a is created by first computing both forward (b^{forw}, where F is the fixed image and M is the moving image) and backward

(b^{back}, where M is the fixed image and F is the moving image) update vector fields in the log domain with the BCH approximation and averaging them at each iteration:

$$a \leftarrow \frac{1}{2} K_{diff} \star (log(exp(a) \circ exp(K_{fluid} \star b^{forw})) - log(exp(-a) \circ exp(K_{fluid} \star b^{back}))) \quad (5.4)$$

Update vector fields themselves are computed by minimizing the global energy between F and M, given current s [189]. Demons regularization is done by applying a Gaussian convolution kernel to the update velocity fields before their exponentials are composed with the current updated velocity field exponential [186, 187].

The Schild's ladder construction is on a path defined by the Lie group exponential of vectors. The SVF is an approximation of a small step of a time-varying velocity field diffeomorphism or a set of vectors. Parallel transport can be used to move these vectors through a geodesic on a manifold from one space to another and preserve their original orientation once in the new space. The path between the initial, I_0, and subsequent time point, I_i, was defined with SVF u, while the path between the initial time point and the template, R_0 (T_0 in Figure 5.2), was defined with SVF v.

The symmetry of the Schild's ladder construction allowed u to be diagonally transported along the curve parameterized by v via composition to estimate $\Pi^v(u)$ (Figure 5.2). $Exp(\Pi^v u)$ can be computed with the composition of the exponential of the SVF from R_0 to the half image between subject time points (or $Exp(-v/2)$ given parameterization by v) and the exponential of the SVF from the half image to R_0 warped by $Exp(\Pi^v u)$ (or ρ). However, estimation of the half step image in the Schild's ladder construction was bypassed to avoid introducing bias to the construction and

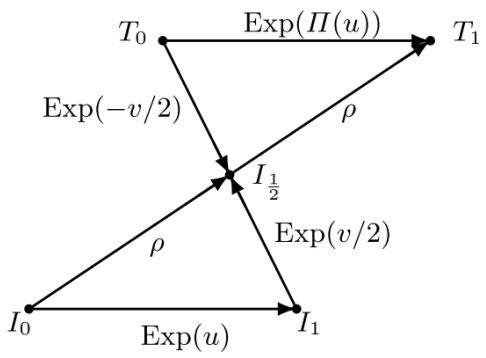

Figure 5.2: Schild's Ladder parallelogram.

Source: M. Lorenzi, N. Ayache, X. Pennec, and Alzheimers Disease Neuroimaging Ini- tiative, Schilds ladder for the parallel transport of deformations in time series of images, *Information Processing in Medical Imaging*, vol. 22, pp. 463-74, 2011.

ρ was instead represented by the composition of $Exp(u)$ and $Exp(v/2)$ [190], leading to:

$$Exp(\Pi(u)) = \rho \circ Exp(-v/2) = Exp(v/2) \circ Exp(u) \circ Exp(-v/2) \tag{5.5}$$

In this study, a custom tool was developed to implement the parallel transport of u (Eq. 5.7) given SVFs u and v and a template image. The custom tool utilized the itkVelocityFieldLieBracketFilter class [191]. Instead of directly computing the compositions, the transport was evaluated directly in the Lie algebra using the BCH formula truncated at the second order (like Eq. 5.3) [190]. The compositions of the exponentials to produce the transport $\Pi^v(u)$ is expressed using the BCH formula as:

$$\Pi^v(u) = BCH(v, BCH(u, -v)) \tag{5.6}$$

and simplifies to:

$$\Pi^v(u) = u + [v, u] + \frac{1}{2}[v, [v, u]] \tag{5.7}$$

5.2.1.3 SVF estimation and parallel transport

Optimal parameters for estimating SVFs for the 2D synthetic image experiment were investigated. images. The main goal of parameter exploration was to ensure the creation of smooth mappings between images in a time series and the template by minimizing sudden, drastic changes in velocity between neighboring voxels to allow image deformation but prevent image folding. Smooth mappings between time series and template images will also allow the creation of a smoother transported SVF via the BCH formula so image information between time points is not lost during transport. The following parameters were held constant for deriving the transformations u and v between the 2D and 3D synthetic images (described in Section 5.2.1) with symmetric demons: number of iterations at each pyramid level of multi-scale registration (three levels at 500, 400, and 300 iterations), SVF update rule (symmetric log-domain), gradient used for computing the demons force (symmetrized), and use of histogram matching. The following parameters for the symmetric log-demons registration algorithm were varied to optimize intensity-based correspondence and SVF parallel transport: smoothing sigma for the velocity field (velSig), smoothing sigma for the update field (upSig), maximum length of an update vector (maxStep), and order of truncation of the Baker-Campbell Hausdorff (BCH) expansion (bch) used to compose the existing and update fields. A base set of values recommended by Lorenzi et al. [190] was used when varying each parameter: velSig = 2.0 mm, upSig = 1.0 mm, maxStep = 1.0 mm, and bch = 2. Since there was a range of parameters that produced good intensity-based correspondence between moving and fixed images, the

effect of changing parameters is most evident when looking at vector fields created from the vector components stored in each voxel of the SVFs. Therefore, at each voxel in an SVF, vectors created by multiplying the stored x- and y-components by the unit vectors of the x- and y-axes were summed to create a new vector for visualization in ParaView (http://www.paraview.org/Wiki/ParaView). A summary of all parameters explored is shown in Table 5.1.

Table 5.1: Summary of parameters explored to optimize registrations between synthetic test images using the symmetric demons registration tool.

Parameter (abbreviation)	Values
Velocity field smoothing sigma (velSig)	0.0 - 4.0 mm
Update field smoothing sigma (upSig)	0.0 - 4.0 mm
Update vector maximum length (maxStep)	0.0 - 5.0 mm
BCH expansion truncation order (bch)	2 - 4

5.2.2 Synthetic warping experiment

5.2.2.1 Imaging data

Twenty-three healthy control participants who were scanned approximately two years apart at the same site were selected for a synthetic warping experiment. A summary of participant characteristics are listed in Table 5.2. Only T1-weighted images from three Siemens PREDICT-HD sites were used for T1 atlas construction and SVF derivation since WM tracts were not needed for this synthetic image experiment. A description of imaging parameters for each site can be found in Table 4.7,

Section 4.2.1.4.

Table 5.2: Summary of demographic and clinical data for healthy control participants used in synthetic warping experiment, including number of participants from each of the three Siemens scanner sites.

	Time Point 1 (Mean; SD (N))	Time Point 2 (Mean; SD (N))
Age (years)	45.3; 10.7 (23)	47.3; 10.7 (23)
Educ (years)	15.4; 2.1 (23)	15.4; 2.1 (23)
Gender	7M/16F (23)	7M/16F (23)
Motor	4.9; 3.3 (23)	2.8; 3.4 (23)
SDMT	54.2; 8.3 (23)	57.1; 9.1 (23)
S Color	84.7; 12.9 (23)	87.4; 15.4 (23)
S Word	104.7; 15.2 (23)	109.0; 16.8 (23)
S Interference	48.0; 9.8 (23)	48.9; 7.8 (23)
TMTA	23.9; 9.3 (23)	20.4; 4.7 (23)
TMTB	55.8; 26.0 (23)	51.0; 22.6 (23)
Site 024	(16)	(16)
Site 027	(1)	(1)
Site 120	(6)	(6)

Note: Educ = Education. Motor = Sum of all items of the UHDRS Motor Assessment scale. SDMT = Symbol Digit Modalities Test. S = Stroop. TMTA = Trail Making Test A. TMTB = Trail Making Test B.

5.2.2.2 Image pre-processing and atlas building

Structural image and DWI pre-processing and unbiased T1-weighted atlas construction followed the methods described in Sections 4.2.2 and 4.2.3, respectively. T1-weighted atlas construction here was slightly different than Section 4.2.3 as there were two T1 images (first and second time points) for each subject, both of which were weighted equally.

5.2.2.3 Synthetic warping tool

The overall purpose of creating images with artificially dilated tissue is to see if the parallel transport tool developed in this study is able to detect known image changes. Thus, a tool was developed to create synthetic SVFs that would dilate tissue in the shape of a sphere around a fiducial. The custom tool also converted the synthetic SVF into a deformation field and applied the deformation to an input image. Creation of a synthetic SVF began with a sphere shell of a user-defined radius whose border values reflected the magnitude of desired tissue dilation around an input fiducial. The sphere shell values were smoothed with a Gaussian filter that was the size of the user-defined radius. The non-zero voxels in the sphere shell were then used to compute vectors to the fiducial relative to a given voxel. The computed vector components were then weighted by values of the Gaussian-smoothed sphere shell image and assigned to an image with vector type voxels that was the same size as the sphere shell image. This vector image served as the synthetic SVF that applied artificial tissue dilations to an image around a fiducial.

For each of the 23 healthy control participants (described in Section 5.2.2), a fiducial was placed in the left lateral ventricle anterior to the caudate in the T1-weighted image acquired during the second scanning session. The fiducial and T1-weighted image were then given to the synthetic SVF tool to create a T1-weighted image whose left lateral ventricle was dilated into the surrounding WM and left caudate. This area of the brain was dilated in order to simulate ventricle enlargement and caudate atrophy seen in HD and possible WM atrophy that may be occurring in

prodromal HD.

5.2.2.4 SVF estimation and parallel transport

Before acquiring the SVFs needed for parallel transport, a short parameter exploration for warping T1 images with symmetric demons was performed. Since the symmetric demons registration tool began to show instability at higher orders of BCH approximation in the synthetic images experiment, only the second order (bch = 2) was explored with T1 images. The following parameters were held constant for deriving a SVF between a T1 image that had been rigidly aligned to a T1 template and the T1 template: number of iterations at each pyramid level of multi-scale registration (three levels at 1,000, 1,000, and 200 iterations), SVF update rule (symmetric log-domain), gradient used for computing the demons force (symmetrized), and use of histogram matching. velSig, upSig, and maxStep were explored (Table 5.3) while monitoring for mean-squared error between moving and fixed images (MSE) and minimum Jacobian determinant values below 0.1.

Table 5.3: Summary of parameters explored to optimize registrations between T1 image and template using the symmetric demons registration tool.

Parameter (abbreviation)	Values
Velocity field smoothing sigma (velSig)	0.75 - 2.00 mm
Update field smoothing sigma (upSig)	0.50 - 1.00 mm
Update vector maximum length (maxStep)	0.20 - 2.00 mm
BCH expansion truncation order (bch)	2

T1 images from both time points were first rigidly aligned to the T1 atlas (R_0) created from the 23 healthy control participants. SVFs (u and v) between time point one (I_0) and unaltered time point two (I_1), time point one (I_0) and artificially dilated time point two (I_1), and time point two (I_1) to T1 atlas (R_0) for each healthy control participant were derived via symmetric demons and transported to the healthy control T1 atlas (R_0) (methods described in Section 5.2.1.2. Once in atlas space, the transported SVF ($\Pi^v(u)$) was converted to a deformation field, which was used to compute a log Jacobian map with the ANTSJacobian tool [155]. Log Jacobian values were computed by taking the logarithm of the determinant of the Jacobian matrix (partial derivatives of the vector components with respect to each image axis) at each voxel. Log Jacobian values close to zero indicated little volume change, while negative values indicated volume decrease and positive values indicated volume increase. Mean log Jacobian values derived from unaltered healthy control images and dilated healthy control images were compared in randomise with age, years of education, gender, site of data acquisition, and time between scans as covariates using randomise (these p-value maps were corrected for multiple comparisons using FSL's FDR tool with a criterion of $q < 0.05$ [192]). Mean log Jacobian values derived from the dilated healthy control images were tested to see if they were greater and less than zero with one-sample t-tests using randomise [180, 193] (these p-value maps were corrected for multiple comparisons using FSL's FDR tool with a criterion of $q < 0.01$ [192]). All statistical tests in randomise were performed using methods previously described (Section 4.2.9.2): TFCE method, a hand-drawn mask covering the area containing

the artificial dilations, and 10,000 permutations [177].

5.2.3 Longitudinal prodromal HD data analysis

5.2.3.1 Imaging and clinical data

Data from healthy control and prodromal HD participants have been analyzed longitudinally to investigate diffusivity along WM tracts in the form of DTI scalars and WM morphology along WM tracts in the form of log Jacobian values. Forty-two healthy control and seventy-four prodromal HD participants who were scanned twice approximately two years apart were selected for longitudinal data analysis. The prodromal CAG-expanded participants were divided into three groups based on their CAG-Age Product or CAP designation: low ($n = 19$; CAP < 287.16), medium ($n = 26$; $287.16 <$ CAP < 367.12), and high ($n = 29$; CAP > 367.12) [116]. A summary of participant characteristics for the first and second time points are listed in Table 5.4. T1-weighted, T2-weighted, and DWI scans were collected for each participant from one of 12 PREDICT-HD sites, where both time points were acquired at the same site. Imaging data was used to create T1 and DTI atlases along with major fiber tracts terminating in the PFC. Scan information can be found in Section 4.2.1.4 in Tables 4.6 (DWI), 4.7 (T1), and 4.8 (T2).

5.2.3.2 Pre-processing, atlas building, fiber tracking

Multiple steps were involved in the longitudinal prodromal HD data analysis including structural image and DWI pre-processing, T1 and DTI atlas construction, whole brain tractography, fiber tract selection (FM, left and right ATR, left and right

IFO, left and right UNC), and scalar image projection to fiber tract skeletons were created using the methods described in Sections 4.2.2, 4.2.3, 4.2.5, 4.2.6, and A.1, respectively. T1 and DTI atlas methods were slightly different than those in Section 4.2.5 as there were two T1 images (first and second time points) for each subject, both of which were weighted equally. In addition to FA, MD, AD, and RD values, log Jacobian values were projected to tract skeletons and analyzed to examine fiber tract WM morphology.

5.2.3.3 Longitudinal change in DTI scalars

5.2.3.3.1 Mean rate of change among groups

The mean rate of change in DTI scalars (FA, MD, AD, and RD) over two years in controls were compared to the mean rate of change for each CAP group (control versus low, control versus medium, and control versus high) and current group versus all groups with higher disease burden (controls versus low, medium, and high; low versus medium and high; medium versus high) in each tract skeleton (FM, left and right ATR, and left and right UNC). It was hypothesized that FA would decrease faster and MD, AD, and RD would increase faster with greater disease burden than controls. randomise, introduced in Section 4.2.9.2, compared the mean rates of change with a linear mixed effects model using the TFCE method and 50,000 permutations [176, 173, 177]. Details on how the GLM for the linear mixed effects model was implemented in randomise can be found in Section B.1. Correction for multiple comparisons was done on the randomise p-value map outputs with the FDR

tool available in FSL with a criterion of $q < 0.05$ [121, 192].

5.2.3.3.2 Correlations: change in DTI scalars, cognitive variables

randomise was also used to determine partial Pearson correlations between change in DTI scalars (FA, MD, AD, and RD) and change in the following cognitive variables for prodromal HD participants only: SDMT, Stroop Word, Stroop Color, Stroop Inference, TMTA, and TMTB. For each statistical inference, the TFCE method, tract skeleton masks, and 50,000 permutations were used. Instead of inputs from each time point, difference images of the skeletonised DTI scalar images and change in cognitive variables between the first and second time points were computed for analysis with the difference in cognitive variables between first and second time points. GLM setup for randomise was identical to methods described in Section A.3. It was hypothesized that DTI scalars that increase with disease burden would positively correlate with changes in cognitive variables that also increase with disease burden and vice versa. Thus, it was hypothesized that MD, AD, and RD would increase with TMTA and TMTB time and decrease with SDMT and Stroop scores, while FA would increase with SDMT and Stroop score and decrease with TMTA and TMTB times. Correction for multiple comparisons was done on the randomise p-value map outputs with the FDR tool available in FSL with a criterion of $q < 0.05$ [121, 192].

5.2.3.4 Log Jacobian analysis on prodromal HD data

T1 images from both time points (I_0 and I_1) were first rigidly aligned to the T1 atlas (R_0) created from the 42 healthy control and 74 prodromal HD participants. SVFs mapping the T1 image from time point one to two (u) and time point two to the T1 atlas (v) were derived using the symmetric demons registration tool with the following parameters: velSig = 1.1 mm, upSig = 1.1 mm, bch = 2, maxStep = 0.5 mmm, three levels of multi-scale registration (400, 300, 300), symmetric log-domain SVF update rule, symmetrised gradient for computing the demons force, and histogram matching. SVFs mapping the change between time points were then transported to the T1 atlas and converted to a deformation field as described in Section 5.2.1.2. Log Jacobian maps were computed from the deformation fields [155] and projected to tract skeletons using methods described in Section 4.2.8. Mean log Jacobian values in each tract were compared between controls and each CAP group and each group to all other groups with greater disease burden using randomise with mean age, years of education, gender, site of data acquisition, and time between scans as covariates. Mean log Jacobian values in tract skeletons were also correlated with the change in cognitive variables. All statistical tests in randomise were performed using methods previously described (Sections 4.2.9.2 and 5.2.3.3.2): TFCE method, tract skeleton masks, and 10,000 permutations [180, 193, 177]. P-value maps resulting from all t-tests were corrected for multiple comparisons using FSL's FDR tool with a criterion of $q < 0.05$ [192].

5.3 Results

5.3.1 Synthetic images experiment

Synthetic 2D circle and ellipse images successfully demonstrated that the parallel transport tool developed here can translate scale and shape changes in a time series of images to a template image. Nearly identical results were achieved with the synthetic 3D circle and ellipse images. The main goal of parameter selection is to ensure the creation of smooth mappings between images in a time series and the template by minimizing sudden, drastic changes in velocity between neighboring voxels to allow image deformation but prevent image folding. Smooth mappings between time series and template images will also allow the creation of a smoother transported SVF via the BCH formula so image information between time points is not lost during transport. The parallel transport tool was able to transport shape and volume changes from 5 to 15% of the original image to the template. The 15% volume change case was the most challenging deformation with the most obvious visible differences (and thus will be discussed here). Figure 5.3 shows the ideal parallel transport of changes over time using images I_0, I_3, R_0, and R_3: 15% volume decrease of the gray circle is transported into the template gray ellipse and the 15% volume increase of the solid white and black semi-circles into the template solid white and black semi-circles. Deformed images and SVF visualizations used to discuss velSig, upSig, and maxStep will be limited to the mapping between I_3 and R_0 (or SVF v) since this mapping was affected more by parameters than the I_0 to I_3 (or SVF u) mapping. SVF u will be used to illustrate effects of the bch parameter.

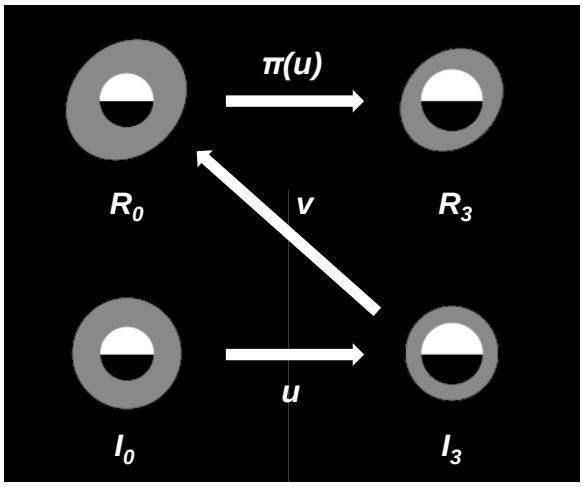

Figure 5.3: Overall scheme of parallel transport using ideal target 2D circles (I_0 and I_3) and ellipses (R_0 and R_3).

Out of the four symmetric demons parameters that were explored (velSig, upSig, maxStep, and bch), velSig was among the parameters that most drastically impacted the success of parallel transport, which is measured by the degree of correspondence between the warped template image and the target warped template image (Figure 5.4). When velSig is set to 0 mm, smoothing the update velocity field alone was not adequate for creating a smooth final mapping between I_3 and R_0, which in turn adversely affected the transported SVF. velSig needed to be greater than 0 mm to allow higher velocity vector components to exist in the final mapping and provide enough smoothing. When velSig was increased to 3.0 mm, higher velocity vector components were being removed, thus preventing the solid semi-circles from shrinking in the I_3 to R_0 mapping and expanding enough in the transported SVF. However, at higher values of velSig, preservation of the gray ellipse in the transported SVF was improved. Deformations also only seemed to succeed when velSig was greater than

upSig if velSig was less than 2.0 mm. Once velSig reached 2.0 mm, upSig did not seem to an effect until it was greater than velSig. When upSig was increased to 4.0 mm, it actually improved gray ellipse shape in the transported SVF while expanding the solid semi-circle area accurately (Figure 5.5).

maxStep was another parameter that drastically affected the outcome of the transported SVF. The size differences between target and source images ranged approximately from 2-6 mm in distance. Therefore, a maxStep size of 0.3 mm was not adequate to produce a successful mapping that encoded the necessary size changes (Figure 5.6). maxStep became unstable at higher values, such as 5.0 mm, and adversely affected the formation of the transported SVF.

Higher intensity-based correspondence was not achieved with higher orders of BCH expansion truncation. SVFs derived with the base testing parameters and bch values of 3 and 4 provided very poor mappings especially for SVF u (Figure 5.7). In order to achieve reasonable mappings, more smoothing is required. Increasing upSig to 4.0 mm while holding the other parameters steady (velSig = 2.0 mm, maxStep = 1.0 mm, bch = 3) produced results similar to those seen with the exact parameters when bch was equal to 2 (not shown).

Figures 5.8 through 5.10 show the final results of the 2D synthetic image experiment using the following parameters: velSig = 2.0 mm, upSig = 4.0 mm, maxStep = 1.0 mm, and bch = 2.

5.3.2 Synthetic warping experiment

Synthetic warping experiment is explained in this section.

5.3.2.1 Atlas building

Figure 5.11 displays the T1-weighted template constructed from data described in Section 5.2.2 and whose space was used for the synthetic warping experiment.

5.3.2.2 Parameter exploration

Based on the short parameter exploration for symmetric demons on T1 images, the following parameters were chosen: velSig = 1.1 mm, upSig = 1.1 mm, and maxStep = 0.5 mm. velSig had to be increased from 0.75 mm in order to prevent negative Jacobian values from appearing in the transformation, but lower than 2.0 mm to preserve correspondence between moving and fixed images. maxStep had to be kept below 1.0 mm to ensure minimum Jacobian values remained in a safe range or above 0.1. As seen in the synthetic images experiment (Section 5.3.1), upSig did not make a large impact on the minimum Jacobian value or moving and fixed image correspondence.

5.3.2.3 Synthetic warping

Figure 5.12 displays a single healthy control participant's T1-weighted image before and after the application of the synthethic SVF. In the middle panel of Figure 5.12, the magnitudes of the vectors responsible for the artificial dilation of the left ventricle are centered around the manually-placed fiducial.

For illustrative purposes, all SVFs encoding the deformation from the first time point to the artificially dilated second time point that were transported to the T1 template were averaged and applied to the T1 template. Figure 5.13 displays the original T1 template, average transported SVF, and T1 template after the application of the average transported SVF. In the warped T1 template, the left ventricle is dilated laterally and the caudate volume has decreased in the same area that contains higher vector magnitudes in the averaged SVF image.

The unpaired t-test showed many voxels with mean log Jacobian values that were significantly less in SVFs derived from the artificial dilations in comparison to the unaltered images in the area where the artificial dilations were placed. In addition, the one-sample t-test showed that WM surrounding the left ventricle contained voxels whose log Jacobian values were significantly less than zero, supporting the fact that the artificial dilations have been transported to the template (Figure 5.14).

5.3.3 Longitudinal prodromal HD analysis

5.3.3.1 Atlas building and fiber tracking

The longitudinal analysis has been conducted on the following T1-weighted and DTI atlases. Figure 5.11 displays the T1-weighted template constructed from data described in Section 5.2.2 and whose space was used for the synthetic warping experiment. Figure 5.15 displayed the T1-weighted and DTI templates constructed form data described in Section 5.2.3 and whose space was used for longitudinal analyses.

Figure 5.16 shows several views of the fiber tracts (FM, left and right ATR, left and right IFO, and left and right UNC) derived from whole brain tractogram of the DTI atlas overlaid on the T1-weighted template for the data described in Section 5.2.3. Different tracts are highlighted with different colors: left UNC (light blue), right UNC (dark blue), FM (yellow), left IFO (light red), right IFO (dark red), left ATR (light green), and right ATR (dark green).

5.3.3.2 Longitudinal change in DTI scalars

5.3.3.2.1 Mean rate of change among groups

Regions with significant differences in DTI scalar mean rate of change listed in Table 5.5 are the same regions defined in Section 4.3.6 in Figures 4.10 through 4.13. When comparing the high CAP group's mean rate of change to those of other groups, the high CAP group always had the highest mean rate of change or played a role in increasing the mean rate of change. No findings were detected for FA. The significant findings in the IFO were generally posterior to the frontal lobe areas except for those with MD and AD. Specifically, the left and right IFOs both had faster mean increases in MD, AD, and RD in the high CAP group in comparison to controls. Mean rates of MD and RD increases in the medium CAP group were also less than the high CAP group's rate in both the left and right IFOs. Significantly faster mean rates of change in all CAP groups (mean of low, medium, and high CAP) versus controls were seen only in the right IFO for MD and AD. The FM had a faster mean increase in MD for the high CAP group than the medium CAP group throughout the structure. The

right UNC had faster mean increases in MD and RD for the high CAP group than the medium CAP group in the area that connects the frontal and temporal lobes. The left ATR was the only tract that seemed to exhibit a full progression of greater mean rates of AD increase due to greater disease burden with significant findings in low versus medium and high CAP groups, medium versus high CAP group, and controls versus high CAP group. However, the only significant mean rate of change difference for AD whose voxel percentage was above 10% was controls versus high CAP group (with medium versus high CAP group for MD) (Figure 5.17).

5.3.3.2.2 Correlations: change in DTI scalars, cognitive variables

Correlations between change in both DTI scalars and cognitive variables were investigated to support findings that suggest changes in DTI scalars are a reflection disease burden. Regions with significant correlations between change in both DTI scalars and cognitive variables listed in Table 5.6 are the same regions defined in Section 4.3.6 in Figures 4.10 through 4.13. Significant correlations between change in both DTI scalars and cognitive variables were again restricted to the scalars MD, AD, and RD. Increases in TMTB time seemed to correlate with increases in DTI scalars most commonly. Positive correlations between increase in TMTB time and increase in MD, AD, and RD were seen throughout the FM and left and right ATRs. In addition, MD and RD increased with TMTB time throughout the right IFO. The second most common significant correlation was with decrease in Stroop Word score. Decreases in Stroop Word score negatively correlated with increases in MD and RD

throughout the FM and left and right ATRs, and to a lesser degree for increases in AD in the FM. Decreases in Stroop Interference score negatively correlated with increases in MD and RD in the left ATR and increases in AD in the right UNC. Increases in TMTA time positvely correlated with increases in MD, AD, and RD in the right ATR (Figure 5.18).

5.3.3.3 Log Jacobian analysis on prodromal HD data

Log Jacobian values in the left ATR for the high CAP group were less than those in the medium CAP group in the area medial to the left rostral middle frontal WM and lateral to the left superior frontal WM. As for correlations with log Jacobian values and cognitive values, there was a significant negative correlation with change in TMTB values in the left ATR and a positive correlation with change in Stroop Color values in the right UNC.

5.4 Discussion

The main goal of this study was to build upon past volume, DTI scalar, and cross-sectional fiber tracking studies related to the frontal lobe in prodromal HD by detecting longitudinal changes in major WM tracts terminating in the PFC over a two year period. One of the longitudinal changes investigated in this study was diffusivity along the WM tracts in the form of DTI scalars. Another type of longitudinal change that was investigated was WM morphology in the form of log Jacobian values along the WM tracts. The objective behind obtaining diffusivity and morphology changes simultaneously in the same tracts was to better characterize WM pathology

in prodromal HD. For the DTI scalar analysis, an unbiased DTI atlas was built using non-linear tranformations derived from T1-weighted images and were used to create four major WM tracts terminating in the PFC: FM, left and right ATR, left and right IFO, and left and right UNC. Tract skeletons were derived for each tract and FA, MD, AD, and RD values were projected to each tract skeleton. The IFOs both had faster mean increases in MD, AD, and RD in the high CAP group in comparison to controls and faster mean increases in MD and RD in the high CAP group than the medium. The FM had a faster mean increase in MD for the high CAP group than the medium, while the right UNC had faster mean increases in MD and RD for the high CAP group in comparison to the medium. As for the left ATR, AD increased faster in the high CAP group versus controls and MD increased faster in the high CAP group versus the medium. As for changes in DTI scalars tracking with changes in cognitive variables, significant changes were restricted to MD, AD, and RD for Stroop Interference, Stroop Word, TMTA, and TMTB. Increases in TMTB time was the most common significant correlation, with findings in the FM, ATRs, and right IFO. Decreases in Stroop Word score was the second most common significant correlation, with findings in the FM and ATRs. Correlations with decreases in Stroop Interference was seen in the left ATR and right UNC, while correlations with increases in TMTA was seen in the right ATR. In regards to examining changes in WM morphology, unbiased T1-weighted and DTI atlases were built for the analyses. A parallel transport tool was then developed to transport longitudinal changes to an atlas space. The parallel transport tool was first demonstrated on synthetic 2D

images (tranport volume decrease of a circle to an ellipse) and an actual T1-weight image with an artificially dilated ventricle (transport artifical warping to T1-weighted template). Then, the parallel transport tool was used to transport changes over a two year period for 42 controls and 74 prodromal HD participants. Log Jacobian values in the high CAP group were lower than the medium CAP group in the area medial to the left rostral middle frontal WM and lateral to the left superior frontal WM. There were minor significant correlations between log Jacobian values and changes in cognitive variables. Together, the gradient of effects seen in the differences in DTI scalar values and their correlations with cognitive variables that have a documented ability in detecting cognitive deficits in prodromal HD participants suggest that DWI can provide reliable markers of disease progression. Specifically, the results of this study suggest that monitoring MD and RD in the right IFO while measuring TMTB time could serve as a reliable biomarker to monitor disease progression in the prodromal HD stage.

The clinical implications of the longitudinal changes that were detected in this study were much like those discussed in the cross-sectional fiber tracking study (Chapter 4). In both cross-sectional and longitudinal studies, differences in MD, AD, and RD were more commonplace than FA. The only difference is the longitudinal results now show that DTI scalar values are changing at different rates over time and the high CAP group is usually changing the fastest. Such information would be useful in a clinical trial since information on rate of DTI scalar change could be used to monitor treatment efficacy. The correlations between changes in cognitive

variables and changes in DTI scalars support the findings between groups because they link poorer cognitive performance with changes in diffusivity that are associated with greater disease burden.

The parallel transport demonstration with 2D synthetic images was successful in illustrating how changes over time can be transported to a template. On the other hand, the average SVF of all transported SVFs derived from artifically dilated T1-weighted images did not deform the T1-weighted template as dramatically as hoped (Figure 5.13). Before SVFs transforming time point 1 to artifically dilated time point 2 were transported to the template, the output image from each SVF derivation was visually inspected to ensure the registration was successful. Correspondence between moving and fixed images was normally acceptable. Therefore, the average SVF that did not warp the T1-weighted template as dramatically as hoped was probably caused by not artificially dilating each time point 2 image in the same area. The slight misalignment of the artificial dilations may have prevented all vectors from accumulating at the border of the left ventricle, thus decreasing the degree of deformation in the average SVF. This may have also caused significantly less log Jacobian values in the images with artificial dilations in comparison to the unaltered images within the left ventricle, in addition to the WM and caudate bordering the ventricle.

One of the limitations of this study was again the use of a tensor-based analysis, which has been discussed in Chapters 3 and 4. However, the main limitation of this study was perhaps using parallel transport on WM tracts and analyzing log Jacobian values to examine morphology was not an optial experimental design for

WM tracts terminating in the PFC. When doing a literature search of manuscripts that have used parallel transport to study longitudinal changes in brain structures, the region of interest is usually a structure with clearly defined borders. The WM tracts in this study did not have borders on the majority of their surfaces because most of these tracts are running parallel to other WM tracts. WM tracts only gain borders when adjacent to another tissue type or are within a gyrus. This may explain why the only significant finding in the log Jacobian analysis was in the portion of the left ATR that was about to enter the superior frontal gyrus (Figure 5.19). Another aspect of this study that could have hindered the success of being able to distinguish differences between groups with log Jacobian values is the frontal lobe is generally a highly variable region even in normal anatomy. Although an atlas space that was representative of the population in question was constructed for this study, registration algorithms can only deform images so much before tissue begins to fold inappropriately.

In order to possibly improve the outcome of using parallel transport to evaluate WM tract morphology, several adjustments could be made. First, the derivation of the SVF from time point 2 to the template could be optimized futher to increase correspondence through parameter exploration or an image normalization step to enhance any border the WM tract may have. Another improvement would be to take advantage of the properties of the SVF by normalizing all transported SVFs to a specific time range before deriving log Jacobian maps for analysis. Also, instead of performing statistics on log Jacobian values, perhaps the eigenvalues of the Jacobian

matrix should be explored. Finally, perhaps these methods should optimized on less variable WM tracts that have well-defined borders such as the corpus callosum.

Future directions include repeating this analysis using higher order models of diffusion to obtain better defined WM tracts and repeating the DTI scalar analysis to other regions of interest relevant to prodromal HD.

5.5 Conclusion

Together, the gradient of effects seen in the differences in DTI scalar values and their correlations with cognitive variables that have a documented ability in detecting cognitive deficits in prodromal HD participants suggest that DWI can provide reliable markers of disease progression. Specifically, the results of this study suggest that monitoring MD and RD in the right IFO while measuring TMTB time could serve as a reliable biomarker to monitor disease progression in the prodromal HD stage.

Table 5.4: Demographic and clinical data from the first and second time points for healthy control and prodromal HD participants for longitudinal data analysis, including number of participants from each site in each group.

	Cont (Mean; SD (N))	Low (Mean; SD (N))	Med (Mean; SD (N))	High (Mean; SD (N))
(1) Age (years)	47.1; 11.0 (42)	33.6; 10.4 (19)	42.8; 10.6 (26)	47.7; 11.0 (29)
(2) Age (years)	49.1; 11.0 (42)	35.6; 10.4 (19)	44.8; 10.6 (26)	49.7; 11.0 (29)
Educ (years)	15.5; 2.1 (42)	14.8; 2.2 (19)	14.7; 2.1 (26)	14.7; 3.3 (29)
Gender	13M/29F (42)	5M/14F (19)	6M/20F (26)	8M/21F (29)
(1) Motor	4.7; 4.5 (42)	4.9; 5.2 (19)	6.5; 3.9 (26)	9.3; 8.5 (29)
(2) Motor	3.2; 5.3 (42)	2.7; 2.6 (19)	6.4; 6.1 (26)	10.3; 11.7 (29)
(1) SDMT	53.5; 10.0 (42)	57.2; 10.2 (19)	53.2; 8.7 (26)	48.7; 8.4 (29)
(2) SDMT	55.5; 11.0 (42)	57.5; 12.0 (19)	54.9; 10.0 (26)	48.4; 8.3 (29)
(1) S Color	81.7; 14.2 (42)	84.1; 8.8 (19)	78.2; 10.1 (26)	76.1; 11.3 (29)
(2) S Color	84.9; 15.2 (42)	85.1; 11.3 (19)	79.8; 11.7 (26)	73.1; 14.0 (29)
(1) S Word	101.6; 17.8 (42)	106.3; 13.9 (19)	99.0; 13.9 (26)	94.6; 15.4 (29)
(2) S Word	103.5; 18.0 (42)	105.3; 9.9 (19)	95.7; 16.9 (26)	90.8; 18.5 (29)
(1) S Inter	47.1; 10.0 (42)	52.5; 12.6 (19)	47.0; 10.8 (26)	43.9; 8.4 (29)
(2) S Inter	47.8; 8.6 (42)	53.3; 14.1 (19)	47.1; 11.2 (26)	43.3; 8.0 (29)
(1) TMTA	23.9; 8.9 (42)	21.9; 7.1 (19)	22.2; 7.6 (26)	24.7; 7.4 (29)
(2) TMTA	22.2; 9.1 (42)	19.2; 4.4 (19)	22.0; 8.0 (26)	24.9; 8.9 (29)
(1) TMTB	53.2; 23.0 (42)	45.7; 13.4 (19)	49.9; 16.9 (26)	59.7; 19.8 (29)
(2) TMTB	50.8; 25.1 (42)	42.7; 13.3 (19)	47.8; 24.8 (26)	58.6; 17.0 (29)
Site 002	(1)	(0)	(0)	(0)
Site 024	(22)	(8)	(14)	(15)
Site 027	(2)	(0)	(0)	(1)
Site 028	(0)	(0)	(0)	(1)
Site 045	(2)	(1)	(1)	(1)
Site 050	(0)	(0)	(0)	(1)
Site 054	(1)	(2)	(4)	(4)
Site 061	(0)	(0)	(1)	(0)
Site 073	(0)	(1)	(0)	(2)
Site 120	(14)	(6)	(6)	(3)
Site 144	(0)	(1)	(0)	(0)
Site 177	(0)	(0)	(0)	(1)

Note: Sites 024, 027, 045, 050, 073, 120, 144 and 177 have Siemens vendor scanners; sites 002, 028 and 061 a Philips vendor scanner; and site 054 a GE vendor scanner. Cont = Controls. Med = Medium. Educ = Education. Motor = Sum of all items of the UHDRS Motor Assessment scale. SDMT = Symbol Digit Modalities Test. S = Stroop. Inter = Interference. TMTA = Trail Making Test A. TMTB = Trail Making Test B.

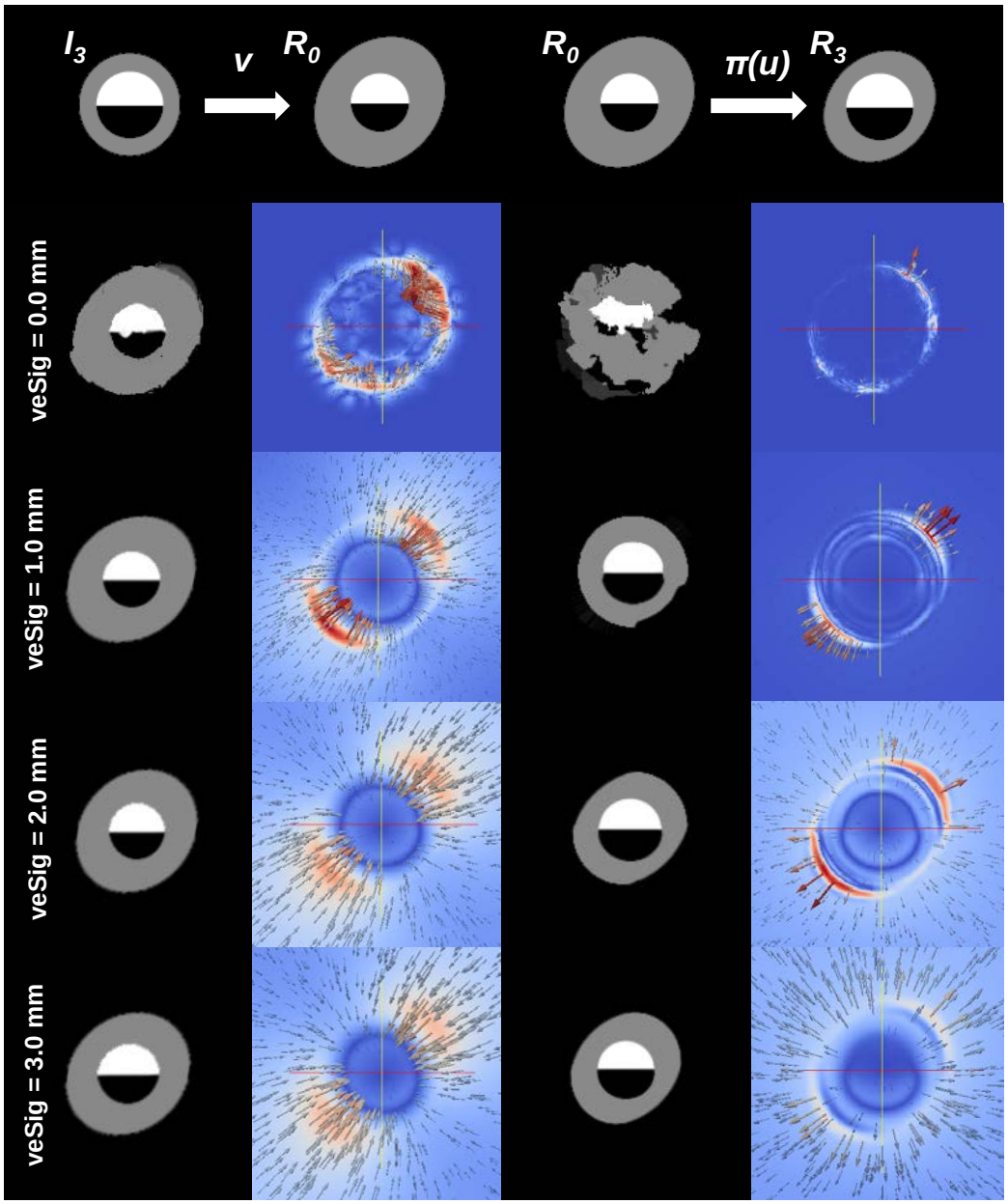

Figure 5.4: Velocity sigma parameter effect on symmetric demons while holding other registration parameters constant. Parameters: upSig = 1.0 mm, maxStep = 1.0 mm, and bch = 2. The first row consists of the ideal results for the transformation being derived. The first and third columns are I_3 deformed into the space of R_0 and R_0 deformed by the transported SVF, respectively. The second and fourth columns are the SVF (target-to-source mapping) from R_0 to I_3 and the transported SVF, respectively. Vector magnitude is scaled from low to high with blue to red. Vector size has been scaled up for illustrative purposes.

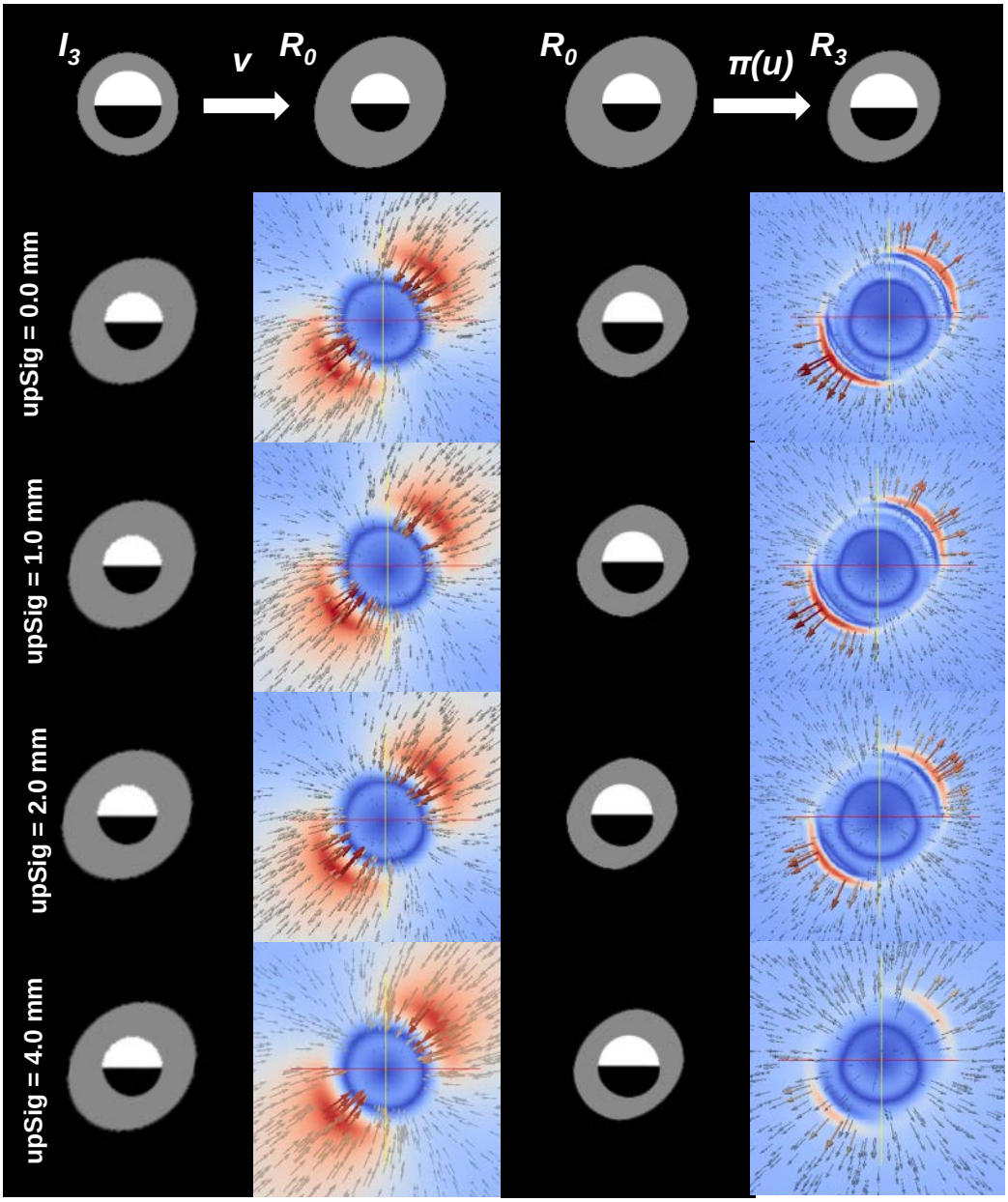

Figure 5.5: Update sigma parameter effect on symmetric demons while holding other registration parameters constant. Parameters: velSig = 2.0 mm, maxStep = 1.0 mm, and bch = 2. The first row consists of the ideal results for the transformation being derived. The first and third columns are I_3 deformed into the space of R_0 and R_0 deformed by the transported SVF, respectively. The second and fourth columns are the SVF (target-to-source mapping) from R_0 to I_3 and the transported SVF, respectively. Vector magnitude is scaled from low to high with blue to red. Vector size has been scaled up for illustrative purposes.

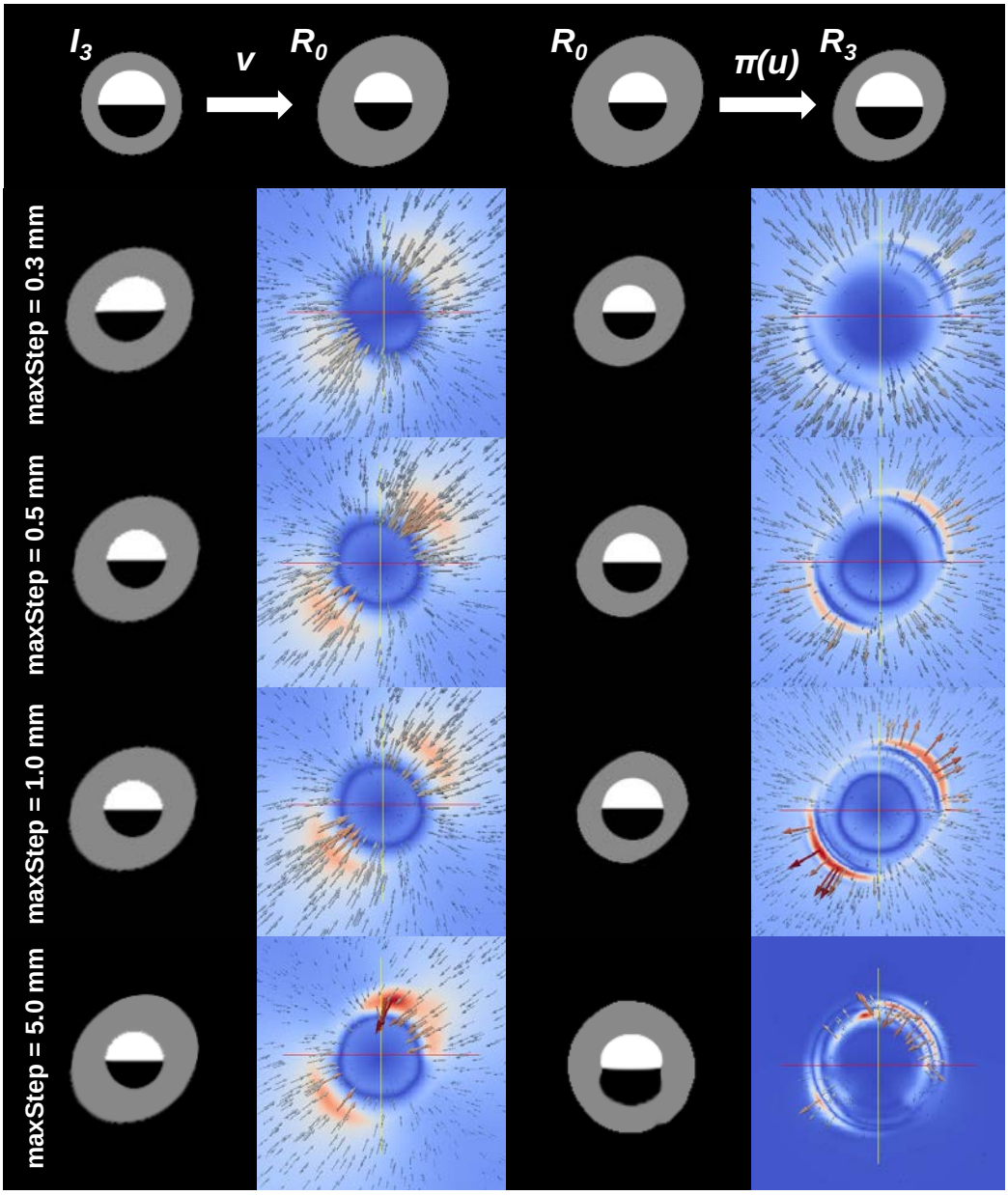

Figure 5.6: Maximum step length parameter effect on symmetric demons while holding other registration parameters constant. Parameters: velSig = 2.0 mm, upSig = 1.0 mm, and bch = 2. The first row consists of the ideal results for the transformation being derived. The first and third columns are I_3 deformed into the space of R_0 and R_0 deformed by the transported SVF, respectively. The second and fourth columns are the SVF (target-to-source mapping) from R_0 to I_3 and the transported SVF, respectively. Vector magnitude is scaled from low to high with blue to red. Vector size has been scaled up for illustrative purposes.

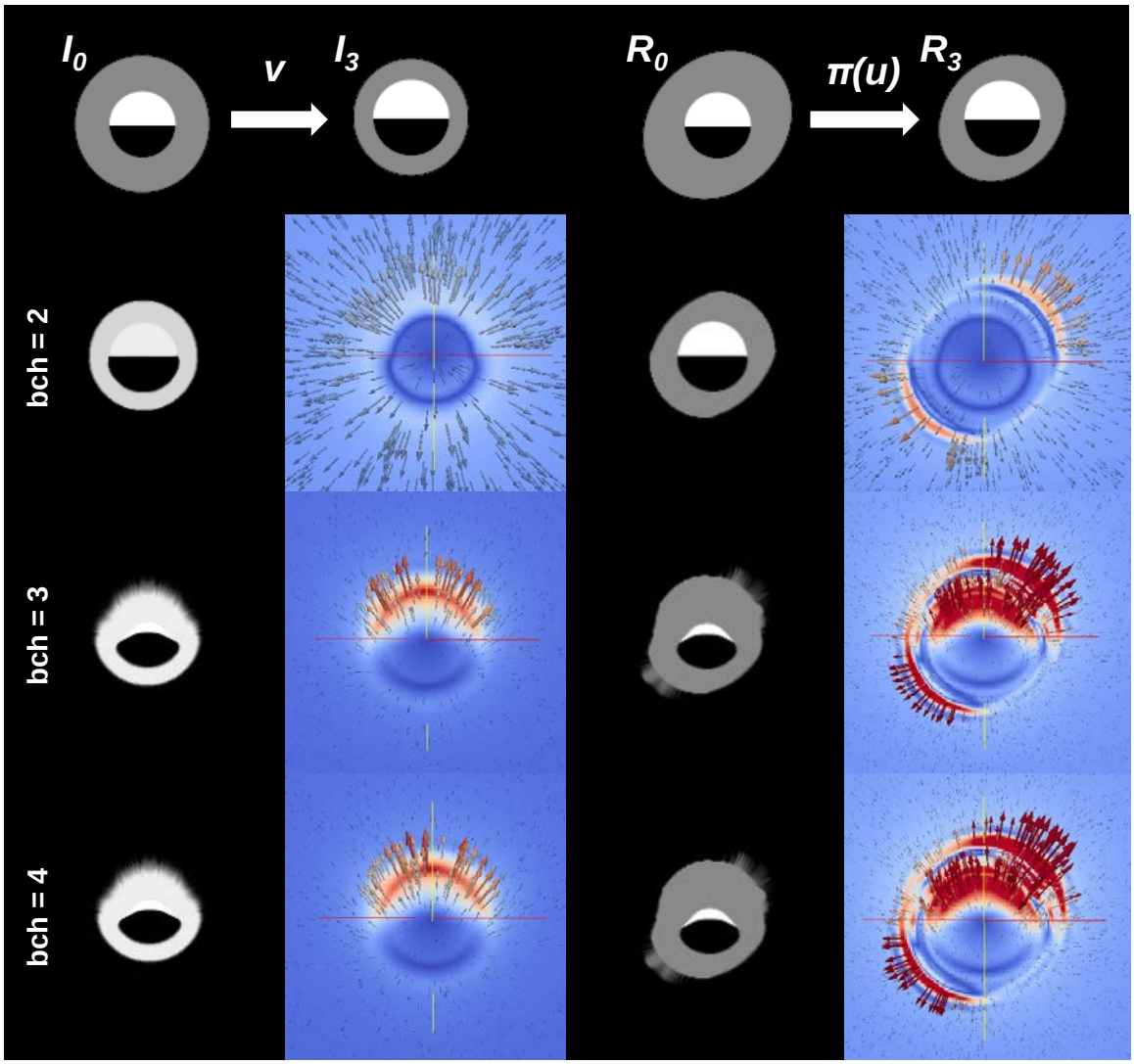

Figure 5.7: Baker-Campbell-Hausdorff truncation order effect on symmetric demons while holding other registration parameters constant. Parameters: velSig = 2.0 mm, upSig = 1.0 mm, and maxStep = 1.0 mm. The first row consists of the ideal results for the transformation being derived. The first and third columns are I_3 deformed into the space of R_0 and R_0 deformed by the transported SVF, respectively. The second and fourth columns are the SVF (target-to-source mapping) from R_0 to I_3 and the transported SVF, respectively. Vector magnitude is scaled from low to high with blue to red. Vector size has been scaled up for illustrative purposes.

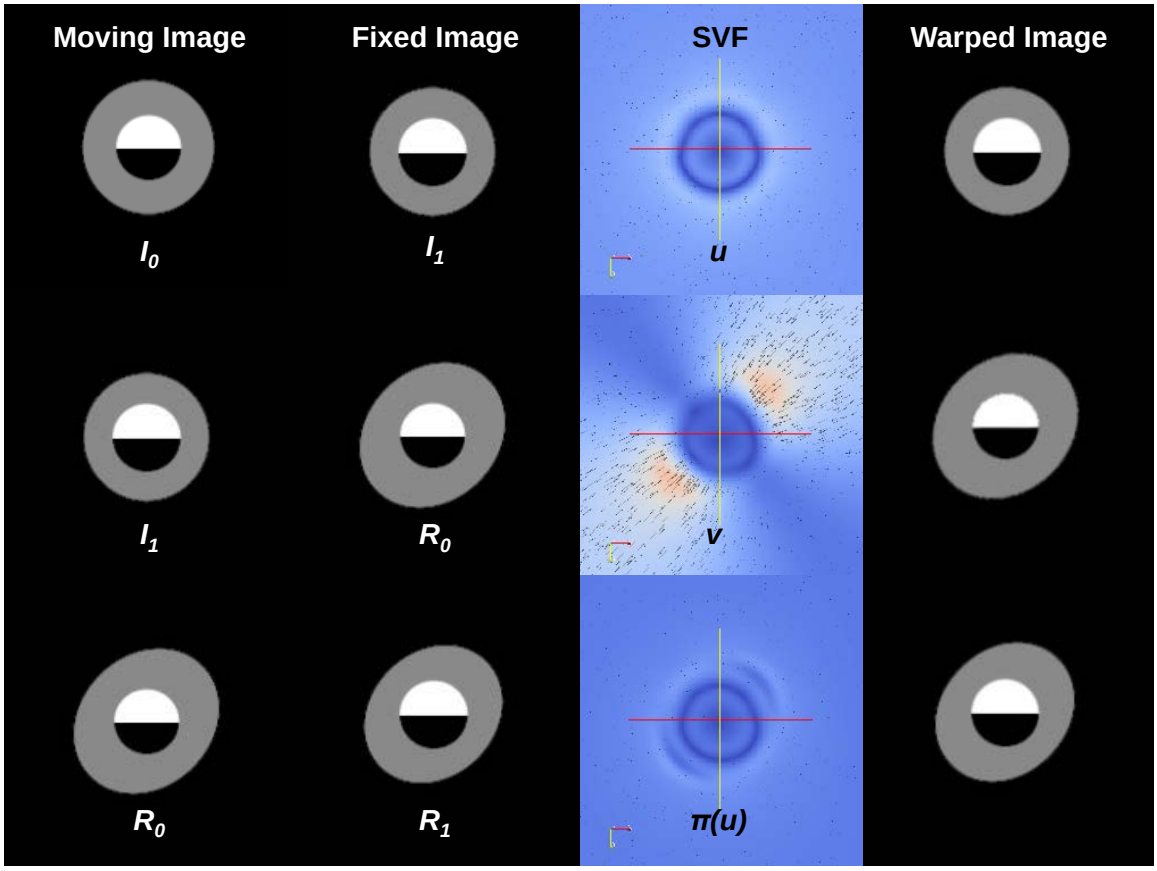

Figure 5.8: 2D Schild's ladder demonstration using test images with 5 percent volume changes (I_1 and R_1) from baseline. Parameters: velSig = 2.0 mm, upSig = 4.0 mm, maxStep = 1.0 mm, and bch = 2. Vector magnitude is scaled from low to high with blue to red.

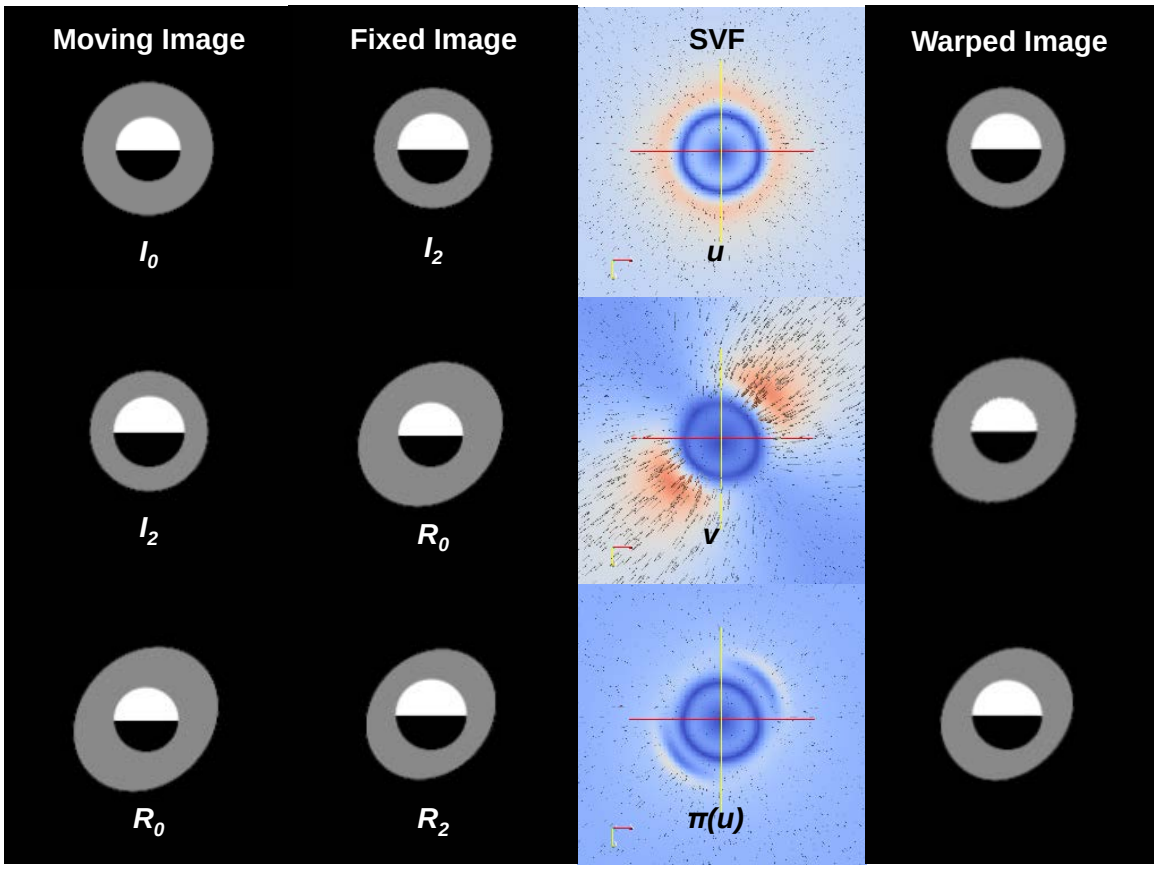

Figure 5.9: 2D Schild's ladder demonstration using test images with 10 percent volume changes (I_2 and R_2) from baseline. Parameters: velSig = 2.0 mm, upSig = 4.0 mm, maxStep = 1.0 mm, and bch = 2. Vector magnitude is scaled from low to high with blue to red.

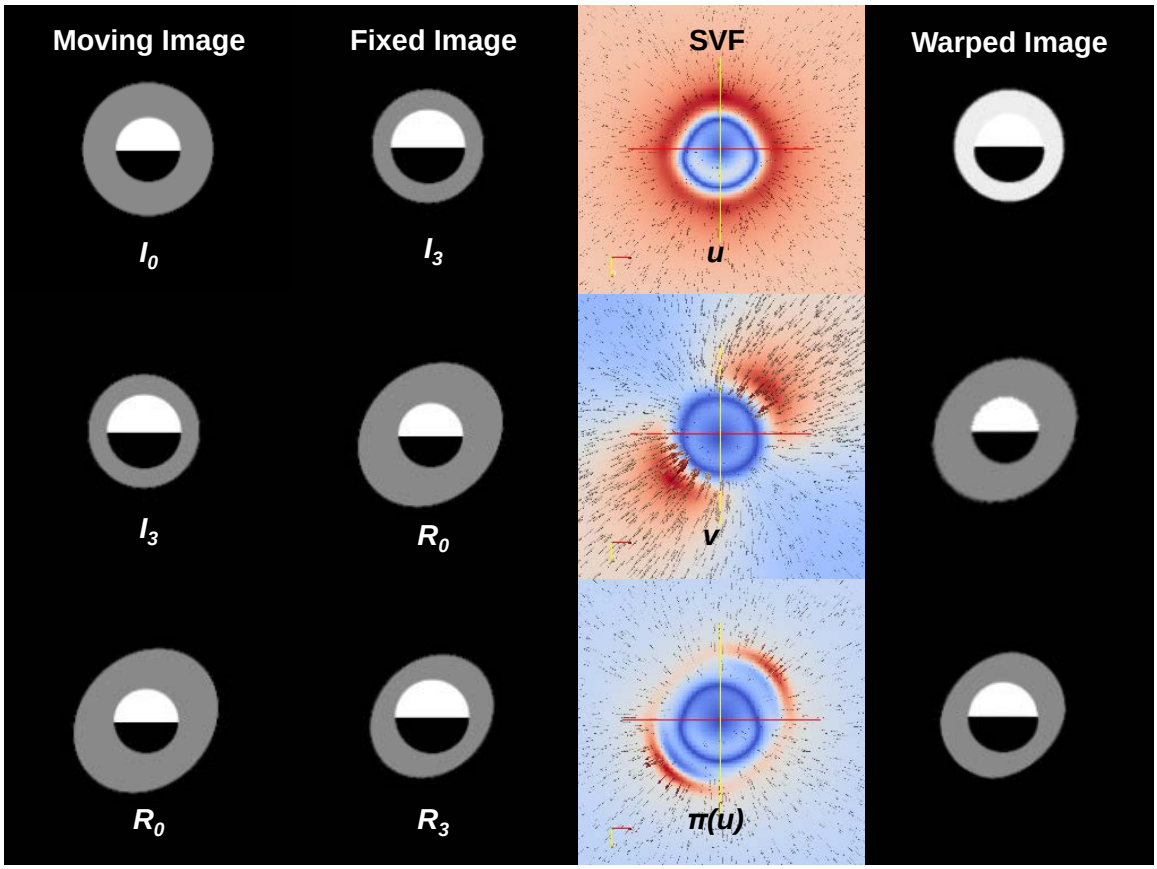

Figure 5.10: 2D Schild's ladder demonstration using test images with 15 percent volume changes (I_3 and R_3) from baseline. Parameters: velSig = 2.0 mm, upSig = 4.0 mm, maxStep = 1.0 mm, and bch = 2. Vector magnitude is scaled from low to high with blue to red.

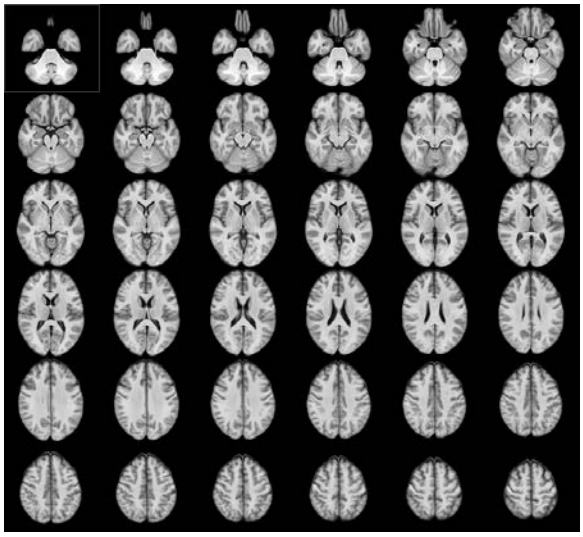

Figure 5.11: T1-weighted atlas for longitudinal control experiment.

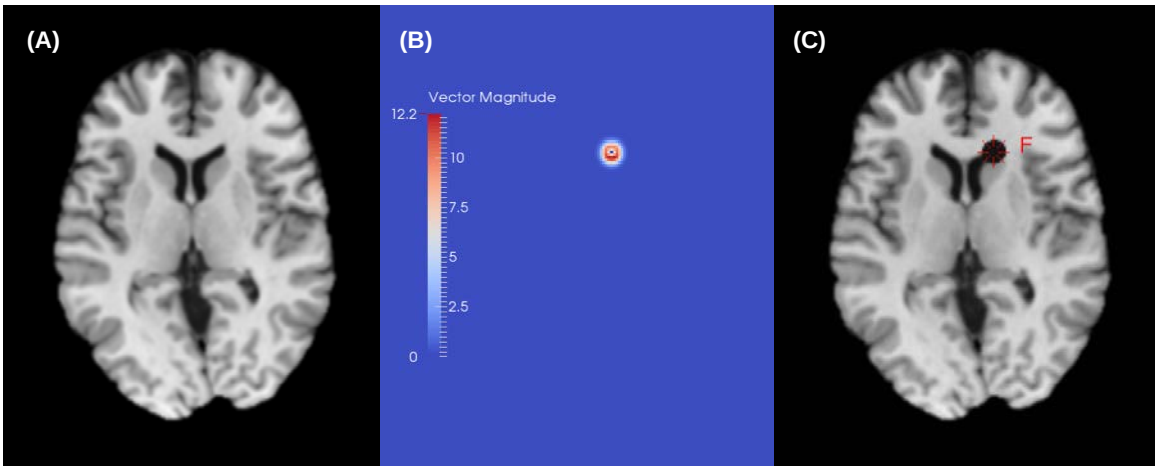

Figure 5.12: Synthetic SVF applied to T1-weighted image. (A) T1-weighted image from the second scanning session for a healthy control participant. (B) Image of vector magnitudes in the synthetic SVF. (C) Same image as the left panel after application of synthetic SVF. Artificial dilation can be seen around in the left ventricle and caudate, surrounding the fiducial.

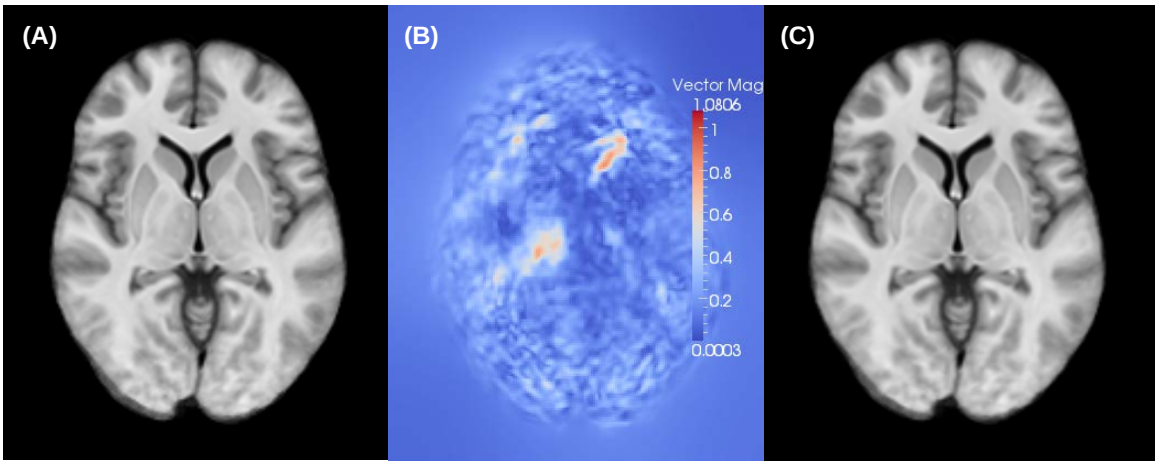

Figure 5.13: Average synthetic SVF applied to T1 atlas. (A) T1-weighted atlas made from healthy control participants before application of average synthetic transported SVF. (B) Image of vector magnitudes in the average transported synthetic SVF. Note the higher magnitudes surrounding the left ventricle. (C) Same image as the left panel after application of average synthetic transported SVF. Artificial dilation can be seen around in the left ventricle and caudate.

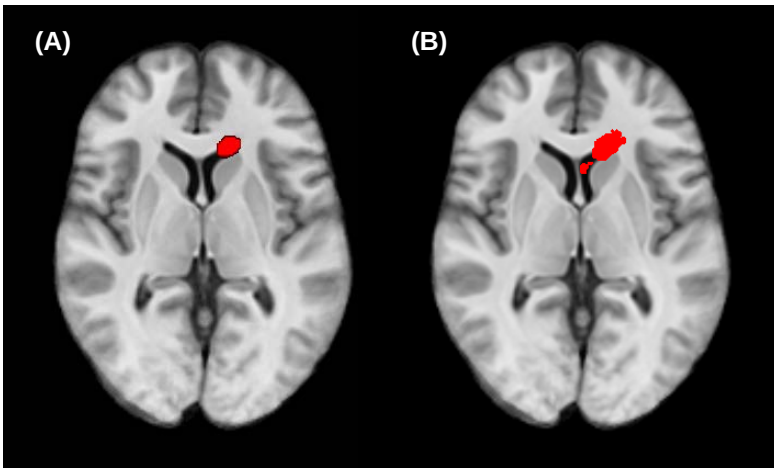

Figure 5.14: Areas with significantly negative log Jacobian values. Axial slices containing showing areas of the SVFs whose log Jacobian values were (A) greater before the application of artifical warping (corrected for multiple comparisons using FDR with a criterion of $q < 0.05$) and (B) significantly less than zero colored (corrected for multiple comparisons using FDR with a criterion of $q < 0.01$). Note that the voxels containing significantly negative log Jacobian values are in the WM bordering the left ventricle reflecting volume contraction in those areas.

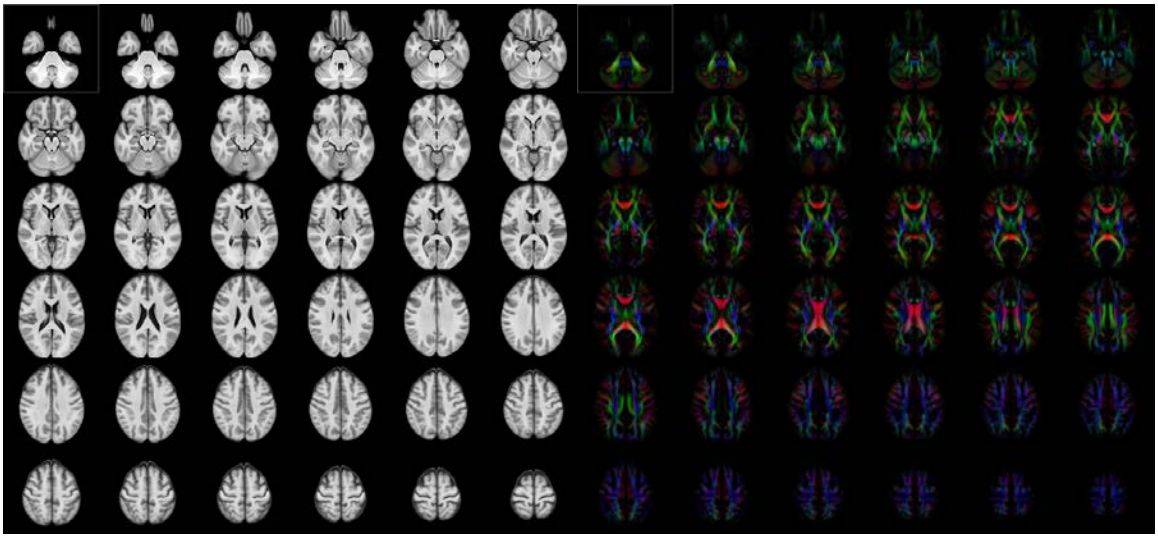

Figure 5.15: T1-weighted and DTI atlases for longitudinal analyses.

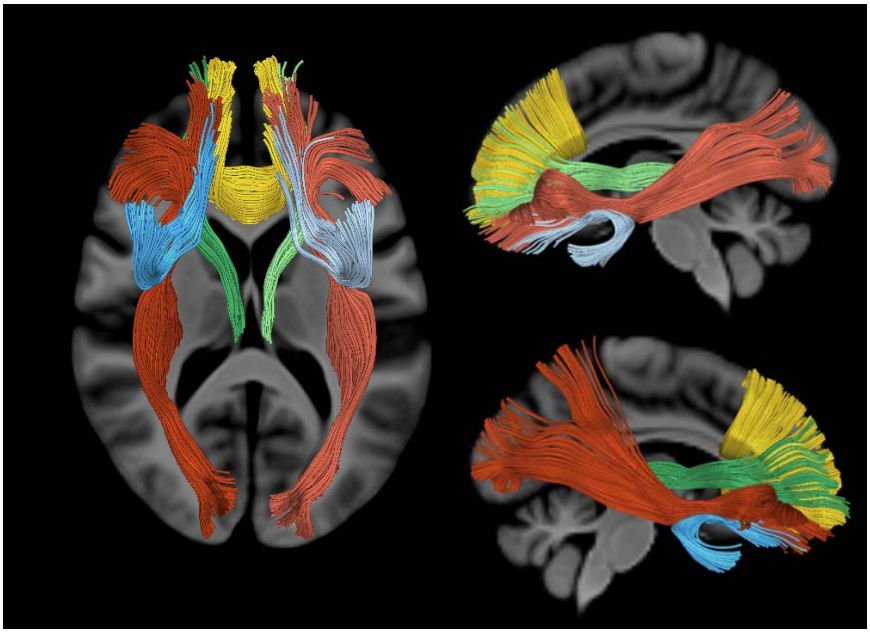

Figure 5.16: All fiber tracts overlaid T1-weighted template for longitudinal analysis. Different tracts are highlighted with different colors: left UNC (light blue), right UNC (dark blue), FM (yellow), left IFO (light red), right IFO (dark red), left ATR (light green), and right ATR (dark green).

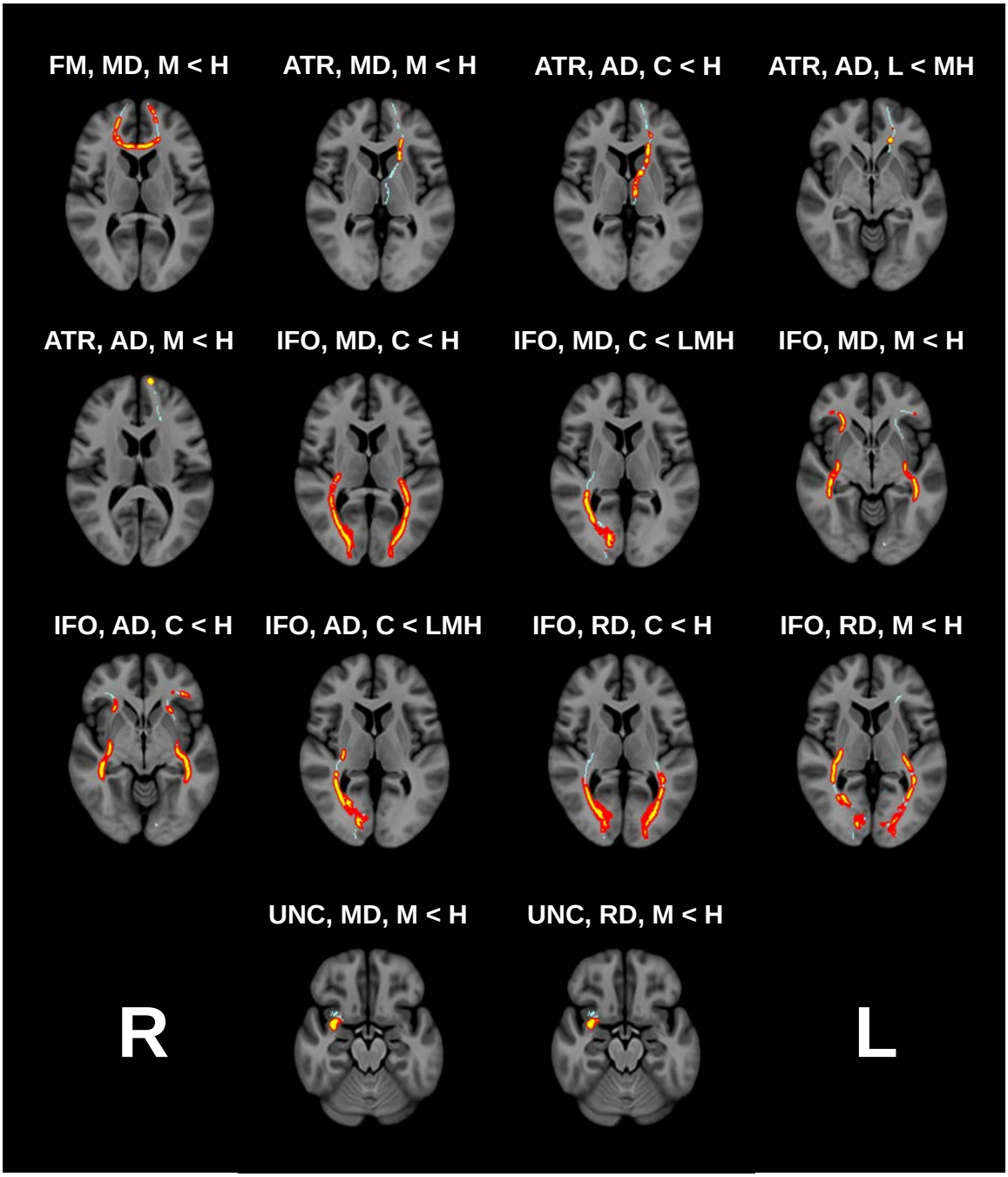

Figure 5.17: Differences in DTI scalar change over time among groups. Highlighted regions (yellow and red) of each tract skeleton overlaid the tract skeleton (light blue) containing voxels with significant differences in DTI scalar change over a two year period between controls (C) and individual CAP groups (L = low, M = medium, H = high) or between the current group and subsequent groups. These results were acquired with the TFCE method at 50,000 permutations, corrected with FDR at a criterion of $q < 0.05$, and are displayed in radiologic convention.

Table 5.5: Percentages of all tract skeleton voxels that contained significant differences in change of DTI scalars between control (C) and CAP groups (L, M, H) and between each group and all subsequent groups over a two year period.

Tract	DTI Scalar	Contrast	Significant voxels (%)	Regions with significant differences
FM	MD	M < H	49.72	2,3,4,5,6,7,8,9,10,11,12
LeftATR	MD	M < H	19.46	2,3,4
	AD	C < H	32.89	1,2,3,4
		L < MH	1.94	3
		M < H	0.21	5
LeftIFO	MD	C < H	41.21	4,6,7,8
		M < H	36.44	4,5,6,7,8
	AD	C < H	36.36	2,4,5,6,7,8
	RD	C < H	27.83	5,6,7,8
		M < H	32.73	3,6,7,8
RightIFO	MD	C < H	37.39	6,7,8
		C < LMH	16.84	6,7
		M < H	46.42	2,3,4,5,6,7,8
	AD	C < H	24.38	2,5,6,7,8
		C < LMH	25.53	2,6,7,8
	RD	C < H	18.56	6,7,8
		M < H	40.48	3,5,6,7,8
RightUNC	MD	M < H	10.78	3,4
	RD	M < H	16.48	3,4

Note: General locations of the significant voxels are noted. These results were acquired with the TFCE method at 50,000 permutations and corrected with FDR at a criterion of $q < 0.05$.

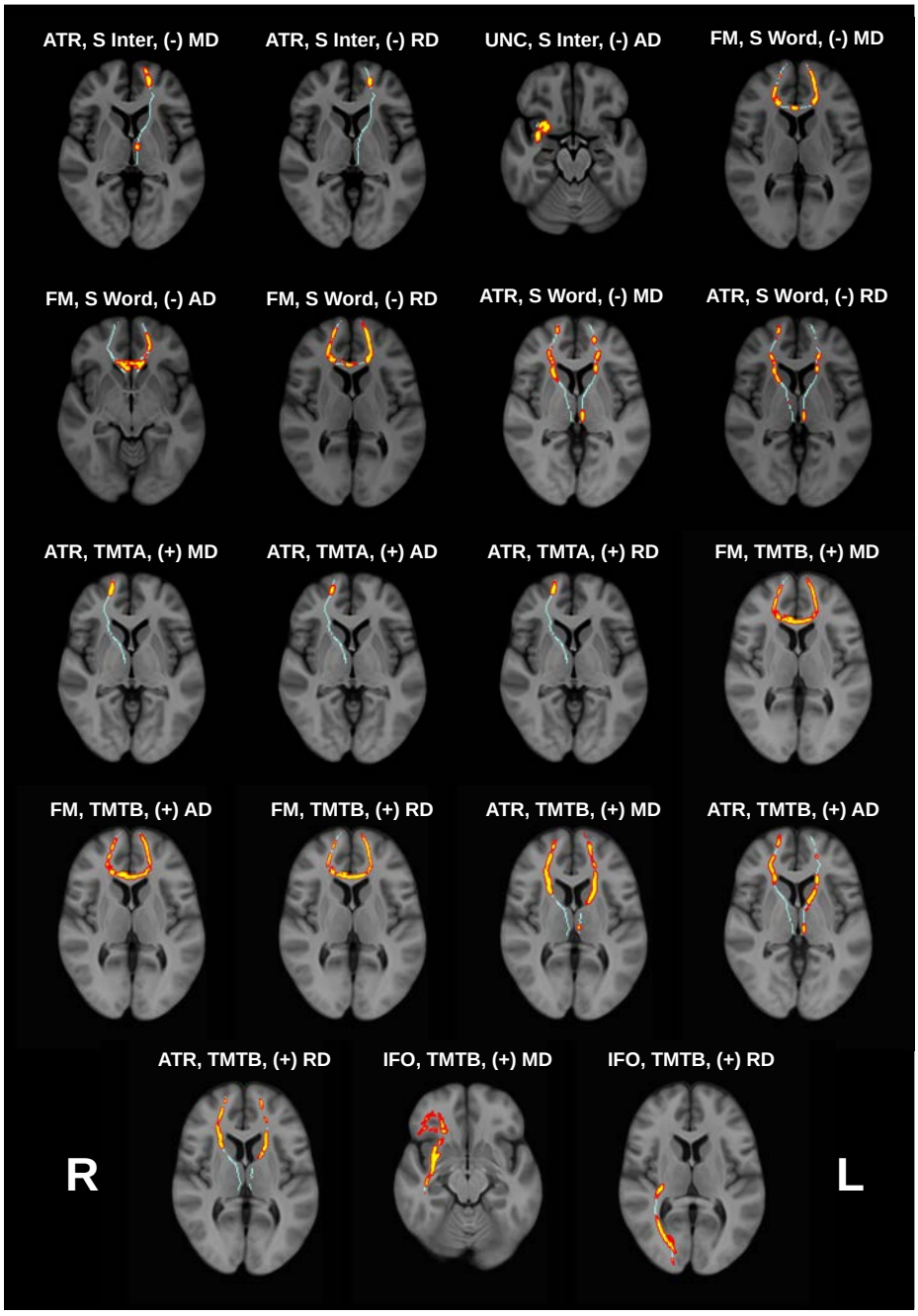

Figure 5.18: Correlations between change in DTI scalars and cognitive variables. Highlighted regions (yellow and red) of each tract skeleton overlaid the tract skeleton (light blue) containing voxels with significant correlations between DTI scalar and cognitive variable change over a two year period in prodromal HD participants. These results were acquired with the TFCE method at 50,000 permutations, corrected with FDR at a criterion of $q < 0.05$, and are displayed in radiologic convention.

Table 5.6: Percentages of all tract skeleton voxels that contained significant correlations between change of DTI scalars and change in cognitive variables in prodromal HD participants and change in cognitive variables and change in cognitive variables and change in cognitive variables over a two year period.

Cognitive variable	DTI Scalar	Contrast	Tract	Significant voxels (%)	Regions with significant differences
S Inter	MD	Negative	LeftATR	18.98	1,4,5
	AD	Negative	RightUNC	16.36	3,4
	RD	Negative	LeftATR	12.40	4
S Word	MD	Negative	FM	45.86	1,3,4,5,6,7,9,10,11,12
			LeftATR	32.62	1,3,4,5
			RightATR	32.25	2,3,4,5
	AD	Negative	FM	12.98	1,4,6,7,9,10,11
	RD	Negative	FM	38.97	2,3,4,5,6,7,8,9,10,11,12
			LeftATR	27.49	1,3,4
			RightATR	27.76	1,2,3,4
TMTA	MD	Positive	RightATR	13.22	4
	AD	Positive	RightATR	6.81	4
	RD	Positive	RightATR	10.05	4
TMTB	MD	Positive	FM	67.24	2,3,4,5,6,7,8,9,10,11,12
			LeftATR	54.43	1,2,3,4
			RightATR	51.55	1,2,3,4
			RightIFO	63.37	1,2,3,4,5,6,7,8
	AD	Positive	FM	55.72	1,2,3,4,5,6,7,8,9,10,11,12
			LeftATR	24.38	1,2,3
			RightATR	38.07	1,3,4
	RD	Positive	FM	63.85	1,2,3,4,5,6,7,8,9,10,11,12
			LeftATR	46.05	1,2,3,4
			RightATR	43.23	2,3,4
			RightIFO	36.90	2,3,4,5,6,7,8

Note: General locations of the significant voxels are noted. These results were acquired with the TFCE method at 50,000 permutations and corrected with FDR at a criterion of $q < 0.05$.

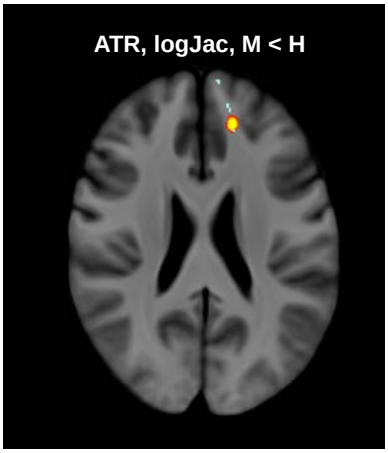

Figure 5.19: Significant differences between log Jacobian values between controls and CAP groups.

CHAPTER 6
CONCLUDING REMARKS

The purpose of this thesis was to address the logistical complexities of performing multi-site longitudinal diffusion-weighted (DWI) studies in clinical trials. The key processing components to accomplish a robust DWI processing system (DICOM conversion, automated quality control, unbiased atlas construction, fiber tracking, and statistical analysis) have been addressed in this work. Tools that solve DICOM compatibility and quality control issues of mulit-site data have been applied to DWI data from healthy controls collected at multiple sites in a DTI scalar reliability analysis. A mean DTI scalar analysis has been performed on a region of interest to investigate how changes in its diffusivity could explain phenotypic characteristics of a neurodegenerative disease. The mean DTI scalar analysis has been extended with cross-sectional and longitudinal fiber tracking analyses that have been performed on four major WM tracts terminating in the region of interest from the DTI scalar analysis. Significant differences in diffusivity have been found at each level of analysis throughout regions of interest among separate groups of the neurodegenerative disease population. In addition, multiple neuropsychological cognitive variables that have a documented ability to track disease progression of the neurodegenerative disease, strongly correlated with many of the DTI scalars in each tract. Collectively, the results of this thesis demonstrates how to use DWI as a reliable biomarker to monitor neurodenerative disease progression in white matter longitudinally using data from multiple sites.

APPENDIX A
CROSS-SECTIONAL STUDIES SUPPLEMENTAL MATERIAL

A.1 Fiber tract selection

A.1.1 Uncinate fasciculus

Coronal and axial views were the most important views for isolating tracts that represented the UNC. In the coronal view, the selection box was resized to encompass the temporal lobe (Figure A.1). Then, all fibers projecting from the temporal lobe but not into the frontal lobe were removed (Figure A.2). Only fibers with curved projections from anterior temporal lobe extending to the medial and lateral orbitofrontal cortex were included in tracts that represented the UNC (Figure A.3) [143, 167, 147, 168].

A.1.2 Forceps minor

Using the coronal and axial views for guidance, a coronal plane anterior to the genu of the corpus callosum that passed through the frontal lobe was placed in one hemisphere to initially select the tracts of the FM (Figure A.4). Another plane was placed in the same position in the contralateral hemisphere to select tracts that exited the frontal lobe and curved into the contralateral hemisphere (Figure A.5). A final plane was placed posterior to the genu to exclude tracts that passed through thefirst two planes but extended outside the frontal lobe (Figure A.6). [143, 167, 147, 168].

A.1.3 Inferior fronto-occipital fasciculus

A coronal plane was placed between the posterior edge of the cingulum and the parieto-occipital sulcus to select the occiptal extensions of the IFO in a single hemisphere. This initial coronal plane does not extent inferiorly beyond the bottom edge of the occipital lobe or a few centimeters above the posterior edge of the cingulum bundle (Figure A.7). A second coronal plane was placed anterior to the anterior edge of the cingulum bundle extended through the entire frontal lobe in the ipsilateral hemisphere of the first coronal plane to select tracts that extended from the occipital lobe to the frontal lobe (Figure A.8). Tracts that terminated too superiorly in the frontal lobes (outside of the orbitofrontal area) were removed (Figure A.9) [143, 167, 147, 168].

A.1.4 Anterior thalamic radiations

A selection box was first placed around the entire thalamus for a given hemisphere to isolate all tracts passing through the thalamus (Figure A.10). A coronal plane was then placed in the middle of the genu in the ipsilateral hemisphere to select the ATR (Figure A.11). Fibers that did not emanate from the mediodorsal nuclei of the thalamus or pass through the anterior limb of the internal capsule were removed (Figure A.12) [143, 167, 147, 168].

A.2 GLM for randomise: t-test

The GLM for the t-tests were set up using two files required by randomise. The first file consisted of the design matrix, where each group (control, low, medium,

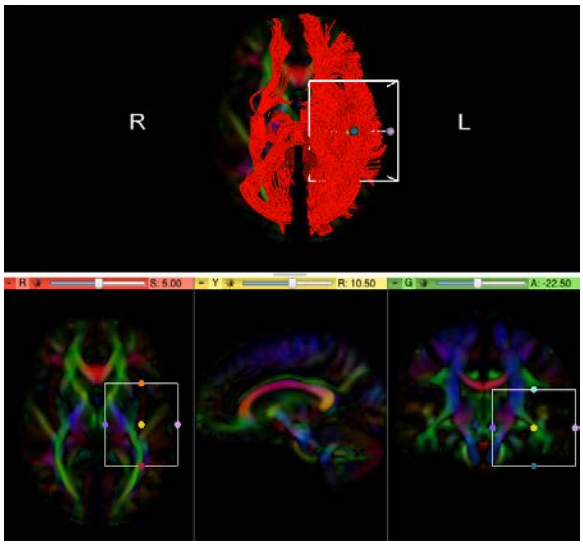

Figure A.1: UNC: First selection box is sized in the coronal and axial views to encompassed the temporal lobe.

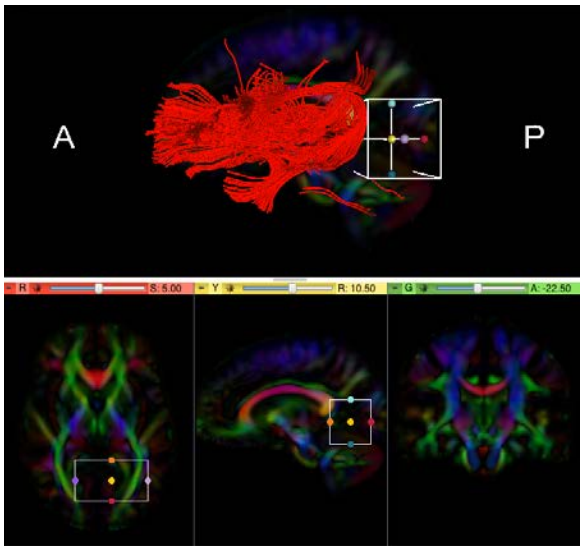

Figure A.2: UNC: Removal of fibers projecting from the temporal lobe but not into the frontal lobe.

and high CAP group) was represented by its own column and membership was coded as 1. Multiple sites of data collection were represented by separate columns with

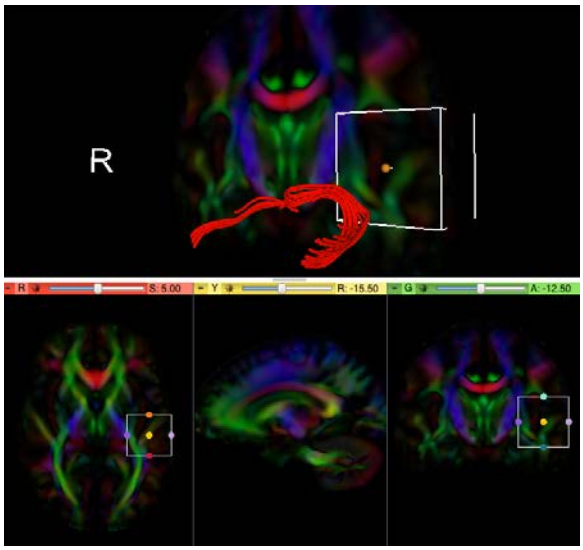

Figure A.3: UNC: Final tract after selection of fibers extending from the anterior temporal lobe to the medial and lateral orbitofrontal cortex.

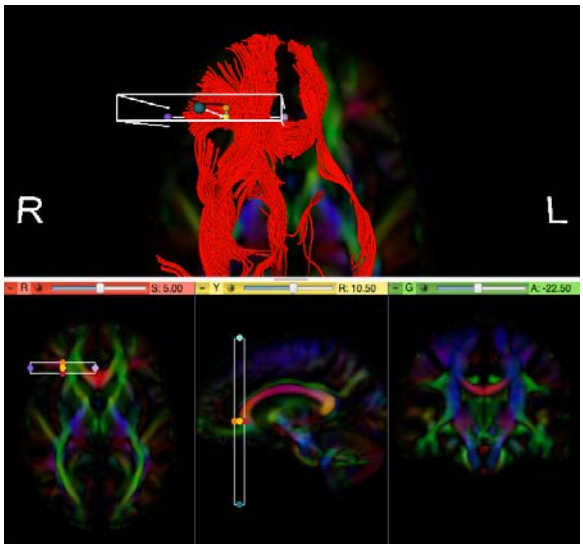

Figure A.4: FM: First selection box was placed anterior to the genu of the corpus callosum and passed through the frontal lobe in one hemisphere.

membership coded as 1, while gender used a single column with female coded as 0. All covariates (age, years of education, gender, and site of data collection) were

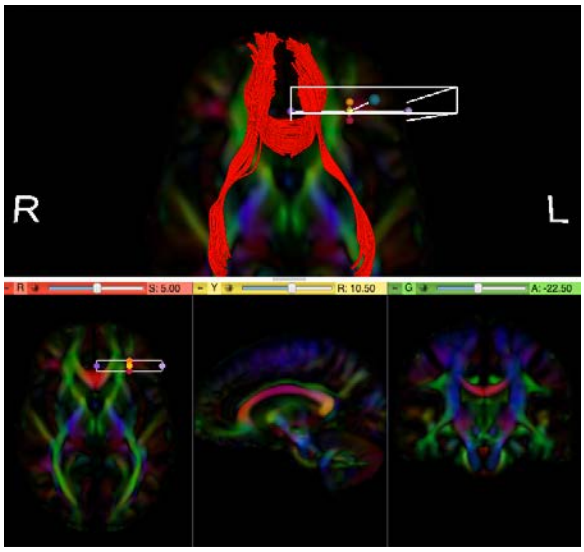

Figure A.5: FM: Contralateral plane anterior to the genu of the corpus callosum.

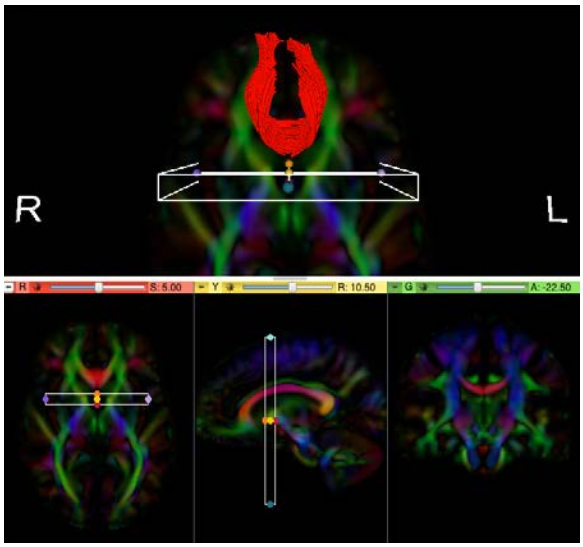

Figure A.6: FM: Final tract after the exclusion of fibers that were located posterior to the frontal lobe.

demeaned by subtracting the mean of the column from each value. Below is an example design matrix that codes three groups, each with three participants whose

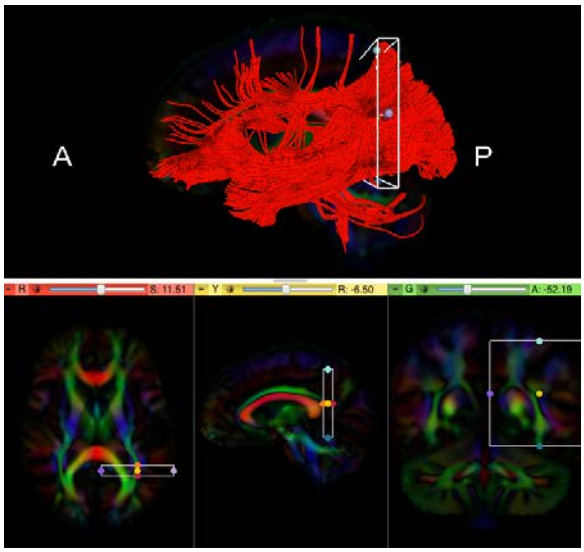

Figure A.7: IFO: First coronal plane used to select fibers passing through the occipital lobe.

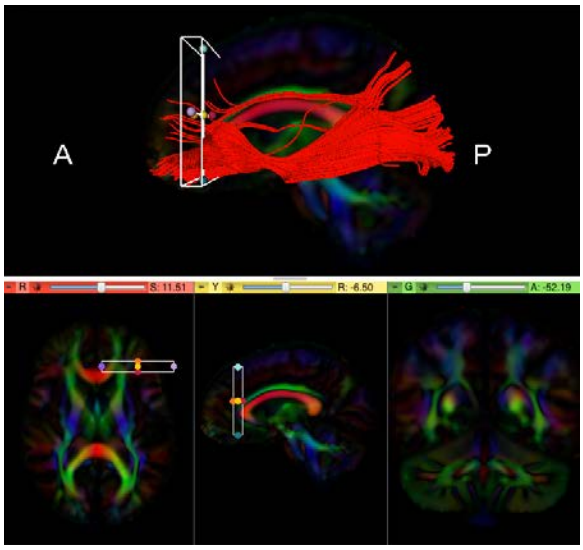

Figure A.8: IFO: Second coronal place used to select fibers that extended anteriorly from the occipital lobe.

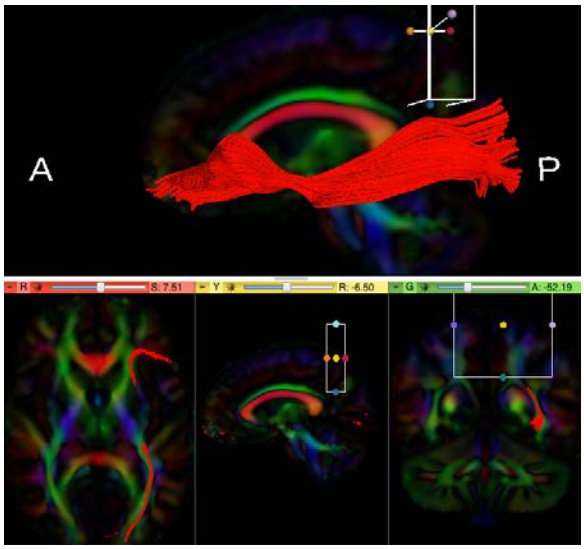

Figure A.9: IFO: Final tract after the removal of fibers terminating outside the orbitofrontal area.

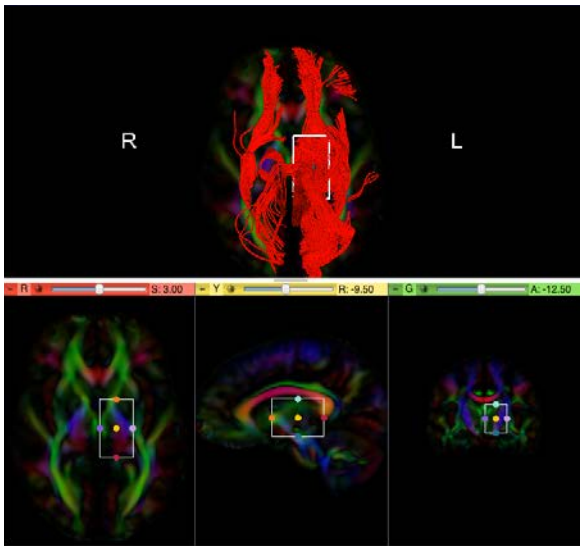

Figure A.10: Anterior thalamic radiations: First selection box used to isolate all fibers emanating from thalamus.

data was collected at one of two sites. In this case, age is an additional covariate.

randomise required some header information: NumWaves (number of columns in

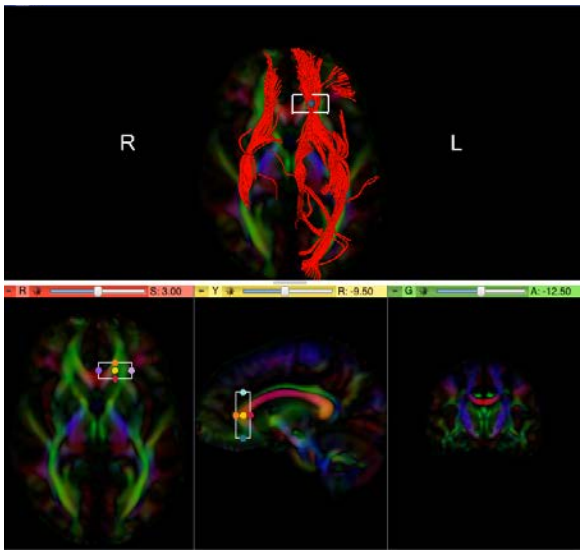

Figure A.11: Anterior thalamic radiations: Coronal plane used to select fibers projecting anteriorly from the thalamus.

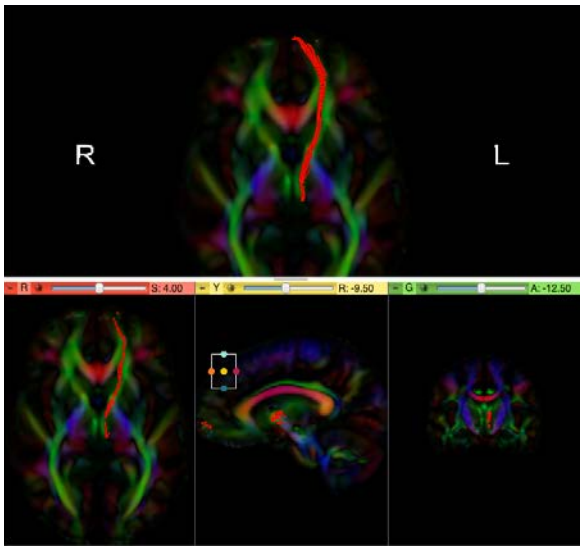

Figure A.12: Anterior thalamic radiations: Final tract after the removal of fibers that did not emanate from the mediodorsal nuclei of the thalamus or pass through the anterior limb of the internal capsule.

design matrix), NumPoints (number of subjects), and Matrix [180, 193].

```
/NumWaves 6

/NumPoints 9

/Matrix

1 0 0 0.44444 -0.44444 -11.66667

1 0 0 -0.55556 0.55556 -29.66667

1 0 0 -0.55556 0.55556 -15.66667

0 1 0 0.44444 -0.44444 23.33333

0 1 0 0.44444 -0.44444 39.33333

0 1 0 -0.55556 0.55556 10.33333

0 0 1 0.44444 -0.44444 -26.66667

0 0 1 0.44444 -0.44444 12.33333

0 0 1 -0.55556 0.55556 -1.66667
```

The headers for each of the columns for the example design matrix are as follows and were not placed in the design matrix file used to run randomise.

```
Group1 Group2 Group3 Site1 Site2 Age_Demean
```

The second file used in setting up the GLM for t-tests was called the contrast file. Using the above example, to test whether the dependent variable of Group 1 is significantly greater than that of Group 2, the contrast file would be coded below [180, 193]. Group 1 is set to 1, Group 2 is set to -1, and all nuisance variables are set to 0. Required header information for the contrast file includes NumWaves (number of columns in the contrast file, which is the same as the design matrix), NumContrasts

(number of rows in the contrast matrix), and Matrix (placed before contrast rows). The headers for each of the columns in the example contrast matrix were the same as the design matrix and were not placed in the contrast matrix file used to run randomise. For this study, DTI scalar values in the tract skeletons of controls were tested to be greater (FA) or less than (MD, AD, RD) those of the CAP groups with t-tests.

```
/NumWaves 6

/NumContrasts 1

/Matrix

1 -1 0 0 0 0
```

A.3 GLM for randomise: correlation analysis

In the design matrix, the groups, sites, and age columns are the same as those used in the t-test, with an additional cognitive variable (demeaned) column. Below is an example design matrix that codes nine participants, each with three participants whose data was collected at one of two sites with age as a covariate. The last column is the demeaned cognitive variable [180, 193].

```
/NumWaves 7

/NumPoints 9

/Matrix

1 0 0 0.44444 -0.44444 -11.66667 -0.77778

1 0 0 -0.55556 0.55556 -29.66667 41.22222
```

```
1 0 0 -0.55556 0.55556 -15.66667 -44.77778

0 1 0 0.44444 -0.44444 23.33333 -9.77778

0 1 0 0.44444 -0.44444 39.33333 26.22222

0 1 0 -0.55556 0.55556 10.33333 -10.77778

0 0 1 0.44444 -0.44444 -26.66667 -9.77778

0 0 1 0.44444 -0.44444 12.33333 10.22222

0 0 1 -0.55556 0.55556 -1.66667 -1.77778
```

The headers for each of the columns for the example design matrix are as follows and were not placed in the design matrix file used to run randomise.

```
Group1 Group2 Group3 Site1 Site2 Age_Demean Cog_Var_Demean
```

In the contrast file, the same headers as the design matrix were used. A positive correlation was coded as 1 in cognitive variable column, while -1 was used for a negative correlation. All other columns were set to 0 [180, 193]. An example contrast matrix to perform correlations that corresponds to the example design matrix is as follows:

```
/NumWaves 5

/NumContrasts 2

/Matrix

0 0 0 0 1

0 0 0 0 -1
```

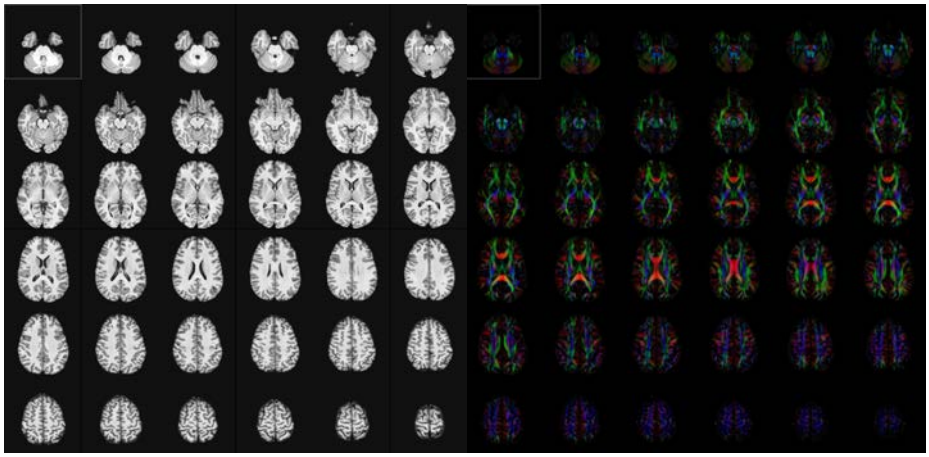

Figure A.13: T1-weighted (left) and DTI templates (right) for SPMS data.

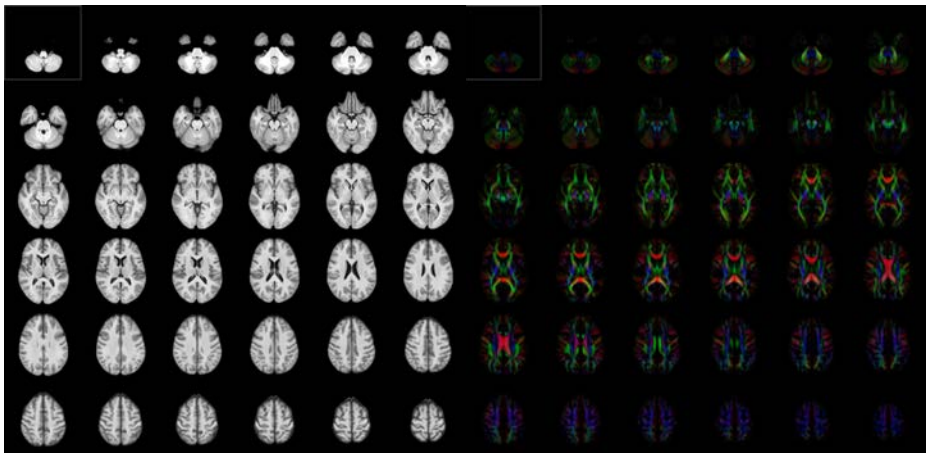

Figure A.14: T1-weighted (left) and DTI templates (right) for MPSS data.

A.4 T1 and DTI atlases

A.5 Results for expanded multi-participant, multi-site data

This section contains the full set of results for the cross-sectional fiber tracking study performed on the expanded multi-participant, multi-site (EMPMS) data introduced in Section 4.2.1.4. An abbreviated version of the EMPMS cross-sectional

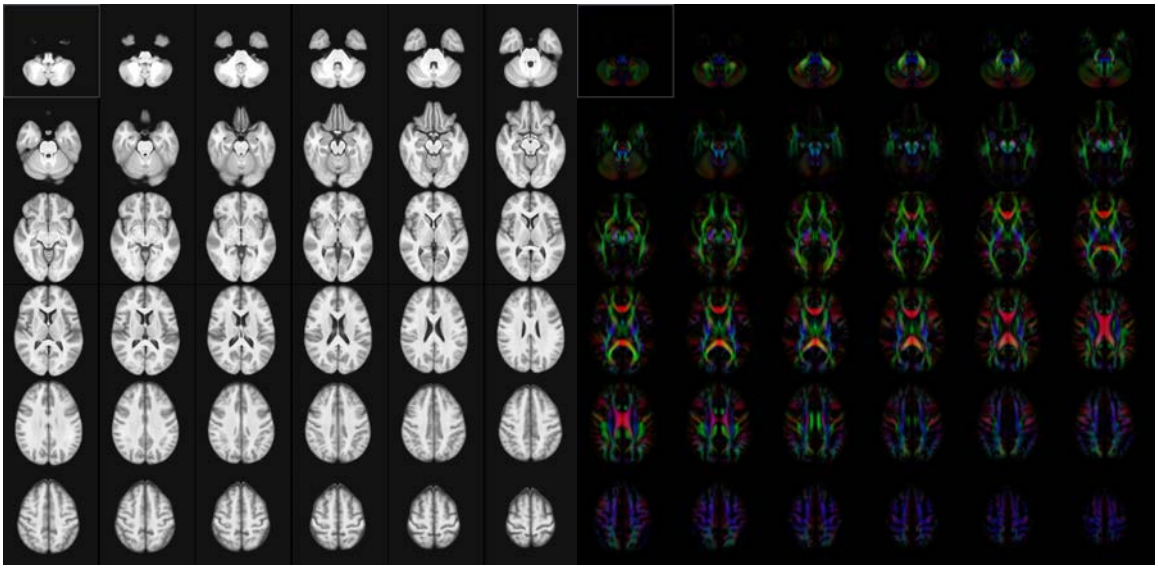

Figure A.15: T1-weighted (left) and DTI templates (right) for MPMS data.

fiber tracking study can be found in Section 4.3.6.

A.5.1 Mean DTI scalar values across tracts and tract skeletons

Figures A.16 through A.22 consist of boxplots of mean FA, MD, AD, and RD across each tract and tract skeleton for controls and each CAP score group (low, medium, and high). Mean DTI scalars are show for each indivudal tract: FM, left and right ATRs, left and right inferior fronto-occipital fasciculi, and left and right uncinate fasciculi. It is important to note that mean DTI scalar values across tract skeletons are generally greater than those across the tracts.

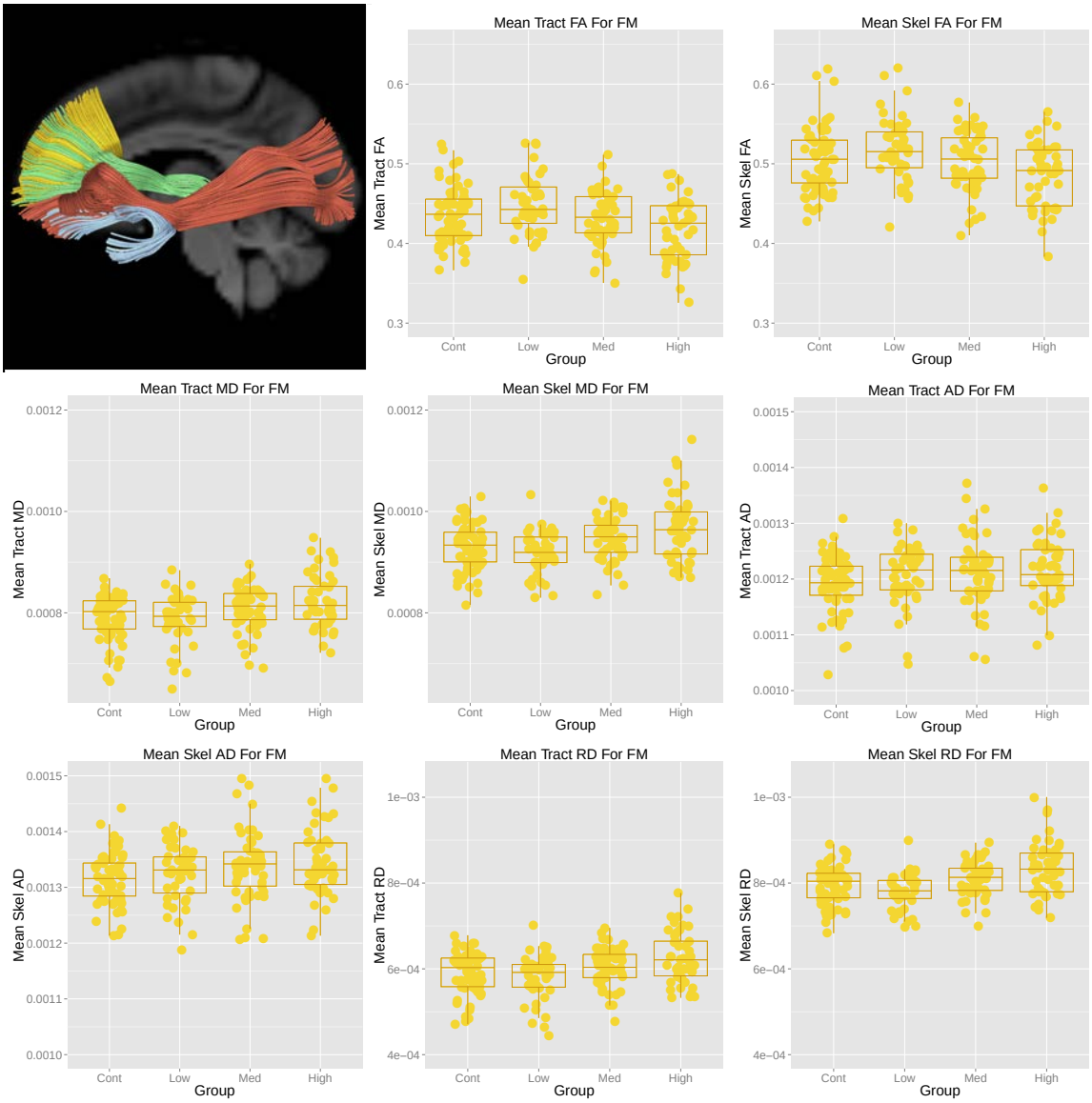

Figure A.16: Mean DTI scalars (FA, MD, AD, and RD) across the entire FM tract and the FM tract skeleton for EMPMS data. FM = Forceps minor. FA = Fractional anisotropy. MD = Mean diffusivity. AD = Axial diffusivity. RD = Radial diffusivity.

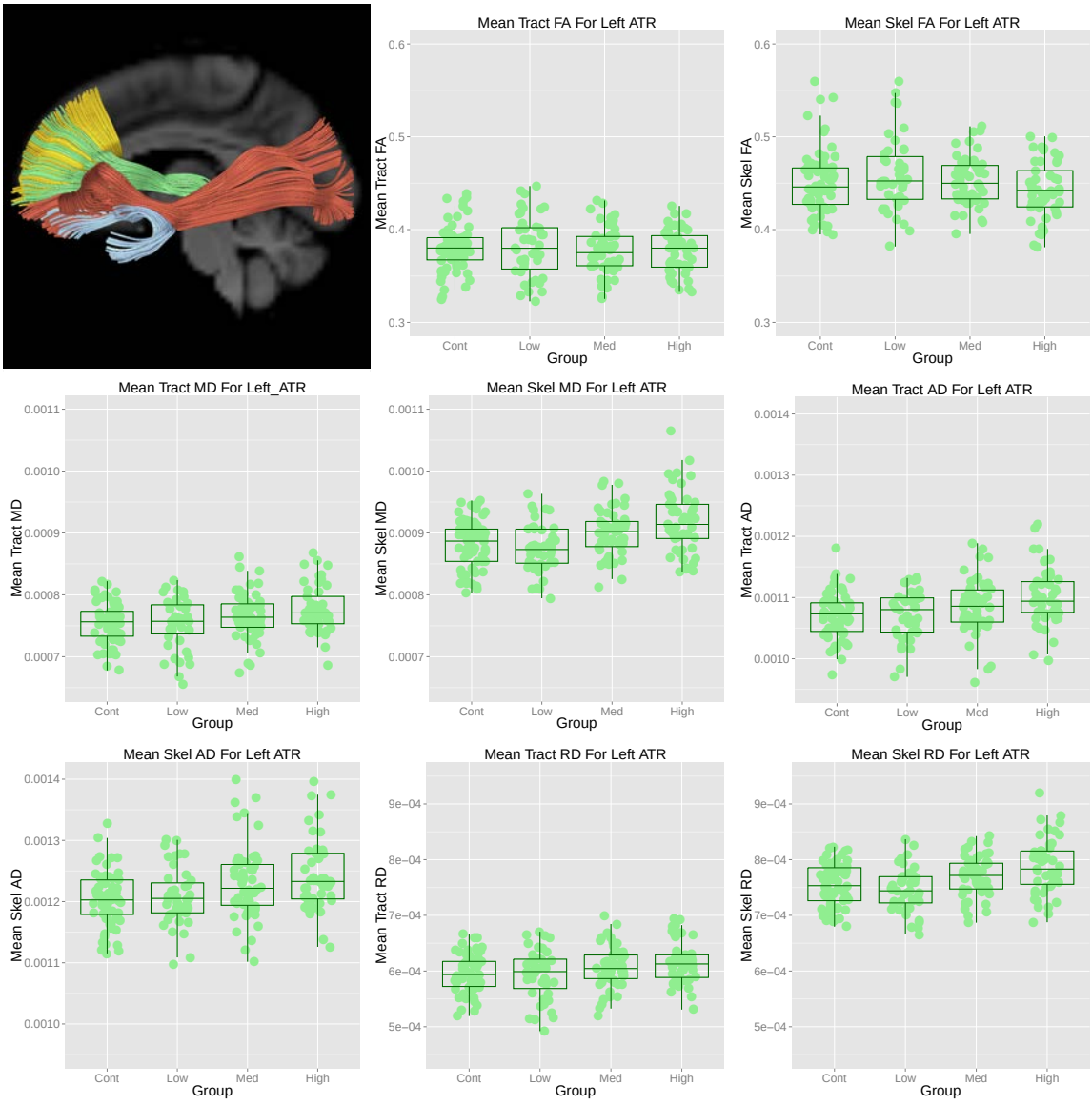

Figure A.17: Mean DTI scalars (FA, MD, AD, and RD) across the entire right ATR tract and the right ATR tract skeleton for EMPMS data. Left ATR = Left anterior thalamic radiations. FA = Fractional anisotropy. MD = Mean diffusivity. AD = Axial diffusivity. RD = Radial diffusivity.

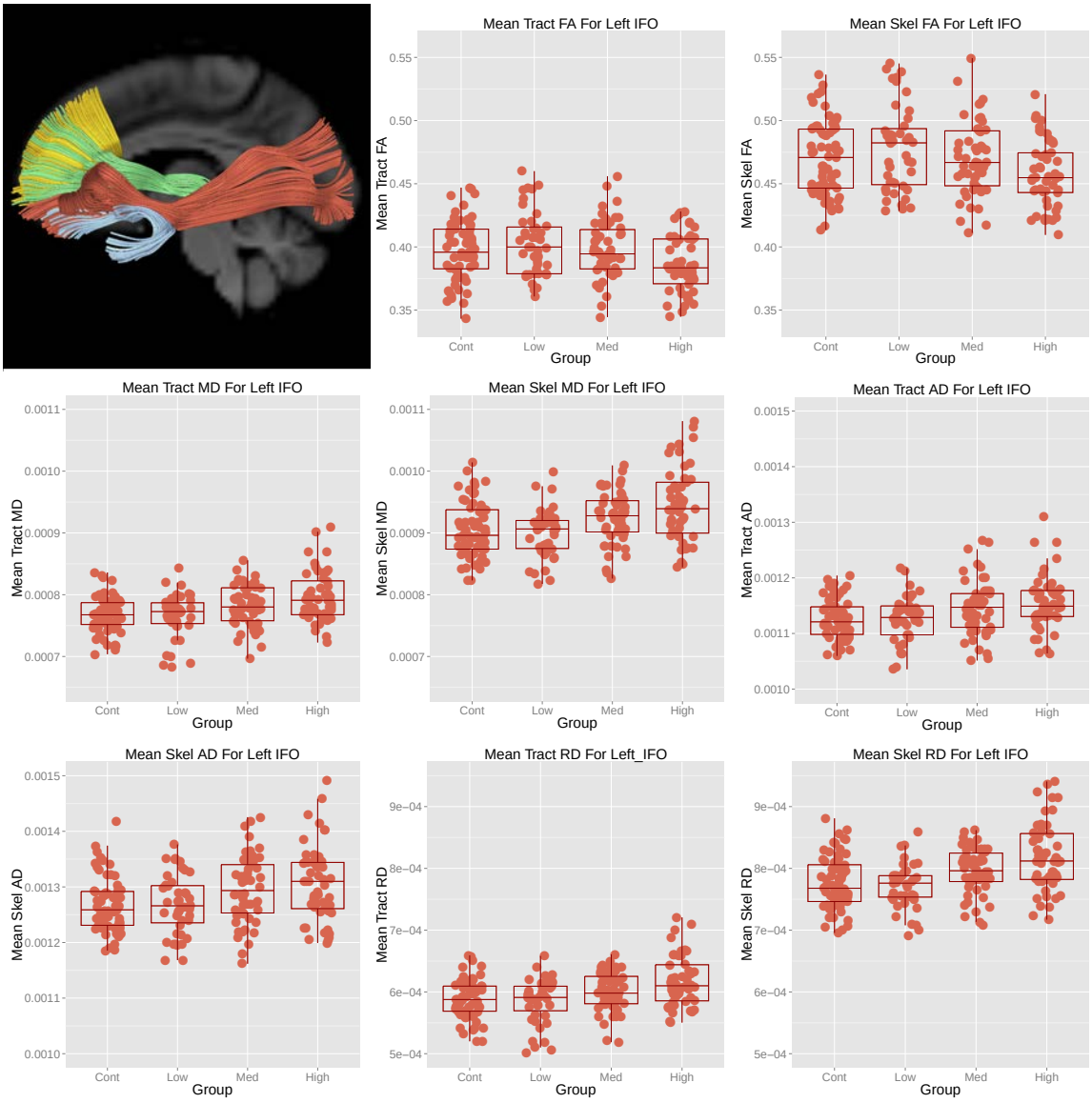

Figure A.18: Mean DTI scalars (FA, MD, AD, and RD) across the entire right IFO tract and the right IFO tract skeleton for EMPMS data. Left IFO = Left inferior fronto-occipital fasciculus. FA = Fractional anisotropy. MD = Mean diffusivity. AD = Axial diffusivity. RD = Radial diffusivity.

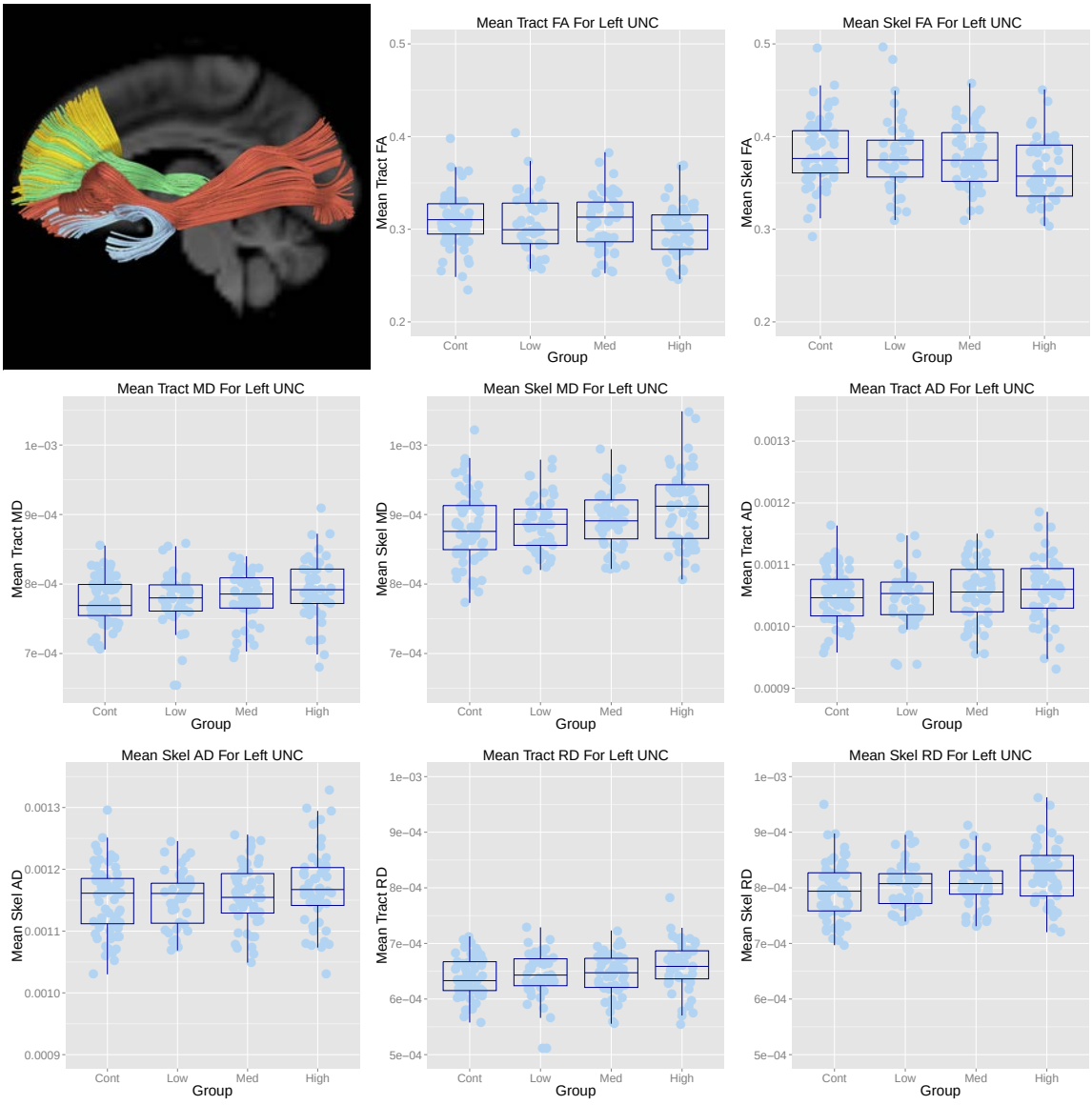

Figure A.19: Mean DTI scalars (FA, MD, AD, and RD) across the entire right UNC tract and the right UNC tract skeleton for EMPMS data. Left UNC = Left uncinate fasciculus. FA = Fractional anisotropy. MD = Mean diffusivity. AD = Axial diffusivity. RD = Radial diffusivity.

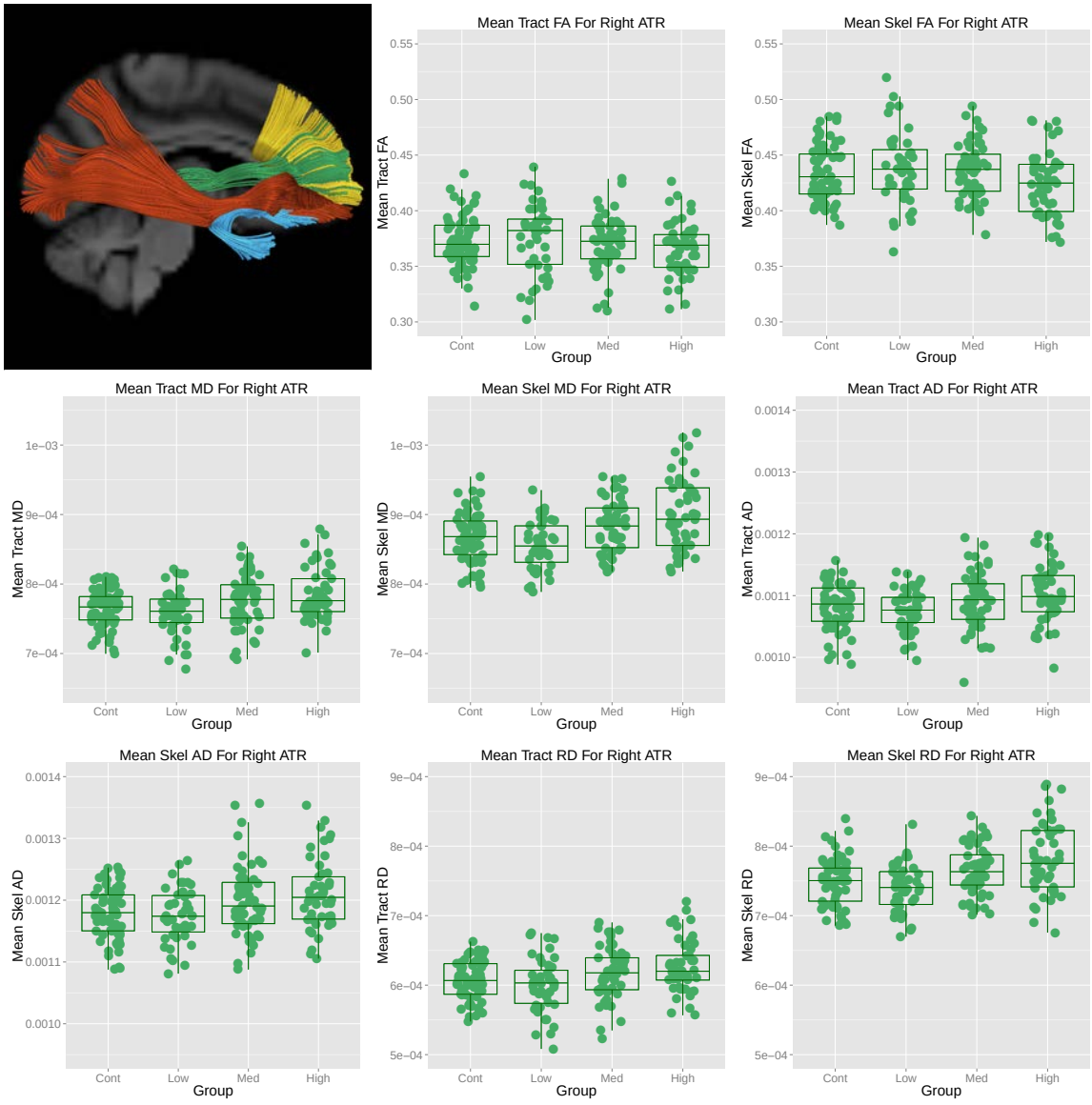

Figure A.20: Mean DTI scalars (FA, MD, AD, and RD) across the entire right ATR tract and the right ATR tract skeleton for EMPMS data. Right ATR = Right anterior thalamic radiations. FA = Fractional anisotropy. MD = Mean diffusivity. AD = Axial diffusivity. RD = Radial diffusivity.

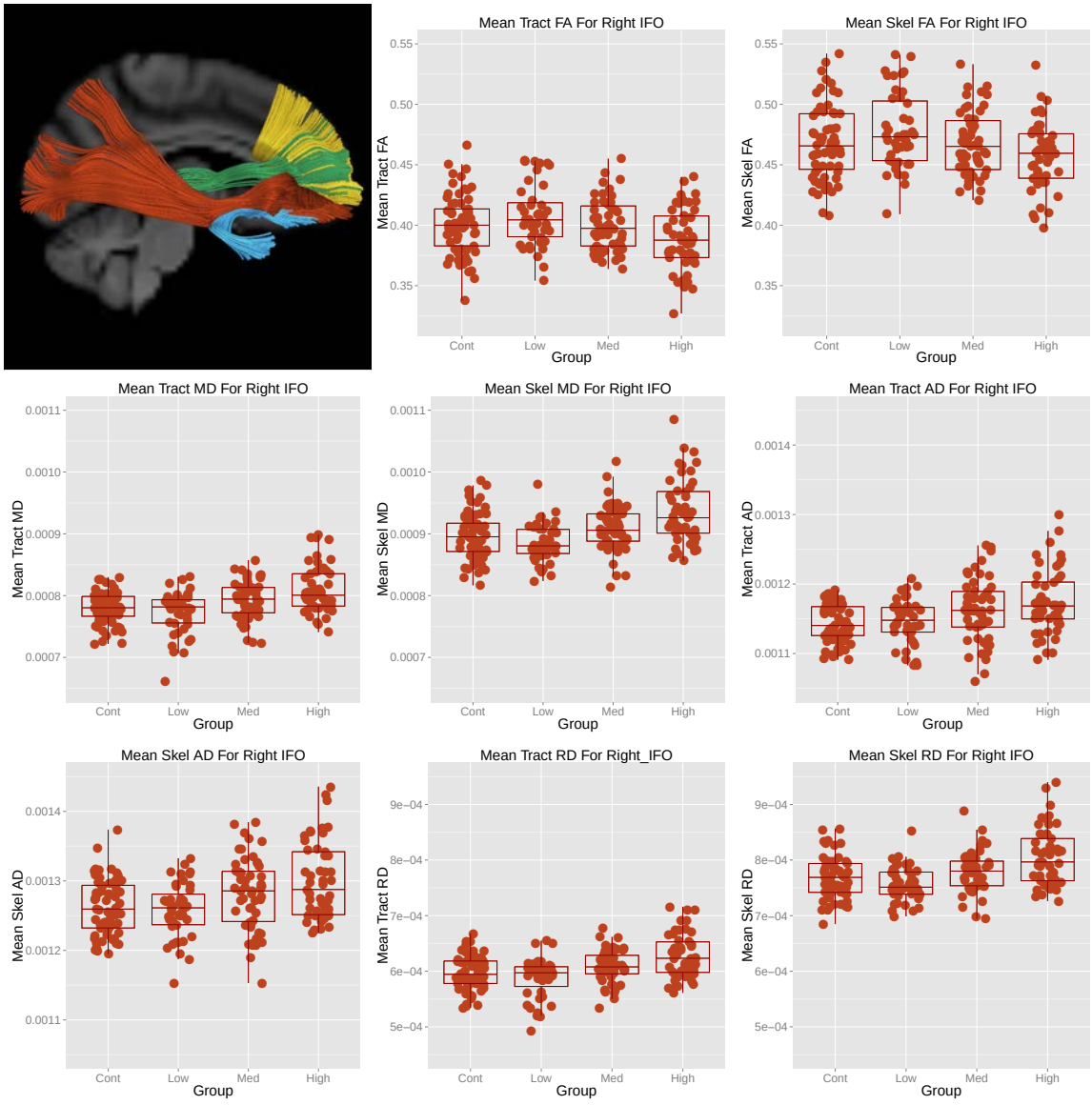

Figure A.21: Mean DTI scalars (FA, MD, AD, and RD) across the entire right IFO tract and the right IFO tract skeleton for EMPMS data. Right IFO = Right inferior fronto-occipital fasciculus. FA = Fractional anisotropy. MD = Mean diffusivity. AD = Axial diffusivity. RD = Radial diffusivity.

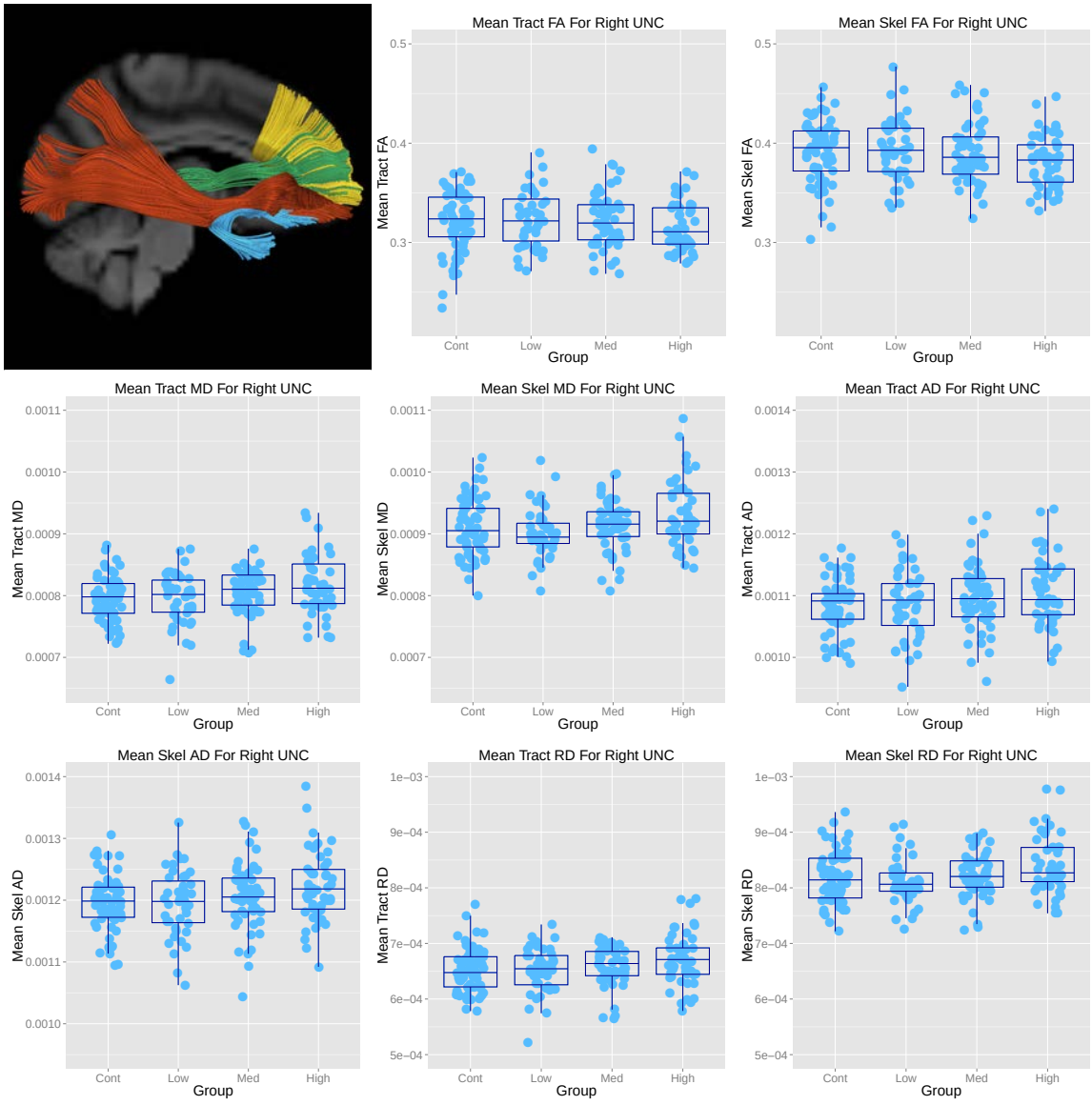

Figure A.22: Mean DTI scalars (FA, MD, AD, and RD) across the entire right UNC tract and the right UNC tract skeleton for EMPMS data. Right UNC = Right uncinate fasciculus. FA = Fractional anisotropy. MD = Mean diffusivity. AD = Axial diffusivity. RD = Radial diffusivity.

Table A.1: Summary of partial correlations between SDMT scores and imaging variables from prodromal HD participants only for left hemisphere regions.

		FA			MD			RD			AD			WM		
Reg	N	Corr	p	q	Corr	p	q	Corr	p	q	Corr	p	q	Corr	p	q
1	51	-0.14	0.34	0.88	-0.06	0.70	0.87	-0.02	0.87	0.92	-0.09	0.55	0.82	-0.01	0.94	0.99
2	51	0.13	0.38	0.88	-0.10	0.50	0.82	-0.12	0.41	0.74	-0.06	0.70	0.82	-0.04	0.80	0.99
3	51	0.25	0.09	0.88	-0.08	0.57	0.86	-0.15	0.32	0.74	0.04	0.79	0.82	0.11	0.48	0.99
4	51	0.01	0.95	0.99	0.06	0.68	0.87	0.03	0.85	0.92	0.10	0.51	0.82	-0.02	0.88	0.99
5	51	0.13	0.39	0.88	-0.14	0.35	0.82	-0.20	0.18	0.68	-0.03	0.82	0.82	-0.02	0.89	0.99
6	51	>-0.01	0.99	0.99	-0.14	0.35	0.82	-0.13	0.38	0.74	-0.13	0.38	0.82	0.07	0.64	0.99
7	51	<0.01	0.99	0.99	-0.10	0.49	0.82	-0.09	0.53	0.84	-0.10	0.52	0.82	-0.03	0.83	0.99
8	51	-0.07	0.64	0.99	0.01	0.97	0.97	0.03	0.86	0.92	-0.04	0.81	0.82	0.11	0.45	0.99
9	51	0.04	0.80	0.99	-0.05	0.72	0.87	-0.06	0.69	0.92	-0.03	0.82	0.82	-0.15	0.33	0.99

Source: J. T. Matsui, J. G. Vaidya, H. J. Johnson, V. A. Magnotta, J. D. Long, J. A. Mills, M. J. Lowe, K. E. Sakaie, S. M. Rao, M. M. Smith, and J. S. Paulsen, Diffusion weighted imaging of prefrontal cortex in prodromal huntingtons disease., Human Brain Mapping, 2013.

Note: FDR correction was performed across regions in both hemispheres. The Pearsons correlation analysis included age, years of education, gender, and site as covariates. WM = white matter volume. Reg = Region. p = Raw p-value. q = FDR q-value. Region 1 = Left caudal middle frontal. Region 2 = Left frontal pole. Region 3 = Left lateral orbitofrontal. Region 4 = Left medial orbitofrontal. Region 5 = Left pars opercularis. Region 6 = Left pars orbitalis. Region 7 = Left pars triangularis. Region 8 = Left rostral middle frontal. Region 9 = Left superior frontal.

Table A.2: Summary of partial correlations between SDMT scores and imaging variables from prodromal HD participants only for right hemisphere regions.

		FA			MD			RD			AD			WM		
Reg	N	Corr	p	q	Corr	p	q	Corr	p	q	Corr	p	q	Corr	p	q
1	51	-0.07	0.65	0.99	-0.11	0.44	0.82	-0.09	0.54	0.82	-0.12	0.40	0.82	>-0.01	0.99	0.99
2	51	0.21	0.16	0.88	-0.14	0.35	0.82	-0.15	0.32	0.74	-0.11	0.47	0.82	-0.12	0.41	0.99
3	51	0.14	0.33	0.88	-0.18	0.22	0.83	-0.20	0.19	0.68	-0.13	0.40	0.82	0.28	0.06	0.99
4	51	<0.01	0.99	0.99	0.02	0.88	0.97	0.01	0.93	0.93	0.03	0.82	0.82	0.21	0.15	0.99
5	51	0.05	0.73	0.99	-0.18	0.23	0.82	-0.19	0.19	0.68	-0.11	0.46	0.82	-0.07	0.64	0.99
6	51	-0.10	0.49	0.98	-0.28	0.05	0.82	-0.24	0.11	0.68	-0.32*	0.03	0.51	-0.01	0.94	0.99
7	51	0.01	0.94	0.99	-0.22	0.14	0.82	-0.23	0.12	0.68	-0.19	0.21	0.82	0.11	0.46	0.99
8	51	-0.17	0.25	0.88	0.01	0.95	0.97	0.05	0.75	0.92	-0.06	0.69	0.82	-0.09	0.56	0.99
9	51	0.14	0.34	0.88	-0.11	0.47	0.82	-0.14	0.35	0.74	-0.05	0.76	0.82	0.11	0.47	0.99

Source: J. T. Matsui, J. G. Vaidya, H. J. Johnson, V. A. Magnotta, J. D. Long, J. A. Mills, M. J. Lowe, K. E. Sakaie, S. M. Rao, M. M. Smith, and J. S. Paulsen, Diffusion weighted imaging of prefrontal cortex in prodromal huntingtons disease., Human Brain Mapping, 2013.

Note: FDR correction was performed across regions in both hemispheres. The Pearsons correlation analysis included age, years of education, gender, and site as covariates. $^*p < 0.05$ before FDR correction. WM = white matter volume. Reg = Region. p = Raw p-value. q = FDR q-value. Region 1 = Right caudal middle frontal. Region 2 = Right frontal pole. Region 3 = Right lateral orbitofrontal. Region 4 = Right medial orbitofrontal. Region 5 = Right pars opercularis. Region 6 = Right pars orbitalis. Region 7 = Right pars triangularis. Region 8 = Right rostral middle frontal. Region 9 = Right superior frontal.

Table A.3: Summary of partial correlations between Trail Making Test A scores and imaging variables from prodromal HD participants only for left hemisphere regions.

		FA			MD			RD			AD			WM		
Reg	N	Corr	p	q	Corr	p	q	Corr	p	q	Corr	p	q	Corr	p	q
1	51	0.07	0.64	0.99	-0.11	0.46	0.69	-0.11	0.47	0.91	-0.10	0.52	0.67	-0.11	0.46	0.84
2	51	-0.23	0.12	0.99	0.05	0.72	0.81	0.05	0.72	0.91	0.01	0.95	0.95	<0.01	0.99	0.99
3	51	-0.10	0.52	0.99	-0.17	0.25	0.69	-0.10	0.48	0.91	-0.26	0.08	0.30	0.10	0.52	0.84
4	51	-0.02	0.90	0.99	-0.32*	0.03	0.39	-0.26	0.07	0.72	-0.32*	0.03	0.30	0.23	0.13	0.84
5	51	-0.15	0.30	0.99	-0.08	0.59	0.72	<0.01	0.98	0.98	-0.16	0.27	0.45	<0.01	0.98	0.99
6	51	0.02	0.90	0.99	-0.15	0.33	0.69	-0.13	0.37	0.91	-0.14	0.34	0.50	0.14	0.34	0.84
7	51	-0.10	0.49	0.99	-0.18	0.22	0.69	-0.12	0.44	0.91	-0.26	0.08	0.30	0.13	0.39	0.84
8	51	-0.08	0.61	0.99	-0.14	0.36	0.69	-0.06	0.67	0.91	-0.26	0.07	0.30	0.15	0.32	0.84
9	51	0.01	0.97	0.99	-0.13	0.40	0.69	-0.10	0.52	0.91	-0.16	0.28	0.45	0.09	0.56	0.84

Source: J. T. Matsui, J. G. Vaidya, H. J. Johnson, V. A. Magnotta, J. D. Long, J. A. Mills, M. J. Lowe, K. E. Sakaie, S. M. Rao, M. M. Smith, and J. S. Paulsen, Diffusion weighted imaging of prefrontal cortex in prodromal huntingtons disease., Human Brain Mapping, 2013.

Note: FDR correction was performed across regions in both hemispheres. The Pearsons correlation analysis included age, years of education, gender, and site as covariates. $^*p < 0.05$ before FDR correction. WM = white matter volume. Reg = Region. p = Raw p-value. q = FDR q-value. Region 1 = Left caudal middle frontal. Region 2 = Left frontal pole. Region 3 = Left lateral orbitofrontal. Region 4 = Left medial orbitofrontal. Region 5 = Left pars opercularis. Region 6 = Left pars orbitalis. Region 7 = Left pars triangularis. Region 8 = Left rostral middle frontal. Region 9 = Left superior frontal.

Table A.4: Summary of partial correlations between Trail Making Test A scores and imaging variables from prodromal HD participants only for right hemisphere regions.

		FA			MD			RD			AD			WM		
Reg	N	Corr	p	q	Corr	p	q	Corr	p	q	Corr	p	q	Corr	p	q
1	51	0.01	0.96	0.99	-0.09	0.53	0.72	-0.07	0.64	0.91	-0.11	0.46	0.64	-0.02	0.87	0.98
2	51	0.03	0.84	0.99	0.01	0.96	0.99	-0.03	0.82	0.92	0.03	0.82	0.92	0.22	0.13	0.84
3	51	>-0.01	0.99	0.99	-0.08	0.60	0.72	-0.07	0.62	0.91	-0.08	0.61	0.73	-0.16	0.28	0.84
4	51	-0.02	0.88	0.99	-0.30*	0.04	0.39	-0.26	0.08	0.72	-0.29*	0.04	0.30	-0.08	0.60	0.84
5	51	>-0.01	0.99	0.99	-0.13	0.39	0.69	-0.08	0.60	0.91	-0.17	0.27	0.45	0.04	0.78	0.98
6	51	0.05	0.72	0.99	<0.01	0.99	0.99	-0.01	0.94	0.98	0.02	0.90	0.95	0.09	0.54	0.84
7	51	-0.11	0.46	0.99	-0.15	0.31	0.69	-0.11	0.47	0.91	-0.19	0.20	0.45	0.16	0.29	0.84
8	51	-0.12	0.44	0.99	-0.12	0.43	0.69	-0.05	0.76	0.91	-0.23	0.12	0.35	0.08	0.61	0.84
9	51	-0.03	0.87	0.99	-0.11	0.44	0.69	-0.08	0.60	0.91	-0.16	0.27	0.45	0.03	0.85	0.98

Source: J. T. Matsui, J. G. Vaidya, H. J. Johnson, V. A. Magnotta, J. D. Long, J. A. Mills, M. J. Lowe, K. E. Sakaie, S. M. Rao, M. M. Smith, and J. S. Paulsen, Diffusion weighted imaging of prefrontal cortex in prodromal huntingtons disease., Human Brain Mapping, 2013.

Note: FDR correction was performed across regions in both hemispheres. The Pearsons correlation analysis included age, years of education, gender, and site as covariates. $^*p < 0.05$ before FDR correction. WM = white matter volume. Reg = Region. p = Raw p-value. q = FDR q-value. Region 1 = Right caudal middle frontal. Region 2 = Right frontal pole. Region 3 = Right lateral orbitofrontal. Region 4 = Right medial orbitofrontal. Region 5 = Right pars opercularis. Region 6 = Right pars orbitalis. Region 7 = Right pars triangularis. Region 8 = Right rostral middle frontal. Region 9 = Right superior frontal.

Table A.5: Summary of partial correlations between Trail Making Test B scores and imaging variables from prodromal HD participants only for left hemisphere regions.

		FA			MD			RD			AD			WM		
Reg	N	Corr	p	q	Corr	p	q	Corr	p	q	Corr	p	q	Corr	p	q
1	50	-0.31*	0.04	0.10	0.11	0.45	0.51	0.21	0.15	0.23	-0.03	0.85	0.99	0.08	0.58	0.81
2	50	-0.23	0.12	0.16	0.05	0.73	0.73	0.06	0.71	0.71	0.01	0.96	0.99	0.02	0.89	0.94
3	50	-0.33*	0.02	0.09	0.19	0.21	0.39	0.25	0.09	0.19	0.05	0.73	0.99	-0.03	0.84	0.94
4	50	-0.24	0.11	0.16	0.14	0.34	0.48	0.21	0.17	0.23	<0.01	0.99	0.99	0.09	0.53	0.81
5	50	-0.23	0.12	0.16	0.17	0.25	0.39	0.24	0.11	0.19	0.05	0.73	0.99	0.20	0.19	0.69
6	50	-0.27	0.07	0.15	0.17	0.25	0.39	0.21	0.16	0.23	0.10	0.53	0.99	0.30*	0.04	0.55
7	50	-0.32*	0.03	0.09	0.17	0.26	0.39	0.24	0.10	0.19	0.01	0.97	0.99	0.25	0.09	0.55
8	50	-0.17	0.26	0.32	0.19	0.21	0.39	0.19	0.20	0.24	0.14	0.35	0.99	0.08	0.59	0.81
9	50	-0.26	0.08	0.15	0.12	0.42	0.51	0.16	0.27	0.31	0.02	0.89	0.99	0.15	0.32	0.75

Source: J. T. Matsui, J. G. Vaidya, H. J. Johnson, V. A. Magnotta, J. D. Long, J. A. Mills, M. J. Lowe, K. E. Sakaie, S. M. Rao, M. M. Smith, and J. S. Paulsen, Diffusion weighted imaging of prefrontal cortex in prodromal huntingtons disease., Human Brain Mapping, 2013.

Note: FDR correction was performed across regions in both hemispheres. The Pearsons correlation analysis included age, years of education, gender, and site as covariates. $^*p < 0.05$ before FDR correction. WM = white matter volume. Reg = Region. p = Raw p-value. q = FDR q-value. Region 1 = Left caudal middle frontal. Region 2 = Left frontal pole. Region 3 = Left lateral orbitofrontal. Region 4 = Left medial orbitofrontal. Region 5 = Left pars opercularis. Region 6 = Left pars orbitalis. Region 7 = Left pars triangularis. Region 8 = Left rostral middle frontal. Region 9 = Left superior frontal.

Table A.6: Summary of partial correlations between Trail Making Test B scores and imaging variables from prodromal HD participants only for right hemisphere regions.

		FA			MD			RD			AD			WM		
Reg	N	Corr	p	q	Corr	p	q	Corr	p	q	Corr	p	q	Corr	p	q
1	50	-0.24	0.11	0.16	0.21	0.16	0.39	0.28	0.06	0.19	0.08	0.61	0.99	0.12	0.42	0.75
2	50	-0.12	0.42	0.42	0.08	0.60	0.63	0.09	0.53	0.57	0.06	0.67	0.99	0.13	0.38	0.75
3	50	-0.36*	0.03	0.07	0.35*	0.02	0.16	0.39**	0.01	0.07	0.22	0.14	0.83	-0.12	0.42	0.75
4	50	-0.43***†	<0.01	0.04	0.13	0.40	0.51	0.25	0.09	0.19	-0.06	0.67	0.99	-0.25	0.09	0.55
5	50	-0.42***†	<0.01	0.04	0.23	0.12	0.39	0.36*	0.01	0.08	>-0.01	0.98	0.99	-0.01	0.95	0.95
6	50	-0.14	0.36	0.40	0.30*	0.05	0.28	0.30*	0.04	0.19	0.26	0.09	0.83	0.21	0.17	0.69
7	50	-0.40**†	<0.01	0.04	0.35*	0.02	0.16	0.44***†	<0.01	0.04	0.20	0.19	0.83	0.04	0.82	0.94
8	50	-0.13	0.38	0.40	0.26	0.08	0.36	0.24	0.10	0.19	0.25	0.09	0.83	0.13	0.38	0.75
9	50	-0.26	0.08	0.15	0.18	0.23	0.39	0.20	0.18	0.23	0.11	0.45	0.99	-0.03	0.83	0.94

Source: J. T. Matsui, J. G. Vaidya, H. J. Johnson, V. A. Magnotta, J. D. Long, J. A. Mills, M. J. Lowe, K. E. Sakaie, S. M. Rao, M. M. Smith, and J. S. Paulsen, Diffusion weighted imaging of prefrontal cortex in prodromal huntingtons disease., Human Brain Mapping, 2013.

Note: FDR correction was performed across regions in both hemispheres. The Pearsons correlation analysis included age, years of education, gender, and site as covariates. $^{*}p < 0.05$ before FDR correction. $^{**}p < 0.01$ before FDR correction. $^{***}p < 0.005$ before FDR correction. $^{\dagger}p < 0.05$ after FDR correction. WM = white matter volume. Reg = Region. p = Raw p-value. q = FDR q-value. Region 1 = Right caudal middle frontal. Region 2 = Right frontal pole. Region 3 = Right lateral orbitofrontal. Region 4 = Right medial orbitofrontal. Region 5 = Right pars opercularis. Region 6 = Right pars orbitalis. Region 7 = Right pars triangularis. Region 8 = Right rostral middle frontal. Region 9 = Right superior frontal.

Table A.7: Summary of partial correlations between Stroop Word scores and imaging variables from prodromal HD participants for left hemisphere regions.

		FA			MD			RD			AD			WM		
Reg	N	Corr	p	q	Corr	p	q	Corr	p	q	Corr	p	q	Corr	p	q
1	49	0.04	0.78	0.81	-0.18	0.25	0.35	-0.19	0.20	0.24	-0.13	0.41	0.67	-0.03	0.82	0.95
2	49	0.27	0.07	0.19	-0.22	0.15	0.26	-0.24	0.12	0.16	-0.16	0.29	0.65	-0.09	0.56	0.95
3	49	0.35*	0.02	0.18	-0.15	0.31	0.38	-0.25	0.10	0.16	0.02	0.87	0.88	0.01	0.94	0.95
4	49	0.12	0.42	0.50	-0.05	0.73	0.73	-0.11	0.47	0.47	0.04	0.80	0.88	-0.10	0.51	0.95
5	49	0.14	0.34	0.46	-0.18	0.23	0.35	-0.25	0.09	0.16	-0.05	0.74	0.88	-0.09	0.54	0.95
6	49	0.29	0.05	0.18	-0.17	0.25	0.35	-0.23	0.13	0.17	-0.08	0.62	0.86	0.04	0.79	0.95
7	49	0.30*	0.05	0.18	-0.16	0.29	0.37	-0.25	0.10	0.16	0.03	0.86	0.88	0.05	0.75	0.95
8	49	0.21	0.17	0.34	-0.23	0.12	0.24	-0.25	0.10	0.16	-0.14	0.36	0.65	0.07	0.65	0.95
9	49	0.31*	0.04	0.18	-0.24	0.11	0.24	-0.28	0.07	0.16	-0.15	0.34	0.65	-0.33*	0.03	0.46

Source: J. T. Matsui, J. G. Vaidya, H. J. Johnson, V. A. Magnotta, J. D. Long, J. A. Mills, M. J. Lowe, K. E. Sakaie, S. M. Rao, M. M. Smith, and J. S. Paulsen, Diffusion weighted imaging of prefrontal cortex in prodromal huntingtons disease., Human Brain Mapping, 2013.

Note: FDR correction was performed across regions in both hemispheres. The Pearsons correlation analysis included age, years of education, gender, and site as covariates. $^*p < 0.05$ before FDR correction. WM = white matter volume. Reg = Region. p = Raw p-value. q = FDR q-value. Region 1 = Left caudal middle frontal. Region 2 = Left frontal pole. Region 3 = Left lateral orbitofrontal. Region 4 = Left medial orbitofrontal. Region 5 = Left pars opercularis. Region 6 = Left pars orbitalis. Region 7 = Left pars triangularis. Region 8 = Left rostral middle frontal. Region 9 = Left superior frontal.

Table A.8: Summary of partial correlations between Stroop Word scores and imaging variables from prodromal HD participants for right hemisphere regions.

		FA			MD			RD			AD			WM		
Reg	N	Corr	p	q	Corr	p	q	Corr	p	q	Corr	p	q	Corr	p	q
1	49	0.10	0.51	0.58	-0.25	0.09	0.24	-0.27	0.08	0.16	-0.18	0.23	0.65	0.17	0.26	0.95
2	49	-0.04	0.81	0.81	0.14	0.35	0.40	0.14	0.36	0.41	0.15	0.33	0.65	-0.05	0.77	0.95
3	49	0.26	0.09	0.20	-0.38**	0.01	0.16	-0.39**	0.01	0.08	-0.30*	0.05	0.52	0.10	0.53	0.95
4	49	0.16	0.29	0.44	-0.08	0.58	0.62	-0.12	0.45	0.47	-0.02	0.88	0.88	0.15	0.34	0.95
5	49	0.17	0.26	0.43	-0.27	0.08	0.23	-0.33*	0.03	0.08	-0.11	0.47	0.70	-0.07	0.67	0.95
6	49	0.14	0.36	0.46	-0.32*	0.03	0.16	-0.33*	0.02	0.08	-0.27	0.08	0.52	-0.16	0.29	0.95
7	49	0.27	0.07	0.19	-0.29	0.06	0.20	-0.36*	0.02	0.08	-0.17	0.25	0.65	-0.07	0.64	0.95
8	49	0.17	0.26	0.43	-0.33*	0.03	0.16	-0.34*	0.02	0.08	-0.26	0.09	0.52	0.02	0.90	0.95
9	49	0.32*	0.03	0.18	-0.32*	0.03	0.16	-0.34*	0.02	0.08	-0.23	0.13	0.57	0.01	0.95	0.95

Source: J. T. Matsui, J. G. Vaidya, H. J. Johnson, V. A. Magnotta, J. D. Long, J. A. Mills, M. J. Lowe, K. E. Sakaie, S. M. Rao, M. M. Smith, and J. S. Paulsen, Diffusion weighted imaging of prefrontal cortex in prodromal huntingtons disease., Human Brain Mapping, 2013.

Note: FDR correction was performed across regions in both hemispheres. The Pearsons correlation analysis included age, years of education, gender, and site as covariates. $^{*}p < 0.05$ before FDR correction. $^{**}p < 0.01$ before FDR correction. WM = white matter volume. Reg = Region. p = Raw p-value. q = FDR q-value. Region 1 = Right caudal middle frontal. Region 2 = Right frontal pole. Region 3 = Right lateral orbitofrontal. Region 4 = Right medial orbitofrontal. Region 5 = Right pars opercularis. Region 6 = Right pars orbitalis. Region 7 = Right pars triangularis. Region 8 = Right rostral middle frontal. Region 9 = Right superior frontal.

Table A.9: Summary of partial correlations between Stroop Color scores and imaging variables from prodromal HD participants for left hemisphere regions.

		FA			MD			RD			AD			WM		
Reg	N	Corr	p	q	Corr	p	q	Corr	p	q	Corr	p	q	Corr	p	q
1	49	-0.02	0.89	0.94	-0.13	0.40	0.56	-0.12	0.42	0.57	-0.11	0.47	0.74	-0.08	0.60	0.88
2	49	0.24	0.12	0.83	-0.10	0.52	0.59	-0.11	0.47	0.57	-0.03	0.86	0.91	-0.10	0.52	0.88
3	49	0.33*	0.03	0.45	-0.18	0.23	0.48	-0.27	0.08	0.38	-0.01	0.93	0.93	0.07	0.65	0.88
4	49	0.13	0.38	0.85	0.04	0.81	0.81	-0.03	0.83	0.83	0.11	0.46	0.74	-0.19	0.21	0.74
5	49	0.02	0.88	0.95	-0.23	0.14	0.48	-0.23	0.13	0.38	-0.16	0.31	0.74	0.06	0.71	0.88
6	49	0.15	0.32	0.83	-0.12	0.45	0.56	-0.14	0.37	0.57	-0.08	0.62	0.74	0.04	0.78	0.88
7	49	0.16	0.29	0.83	-0.16	0.31	0.55	-0.20	0.19	0.48	-0.04	0.78	0.88	0.10	0.50	0.88
8	49	0.09	0.54	0.94	-0.12	0.42	0.56	-0.13	0.39	0.57	-0.08	0.62	0.74	0.27	0.07	0.67
9	49	0.04	0.78	0.94	-0.11	0.46	0.56	-0.10	0.51	0.57	-0.12	0.42	0.74	-0.03	0.83	0.88

Source: J. T. Matsui, J. G. Vaidya, H. J. Johnson, V. A. Magnotta, J. D. Long, J. A. Mills, M. J. Lowe, K. E. Sakaie, S. M. Rao, M. M. Smith, and J. S. Paulsen, Diffusion weighted imaging of prefrontal cortex in prodromal huntingtons disease., Human Brain Mapping, 2013.

Note: FDR correction was performed across regions in both hemispheres. The Pearsons correlation analysis included age, years of education, gender, and site as covariates. $^*p < 0.05$ before FDR correction. WM = white matter volume. Reg = Region. p = Raw p-value. q = FDR q-value. Region 1 = Left caudal middle frontal. Region 2 = Left frontal pole. Region 3 = Left lateral orbitofrontal. Region 4 = Left medial orbitofrontal. Region 5 = Left pars opercularis. Region 6 = Left pars orbitalis. Region 7 = Left pars triangularis. Region 8 = Left rostral middle frontal. Region 9 = Left superior frontal.

Table A.10: Summary of partial correlations between Stroop Color scores and imaging variables from prodromal HD participants for right hemisphere regions.

		FA			MD			RD			AD			WM		
Reg	N	Corr	p	q	Corr	p	q	Corr	p	q	Corr	p	q	Corr	p	q
1	49	0.04	0.81	0.94	-0.19	0.21	0.48	-0.18	0.24	0.48	-0.16	0.28	0.74	0.11	0.47	0.88
2	49	-0.07	0.64	0.94	0.12	0.43	0.56	0.10	0.49	0.57	0.15	0.34	0.74	-0.02	0.91	0.91
3	49	0.22	0.14	0.83	-0.36*	0.02	0.29	-0.36*	0.01	0.27	-0.29	0.06	0.74	0.20	0.19	0.74
4	49	<0.01	0.98	0.98	-0.08	0.59	0.63	-0.08	0.62	0.66	-0.08	0.62	0.74	0.13	0.40	0.88
5	49	0.06	0.70	0.94	-0.24	0.11	0.48	-0.26	0.09	0.38	-0.15	0.32	0.74	0.09	0.54	0.88
6	49	0.16	0.31	0.83	-0.23	0.13	0.48	-0.25	0.10	0.38	-0.18	0.24	0.74	-0.03	0.82	0.88
7	49	0.18	0.23	0.83	-0.19	0.22	0.48	-0.24	0.11	0.38	-0.10	0.52	0.74	-0.06	0.70	0.88
8	49	0.02	0.87	0.94	-0.20	0.19	0.48	-0.19	0.22	0.48	-0.18	0.23	0.74	0.31*	0.04	0.67
9	49	0.10	0.52	0.94	-0.18	0.24	0.48	-0.17	0.27	0.48	-0.18	0.23	0.74	0.24	0.11	0.68

Source: J. T. Matsui, J. G. Vaidya, H. J. Johnson, V. A. Magnotta, J. D. Long, J. A. Mills, M. J. Lowe, K. E. Sakaie, S. M. Rao, M. M. Smith, and J. S. Paulsen, Diffusion weighted imaging of prefrontal cortex in prodromal huntingtons disease., Human Brain Mapping, 2013.

Note: FDR correction was performed across regions in both hemispheres. The Pearsons correlation analysis included age, years of education, gender, and site as covariates. $^*p < 0.05$ before FDR correction. WM = white matter volume. Reg = Region. p = Raw p-value. q = FDR q-value. Region 1 = Right caudal middle frontal. Region 2 = Right frontal pole. Region 3 = Right lateral orbitofrontal. Region 4 = Right medial orbitofrontal. Region 5 = Right pars opercularis. Region 6 = Right pars orbitalis. Region 7 = Right pars triangularis. Region 8 = Right rostral middle frontal. Region 9 = Right superior frontal.

Table A.11: Summary of partial correlations between Stroop Interference scores and imaging variables from prodromal HD participants only for left hemisphere regions.

		FA			MD			RD			AD			WM		
Reg	N	Corr	p	q	Corr	p	q	Corr	p	q	Corr	p	q	Corr	p	q
1	49	0.04	0.79	0.84	-0.02	0.89	0.89	-0.05	0.73	0.82	0.02	0.89	0.96	0.11	0.49	0.83
2	49	0.20	0.20	0.74	-0.06	0.67	0.85	-0.10	0.51	0.76	0.01	0.96	0.96	-0.06	0.71	0.87
3	49	0.31*	0.04	0.52	-0.06	0.71	0.85	-0.15	0.32	0.73	0.11	0.46	0.89	0.02	0.88	0.88
4	49	0.03	0.87	0.87	0.15	0.33	0.81	0.10	0.49	0.76	0.17	0.27	0.89	-0.17	0.26	0.66
5	49	0.12	0.42	0.83	-0.11	0.48	0.85	-0.19	0.22	0.66	0.01	0.92	0.96	0.16	0.29	0.66
6	49	0.07	0.63	0.83	-0.07	0.65	0.85	-0.06	0.69	0.82	-0.07	0.65	0.89	-0.04	0.80	0.87
7	49	0.07	0.65	0.83	-0.04	0.79	0.85	-0.07	0.66	0.82	0.02	0.92	0.96	0.16	0.28	0.66
8	49	0.14	0.37	0.83	-0.09	0.57	0.85	-0.11	0.48	0.76	-0.01	0.93	0.96	0.29	0.06	0.66
9	49	0.08	0.60	0.83	-0.09	0.55	0.85	-0.07	0.63	0.82	-0.10	0.50	0.89	-0.15	0.33	0.66

Source: J. T. Matsui, J. G. Vaidya, H. J. Johnson, V. A. Magnotta, J. D. Long, J. A. Mills, M. J. Lowe, K. E. Sakaie, S. M. Rao, M. M. Smith, and J. S. Paulsen, Diffusion weighted imaging of prefrontal cortex in prodromal huntingtons disease., Human Brain Mapping, 2013.

Note: FDR correction was performed across regions in both hemispheres. The Pearsons correlation analysis included age, years of education, gender, and site as covariates. $^*p < 0.05$ before FDR correction. WM = white matter volume. Reg = Region. p = Raw p-value. q = FDR q-value. Region 1 = Left caudal middle frontal. Region 2 = Left frontal pole. Region 3 = Left lateral orbitofrontal. Region 4 = Left medial orbitofrontal. Region 5 = Left pars opercularis. Region 6 = Left pars orbitalis. Region 7 = Left pars triangularis. Region 8 = Left rostral middle frontal. Region 9 = Left superior frontal.

Table A.12: Summary of partial correlations between Stroop Interference scores and imaging variables from prodromal HD participants only for right hemisphere regions.

		FA			MD			RD			AD			WM		
Reg	N	Corr	p	q	Corr	p	q	Corr	p	q	Corr	p	q	Corr	p	q
1	49	0.10	0.52	0.83	-0.14	0.36	0.81	-0.16	0.28	0.73	-0.08	0.61	0.89	0.16	0.31	0.66
2	49	0.10	0.51	0.83	0.04	0.81	0.85	0.03	0.84	0.89	0.08	0.61	0.89	-0.08	0.62	0.87
3	49	0.26	0.09	0.52	-0.27	0.07	0.75	-0.30*	0.05	0.55	-0.18	0.25	0.89	0.21	0.17	0.66
4	49	-0.05	0.73	0.84	-0.05	0.73	0.85	-0.02	0.91	0.91	-0.09	0.56	0.89	0.05	0.72	0.87
5	49	0.08	0.61	0.83	-0.20	0.18	0.75	-0.25	0.09	0.55	-0.08	0.59	0.89	0.10	0.51	0.83
6	49	0.11	0.45	0.83	-0.19	0.21	0.75	-0.19	0.22	0.66	-0.17	0.25	0.89	-0.03	0.82	0.87
7	49	0.26	0.09	0.52	-0.20	0.19	0.75	-0.27	0.07	0.55	-0.09	0.55	0.89	0.05	0.76	0.87
8	49	0.04	0.79	0.84	-0.14	0.35	0.81	-0.13	0.38	0.75	-0.13	0.40	0.89	0.21	0.16	0.66
9	49	0.19	0.21	0.74	-0.21	0.17	0.75	-0.20	0.18	0.66	-0.18	0.24	0.89	0.21	0.17	0.66

Source: J. T. Matsui, J. G. Vaidya, H. J. Johnson, V. A. Magnotta, J. D. Long, J. A. Mills, M. J. Lowe, K. E. Sakaie, S. M. Rao, M. M. Smith, and J. S. Paulsen, Diffusion weighted imaging of prefrontal cortex in prodromal huntingtons disease., Human Brain Mapping, 2013.

Note: FDR correction was performed across regions in both hemispheres. The Pearsons correlation analysis included age, years of education, gender, and site as covariates. $^*p < 0.05$ before FDR correction. WM = white matter volume. Reg = Region. p = Raw p-value. q = FDR q-value. Region 1 = Right caudal middle frontal. Region 2 = Right frontal pole. Region 3 = Right lateral orbitofrontal. Region 4 = Right medial orbitofrontal. Region 5 = Right pars opercularis. Region 6 = Right pars orbitalis. Region 7 = Right pars triangularis. Region 8 = Right rostral middle frontal. Region 9 = Right superior frontal.

APPENDIX B
LONGITUDINAL FIBER TRACKING STUDY SUPPLEMENTAL MATERIAL

B.1 GLM for randomise: linear mixed effects analysis

Three files were required to build a linear mixed effects GLM in randomise for two time points: design matrix, contrast, and group files. All time points for a given participant was considered a block for permuting. Random effects for individual participants were accounted for with intercept columns for each participant in the design matrix. Age was used as time indicators, where each group had a column for age in the design matrix. The remaining covariates (gender, education in years, and site of data acquisition) were each represented in the design matrix with a column for each group. A simplified design matrix for comparing mean change in two groups with six participants over two time points, where age, gender, and two sites are covariates (covariates were demeaned before being split into columns) is shown below [193, 180]:

```
/NumWaves 14

/NumPoints 12

/Matrix

-0.5 0 0.5 0 0.5 0 -0.5 0 1 0 0 0 0 0

1.5 0 0.5 0 0.5 0 -0.5 0 1 0 0 0 0 0

38.5 0 -0.5 0 -0.5 0 0.5 0 0 1 0 0 0 0

40.5 0 -0.5 0 -0.5 0 0.5 0 0 1 0 0 0 0

-25.5 0 -0.5 0 -0.5 0 0.5 0 0 0 1 0 0 0
```

```
-23.5 0 -0.5 0 -0.5 0 0.5 0 0 0 1 0 0 0
0 3.5 0 0.5 0 0.5 0 -0.5 0 0 0 1 0 0
0 5.5 0 0.5 0 0.5 0 -0.5 0 0 0 1 0 0
0 -17.5 0 0.5 0 -0.5 0 0.5 0 0 0 0 1 0
0 -15.5 0 0.5 0 -0.5 0 0.5 0 0 0 0 1 0
0 -4.5 0 -0.5 0 0.5 0 -0.5 0 0 0 0 0 1
0 -2.5 0 -0.5 0 0.5 0 -0.5 0 0 0 0 0 1
```

The headers for the columns of the above example design matrix are as follows and were not placed in the design matrix file used to run randomise (G = group, S = subject, Int = intercept):

```
G1Age G2Age G1Gender G2Gender G1Site1 G2Site1 G1Site2 G2Site2 S1Int
S2Int S3Int S4Int S5Int S6Int
```

The contrast file contained the contrasts and had the same column headers as the design matrix but slightly different header information. Below is an example contrast corresponding to the example design matrix to test if group 2 is increasing faster than group 1 (or is group 1 is decreasing faster than group 2):

```
/NumWaves 14
/NumContrasts 1
/Matrix
-1 1 0 0 0 0 0 0 0 0 0 0 0 0
```

The group file contained a single column assigning a number to each participant, making each participant a permutable block for randomise:

```
/NumWaves 1

/NumPoints 12

/Matrix

1

1

2

2

3

3

4

4

5

5

6

6
```

REFERENCES

[1] M. Catani, R. J. Howard, S. Pajevic, and D. K. Jones, "Virtual in Vivo Interactive Dissection of White Matter Fasciculi in the Human Brain," *NeuroImage*, vol. 17, pp. 77–94, 2002.

[2] J. S. Paulsen, M. Hayden, J. C. Stout, D. R. Langbehn, E. Aylward, C. A. Ross, M. Guttman, M. Nance, K. Kieburtz, D. Oakes, I. Shoulson, E. Kayson, S. Johnson, E. Penziner, and Predict-HD Investigators of the Huntington Study Group, "Preparing for preventive clinical trials: the Predict-HD study," *Archives of Neurology*, vol. 63, pp. 883–90, 2006.

[3] J. S. Paulsen, V. A. Magnotta, A. E. Mikos, H. L. Paulson, E. Penziner, N. C. Andreasen, and P. C. Nopoulos, "Brain structure in preclinical Huntington's disease," *Biological Psychiatry*, vol. 59, pp. 57–63, 2006.

[4] Huntington's Disease Collaborative Research Group, M. E. Macdonald, C. M. Ambrose, M. P. Duyao, R. H. Myers, C. Lin, L. Srinidhi, G. Barnes, S. A. Taylor, M. James, N. Groat, H. Macfarlane, B. Jenkins, M. A. Anderson, N. S. Wexler, J. F. Gusella, L. Riba-ramirer, M. Shah, V. P. Stanton, S. A. Strobel, K. M. Draths, J. L. Wales, P. Dervan, D. E. Housman, T. Fielder, J. J. Wasmuth, D. Tagle, J. Valdes, L. Elmer, M. Allard, L. Castilla, M. Swaroop, K. Blanchard, G. P. Bates, S. Baxendale, H. Hummerich, S. Kirby, M. North, S. Youngman, R. Mott, G. Zehetner, Z. Sedlacek, R. Snell, T. Holloway, K. Gillespie, N. Datson, D. Shaw, and P. S. Harper, "A Novel Gene Containing a Trinucleotide That Is Expanded and Unstable on Huntingtons Disease Chromosomesx," *Cell*, vol. 72, pp. 971–983, 1993.

[5] M. R. Hayden, *Huntington's chorea*, New York, 1981.

[6] P. S. Harper, *Huntington's disease*, W.B. Saunders, London; Philadelphia, 1991.

[7] J. S. Paulsen, D. R. Langbehn, J. C. Stout, E. Aylward, C. A. Ross, M. Nance, M. Guttman, S. Johnson, M. MacDonald, L. J. Beglinger, K. Duff, E. Kayson, K. Biglan, I. Shoulson, D. Oakes, and M. Hayden, "Detection of Huntington's disease decades before diagnosis: the Predict-HD study.," *Journal of Neurology, Neurosurgery & Psychiatry*, vol. 79, pp. 874–880, 2008.

[8] S. J. Tabrizi, R. I. Scahill, A. Durr, R. A. Roos, B. R. Leavitt, R. Jones, G. B. Landwehrmeyer, N. C. Fox, H. Johnson, S. L. Hicks, C. Kennard, D. Craufurd, C. Frost, D. R. Langbehn, R. Reilmann, and J. C. Stout, "Biological and clinical changes in premanifest and early stage Huntington's disease in the TRACK-HD study: the 12-month longitudinal analysis," *Lancet Neurology*, vol. 10, pp. 31–42, 2011.

[9] T. L. Jernigan, D. P. Salmon, N. Butters, and J. R. Hesselink, "Cerebral Structure on MRI, Part II: Specific Changes in Alzheimer's and Huntington's Diseases," *Biological Psychiatry*, vol. 29, pp. 68–81, 1991.

[10] J. R. Campodonico, E. Aylward, A.-m. M. Codori, C. Young, L. Krafft, M. Magdalinski, N. Ranen, P. R. Slavney, and J. Brandt, "When does Huntingtons disease begin?," *Journal of the International Neuropsychological Society*, vol. 4, pp. 467–473, 1998.

[11] G. Harris, N. C. Andreasen, T. Cizadlo, J. M. Bailey, H. J. Bockholt, V. A. Magnotta, and S. Arndt, "Improving tissue classification in MRI: a three-dimensional multispectral discriminant analysis method with automated training class selection.," *Journal of Computer Assisted Tomography*, vol. 23, pp. 144–54, 1999.

[12] E. H. Aylward, A. M. Codori, P. E. Barta, G. D. Pearlson, G. J. Harris, and J. Brandt, "Basal ganglia volume and proximity to onset in presymptomatic Huntington disease.," *Archives of Neurology*, vol. 53, pp. 1293–1296, 1996.

[13] J. S. Paulsen, P. C. Nopoulos, E. Aylward, C. A. Ross, H. Johnson, V. A. Magnotta, A. Juhl, R. K. Pierson, J. Mills, D. Langbehn, and M. Nance, "Striatal and white matter predictors of estimated diagnosis for Huntington disease.," *Brain Research Bulletin*, vol. 82, pp. 201–7, 2010.

[14] L. J. Beglinger, P. C. Nopoulos, R. E. Jorge, D. R. Langbehn, A. E. Mikos, D. J. Moser, K. Duff, R. G. Robinson, and J. S. Paulsen, "White matter volume and cognitive dysfunction in early Huntington's disease.," *Behavioural Neurology*, vol. 18, pp. 102–107, 2005.

[15] E. H. Aylward, N. B. Anderson, F. W. Bylsma, M. V. Wagster, P. E. Barta, M. Sherr, J. Feeney, A. Davis, A. Rosenblatt, G. D. Pearlson, and C. A. Ross, "Frontal lobe volume in patients with Huntington's disease.," *Neurology*, vol. 50, pp. 252–258, 1998.

[16] E. H. Aylward, P. C. Nopoulos, C. A. Ross, D. R. Langbehn, R. K. Pierson, J. A. Mills, H. J. Johnson, V. A. Magnotta, A. R. Juhl, and J. S. Paulsen, "Longitudinal change in regional brain volumes in prodromal Huntington disease," *Journal of Neurology, Neurosurgery, & Psychiatry*, vol. 82, pp. 405–10, 2011.

[17] P. J. Basser, "Inferring microstructural features and the physiological state of tissues from diffusion-weighted images.," *NMR in Biomedicine*, vol. 8, pp. 333–334, 1995.

[18] P. J. Basser and C. Pierpaoli, "Microstructural and physiological features of tissues elucidated by quantitative-diffusion-tensor MRI.," *Journal of Magnetic Resonance, Series B*, vol. 111, pp. 209–219, 1996.

[19] D. K. Jones, T. R. Knösche, and R. Turner, "White matter integrity, fiber count, and other fallacies: The do's and don'ts of diffusion MRI.," *NeuroImage*, 2012.

[20] H. D. Rosas, D. S. Tuch, N. D. Hevelone, A. K. Zaleta, M. Vangel, S. M. Hersch, and D. H. Salat, "Diffusion tensor imaging in presymptomatic and early Huntington's disease: Selective white matter pathology and its relationship to clinical measures.," *Movement Disorders*, vol. 21, pp. 1317–25, 2006.

[21] R. Della Nave, A. Ginestroni, C. Tessa, M. Giannelli, S. Piacentini, M. Filippi, and M. Mascalchi, "Regional distribution and clinical correlates of white matter structural damage in Huntington disease: a tract-based spatial statistics study.," *AJNR. American Journal of Neuroradiology*, vol. 31, pp. 1675–1681, 2010.

[22] D. Stoffers, S. Sheldon, J. M. Kuperman, J. Goldstein, J. Corey-Bloom, and A. R. Aron, "Contrasting gray and white matter changes in preclinical Huntington disease: an MRI study.," *Neurology*, vol. 74, pp. 1208–1216, 2010.

[23] I. Bohanna, N. Georgiou-Karistianis, A. Sritharan, H. Asadi, L. Johnston, A. Churchyard, and G. Egan, "Diffusion tensor imaging in Huntington's disease reveals distinct patterns of white matter degeneration associated with motor and cognitive deficits.," *Brain Imaging and Behavior*, vol. 5, pp. 171–180, 2011.

[24] M. Mascalchi, F. Lolli, R. D. Nave, C. Tessa, R. Petralli, C. Gavazzi, L. S. Politi, M. Macucci, M. Filippi, and S. Piacentini, "Huntington disease: volumetric, diffusion-weighted, and magnetization transfer MR imaging of brain.," *Radiology*, vol. 232, pp. 867–873, 2004.

[25] K. E. Weaver, T. L. Richards, O. Liang, M. Y. Laurino, A. Samii, and E. H. Aylward, "Longitudinal diffusion tensor imaging in Huntington's Disease," *Experimental Neurology*, vol. 216, pp. 525–529, 2009.

[26] H. D. Rosas, S. Y. Lee, A. C. Bender, A. K. Zaleta, M. Vangel, P. Yu, B. Fischl, V. Pappu, C. Onorato, J.-H. Cha, D. H. Salat, and S. M. Hersch, "Altered white matter microstructure in the corpus callosum in Huntington's disease: implications for cortical "disconnection".," *NeuroImage*, vol. 49, pp. 2995–3004, 2010.

[27] A. Sritharan, G. F. Egan, L. Johnston, M. Horne, J. L. Bradshaw, I. Bohanna, H. Asadi, R. Cunnington, A. J. Churchyard, P. Chua, M. Farrow, and N. Georgiou-Karistianis, "A longitudinal diffusion tensor imaging study in symptomatic Huntington's disease," *Journal of Neurology, Neurosurgery, & Psychiatry*, vol. 81, pp. 257–262, 2010.

[28] H.-P. Müller, V. Glauche, M. J. U. Novak, T. Nguyen-Thanh, A. Unrath, N. Lahiri, J. Read, M. J. Say, S. J. Tabrizi, J. Kassubek, and S. Kloppel, "Stability of white matter changes related to Huntington's disease in the presence of imaging noise: a DTI study.," *PLoS Currents*, vol. 3, pp. RRN1232–RRN1232, 2011.

[29] M. Di Paola, E. Luders, A. Cherubini, C. Sanchez-Castaneda, P. M. Thompson, a. W. Toga, C. Caltagirone, S. Orobello, F. Elifani, F. Squitieri, and U. Sabatini, "Multimodal MRI Analysis of the Corpus Callosum Reveals White Matter Differences in Presymptomatic and Early Huntington's Disease.," *Cerebral Cortex*, vol. 22, pp. 2858–2866, 2012.

[30] E. M. Dumas, S. J. A. van den Bogaard, M. E. Ruber, R. R. Reilman, J. C. Stout, D. Craufurd, S. L. Hicks, C. Kennard, S. J. Tabrizi, M. A. van Buchem, J. van der Grond, and R. A. C. Roos, "Early changes in white matter pathways of the sensorimotor cortex in premanifest Huntington's disease.," *Human Brain Mapping*, vol. 33, pp. 203–212, 2012.

[31] G. E. Alexander, M. R. DeLong, and P. L. Strick, "Parallel organization of functionally segregated circuits linking basal ganglia and cortex.," *Annual Review of Neuroscience*, vol. 9, pp. 357–381, 1986.

[32] T. Arikuni and K. Kubota, "The organization of prefrontocaudate projections and their laminar origin in the macaque monkey: a retrograde study using HRP-gel.," *Journal of Comparative Neurology*, vol. 244, pp. 492–510, 1986.

[33] J. C. Hedreen and S. E. Folstein, "Early loss of neostriatal striosome neurons in Huntington's disease.," *Journal of Neuropathology & Experimental Neurology*, vol. 54, pp. 105–120, 1995.

[34] A. D. Lawrence, J. R. Hodges, A. E. Rosser, A. Kershaw, D. C. Rubinsztein, T. W. Robbins, B. J. Sahakian, and C. Ffrench-Constant, "Evidence for specific cognitive deficits in preclinical Huntingtons disease," *Brain*, vol. 121, pp. 1329–1341, 1998.

[35] S. A. J. Reading, M. A. Yassa, A. Bakker, A. C. Dziorny, L. M. Gourley, V. Yallapragada, A. Rosenblatt, R. L. Margolis, E. H. Aylward, J. Brandt, S. Mori, P. van Zijl, S. S. Bassett, and C. A. Ross, "Regional white matter change in pre-symptomatic Huntington's disease: a diffusion tensor imaging study.," *Psychiatry Research*, vol. 140, pp. 55–62, 2005.

[36] V. A. Magnotta, J. Kim, T. Koscik, L. J. Beglinger, D. Espinso, D. Langbehn, P. Nopoulos, and J. S. Paulsen, "Diffusion Tensor Imaging in Preclinical Huntington's Disease.," *Brain Imaging and Behavior*, vol. 3, pp. 77–84, 2009.

[37] C. Delmaire, E. M. Dumas, M. a. Sharman, S. J. a. van den Bogaard, R. Valabregue, C. Jauffret, D. Justo, R. Reilmann, J. C. Stout, D. Craufurd, S. J. Tabrizi, R. a. C. Roos, A. Durr, and S. Lehéricy, "The structural correlates of functional deficits in early huntington's disease.," *Human brain mapping*, vol. 000, 2012.

[38] D. K. Jones, A. Simmons, S. C. Williams, and M. A. Horsfield, "Non-invasive assessment of axonal fiber connectivity in the human brain via diffusion tensor MRI.," *Magnetic Resonance in Medicine*, vol. 42, pp. 37–41, 1999.

[39] P. J. Basser, S. Pajevic, C. Pierpaoli, J. Duda, and A. Aldroubi, "In vivo fiber tractography using DT-MRI data.," *Magnetic Resonance in Medicine*, vol. 44, pp. 625–32, 2000.

[40] S. Klöppel, B. Draganski, C. V. Golding, C. Chu, Z. Nagy, P. a. Cook, S. L. Hicks, C. Kennard, D. C. Alexander, G. J. M. Parker, S. J. Tabrizi, and R. S. J. Frackowiak, "White matter connections reflect changes in voluntary-guided saccades in pre-symptomatic Huntington's disease.," *Brain : a journal of neurology*, vol. 131, pp. 196–204, 2008.

[41] L. Marrakchi-Kacem, C. Delmaire, A. Tucholka, P. Roca, P. Guevara, F. Poupon, J. Yelnik, A. Durr, J.-F. Mangin, S. Lehericy, and C. Poupon, "Analysis of the striato-thalamo-cortical connectivity on the cortical surface to infer biomarkers of Huntington's disease.," *Medical Image Computing and Computer-Assisted Intervention*, vol. 13, pp. 217–224, 2010.

[42] I. Bohanna, N. Georgiou-Karistianis, and G. F. Egan, "Connectivity-based segmentation of the striatum in Huntington's disease: vulnerability of motor pathways.," *Neurobiology of Disease*, vol. 42, pp. 475–81, 2011.

[43] E. H. Aylward, Q. Li, O. C. Stine, N. Ranen, M. Sherr, P. E. Barta, F. W. Bylsma, G. D. Pearlson, and C. a. Ross, "Longitudinal change in basal ganglia volume in patients with Huntington's disease," *Neurology*, vol. 48, pp. 394–399, 1997.

[44] H. H. Ruocco, L. Bonilha, L. M. Li, I. Lopes-Cendes, and F. Cendes, "Longitudinal analysis of regional grey matter loss in Huntington disease: effects of the length of the expanded CAG repeat," *Journal of Neurology, Neurosurgery, & Psychiatry*, vol. 79, pp. 130–5, 2008.

[45] W. Vandenberghe, P. Demaerel, R. Dom, and F. Maes, "Diffusion-weighted versus volumetric imaging of the striatum in early symptomatic Huntington disease," *Journal of Neurology*, vol. 256, pp. 109–14, 2009.

[46] N. Z. Hobbs, J. Barnes, C. Frost, S. M. D. Henley, E. J. Wild, K. Macdonald, R. a. Barker, R. I. Scahill, N. C. Fox, and S. J. Tabrizi, "Onset and progression of pathologic atrophy in Huntington disease: a longitudinal MR imaging study," *AJNR. American Journal of Neuroradiology*, vol. 31, pp. 1036–41, 2010.

[47] N. Z. Hobbs, S. M. D. Henley, G. R. Ridgway, E. J. Wild, R. a. Barker, R. I. Scahill, J. Barnes, N. C. Fox, and S. J. Tabrizi, "The progression of regional atrophy in premanifest and early Huntington's disease: a longitudinal voxel-based morphometry study," *Journal of Neurology, Neurosurgery, & Psychiatry*, vol. 81, pp. 756–63, 2010.

[48] H. D. Rosas, M. Reuter, G. Doros, S. Y. Lee, T. Triggs, K. Malarick, B. Fischl, D. H. Salat, and S. M. Hersch, "A tale of two factors: what determines the rate of progression in Huntington's disease? A longitudinal MRI study," *Movement Disorders*, vol. 26, pp. 1691–7, 2011.

[49] S. J. Tabrizi, R. Reilmann, R. a. C. Roos, A. Durr, B. Leavitt, G. Owen, R. Jones, H. Johnson, D. Craufurd, S. L. Hicks, C. Kennard, B. Landwehrmeyer, J. C. Stout, B. Borowsky, R. I. Scahill, C. Frost, and D. R. Langbehn, "Potential endpoints for clinical trials in premanifest and early Huntington's disease in the TRACK-HD study: analysis of 24 month observational data," *Lancet Neurology*, vol. 11, pp. 42–53, 2012.

[50] C. M. Kipps, A. J. Duggins, N. Mahant, L. Gomes, J. Ashburner, and E. A. McCusker, "Progression of structural neuropathology in preclinical Huntington's disease: a tensor based morphometry study," *Journal of Neurology, Neurosurgery, & Psychiatry*, vol. 76, pp. 650–5, 2005.

[51] F. Squitieri, M. Cannella, M. Simonelli, J. Sassone, T. Martino, E. Venditti, A. Ciammola, C. Colonnese, L. Frati, and A. Ciarmiello, "Distinct Brain Volume Changes Correlating with Clinical Stage, Disease Progression Rate, Mutation Size, and Age at Onset Prediction as Early Biomarkers of Brain Atrophy in Huntington's Disease," *CNS Neuroscience & Therapeutics*, vol. 15, pp. 1–11, 2009.

[52] D. S. A. Majid, A. R. Aron, W. Thompson, S. Sheldon, S. Hamza, D. Stoffers, D. Holland, J. Goldstein, J. Corey-Bloom, and A. M. Dale, "Basal ganglia atrophy in prodromal Huntington's disease is detectable over one year using automated segmentation," *Movement Disorders*, vol. 26, pp. 2544–51, 2011.

[53] S. M. D. Henley, C. Frost, D. G. MacManus, T. T. Warner, N. C. Fox, and S. J. Tabrizi, "Increased rate of whole-brain atrophy over 6 months in early Huntington disease," *Neurology*, vol. 67, pp. 694–6, 2006.

[54] D. S. A. Majid, D. Stoffers, S. Sheldon, S. Hamza, W. K. Thompson, J. Goldstein, J. Corey-Bloom, and A. R. Aron, "Automated structural imaging analysis detects premanifest Huntington's disease neurodegeneration within 1 year," *Movement Disorders*, vol. 26, pp. 1481–8, 2011.

[55] E. O. Stejskal and J. E. Tanner, "Spin Diffusion Measurements: Spin Echoes in the Presence of a Time-Dependent Field Gradient," *Journal of Chemical Physics*, vol. 42, pp. 288, 1965.

[56] E. O. Stejskal, "Use of Spin Echoes in a Pulsed Magnetic-Field Gradient to Study Anisotropic, Restricted Diffusion and Flow," *Journal of Chemical Physics*, vol. 43, pp. 3597, 1965.

[57] R. V. Mulkern, H. Gudbjartsson, C. F. Westin, H. P. Zengingonul, W. Gartner, C. R. Guttmann, R. L. Robertson, W. Kyriakos, R. Schwartz, D. Holtzman, F. a. Jolesz, and S. E. Maier, "Multi-component apparent diffusion coefficients in human brain.," *NMR in Biomedicine*, vol. 12, pp. 51–62, 1999.

[58] C. A. Clark and D. Le Bihan, "Water diffusion compartmentation and anisotropy at high b values in the human brain," *Magnetic Resonance in Medicine*, vol. 44, pp. 852–859, 2000.

[59] R. V. Mulkern, H. P. Zengingonul, R. L. Robertson, P. Bogner, K. H. Zou, H. Gudbjartsson, C. R. G. Guttmann, D. Holtzman, W. Kyriakos, F. A. Jolesz, and S. E. Maier, "Multi-component apparent diffusion coefficients in human brain: Relationship to spin-lattice relaxation," *Magnetic Resonance in Medicine*, vol. 44, pp. 292–300, 2000.

[60] R. V. Mulkern, S. Vajapeyam, R. L. Robertson, P. a. Caruso, M. J. Rivkin, and S. E. Maier, "Biexponential apparent diffusion coefficient parametrization in adult vs newborn brain.," *Magnetic Resonance Imaging*, vol. 19, pp. 659–68, 2001.

[61] P. J. Basser, J. Mattiello, and D. LeBihan, "MR diffusion tensor spectroscopy and imaging.," *Biophysical Journal*, vol. 66, pp. 259–67, 1994.

[62] P. J. Basser, J. Mattiello, and D. Lebihan, "Estimation of the Effective Self-Diffusion Tensor from the NMR Spin Echo," *Journal of Magnetic Resonance, Series B*, vol. 103, pp. 247–254, 1994.

[63] P. B. Kingsley, "Introduction to Diffusion Tensor Imaging Mathematics: Part III. Tensor Calculation, Noise, Simulations, and Optimization," *Concepts In Magnetic Resonance Part A*, vol. 28A, pp. 155–179, 2006.

[64] P. B. Kingsley, "Introduction to Diffusion Tensor Imaging Mathematics: Part II. Anisotropy, Diffusion-Weighting Factors, and Gradient Encoding Schemes," *Concepts In Magnetic Resonance Part A*, vol. 28A, pp. 123–154, 2006.

[65] J. Mattiello, P. J. Basser, and D. Le Bihan, "The b matrix in diffusion tensor echo-planar imaging.," *Magnetic Resonance in Medicine*, vol. 37, pp. 292–300, 1997.

[66] K. M. Hasan, D. L. Parker, and A. L. Alexander, "Comparison of gradient encoding schemes for diffusion-tensor MRI," *Journal of Magnetic Resonance Imaging*, vol. 13, pp. 769–780, 2001.

[67] L.-C. Chang, D. K. Jones, and C. Pierpaoli, "RESTORE: robust estimation of tensors by outlier rejection.," *Magnetic Resonance in Medicine*, vol. 53, pp. 1088–95, 2005.

[68] T. Rowland and E. W. Weisstein, "Tensor," http://mathworld.wolfram.com/Tensor.html, 2013, Accessed November 15, 2013.

[69] E. W. Weisstein, "Symmetric Tensor," http://mathworld.wolfram.com/ SymmetricTensor.html, 2013, Accessed November 15, 2013.

[70] K. M. Hasan and P. A. Narayana, "Computation of the fractional anisotropy and mean diffusivity maps without tensor decoding and diagonalization: Theoretical analysis and validation," *Magnetic Resonance in Medicine*, vol. 50, pp. 589–598, 2003.

[71] P. B. Kingsley, "Introduction to Diffusion Tensor Imaging Mathematics: Part I. Tensors, Rotations, and Eigenvectors," *Concepts In Magnetic Resonance Part A*, vol. 28A, pp. 101–122, 2006.

[72] K. M. Hasan, P. J. Basser, D. L. Parker, and A. L. Alexander, "Analytical computation of the eigenvalues and eigenvectors in DT-MRI.," *Journal of Magnetic Resonance*, vol. 152, pp. 41–7, 2001.

[73] S.-K. Song, S.-W. Sun, W.-K. Ju, S.-J. Lin, A. H. Cross, and A. H. Neufeld, "Diffusion tensor imaging detects and differentiates axon and myelin degeneration in mouse optic nerve after retinal ischemia.," *NeuroImage*, vol. 20, pp. 1714–1722, 2003.

[74] S.-K. Song, S.-W. Sun, M. J. Ramsbottom, C. Chang, J. Russell, and A. H. Cross, "Dysmyelination revealed through MRI as increased radial (but unchanged axial) diffusion of water.," *Neuroimage*, vol. 17, pp. 1429–1436, 2002.

[75] S.-K. Song, J. Yoshino, T. Q. Le, S.-J. Lin, S.-W. Sun, A. H. Cross, and R. C. Armstrong, "Demyelination increases radial diffusivity in corpus callosum of mouse brain.," *NeuroImage*, vol. 26, pp. 132–140, 2005.

[76] E. Pagani, M. Filippi, M. A. Rocca, and M. a. Horsfield, "A method for obtaining tract-specific diffusion tensor MRI measurements in the presence of disease: application to patients with clinically isolated syndromes suggestive of multiple sclerosis.," *NeuroImage*, vol. 26, pp. 258–265, 2005.

[77] B. Bucur, D. J. Madden, J. Spaniol, J. M. Provenzale, R. Cabeza, L. E. White, and S. A. Huettel, "Age-related slowing of memory retrieval: contributions of perceptual speed and cerebral white matter integrity.," *Neurobiology of Aging*, vol. 29, pp. 1070–1079, 2008.

[78] J. Dubois, G. Dehaene-Lambertz, C. Soarès, Y. Cointepas, D. Le Bihan, and L. Hertz-Pannier, "Microstructural correlates of infant functional development: example of the visual pathways.," *Journal of Neuroscience*, vol. 28, pp. 1943–1948, 2008.

[79] P. J. Basser, "Fiber-Tractography via Diffusion Tensor MRI (DT-MRI)," *Proceedings of the 6th Annual Meeting ISMRM*, p. 1226, 1998.

[80] T. E. Conturo, N. F. Lori, T. S. Cull, E. Akbudak, A. Z. Snyder, J. S. Shimony, R. C. McKinstry, H. Burton, and M. E. Raichle, "Tracking neuronal fiber pathways in the living human brain.," *Proceedings of the National Academy of Sciences of the United States of America*, vol. 96, pp. 10422–7, 1999.

[81] S. Mori, B. J. Crain, V. P. Chacko, and P. C. van Zijl, "Three-dimensional tracking of axonal projections in the brain by magnetic resonance imaging.," *Annals of Neurology*, vol. 45, pp. 265–9, 1999.

[82] S. Pajevic, A. Aldroubi, and P. J. Basser, "A continuous tensor field approximation of discrete DT-MRI data for extracting microstructural and architectural features of tissue.," *Journal of Magnetic Resonance*, vol. 154, pp. 85–100, 2002.

[83] M. Lazar and A. L. Alexander, "An error analysis of white matter tractography methods: synthetic diffusion tensor field simulations.," *NeuroImage*, vol. 20, pp. 1140–53, 2003.

[84] D. Weinstein, G. Kindlmann, and E. Lundberg, "Tensorlines: advection-diffusion based propagation through diffusion tensor fields," *IEEE Visualization*, pp. 249–253, 1999.

[85] A. L. Alexander, "Deterministic White Matter Tractography," in *Diffusion MRI: Theory, Methods, and Applications*, D. K. Jones, Ed., chapter 22, pp. 383–395. Oxford University Press, Inc., 2011.

[86] P. Cheng, V. A. Magnotta, D. Wu, P. Nopoulos, D. J. Moser, J. Paulsen, R. Jorge, and N. C. Andreasen, "Evaluation of the GTRACT diffusion tensor tractography algorithm: a validation and reliability study.," *NeuroImage*, vol. 31, pp. 1075–1085, 2006.

[87] B. W. Kreher, I. Mader, and V. G. Kiselev, "Gibbs tracking: a novel approach for the reconstruction of neuronal pathways.," *Magnetic Resonance in Medicine*, vol. 60, pp. 953–63, 2008.

[88] A. Ozcan, "(Mathematical) Necessary conditions for the selection of gradient vectors in DTI.," *Journal of Magnetic Resonance*, vol. 172, pp. 238–41, 2005.

[89] D. Güllmar, J. Haueisen, J. R. J. R. Reichenbach, and D. Gllmar, "Analysis of b-value calculations in diffusion weighted and diffusion tensor imaging," *Concepts in Magnetic Resonance Part A*, vol. 25A, pp. 53–66, 2005.

[90] S. T. Wong and M. S. Roos, "A strategy for sampling on a sphere applied to 3D selective RF pulse design.," *Magnetic Resonance in Medicine*, vol. 32, pp. 778–84, 1994.

[91] N. G. Papadakis, D. Xing, G. C. Houston, J. M. Smith, M. I. Smith, M. F. James, A. A. Parsons, C. L.-H. Huang, L. D. Hall, T. A. Carpenter, A. S. Of, R. Invariant, S. I. Of, and D. Anisotropy, "A study of rotationally invariant and symmetric indices of diffusion anisotropy," *Magnetic Resonance Imaging*, vol. 17, pp. 881–892, 1999.

[92] P. G. Batchelor, D. Atkinson, D. L. G. Hill, F. Calamante, and A. Connelly, "Anisotropic noise propagation in diffusion tensor MRI sampling schemes.," *Magnetic Resonance in Medicine*, vol. 49, pp. 1143–51, 2003.

[93] D. K. Jones, "Determining and visualizing uncertainty in estimates of fiber orientation from diffusion tensor MRI.," *Magnetic Resonance in Medicine*, vol. 49, pp. 7–12, 2003.

[94] D. K. Jones, "The effect of gradient sampling schemes on measures derived from diffusion tensor MRI: a Monte Carlo study.," *Magnetic Resonance in Medicine*, vol. 51, pp. 807–15, 2004.

[95] T. G. Reese, O. Heid, R. M. Weisskoff, and V. J. Wedeen, "Reduction of eddy-current-induced distortion in diffusion MRI using a twice-refocused spin echo.," *Magnetic Resonance in Medicine*, vol. 49, pp. 177–82, 2003.

[96] D. J. Larkman and R. G. Nunes, "Parallel magnetic resonance imaging.," *Physics in Medicine and Biology*, vol. 52, pp. R15–55, 2007.

[97] S. Skare, R. D. Newbould, D. B. Clayton, G. W. Albers, S. Nagle, and R. Bammer, "Clinical multishot DW-EPI through parallel imaging with considerations of susceptibility, motion, and noise.," *Magnetic Resonance in Medicine*, vol. 57, pp. 881–90, 2007.

[98] A. Pfefferbaum, E. Adalsteinsson, and E. V. Sullivan, "Replicability of diffusion tensor imaging measurements of fractional anisotropy and trace in brain.," *Journal of Magnetic Resonance Imaging*, vol. 18, pp. 427–33, 2003.

[99] M. Cercignani, R. Bammer, M. P. Sormani, F. Fazekas, and M. Filippi, "Inter-sequence and inter-imaging unit variability of diffusion tensor MR imaging histogram-derived metrics of the brain in healthy volunteers.," *AJNR. American Journal of Neuroradiology*, vol. 24, pp. 638–43, 2003.

[100] C. Vollmar, J. O'Muircheartaigh, G. J. Barker, M. R. Symms, P. Thompson, V. Kumari, J. S. Duncan, M. P. Richardson, and M. J. Koepp, "Identical, but not the same: intra-site and inter-site reproducibility of fractional anisotropy measures on two 3.0T scanners.," *NeuroImage*, vol. 51, pp. 1384–1394, 2010.

[101] E. Pagani, J. G. Hirsch, P. J. W. Pouwels, M. A. Horsfield, E. Perego, A. Gass, S. D. Roosendaal, F. Barkhof, F. Agosta, M. Rovaris, D. Caputo, A. Giorgio, J. Palace, S. Marino, N. D. Stefano, S. Ropele, F. Fazekas, and M. Filippi, "Intercenter Differences in Diffusion Tensor MRI Acquisition," *Journal of Magnetic Resonance Imaging*, vol. 31, pp. 1458–1468, 2010.

[102] L. E. Danielian, N. K. Iwata, D. M. Thomasson, and M. K. Floeter, "Reliability of fiber tracking measurements in diffusion tensor imaging for longitudinal study.," *NeuroImage*, vol. 49, pp. 1572–80, 2010.

[103] J. Y. Wang, H. Abdi, K. Bakhadirov, R. Diaz-Arrastia, and M. D. Devous, "A comprehensive reliability assessment of quantitative diffusion tensor tractography.," *NeuroImage*, vol. 60, pp. 1127–1138, 2012.

[104] C. Andreasen, T. Cizadlo, V. W. Swayze, N. C. Andreasen, G. Cohen, G. Harris, J. Parkkinen, and K. Rezai, "Image processing for the study of brain structure and function: problems and programs.," *Journal of Neuropsychiatry and Clinical Neurosciences*, vol. 4, pp. 125–33, 1992.

[105] N. C. Andreasen, T. Cizadlo, G. Harris, V. Swayze, D. S. O'Leary, G. Cohen, J. Ehrhardt, and W. T. Yuh, "Voxel processing techniques for the antemortem study of neuroanatomy and neuropathology using magnetic resonance imaging.," *The Journal of Neuropsychiatry & Clinical Neurosciences*, vol. 5, pp. 121–130, 1993.

[106] V. a. Magnotta, G. Harris, N. C. Andreasen, D. S. O'Leary, W. T. C. Yuh, and D. Heckel, "Structural MR image processing using the BRAINS2 toolbox.," *Computerized Medical Imaging and Graphics*, vol. 26, pp. 251–64, 2002.

[107] R. Pierson, H. Johnson, G. Harris, H. Keefe, J. S. Paulsen, N. C. Andreasen, and V. a. Magnotta, "Fully automated analysis using BRAINS: AutoWorkup.," *NeuroImage*, vol. 54, pp. 328–336, 2011.

[108] V. A. Magnotta, D. Heckel, N. C. Andreasen, T. Cizadlo, P. W. Corson, J. C. Ehrhardt, W. T. C. Yuh, and P. Westmoreland, "Measurement of brain structures with artificial neural networks: two- and three-dimensional applications.," *Radiology*, vol. 211, pp. 781–90, 1999.

[109] N. C. Andreasen, R. Rajarethinam, T. Cizadlo, S. Arndt, V. W. Swayze, L. A. Flashman, D. S. O'Leary, J. C. Ehrhardt, and W. T. Yuh, "Automatic atlas-based volume estimation of human brain regions from MR images.," *Journal of Computer Assisted Tomography*, vol. 20, pp. 98–106, 1996.

[110] Slicer, "DicomToNrrdConverter online documentation," http://www.slicer.org/slicerWiki/index.php/Documentation/4.0/Modules/DicomToNrrdConverter, 2013, Accessed November 15, 2013.

[111] BRAINSia, "DWIConvert repository," https://github.com/BRAINSia/BRAINSTools/tree/master/DWIConvert, 2013, Accessed November 15, 2013.

[112] NEMA, "DICOM: Digital Imaging and Communications in Medicine," .

[113] Z. Liu, Y. Wang, G. Gerig, S. Gouttard, R. Tao, T. Fletcher, and M. Styner, "Quality control of diffusion weighted images," *Proc eedings of SPIE*, vol. 7628, pp. 76280J–1, 2010.

[114] D. Mattes, D. R. Haynor, H. Vesselle, T. K. Lewellen, and W. Eubank, "PET-CT image registration in the chest using free-form deformations.," *IEEE Transactions on Medical Imaging*, vol. 22, pp. 120–8, 2003.

[115] S. Kabus, T. Netsch, B. Fischer, and J. Modersitzki, "B-spline registration of 3D images with Levenberg-Marquardt optimization," *Proceedings of SPIE*, vol. 5370, pp. 304–313, 2004.

[116] Y. Zhang, J. D. Long, J. a. Mills, J. H. Warner, W. Lu, and J. S. Paulsen, "Indexing disease progression at study entry with individuals at-risk for Huntington disease.," *American Journal of Medical Genetics Part B Neuropsychiatric Genetics*, vol. 156B, pp. 751–763, 2011.

[117] H. S. Group and Huntington Study Group, "Unified Huntingtons Disease Rating Scale: Reliability and Consistency," *Movement Disorders*, vol. 11, pp. 136–142, 1996.

[118] A. Smith, *Symbol Digit Modalities Test. Manual (revised)*, Western Psychological Services., Los Angeles, 1991.

[119] J. R. Stroop, "Studies of interference in serial verbal reactions.," *Journal of Experimental Psychology*, vol. 18, pp. 643–662, 1935.

[120] R. M. Reitan, "Validity of the Trail Making Test as an indicator of organic brain damage," *Perceptual & Motor Skills*, vol. 8, pp. 271–276, 1958.

[121] Y. Benjamini and Y. Hochberg, "Controlling the false discovery rate: a practical and powerful approach to multiple testing," *Journal of the Royal Statistical Society: Series B*, vol. 57, pp. 289–300, 1995.

[122] J. C. Stout, J. S. Paulsen, S. Queller, A. C. Solomon, K. B. Whitlock, J. C. Campbell, N. Carlozzi, K. Duff, L. J. Beglinger, D. R. Langbehn, S. a. Johnson, K. M. Biglan, and E. H. Aylward, "Neurocognitive signs in prodromal Huntington disease.," *Neuropsychology*, vol. 25, pp. 1–14, 2011.

[123] M. Takahashi, D. B. Hackney, G. Zhang, S. L. Wehrli, A. C. Wright, W. T. O'Brien, H. Uematsu, F. W. Wehrli, and M. E. Selzer, "Magnetic resonance microimaging of intraaxonal water diffusion in live excised lamprey spinal cord.," *Proceedings of the National Academy of Sciences of the United States of America*, vol. 99, pp. 16192–6, 2002.

[124] J. Acosta-Cabronero, G. B. Williams, G. Pengas, and P. J. Nestor, "Absolute diffusivities define the landscape of white matter degeneration in Alzheimer's disease.," *Brain*, vol. 133, pp. 529–39, 2010.

[125] A. Privat, C. Jacque, J. M. Bourre, P. Dupouey, and N. Baumann, "Absence of the major dense line in myelin of the mutant mouse "shiverer".," *Neuroscience Letters*, vol. 12, pp. 107–12, 1979.

[126] J. Rosenbluth, "Central myelin in the mouse mutant shiverer.," *Journal of Comparative Neurology*, vol. 194, pp. 639–48, 1980.

[127] Y. Inoue, R. Nakamura, K. Mikoshiba, and Y. Tsukada, "Fine structure of the central myelin sheath in the myelin deficient mutant Shiverer mouse, with special reference to the pattern of myelin formation by oligodendroglia.," *Brain Research*, vol. 219, pp. 85–94, 1981.

[128] X. Y. Shen, S. Billings-Gagliardi, R. L. Sidman, and M. K. Wolf, "Myelin deficient (shimld) mutant allele: morphological comparison with shiverer (shi) allele on a B6C3 mouse stock.," *Brain Research*, vol. 360, pp. 235–47, 1985.

[129] G. M. Halliday, D. A. McRitchie, V. Macdonald, K. L. Double, R. J. Trent, and E. McCusker, "Regional specificity of brain atrophy in Huntington's disease.," *Experimental Neurology*, vol. 154, pp. 663–72, 1998.

[130] A. M. Fjell, L. T. Westlye, D. N. Greve, B. Fischl, T. Benner, A. J. W. van der Kouwe, D. Salat, A. Bjø rnerud, P. Due-Tø nnessen, and K. B. Walhovd, "The relationship between diffusion tensor imaging and volumetry as measures of white matter properties.," *NeuroImage*, vol. 42, pp. 1654–68, 2008.

[131] C. K. Tamnes, Y. Ostby, A. M. Fjell, L. T. Westlye, P. Due-Tø nnessen, and K. B. Walhovd, "Brain maturation in adolescence and young adulthood: regional age-related changes in cortical thickness and white matter volume and microstructure.," *Cerebral Cortex*, vol. 20, pp. 534–48, 2010.

[132] D. H. Salat, D. N. Greve, J. L. Pacheco, B. T. Quinn, K. G. Helmer, R. L. Buckner, and B. Fischl, "Regional white matter volume differences in nondemented aging and Alzheimer's disease.," *NeuroImage*, vol. 44, pp. 1247–58, 2009.

[133] J. M. Fuster, *The Prefrontal Cortex*, Academic Press/Elsevier, Amsterdam, Boston, 2009.

[134] J. L. Perry, J. E. Joseph, Y. Jiang, R. S. Zimmerman, T. H. Kelly, M. Darna, P. Huettl, L. P. Dwoskin, and M. T. Bardo, "Prefrontal cortex and drug abuse vulnerability: translation to prevention and treatment interventions.," *Brain Research Reviews*, vol. 65, pp. 124–49, 2011.

[135] J. J. F. O'Rourke, L. J. Beglinger, M. M. Smith, J. Mills, D. J. Moser, K. C. Rowe, D. R. Langbehn, and K. Duff, "The Trail Making Test in prodromal Huntington disease: Contributions of disease progression to test performance," *Journal of Clinical and Experimental Neuropsychology*, vol. 33, pp. 567–579, 2011.

[136] J. H. Jensen, J. A. Helpern, A. Ramani, H. Lu, and K. Kaczynski, "Diffusional kurtosis imaging: the quantification of non-gaussian water diffusion by means of magnetic resonance imaging.," *Magnetic Resonance in Medicine*, vol. 53, pp. 1432–40, 2005.

[137] J. A. Helpern, C. Lo, C. Hu, M. F. Falangola, O. Rapalino, and J. H. Jensen, "Diffusional kurtosis imaging in acute human stroke," in *Proc Intl Soc Mag Reson Med 17*, 2009, p. 3493.

[138] J. Lätt, D. Van Westen, M. Nilsson, R. Wirestam, F. Stå hlberg, S. Holtå s, and S. Brockstedt, "Diffusion time dependent kurtosis maps visualize ischemic lesions in stroke patients," in *Proc Intl Soc Mag Reson Med 17*, 2009, p. 40.

[139] M. F. Falangola, J. H. Jensen, J. S. Babb, C. Hu, F. X. Castellanos, A. Di Martino, S. H. Ferris, and J. A. Helpern, "Age-related non-Gaussian diffusion patterns in the prefrontal brain.," *Journal of Magnetic Resonance Imaging*, vol. 28, pp. 1345–50, 2008.

[140] A. Ramani, J. H. Jensen, K. U. Szulc, O. Ali, C. Hu, H. Lu, J. D. Brodle, and J. A. Helpern, "Assessment of abnormalities in the cerebral microstructure of schizophrenia patients: a diffusional kurtosis imaging study," in *Proc Intl Soc Mag Reson Med 15*, 2007, p. 648.

[141] J. A. Helpern, M. F. Falangola, A. Di Martino, A. Ramani, J. S. Babb, C. Hu, J. H. Jensen, and F. X. Castellanos, "Alterations in brain microstructure in ADHD by diffusional kurtosis imaging," *Proc Intl Soc Mag Reson Med 15*, vol. 12, pp. 1580, 2007.

[142] D. S. Tuch, T. G. Reese, M. R. Wiegell, N. Makris, J. W. Belliveau, and V. J. Wedeen, "High angular resolution diffusion imaging reveals intravoxel white matter fiber heterogeneity.," *Magnetic resonance in medicine : official journal of the Society of Magnetic Resonance in Medicine / Society of Magnetic Resonance in Medicine*, vol. 48, pp. 577–82, 2002.

[143] S. Wakana, H. Jiang, L. M. Nagae-Poetscher, S. Mori, and P. C. M. van Zijl, "Fiber Tractbased Atlas of Human White Matter Anatomy," *Radiology*, pp. 21–29, 2004.

[144] L. K. Paul, "Developmental malformation of the corpus callosum: a review of typical callosal development and examples of developmental disorders with callosal involvement.," *Journal of neurodevelopmental disorders*, vol. 3, pp. 3–27, 2011.

[145] Y. D. Van der Werf, J. Jolles, M. P. Witter, and H. B. M. Uylings, "Contributions of thalamic nuclei to declarative memory functioning.," *Cortex; a journal devoted to the study of the nervous system and behavior*, vol. 39, pp. 1047–62, 2003.

[146] D. Mamah, T. E. Conturo, M. P. Harms, E. Akbudak, L. Wang, A. R. McMichael, M. H. Gado, D. M. Barch, and J. G. Csernansky, "Anterior thalamic radiation integrity in schizophrenia: a diffusion-tensor imaging study.," *Psychiatry research*, vol. 183, pp. 144–50, 2010.

[147] M. Catani and M. Thiebaut de Schotten, "A diffusion tensor imaging tractography atlas for virtual in vivo dissections.," *Cortex; a journal devoted to the study of the nervous system and behavior*, vol. 44, pp. 1105–32, 2008.

[148] M. Catani, M. P. G. Allin, M. Husain, L. Pugliese, M. M. Mesulam, R. M. Murray, and D. K. Jones, "Symmetries in human brain language pathways correlate with verbal recall.," *Proceedings of the National Academy of Sciences of the United States of America*, vol. 104, pp. 17163–8, 2007.

[149] S. Epelbaum, P. Pinel, R. Gaillard, C. Delmaire, M. Perrin, S. Dupont, S. Dehaene, and L. Cohen, "Pure alexia as a disconnection syndrome: new diffusion imaging evidence for an old concept.," *Cortex; a journal devoted to the study of the nervous system and behavior*, vol. 44, pp. 962–74, 2008.

[150] F. Doricchi, M. Thiebaut de Schotten, F. Tomaiuolo, and P. Bartolomeo, "White matter (dis)connections and gray matter (dys)functions in visual neglect: gaining insights into the brain networks of spatial awareness.," *Cortex; a journal devoted to the study of the nervous system and behavior*, vol. 44, pp. 983–95, 2008.

[151] D. Rudrauf, S. Mehta, and T. J. Grabowski, "Disconnection's renaissance takes shape: Formal incorporation in group-level lesion studies.," *Cortex; a journal devoted to the study of the nervous system and behavior*, vol. 44, pp. 1084–96, 2008.

[152] R. J. Von Der Heide, L. M. Skipper, E. Klobusicky, and I. R. Olson, "Dissecting the uncinate fasciculus: disorders, controversies and a hypothesis.," *Brain : a journal of neurology*, vol. 136, pp. 1692–707, 2013.

[153] BRAINSia, "BRAINSTools," https://github.com/BRAINSia/BRAINSTools, 2013, Accessed November 15, 2013.

[154] B. B. Avants, C. L. Epstein, M. Grossman, and J. C. Gee, "Symmetric diffeomorphic image registration with cross-correlation: evaluating automated labeling of elderly and neurodegenerative brain.," *Medical image analysis*, vol. 12, pp. 26–41, 2008.

[155] B. B. Avants, N. J. Tustison, and H. J. Johnson, "Advanced Normalization Tools," http://stnava.github.io/ANTs, 2013, Accessed November 15, 2013.

[156] A. Ghayoor, J. G. Vaidya, and H. J. Johnson, "Development of a novel constellation based landmark detection algorithm," in *SPIE Medical Imaging*. 2013, pp. 86693F–86693F–6, International Society for Optics and Photonics.

[157] B. B. Avants, C. L. Epstein, and J. C. Gee, "Geodesic Image Normalization in the Space of Diffeomorphisms," *Mathematical Foundations of Computational Anatomy*, pp. 125–135, 2006.

[158] D. C. Alexander, C. Pierpaoli, P. J. Basser, and J. C. Gee, "Spatial Transformations of Diffusion Tensor Magnetic Resonance Images," *IEEE transactions on medical imaging*, vol. 20, pp. 1131–1139, 2001.

[159] F. Budin, S. Bouix, M. Shenton, M. Styner, and I. Oguz, "An ITK Implementation of a Diffusion Tensor Images Resampling Filter," *Insight Journal*, pp. 1–12, 2011.

[160] A. Kaiser, "DTIAtlasBuilder," https://github.com/NIRALUser/DTIAtlasBuilder, 2013, Accessed November 15, 2013.

[161] V. Arsigny, P. Fillard, X. Pennec, and N. Ayache, "Log-Euclidean metrics for fast and simple calculus on diffusion tensors.," *Magnetic Resonance in Medicine*, vol. 56, pp. 411–21, 2006.

[162] B. Avants and J. C. Gee, "Geodesic estimation for large deformation anatomical shape averaging and interpolation.," *NeuroImage*, vol. 23 Suppl 1, pp. S139–S150, 2004.

[163] B. B. Avants, P. Yushkevich, J. Pluta, D. Minkoff, M. Korczykowski, J. Detre, and J. C. Gee, "The optimal template effect in hippocampus studies of diseased populations.," *NeuroImage*, vol. 49, pp. 2457–66, 2010.

[164] N. J. Tustison, B. B. Avants, P. a. Cook, J. Kim, J. Whyte, J. C. Gee, and J. R. Stone, "Logical circularity in voxel-based analysis: Normalization strategy may induce statistical bias.," *Human brain mapping*, vol. 000, 2012.

[165] D. Wassermann, "TractographyLabelMapSeeding," http://www.slicer.org /slicerWiki/index.php/Documentation/4.0/Modules/TractographyLabelMap-Seeding, 2013, Accessed November 15, 2013.

[166] D. Wassermann, "TractographyDisplay," http://www.slicer.org /slicerWiki/index.php/Documentation/4.2/Modules/TractographyDisplay, 2013, Accessed November 15, 2013.

[167] S. Wakana, A. Caprihan, M. M. Panzenboeck, J. H. Fallon, M. Perry, R. L. Gollub, K. Hua, J. Zhang, H. Jiang, P. Dubey, A. Blitz, P. van Zijl, and S. Mori, "Reproducibility of quantitative tractography methods applied to cerebral white matter.," *NeuroImage*, vol. 36, pp. 630–44, 2007.

[168] K. Oishi, A. Faria, P. C. M. van Zijl, and S. Mori, *MRI Atlas of Human White matter*, Academic Press/Elsevier, 2 edition, 2010.

[169] D. Wassermann, L. Bloy, E. Kanterakis, R. Verma, and R. Deriche, "Unsupervised white matter fiber clustering and tract probability map generation: applications of a Gaussian process framework for white matter fibers.," *NeuroImage*, vol. 51, pp. 228–41, 2010.

[170] D. Wassermann, E. Kanterakis, R. C. Gur, R. Deriche, and R. Verma, "Diffusion-based population statistics using tract probability maps.," *Medical Image Computing and Computer-Assisted Intervention*, vol. 13, pp. 631–9, 2010.

[171] S. M. Smith, M. Jenkinson, H. Johansen-Berg, D. Rueckert, T. E. Nichols, C. E. Mackay, K. E. Watkins, O. Ciccarelli, M. Z. Cader, P. M. Matthews, and T. E. J. Behrens, "Tract-based spatial statistics: voxelwise analysis of multi-subject diffusion data.," *NeuroImage*, vol. 31, pp. 1487–505, 2006.

[172] S. M. Smith, M. Jenkinson, M. W. Woolrich, C. F. Beckmann, T. E. J. Behrens, H. Johansen-Berg, P. R. Bannister, M. De Luca, I. Drobnjak, D. E. Flitney, R. K. Niazy, J. Saunders, J. Vickers, Y. Zhang, N. De Stefano, J. M. Brady, and P. M. Matthews, "Advances in functional and structural MR image analysis and implementation as FSL.," *NeuroImage*, vol. 23 Suppl 1, pp. S208–19, 2004.

[173] T. E. Nichols and A. P. Holmes, "Nonparametric permutation tests for functional neuroimaging: a primer with examples.," *Human brain mapping*, vol. 15, pp. 1–25, 2002.

[174] M. J. Anderson and J. Robinson, "Permutation tests for linear models," *Australian & New Zealand Journal of Statistics*, vol. 43, pp. 75–88, 2001.

[175] A. Burzynska, C. Preuschhof, L. Bäckman, L. Nyberg, S.-C. Li, U. Lindenberger, and H. Heekeren, "Age-related differences in white matter microstructure: Region-specific patterns of diffusivity," *NeuroImage*, vol. 49, pp. 2104–2112, 2010.

[176] a. P. Holmes, R. C. Blair, J. D. Watson, and I. Ford, "Nonparametric analysis of statistic images from functional mapping experiments.," *Journal of cerebral blood flow and metabolism : official journal of the International Society of Cerebral Blood Flow and Metabolism*, vol. 16, pp. 7–22, 1996.

[177] S. M. Smith and T. E. Nichols, "Threshold-free cluster enhancement: addressing problems of smoothing, threshold dependence and localisation in cluster inference.," *NeuroImage*, vol. 44, pp. 83–98, 2009.

[178] J. T. Matsui, J. G. Vaidya, H. J. Johnson, V. A. Magnotta, J. D. Long, J. A. Mills, M. J. Lowe, K. E. Sakaie, S. M. Rao, M. M. Smith, and J. S. Paulsen, "Diffusion weighted imaging of prefrontal cortex in prodromal huntington's disease.," *Human Brain Mapping*, 2013.

[179] R. S. Desikan, F. Ségonne, B. Fischl, B. T. Quinn, B. C. Dickerson, D. Blacker, R. L. Buckner, A. M. Dale, R. P. Maguire, B. T. Hyman, M. S. Albert, and R. J. Killiany, "An automated labeling system for subdividing the human cerebral cortex on MRI scans into gyral based regions of interest," *NeuroImage*, vol. 31, pp. 968–980, 2006.

[180] M. Webster, "Randomise," http://fsl.fmrib.ox.ac.uk/fsl/fslwiki/Randomise, 2013, Accessed November 15, 2013.

[181] T. E. Nichols, "Randomise Theory," http://fsl.fmrib.ox.ac.uk/fsl/fslwiki/Randomise/Theory, 2013, Accessed November 15, 2013.

[182] K. J. Friston, a. Holmes, J. B. Poline, C. J. Price, and C. D. Frith, "Detecting activations in PET and fMRI: levels of inference and power.," *NeuroImage*, vol. 4, pp. 223–35, 1996.

[183] K. J. Friston, K. J. Worsley, R. S. J. Frackowiak, J. C. Mazziotta, and A. C. Evans, "Assessing the significance of focal activations using their spatial extent," *Human Brain Mapping*, vol. 1, pp. 210–220, 1993.

[184] C. R. Genovese, N. a. Lazar, and T. Nichols, "Thresholding of statistical maps in functional neuroimaging using the false discovery rate.," *NeuroImage*, vol. 15, pp. 870–8, 2002.

[185] M. Lorenzi and X. Pennec, "Geodesics, Parallel Transport & One-Parameter Subgroups for Diffeomorphic Image Registration," *International Journal of Computer Vision*, 2012.

[186] T. Vercauteren, X. Pennec, A. Perchant, and N. Ayache, "Symmetric log-domain diffeomorphic registration: a demons-based approach.," *Medical Image Computing and Computer-Assisted Intervention*, vol. 11, pp. 754–761, 2008.

[187] T. Vercauteren, X. Pennec, A. Perchant, and N. Ayache, "Diffeomorphic demons: efficient non-parametric image registration.," *NeuroImage*, vol. 45, pp. S61–72, 2009.

[188] P. Cachier, E. Bardinet, D. Dormont, X. Pennec, and N. Ayache, "Iconic feature based nonrigid registration: the PASHA algorithm," *Computer Vision and Image Understanding*, vol. 89, pp. 272–298, 2003.

[189] T. Vercauteren, X. Pennec, E. Malis, A. Perchant, and N. Ayache, "Insight into efficient image registration techniques and the demons algorithm.," *Information processing in medical imaging : proceedings of the ... conference*, vol. 20, pp. 495–506, 2007.

[190] M. Lorenzi, N. Ayache, X. Pennec, and Alzheimer's Disease Neuroimaging Initiative, "Schild's ladder for the parallel transport of deformations in time series of images," *Information Processing in Medical Imaging*, vol. 22, pp. 463–74, 2011.

[191] F. Dru and T. Vercauteren, "An ITK Implementation of the Symmetric Log-Domain Diffeomorphic Demons Algorithm," pp. 1–10, 2009.

[192] M. Jenkinson, "FDR," http://fsl.fmrib.ox.ac.uk/fsl/fslwiki/FDR, 2013, Accessed November 15, 2013.

[193] T. E. Nichols, "GLM," http://fsl.fmrib.ox.ac.uk/fsl/fslwiki/GLM, 2013, Accessed November 15, 2013.